STUDIES OF LONGITUDINAL BEAM DYNAMICS
WITH STRONG SPACE CHARGE EFFECTS
USING A SMALL ISOCHRONOUS RING

by

Jose Alberto Rodriguez

A DISSERTATION

Submitted to
Michigan State University
in partial fulfillment of the requirements
for the degree of

DOCTOR OF PHYLOSOPHY

Department of Physics and Astronomy

2004

ABSTRACT

STUDIES OF LONGITUDINAL BEAM DYNAMICS
WITH STRONG SPACE CHARGE EFFECTS
USING A SMALL ISOCHRONOUS RING

by

Jose Alberto Rodriguez

In recent years, based on the successful operation of the PSI cyclotron, a number of authors have proposed to use high power cyclotrons for various applications. Space charge forces become especially relevant in these machines due to the large beam currents involved. There is a consensus in the cyclotron community that a deeper knowledge of these forces is necessary to successfully build such a cyclotron. This dissertation is part of an effort carried out at the National Superconducting Cyclotron Laboratory (NSCL) to better understand these effects. Using a Small Isochronous Ring (SIR) that works in a space charge dominated regime, we are able to observe and study some of the same space charge effects that are expected in much larger machines. The focus of this dissertation is to describe the injection and extraction line of SIR as well as its control system. We will also discuss the results of simulations performed to describe the beam dynamics in SIR and how those results compare with the experiments.

Dedicado a mis padres.
Gracias.

ACKNOWLEDGMENTS

A lot of people at the NSCL have collaborated one way or another in the SIR project. I am grateful to all of them.

In particular I would like to thank Professor Felix Marti. He has guided me, as my supervisor, through the past few years. His expertise has been absolutely critical to build SIR. It has been a pleasure and a great opportunity to work for him. I will not forget how much he has helped me. Thank you very much.

I also want to say thank you to Eduard Pozdeyev. He came up with the idea of SIR. We spent many hours together designing and building it. During that time, we developed a great friendship. Thank you very much.

Richard York has played a very important role in the SIR project. His interest and support has been essential in getting it built. Thank you very much.

Roger Zink, Renan Fontus and John Bierwagen have worked in the mechanical design of SIR. Working with them has been a great experience. Thank you for your critical contribution. I will not forget it.

Dave Sanderson has aligned all the elements of SIR. He also gave us a lot of advices on vacuum equipment. Don Lawton, Al Zeller, Dallas Cole, Scott Hitchcock and Dan Pedtke have collaborated in different ways with their expertise and a lot of ideas. I am grateful to all of them.

David Devereaux has helped us assembling SIR. I wish you the best in your future.

My first physics teacher, Don Juan Carlos Perez at the "Salesianos de Atocha" school, played a very important role in my life. Because of him, I started

TABLE OF CONTENTS

LIST OF TABLES

LIST OF FIGURES

Note: Some of the figures in this document use color.

xiv

SYMBOLS AND ABBREVIATIONS

COSY   Code to perform beam dynamics calculations

CYCO   Code to perform beam dynamics calculations with strong space charge forces

dB $Gain(dB) \equiv 10 \cdot \log_{10}\left(\dfrac{P_{OUT}}{P_{IN}}\right)$ where P_{IN} and P_{OUT} are input and output power respectively

dBm $P_{OUT}(dBm) \equiv 10 \cdot \log_{10}\left(\dfrac{P_{OUT}(mW)}{1mW}\right)$

EPAC   European Particle Accelerator Conference

ECRIS   ECR Ion Source conference

FFT   Fast Fourier Transform

LabVIEW   LABoratory Virtual Instrument Engineering Workbench

LINAC   LINear ACcelerator

LCW   Low Conductivity Water

MatLab   MATrices LABoratory

MHV   Miniature High Voltage connector

MSU   Michigan State University

NSCL   National Superconducting Cyclotron Laboratory

OFHC   Oxygen Free High Conductivity

PAC   Particle Accelerator Conference

PRST-AB   Physical Review Special Topics – Accelerators and Beams

PSI   Paul Scherrer Institute

PXI   Pci eXtensions for Instrumentation

RFQ   Radio Frequency Quadrupole

SCUBEEx   Self Consistent Unbiased Elliptical Exclusion algorithm

SHV   Safe High Voltage connector

SIMION   Code to perform calculations of electrostatic fields and to track ions in those fields

SIR	Small Isochronous Ring
SMA	Sub-Miniature type A connector
SNS	Spallation Neutron Source
Tcl/Tk	Tool Command Language / Tool Kit
TDR	Time Domain Reflectometer

1.   INTRODUCTION

In recent years, a number of authors have proposed using high power cyclotrons (typically 1 GeV energy and 10 mA beam current) for different applications including neutron generators, production of tritium, radioactive waste transmutation and driving thermonuclear reactors. Some of the details of these proposals are briefly discussed in the next section of this chapter.

The repulsion among ions in a bunch (i.e. space charge forces) at these current levels become very important and must be considered when such a machine is designed.

While the vertical size of the bunch can be controlled by increasing the vertical focusing strength, the longitudinal space charge electric field will induce energy spread within the bunch. Ions in the head (i.e. front portion) of the bunch will gain energy, while those in the tail will lose it. Since cyclotrons are isochronous, the length of the bunch will not change but the radial size of the bunch will increase. Ions in the head will describe a trajectory with a larger radius though maintaining a constant revolution frequency despite their higher energy. In a similar way, the radial position of ions in the tail will be reduced. Refer to [1] for a complete description of this process.

This effect reduces the turn separation making beam extraction difficult. Part of the beam is lost in the extraction deflector and these losses induce activation and heating of the deflector that are not acceptable at this power level.

The operation of the PSI Injector II cyclotron (2 mA average current) has proven that if the length of the injected bunches is short enough (~ 1-2 cm), the

transverse size of the bunch does not grow and adequate turn separation is maintained.

Even though some understanding about space charge effects in the isochronous regime exists, this knowledge is not yet complete. Quoting from [2]:

"Available technologies and experience at PSI are a realistic basis for the design of a cyclotron as a 10 MW proton driver. While scaling laws are seen to apply in a wide range, further progress in the simulation of space charge dominated beams is needed to estimate the ultimate performance of this type of accelerator."

This dissertation is part of an effort carried out at the National Superconducting Cyclotron Laboratory (NSCL) at Michigan State University (MSU) to better understand these effects. Several years ago, Eduard Pozdeyev and Felix Marti started this effort by developing a computer code for beam dynamics simulations in this regime. The results of these preliminary calculations showed interesting behaviors that were not intuitive. They decided to find a way to experimentally validate the results of the simulations. The possibility of requesting beam time at the PSI Injector II was studied.

Since space charge effects are greater at lower beam energies, it is possible to experimentally study these effects with a much lower energy and beam current machine. As described in section 1.3, only 12.9 μA of H_2^+ at 20 keV is necessary to experience similar space charge forces to those in the PSI Injector II cyclotron. A small dedicated machine would also have a number of advantages. Some of them are explained in section 1.4.

The decision was made to build such a machine. It was called the Small Isochronous Ring (SIR). At that time, I joined the group and it was decided that I would mainly work in the injection and extraction lines while another graduate student, Eduard Pozdeyev, would work on the ring (complete description in [3]).

The focus of this dissertation is to describe the injection and extraction line of SIR as well as its control system. We will also discuss the results of simulations performed to describe the beam dynamics in SIR and how some of those results compare with the experiments.

1.1. High power cyclotrons

The PSI high intensity cyclotron presently has the highest beam power of any accelerator in the world. It is capable of delivering 2 mA of a 590 MeV proton beam yielding 1.18 MW of beam power. (Presumably, the Spallation Neutron Source (SNS) will soon be capable of delivering 1.4 mA of a 1 GeV H$^-$ beam surpassing the PSI facility.)

At PSI, a Cockcroft-Walton generator is used as a preinjector accelerating ions up to 870 keV. This beam is bunched a way such that when the bunches are accelerated to 72 MeV, their length is approximately equal to their diameter. As previously mentioned, these "circular" bunches do not deform as they are accelerated through the machine. Therefore, the turn separation does not vanish and the extraction losses are kept below 0.02 %.

By the time the bunches are injected into the ring cyclotron, they have elongated due to longitudinal space charge forces in the transfer line. Therefore,

they experience the radial tilting of the bunch described before although it is not large enough to completely lose the turn separation (~ 6 mm). This distance is doubled at the extraction point by injecting the bunches off-center, inducing a betatron oscillation. The 12 mm separation is enough to keep losses in the deflector low when the 590 MeV beam is extracted.

P. A. Schmelzbach et al. proposed in [2] a 10 mA 1 GeV machine directly extrapolating the current PSI cyclotrons scheme. They suggest using an RFQ as a preinjector into a 120 MeV injector cyclotron as an alternative to the Cockcroft-Walton generator.

They propose adding two more accelerating cavities in the injector cyclotron to double the energy gain per revolution. The additional energy gain is to provide adequate turn separation despite a larger transverse size of the circular bunches due to the increase in charge density.

A rebuncher may be used between the injector cyclotron and the main cyclotron to reduce the bunch elongation produced by the energy spread induced by space charge forces in the transport line.

A 6.3 MeV energy gain per revolution as opposed to the 2.4 MeV in the current design is needed to maintain the turn separation in the main cyclotron. Eight 1 MV accelerating cavities instead of four 730 kV structures would be used in this scheme.

Other high power cyclotrons have been proposed for a number of applications. Some of them are listed here.

V. P. Dmitrievsky et al. propose in [4] a three-cyclotron complex to accelerate a 10 mA H^+ beam to 800 MeV. A four-sector cyclotron (Ci-15) would be used as a preinjector to accelerate the beam from 0.5 MeV to 15 MeV. The beam is then injected into the second four-sector cyclotron (C-60) to reach 60 MeV energy. The process is repeated with a third ten-sector cyclotron (C-800) to achieve the desired final energy (800 MeV).

L. Calabretta et al. propose in [5] a superconducting cyclotron to accelerate 10 mA of H_2^+ up to 1 GeV per nucleon. The beam would be stripped in order to extract it. In this case, a good turn separation is not so critical since protons have a lower magnetic rigidity. Due to the higher rigidity of H_2^+, a stronger magnetic field is needed for the size of the machine to be as small as it would be if protons were used.

T. Kuo et al. propose in [6] a cyclotron to accelerate 10 mA of H^- to energies up to 120 MeV as an injector to a larger machine. As in the previous proposal, extraction by stripping would relax the turn separation requirements. At the same time, the beam rigidity is similar to that of protons. Although, the low binding energy of the second electron (0.7 eV) increases the vacuum requirements and limits the maximum usable magnetic field.

G. Kim et al. propose in [7] a stack of five superconducting cyclotrons. Each of them delivers 2 mA of 1 GeV protons yielding 10 MW of combined beam power. The space charge regime in which each cyclotron operates is similar to that of the current PSI machine which has been proven to work well. On the other hand, the design of the magnets is far from trivial.

Several options for high power cyclotrons have been discussed. None of them is free of problems and their feasibility still needs to be demonstrated. The successful operation of PSI proves that the longitudinal space charge effects can be managed. Although, a better understanding is needed if the beam current limit has to be pushed further.

1.2.   Description of SIR

The Small Isochronous Ring (Figure 1) consists of four 90° dipole magnets. Their bending radius is 45 cm and the distance between them is 94 cm giving a total circumference of 6.58 m. The angle of the pole tips and the distance between magnets is such that the ring is isochronous. Dipole and quadrupole corrector coils as well as an electrostatic quadrupole in each straight section can be used to correct possible deviations from isochronism due to misalignments or manufacturing errors. They can also be used to change the tune of the ring or move out of the isochronous condition.

The impact of the earth's magnetic field and other residual fields on the beam dynamics was studied to ascertain the lowest beam energy. It was determined that the impact of these fields on a 20 keV H_2^+ beam was small enough not to significantly affect the beam dynamics. Therefore, the ring is typically operated between 20 and 30 keV.

Two turbopumps in the ring and another two in the injection line are enough to reach a pressure lower than 10^{-8} Torr when there is no gas load from the source. When the source is used, the pressure raises to ~ $5 \cdot 10^{-8}$ Torr. The

half life of the beam for these pressures in the ring is several hundred revolutions. The break up of the bunch is typically observed after a few tens of revolutions. A complete description of the ring can be found in reference [3].

Figure 1: Picture of the Small Isochronous Ring (SIR).

The chopper in the injection line allows injecting bunches with different lengths (as short as 100 ns and as long as the ring circumference). The extraction line is located on the opposite side of the ring. The bunch can be extracted after a variable number of turns which allows studying turn by turn evolution. It can be sent to a phosphor screen to study its transverse properties or to a fast Faraday cup to study its longitudinal profile.

The injection and extraction lines are described in detail in chapters 2 and 3 of this dissertation. The main parameters of SIR are summarized in Table 1.

PARAMETER	VALUE
Ions	H^+, H_2^+, H_3^+
Beam Energy	Up to 30 keV
Beam Current	Up to 40 µA for H_2^+
Bunch Length	From ~ 100 ns to ~ 5 µs
ε_{RMS}	Typically ~ 2-3 π·mm·mrad for 20 keV, 10 µA H_2^+ beam
Ring Circumference	6.58 m
Dipole typical field	~ 800 Gauss
Dipole Bending Angle (Radius)	90° (45 cm)
Dipoles Pole Face Angle	26°
Horizontal Tune: ν_X	1.14 (with zero beam current)
Vertical Tune: ν_Y	1.11 (with zero beam current)
Diagnostics Extraction	Phosphor Screen Fast Faraday Cup (~ 2 ns time resolution)
Diagnostics Injection	Emittance Measurement System Faraday Cup Phosphor Screen
Diagnostics Ring	4 Scanning Wires
Pumping System	4 x 500 L/s Turbopumps
Pressure in the Ring with no hydrogen load from the source	< 10^{-8} Torr
Pressure in the Ring with hydrogen load from the source	~ $5·10^{-8}$ Torr
Beam Half-life	245 Turns for 20 keV H_2^+

Table 1: Main parameters of SIR.

1.3.   Scaling of space charge forces

As described in reference [3], the space charge forces that bunches with similar sizes experience in the isochronous regime scale with a scaling factor (k) given by the following expression:

$$k \equiv \frac{q \cdot I_{AV}}{\gamma^5 \cdot m \cdot h \cdot \omega^3} \qquad I_{AV} = \frac{I_{PEAK} \cdot h \cdot L_{BUNCH}}{2\pi \cdot R_{AV}}$$

where q and m are the charge and mass of the ions, γ is the relativistic gamma factor, h is the rf harmonic number, ω is the revolution frequency, I_{AV} is the average beam current, I_{PEAK} is the peak bunch current, R_{AV} is the average radius of the circumference described by the bunch, and L_{BUNCH} is the length of the bunch.

Using this expression, we can evaluate the space charge regime in which some of the machines, mentioned in section 1.1, function. We can, then, find under what conditions SIR operates in the same space charge regime. It is worth mentioning here that SIR does not have acceleration capabilities. In this case, the beam peak current is used, eliminating the dependence of the scaling factor (k) on the rf harmonic number.

The space charge region that can be explored by SIR is shown as a shaded red area in Figure 2. The figure shows the values of the space charge scaling factor (k) as a function of the bunch peak current. This region has been defined by four conditions:

- The lower current limit (5 µA) is defined by the noise to signal ratio in the measurements of the longitudinal profile using the fast Faraday cup. As discussed in section 3.3, the noise level in these measurements is equivalent to a ± 0.5 µA variation in beam current.

- Even though beam currents higher than 40 µA could be extracted from the source, it would require increasing the gas pressure and filament power. Raising the gas pressure in the source results in higher pressures in the ring reducing the beam lifetime. Increasing the filament power reduces the filament lifetime.
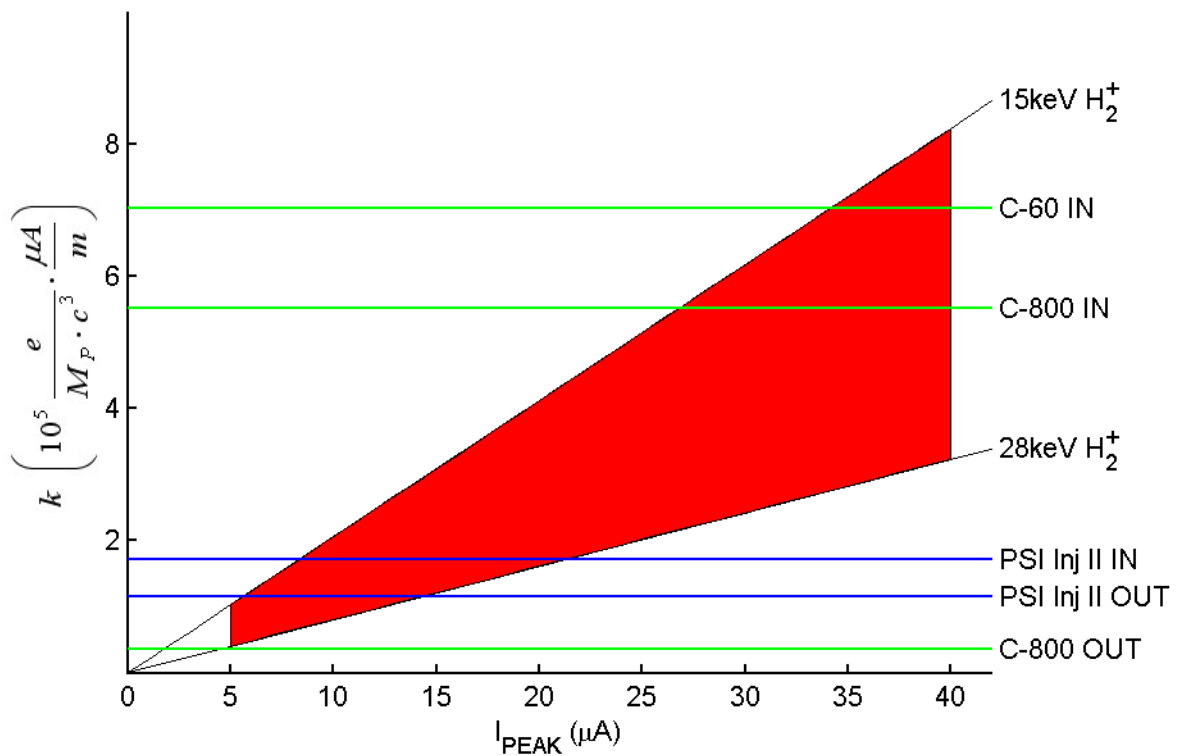
Figure 2: The space charge regime, defined by the scaling factor k, in which SIR can operate is displayed in shaded red. The value of the scaling factors for other machines described in section 1.1 are represented by horizontal lines. The tag IN refers to the first revolution in those machines, while the tag OUT refers to the last revolution.

- The voltage rating of the power supply driving the dipoles in the ring limits the maximum magnetic field achievable, resulting in a maximum H_2^+ beam energy of 28 keV.

- As discussed in chapter 7, the beam lifetime is shorter when the energy is lower (i.e. higher electron capture cross-section). The beam also becomes more susceptible to residual magnetic fields for energies below 15 keV.

The horizontal lines in Figure 2 represent the value of the scaling factor (k) at which some of the machines described in the previous section operate. The operating parameters of the PSI Injector II when the beam is first injected and right before extraction are listed in Table 2. These parameters are used to calculate the scaling factor (k). The peak current necessary in SIR to have the same scaling factor is then calculated.

Parameter	PSI Inj. II (first turn)	SIR	PSI Inj. II (last turn)	SIR
Ion	H^+	H_2^+	H^+	H_2^+
q	1	1	1	1
m	1	2	1	2
E (keV)	870	20	72000	20
β	$4.3 \cdot 10^{-2}$	$4.6 \cdot 10^{-3}$	0.37	$4.6 \cdot 10^{-3}$
$\gamma - 1$	$0.9 \cdot 10^{-3}$	$1.1 \cdot 10^{-5}$	$7.7 \cdot 10^{-2}$	$1.1 \cdot 10^{-5}$
R_{AV} (m)	0.41	1.05	3.5	1.05
h	10	1	10	1
ω/c (m^{-1})	0.105	$4.4 \cdot 10^{-3}$	0.105	$4.4 \cdot 10^{-3}$

$k \left(\dfrac{e}{M_{PROTON} \cdot c^3} \cdot \dfrac{\mu A}{m} \right)$	$1.72 \cdot 10^5$	$1.72 \cdot 10^5$	$1.19 \cdot 10^5$	$1.19 \cdot 10^5$
I_{AV} (µA)	$2 \cdot 10^3$	$2.93 \cdot 10^{-2}$	$2 \cdot 10^3$	$2.03 \cdot 10^{-2}$
L_{BUNCH} (cm)	1.5	1.5	1.5	1.5
I_{PEAK} (µA)	$3.4 \cdot 10^4$	12.9	$2.9 \cdot 10^5$	8.9
T_{BUNCH} (ns)	1.16	10.88	0.14	10.88
BW_{MIN}	602 MHz	64 MHz	5.18 GHz	64 MHz
Q_{BUNCH} (e)	$0.25 \cdot 10^9$	$0.88 \cdot 10^6$	$0.25 \cdot 10^9$	$0.60 \cdot 10^6$
P_{AV}	1.74 kW	< 1 mW	144 kW	< 1 mW

Table 2: Comparison between main parameters of SIR and the PSI Injector II. Parameters of a bunch in SIR (column 2) are such that the space charge forces experienced are equivalent to those felt by a bunch with the parameters listed in column 1 during its first revolution in the PSI Injector II cyclotron. In a similar way, the last revolution of the beam in PSI Injector II (column 3) is compared to SIR in column 4.

A 20 keV H_2^+ bunch with peak current equal to 12.9 µA, in SIR, will experience the same space charge forces as the 870 keV H^+ 34 mA peak current bunch when it is first injected in the PSI Injector II cyclotron. A lower peak current in SIR (8.9 µA) is enough to emulate space charge forces before extraction of the cyclotron (72 MeV).

1.4.   Advantages of SIR

When Eduard Pozdeyev and Felix Marti started studying the effect of space charge forces in the isochronous regime, the possibility of using the PSI Injector II cyclotron to validate the computer simulations was considered. It soon

became apparent that building a small ring that would work in the same space charge regime had many advantages. Some of them are enumerated below:

TIME RESOLUTION

The time resolution of the diagnostics necessary to characterize the beam longitudinally strongly depends on the energy of the beam. For example, to be able to measure the longitudinal profiles of ~ 1.5 cm long bunches (140 picoseconds) after they are extracted from the PSI Injector II, the bandwidth (BW_{MIN}) of the electronics should not be lower than 5.2 GHz since:

$$BW_{MIN} = \frac{0.35}{0.5 \cdot T_{BUNCH}}$$

Justification of this relationship can be found in [8]. Even though, fast Faraday cups with 6 GHz bandwidth have been reported [9], they would not be appropriate for the required beam power.

On the other hand, 64 MHz bandwidth is enough to have the same resolution in a low energy and low current machine like SIR operating in the same space charge regime.

BEAM POWER

The beam power extracted from the PSI Injector II is as high as 144 kW. The duty cycle could be lowered thus reducing the total beam power either by pulsing the injected beam or the extracted beam. Fast Faraday cups capable of handling 4 kW are available [10] but their bandwidth is not large (2 GHz).

In contrast, the beam power in SIR is so low that cooling is not required.

AVAILABILITY

Machines like PSI are routinely overbooked and getting beam time to perform beam dynamics studies is very difficult.

FLEXIBILITY

As described in the previous section, the space charge regime that can be studied with SIR cover a large region, even to regimes where no other machine operates.

Bunches can also be extracted after a variable number of turns providing a unique opportunity to study the time evolution of the bunches instead of only obtaining a final picture when the beam is extracted from the PSI Injector II.

1.5.   Objectives of SIR

Analytical treatment of the beam dynamics of space charge dominated beams is a complex problem. The few models available are frequently overly simplistic and are not able to accurately describe the physics involved. It is often necessary to use numerical calculations to reproduce the behavior observed in the beam. These computer codes have to calculate the ions trajectories in external magnetic and electric fields. They also have to include the electric field produced by the rest of the charge distribution in the bunch.

The number of ions (N_{IONS}) in a typical bunch when it is injected into the PSI Injector II cyclotron is given by the expression:

$$N_{IONS} = \frac{1}{e} \cdot Q_{BUNCH} = \frac{1}{e} \cdot I_{PEAK} \cdot T_{BUNCH} = \frac{1}{e} \cdot \frac{I_{AV} \cdot 2\pi \cdot R_{AV}}{h \cdot L_{BUNCH}} \cdot \frac{L_{BUNCH}}{c \cdot \beta}$$

where Q_{BUNCH} is the total charge of the bunch, T_{BUNCH} is the length of the bunch in time, c is the speed of light and β is the relativistic beta factor. Using the known values for these parameters listed in Table 2, we can determine that $N_{IONS} = 0.25 \cdot 10^9$.

Even modern computers are not able to exactly calculate the electric field produced by such a large number of ions and to track their beam trajectories. Some assumptions need to be made. Different codes will treat the problem differently. Macroparticles are used to represent a large number of ions significantly reducing the computational time. The vacuum chamber geometry is simplified (i.e. the image charges are not accurately described). The space charge electric field is not calculated at every macroparticle position; instead it is calculated in a reduced number of points and then interpolated for every macroparticle.

In order to determine if these assumptions are reasonable, the results of the simulations must be validated with experimental measurements. SIR can be used to confirm that the simplifications used by different codes are reasonable.

As described in section 1.3, the space charge effects approximately scale with beam current and energy. Therefore, it is also expected that effects that are observed in SIR can be directly extrapolated to larger machines.

1.6. Brief description of the contents of the rest of the chapters

Chapter 2 is devoted to the injection line of SIR. The requirements and the general layout of the line are discussed before each of the elements is individually described. The chapter closes with a discussion on the beam dynamics in the injection and other injection schemes that were also considered.

The extraction line elements: deflector plates and the two fast Faraday cups used to measure the longitudinal beam profiles are described in chapter 3. The electronics and control system of SIR are discussed in chapter 4.

Different sources of beam variability in the injection line and their impact on the beam matching are analyzed in chapter 5. A partial characterization of the ion source is presented in chapter 6. The results of the experiments conducted to determine the beam lifetime for different gas pressures in the ring and different beam energies are shown in chapter 7.

The results of the beam dynamics simulations performed with CYCO are presented in chapter 8 and 9. Some preliminary considerations (such as an analysis of the stability of the code and methodology used to do the analysis of data) are included in chapter 8. The dependence on space charge effects of beam parameters (such as emittance and peak current) are discussed in chapter 9.

Some of the space charge related measurements performed in SIR are presented in chapter 10 where they are also compared with the results of the simulations.

2. INJECTION LINE OF SIR

2.1. Introduction

This chapter describes the injection line of the Small Isochronous Ring. The chapter starts with a section where the requirements of the injection line are enumerated and discussed, followed by a general description of the line after which each element is individually described. The chapter closes with a section where the beam dynamics in the line is described and a discussion about other injection schemes that were also considered.

2.2. Requirements

IONS vs. ELECTRONS

The decision to use ions was made early in the project. Due to their larger mass, ions are much less likely to be perturbed by residual magnetic fields than electrons with the same energy. (Keeping the energy low was important to accentuate the space charge forces.)

Using ions has some disadvantages. They are more difficult to produce and the gas flow from the source raises the pressure in the ring reducing the beam lifetime. A multi-cusp ion source was borrowed from Lawrence Berkeley National Laboratory. This source was capable of producing the desired H^+ and H_2^+ beam currents. The pressure in the ring due to the gas flow from the source and its effect in the beam lifetime were estimated (see section 4.7 of [3]). The

results showed that the beam lifetime would be long enough to observe the desired space charge effects. Lifetimes measurements that confirm these estimates (see chapter 7) have been performed.

ENERGY

It was determined that the optimal beam energy to observe the desired space charge effects was 20 keV. The injection line and the ring were designed to handle up to 30 keV H_2^+ beams to be able to characterize the beam energy dependence of space charge effects.

TRANSVERSE BEAM PROPERTIES

The transverse structure of the injected beam had to be matched to the closed orbit solution of the ring. (I.E. the injection point (x_o and y_o) and the α_x, α_y, β_x and β_y of the beam were fixed). The injection line had to be able to shape the beam coming from the source to match the injection parameters. The beam emittance (< 50 π mm mrad) is significantly smaller than the dynamic aperture of the ring. Refer to section 3.2.2 of [3] for a discussion of this issue.

LONGITUDINAL BEAM PROPERTIES

With respect to the longitudinal beam structure, bunches as short as a few centimeters and as long as the length of the circumference of the ring with no energy spread had to be injected.

BEAM CURRENT

The peak beam current of the bunch had to be accurately determined and should be able to be as large as 40 µA to cover the current range in which the desired space charge effects were expected to appear.

PRESSURE IN THE RING

It was estimated in page 131 of reference [3] that the pressure in the ring should be below 10^{-7} Torr for the lifetime of the beam to be long enough to see the space charge effects predicted by the simulations. Since the pressure in the ring is mainly determined by the gas flow from the ion source, the injection line length, vacuum pipe diameters and distribution of the turbopumps along the line are critical to determine the final pressure distribution in the machine.

OTHER REQUIREMENTS

There were also other restrictions that were not related to the physics of the problem to be studied. The whole machine had to fit in the room that was assigned for the project and the cost of the injection line had to be kept as low as possible.

2.3.   General Description

Figure 3 shows a schematic view of the injection line of SIR where the different elements and their relative positions are listed. Figure 4 shows a picture of the injection line.

A multi-cusp ion source is used to produce a beam that includes H^+, H_2^+ and H_3^+ ions. The energy of the beam is defined by the bias voltage of the

source. An Einzel lens follows the source and is used to focus the divergent extracted beam. The puller of the source is used as the first ground electrode of the lens.
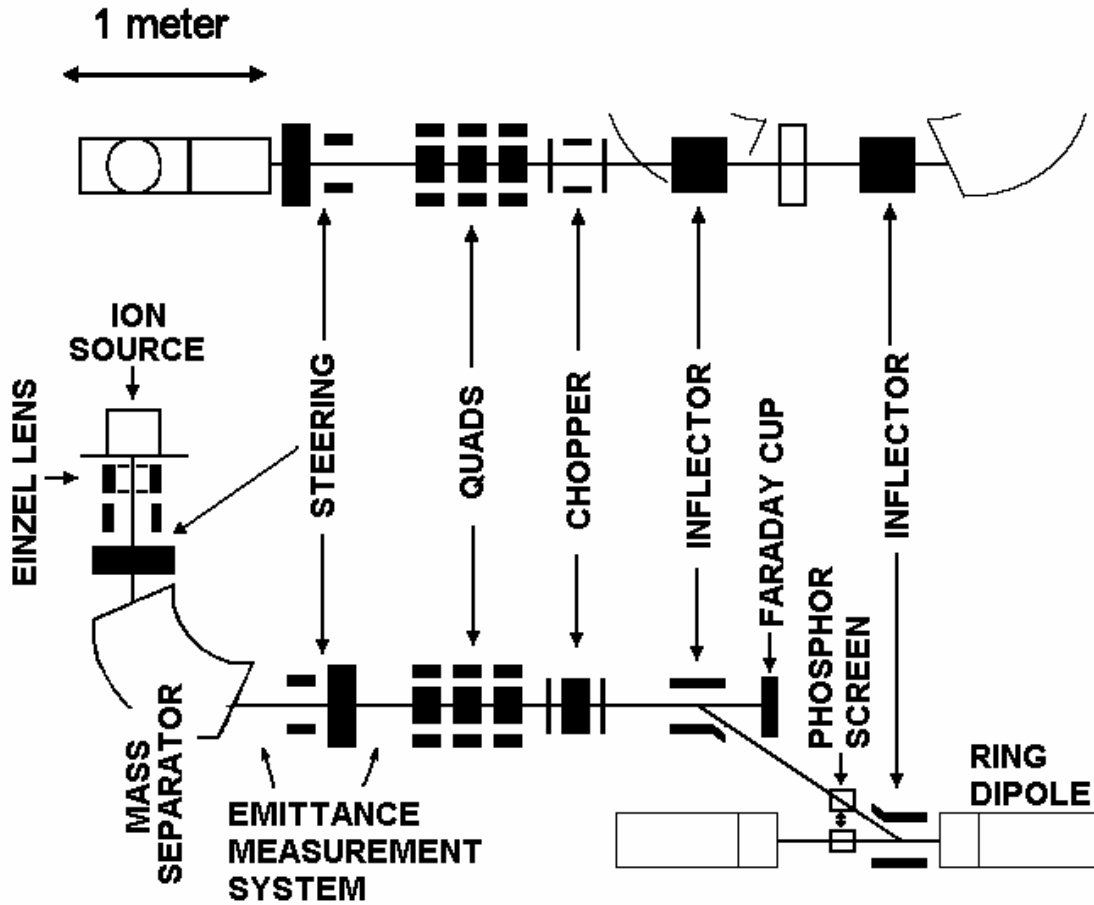
Figure 3: Schematic top and side view of the injection line of SIR.

The first two pairs of steering plates are located after the Einzel lens. A set of identical plates is located in the emittance measurement box. These plates can be used to steer the beam in both planes to correct for misalignments in the injection line and perturbations of the beam trajectory due to residual magnetic fields.

A dipole magnet located in between the two sets of steering plates is used to separate the different ions. The magnet is identical to those used in the ring. A complete description of the design can be found in page 91 of reference [3].

There is a diagnostic unit right after the dipole magnet. It consists of two pairs of movable slits. Each pair lays in either the vertical or horizontal plane and the slits are followed by a shielded Faraday cup to collect the beam current that passes through. A map of the x-x' or y-y' phase space can be captured by moving the slits and measuring the beam current. Fitting the data to an ellipse, the Courant-Snyder parameters [defined in page 49 of reference 11] at that position can be determined. These data can also be used to measure the beam emittance completing the transverse characterization of the beam.
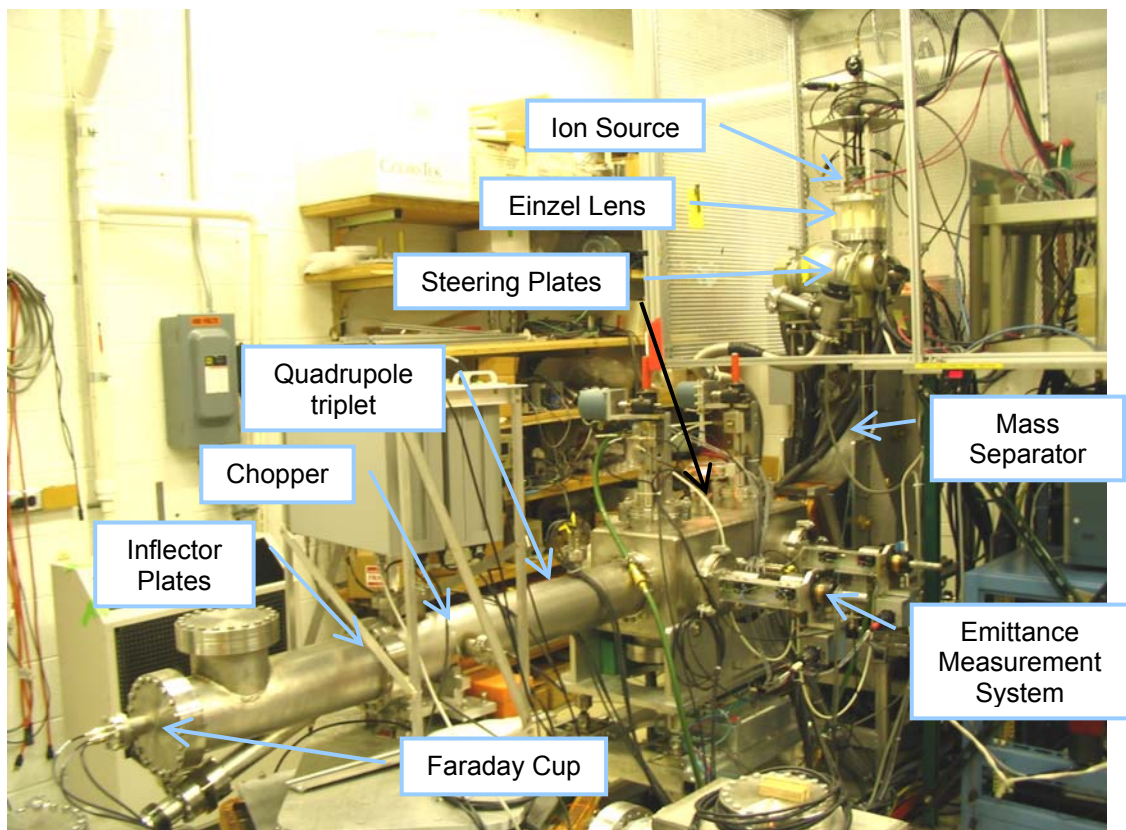
Figure 4: Picture of the injection line of SIR.

A triplet of electrostatic quadrupoles right after the emittance measurement system is used to match the beam to the closed orbit solution of the ring. Since four independent parameters must be adjusted (α_x, α_y, β_x and β_y), the Einzel lens is also used.

The quadrupole triplet is followed by a chopper. The chopper consists of two electrostatic plates that are pulsed to high voltage when the beam is chopped and grounded when the beam is injected.

The first pair of inflector plates follows the chopper. These plates deflect the beam 17.5^o toward the ring. As an alternative, the inflector can be turned off to let the beam go straight toward the shielded Faraday cup located at the end of the injection line where the beam current can be measured.

2.4.   Ion Source

A filament driven multi-cusp ion source is used to produce the beam. Pictures of the source can be seen in Figure 94 and Figure 103. This source was borrowed from Lawrence Berkeley National Laboratory. More information about this and similar ion sources can be found in [12] and in page 203 of [13].

Hydrogen is injected into the source from a side port. The flow of hydrogen is controlled using a needle valve and monitored by a Pirani gauge installed in the gas line. The typical working pressure inside the source is in the range of 1 to 10 mTorr depending on the desired extracted current.

Current from the filament power supply (~ from 35 A to 50 A) is passed through a thoriated molybdenum filament made out of a welding rod. The

filament warms up emitting electrons. A voltage difference (~ 100 V) between the filament and the rest of the source maintained by the arc power supply, accelerates the electrons toward the walls of the source. In this process, they collide with hydrogen molecules knocking out electrons and forming the plasma. Some of the ions in this plasma will eventually move toward the plasma electrode where the electric field between source and puller will extract some of them forming the beam. The energy of the beam will be defined by the potential difference between the source and ground.

Figure 5 shows the schematics of the wiring of the source. The ion source and the associated instrumentation are all biased to the same high voltage of the source. An isolation transformer provides the necessary ac power for these instrumentation. A safety interlock system, designed by D. Pedtke from the electronics department at the NSCL, turns off the power to the transformer and the high voltage power supplies if the door of the high voltage cage, where everything is enclosed, is opened. It also grounds the whole system using a high voltage relay. The high voltage is monitored using a high voltage probe. The value of the voltage is displayed next to the door of the cage. A red light also warns the user when the high voltage is on.

As a redundant safety precaution, every time the door of the cage is unlocked, the high voltage sections are manually grounded using a grounding rod. In addition to the safety interlock, there is another interlock to protect the source from failures in the cooling system that turns off the ac power of the filament power supply if the temperature of the source rises too much.
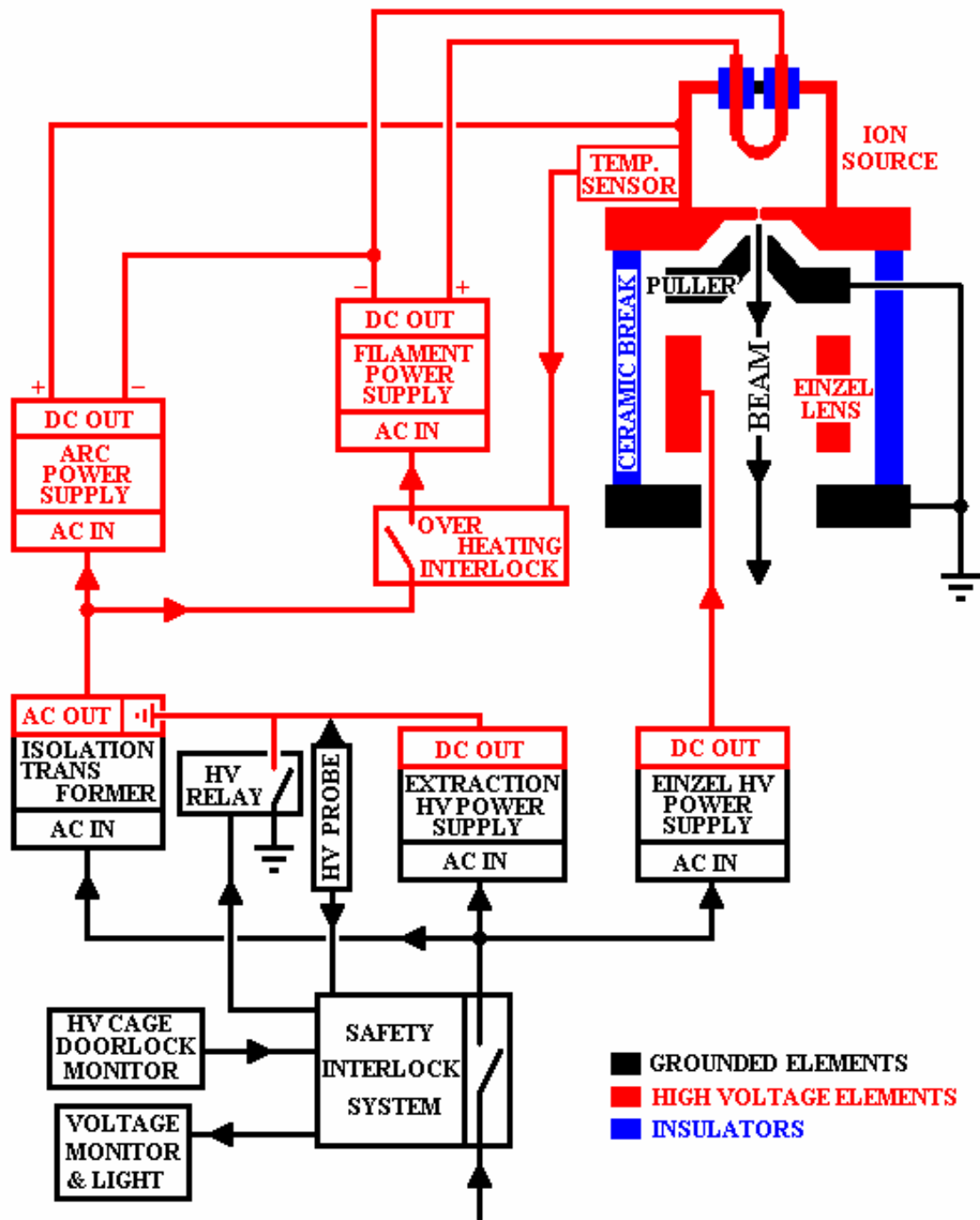
Figure 5: Wiring diagram of the ion source and its associated electronics.

Refer to chapter 6 for a characterization of the source where extracted current, emittance of the beam and relative abundance of different mass species for different conditions in the source are discussed.

2.5. Einzel lens

An Einzel lens (Figure 6) is used to focus the beam coming out of the source. When the beam is extracted, it has a large angular divergence and, in absent of strong focusing, it would be lost.
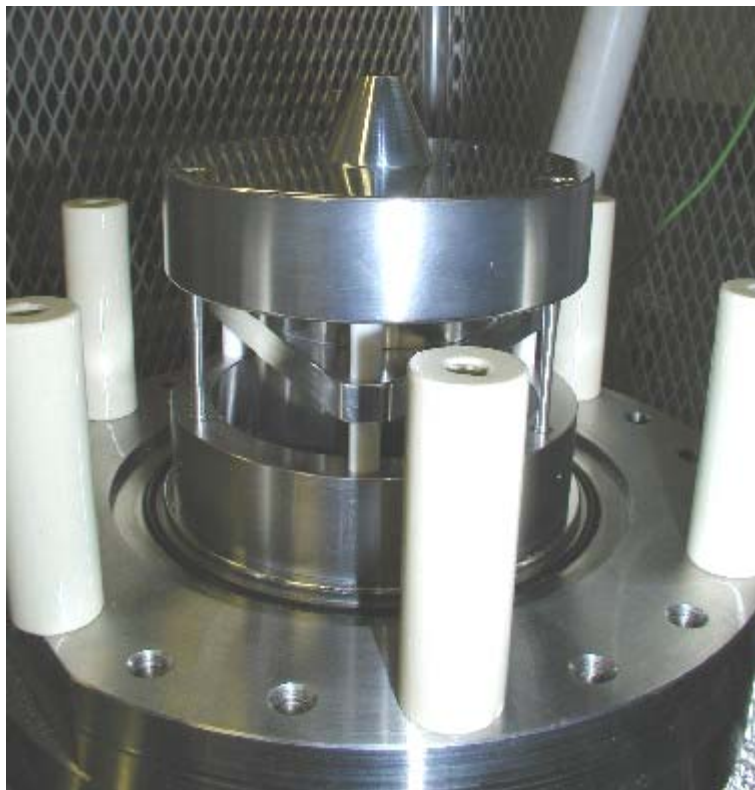
Figure 6: Picture of the Einzel lens and puller of the ion source used in the injection line of SIR.

The Einzel lens consists of three different electrodes. The first one is a stainless steel cylinder that is attached to the modified 8" flange that holds the

whole structure. The second one is an aluminum cylinder with three wings that is biased to high voltage. The third electrode is also made out aluminum. It is grounded and it is used as a puller of the source. The three electrodes are positioned and aligned by three macor spacers and clamped together with three screws.

A polyethylene insulated cable (rated to 40 kV) is used to connect the pin of the high voltage vacuum feedthrough and the high voltage electrode of the Einzel lens. An alumina tube is used around the pin to increase insulation.

Figure 9 shows a picture of a previous version of the Einzel lens. Some of the problems that were found with it and later solved in the final version are:

- The distance between puller and the flange that holds the ion source was increased. The distance between the high voltage Einzel lens electrode and the puller and ground electrode were also increased. On some occasions, sparks were produced when the source and/or the Einzel lens were biased to maximum voltage (30 kV). It was determined, that the distance between electrodes could be increased, thus decreasing the electric fields in the surfaces, without compromising the performance.

- The aperture of the puller was increased. It was believed that some of the sparks could be triggered by electrons emitted from the surface of the puller when they were hit by the extracted beam. A larger aperture also decreases the chances of dust from the filament of the source depositing in the surface of the puller that would likely trigger sparks.

- The six macor spacers that were used to separate and align the puller, high voltage electrode of the lens and ground electrode were perturbing the electric field of the Einzel lens. This perturbation was generating a three-fold symmetry in the beam that could clearly be observed in the phosphor screen. The spacers were electrically hidden from the beam in the new design by displacing them further away from the beam axis and behind the high voltage electrode.
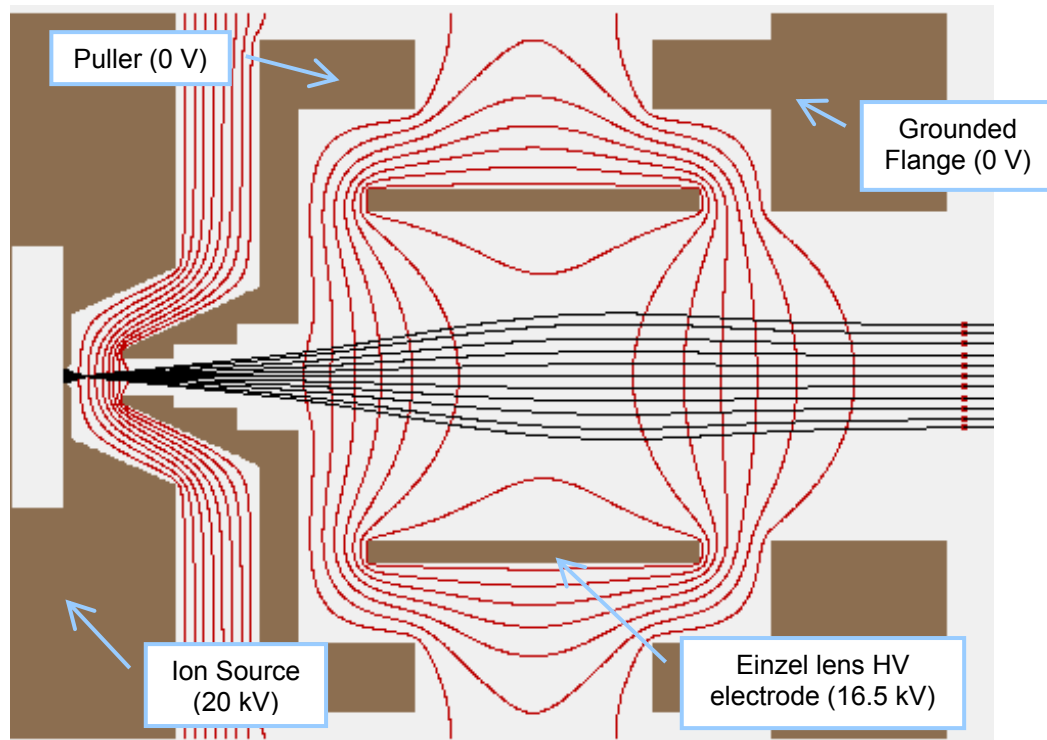
Figure 7: Simion model of the Einzel lens and source extraction region of the injection line of SIR. Equipotential lines are shown in red. Several ions were tracked and their trajectories are displayed in black.

Simulations were performed to minimize the non-linear effects introduced in the beam by the Einzel lens. Calculations of the electric fields and tracking of particles were performed using SIMION [14]. Figure 7 shows the equipotential

lines (in red) when the source is biased to 20 kV and the high voltage electrode of the lens to 16.5 kV. We can also see the focusing effect of the Einzel lens in the ion trajectories (in black).

The focusing distances for different voltages in the lens were calculated for 20 keV ions entering the lens at different distances from the beam axis. The results are shown in Figure 8.

It can be observed that the focusing distance depends on the distance to the beam axis when entering the lens. This dependency denotes the presence of some non-linear effects despite the effort to minimize them.
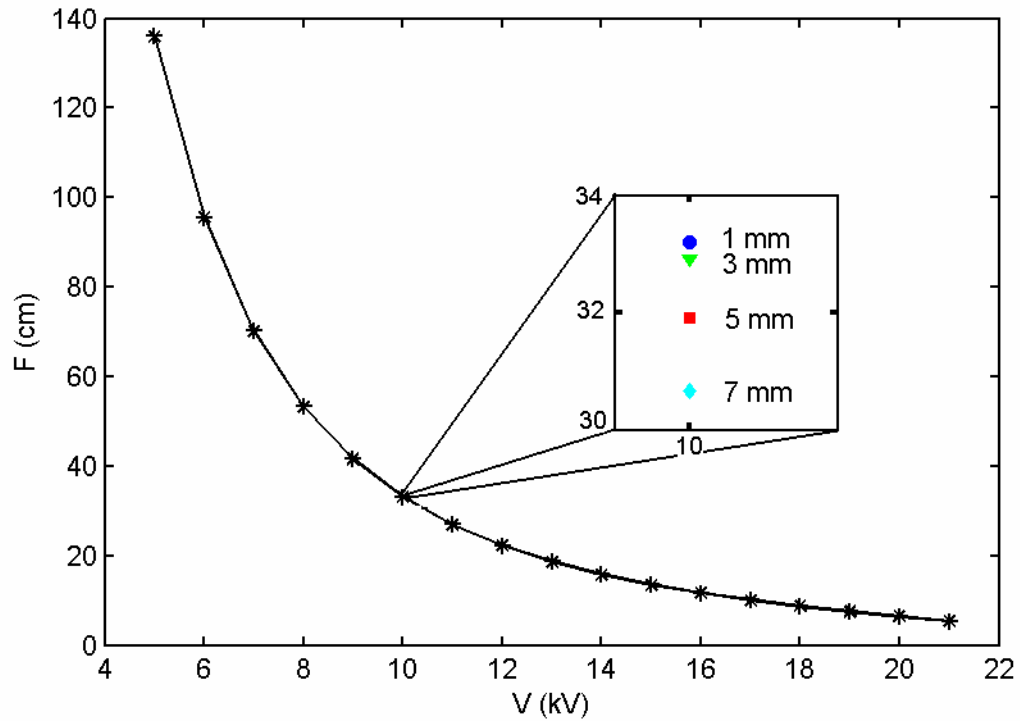
Figure 8: Focusing distance of the Einzel lens when biased to different voltages for a 20 keV beam. The picture was expanded for 10 kV. The non-linear effects of the lens can be observed in the dispersion of the focusing distances for ions entering the source 1, 3, 5 and 7mm away from the beam axis.

2.6. Steering

Two pairs of Oxygen Free High Conductivity (OFHC) copper plates are used to steer the beam in both planes. They are located right after the Einzel lens (Figure 9) and before the mass separator. Two more pairs of identical plates located inside the emittance measurement box in between scanning slits are also used.

The length of the plates is 9 cm, the width is 8.9 cm and their thickness is 1.3 cm. They are separated by 5 cm and the gap between plates with different polarities is 6 cm.
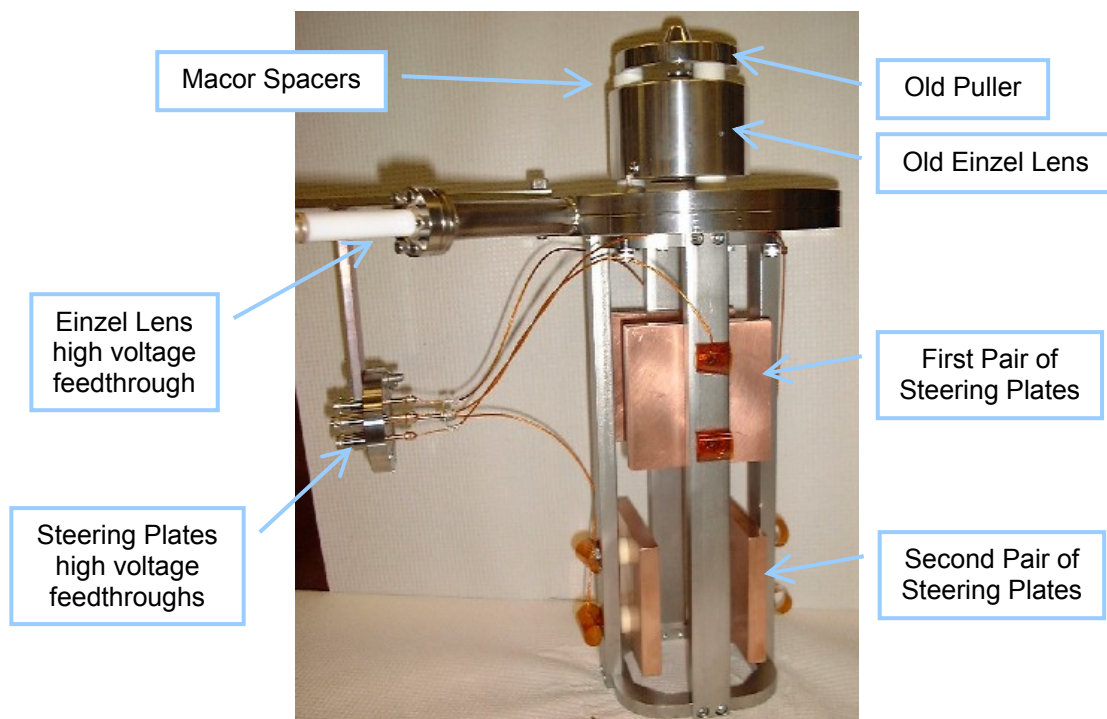
Figure 9: Picture of the first two pairs of steering plates in the injection line of SIR. An old version of the Einzel lens and puller can be seen in top of the 8" flange that supports the whole structure.

Each plate is positioned with respect to the stainless steel frame that supports them by two alumina washers and held with screws. The head of the screw is electrically insulated from the frame by alumina washers. Kapton coated coaxial cables run between the head of the screws and the pins of a Miniature High Voltage (MHV) vacuum feedthrough.

The purpose of the steering plates is to have the capability to correct the beam orbit if it is perturbed by residual magnetic fields or misalignments of the different optical elements. The plates are capable of deflecting a 30 keV beam by ± 65 mrad when biased to ± 1 kV.

Besides the four pairs of plates mentioned before, the inflector plates and the bending magnet can also be used for steering purposes. The current of the injection line magnet can be changed independently from that of the magnets in the ring. The voltage in the first and second pair of inflector plates can also be adjusted separately.

2.7.   Mass Separator

A dipole magnet, identical to those used in the ring, is used to select one of the three mass states (H^+, H_2^+ or H_3^+) produced by the ion source (Figure 10). Refer to section 4.2 and 4.3 of [3] for a complete description of the magnets.

The magnet is located in between the first set of steering plates and the emittance measuring system.

A non-relativistic ion with mass m, charge q and energy E will describe a circle with radius R when injected in a magnetic field B perpendicular to its momentum.

$$R = \frac{\sqrt{2 \cdot m \cdot E}}{q \cdot B}$$

The relationship between the curvature radius of the trajectories of two ions with the same charge and energy can be written as:

$$R = R_0 \cdot \sqrt{\frac{m}{m_0}}$$
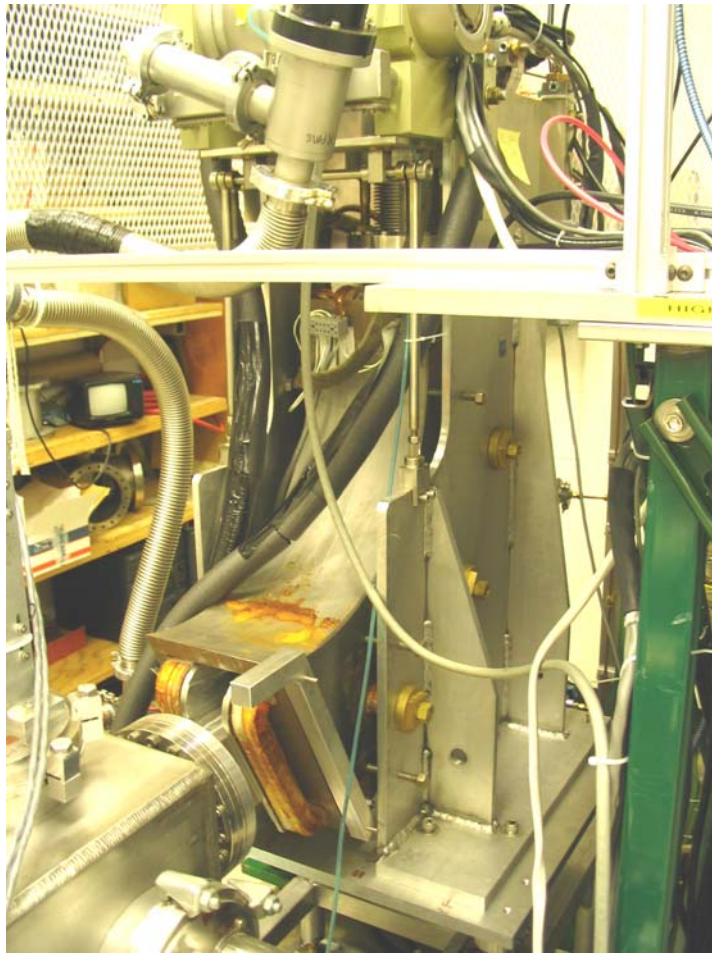
Figure 10: Picture of the mass separator used in the injection line of SIR.

In our case, the dipole bending radius is 45 cm for the beam that is selected. The bending radii for different ions are listed in Table 3.

Figure 11 shows a graphical representation of the trajectories of ions with different masses and their collision point with the beam vacuum chamber. It can be seen that every mass species can be clearly separated from the others.

		Selected mass		
		H^+	H_2^+	H_3^+
Radius of Curvature (cm)	H^+	45.0	31.8	26.0
	H_2^+	63.6	45.0	36.7
	H_3^+	77.9	55.1	45.0

Table 3: Radius of curvature for different mass species in the mass separator of the injection line of SIR when the H^+, H_2^+ or H_3^+ species is selected.
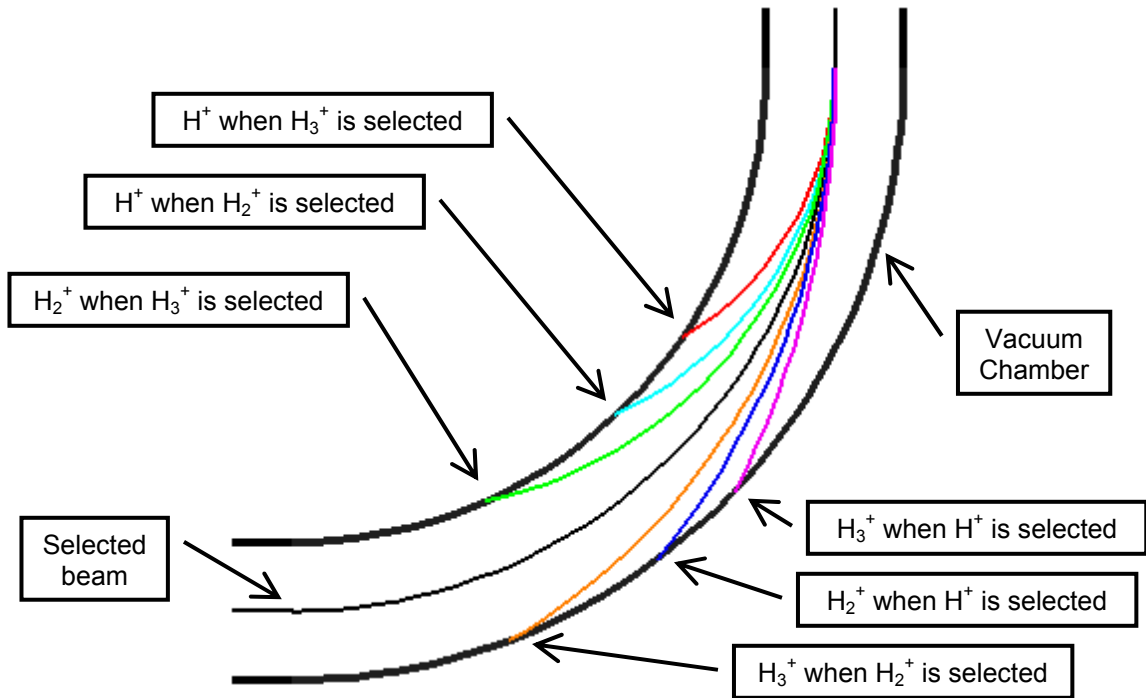
Figure 11: Selection of ions with different masses in the mass separator of the injection line of SIR.

2.8. Emittance Measurement System

A diagnostic box located between the mass separator and the quadrupole triplet is used to characterize the beam transversely (Figure 12). It consists of two pairs of scanning slits that can be moved in the vertical or horizontal plane. The second slit of each pair is followed by a shielded Faraday cup to collect the current that makes it through both slits.
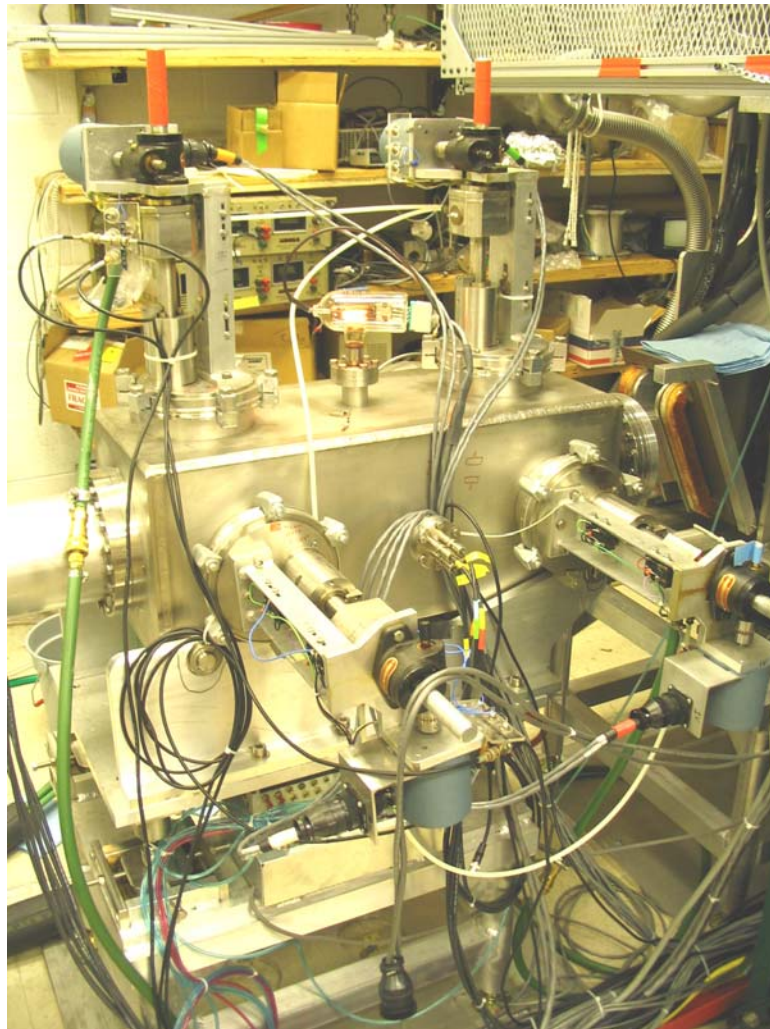
Figure 12: Picture of the emittance measurement system used to transversely characterize the beam coming from the ion source.

This system can be used to get information about the transverse phase space of the beam. The first slit lets a fraction of the beam with a well defined position go through. Of this fraction, just that portion with a well defined angular range will go through the second slit and be collected in the Faraday cup.

This information is used to readjust the Einzel lens and the quadrupole triplet to match the beam to the closed orbit solution of the ring when it is injected.

The system can also be used to measure transverse beam profiles if the first scanning slit is retracted and just the second one is used.

The scanning drives were already available at the NSCL. Each of them consists of a copper frame that holds a molybdenum slit. The copper frame is soldered to a modified 2 ¾" flange. This flange is attached to a nipple held by an ISO-160 flange. In between the two flanges, a welded edge stainless steel bellows is used to allow the linear motion of the copper frame. A shaft, which can be moved by a stepper motor, is used to push the copper frame in and out.

A shielded Faraday cup is mounted behind the copper frame of two of the scanning drives. The current collector is attached to a G-10 piece. A copper ring, that can be negatively biased to act as an electron suppressor, is mounted on ceramic balls that rest in the current collector.

The diagnostic box that contains the scanning slits was designed to position them in an optimal way. The typical size of the beam at the first slit position is ~ 1 cm diameter and its envelope typically goes through a waist at this point when shaped for ring injection. If the beam emittance is equal to 50 π mm

mrad, and the first slit is positioned in the beam axis, the angle dispersion of the surviving beam will be ±10 mrad. Since the distance between slits is 47.5 cm, the beam diameter in the second slit will be 9.5 mm (approximately the size in the first slit).

The aperture of the slits is 0.5 mm. For a 10 µA beam with the previous characteristics, we can expect beam currents of ~ 25 nA to go through both slits. If the aperture of the slits were reduced, the collected currents would be much smaller approaching noise level. If the aperture of the slits were enlarged, we would lose resolution of the measurements.

2.9.   Quadrupole triplet

An electrostatic quadrupole triplet is used to shape (together with the Einzel lens) the beam transversely so that it is matched to the closed orbit solution of the ring by the time it reaches the injection point (Figure 13 & Figure 14). It is positioned in between the emittance measurement system and the chopper.

The length of the first quadrupole is 10.5 cm, the length of the second is 14 cm and the length of the third is 6 cm. The distance between them is 9 cm and the distance from beam axis to electrodes is 3.5 cm. The traditional hyperbolic shape of the electrodes was substituted by a circular shape to simplify the machining. Its curvature radius is 4.04 cm (= 1.15 x 3.5 cm) to best approximate the required fields. Simulations where ions were tracked in the calculated 3D fields showed a negligible effect of this modified geometry.

Each electrode is positioned with respect to the stainless steel frame that supports them by two alumina washers and held with screws. The head of the screw is electrically insulated from the frame by alumina washers. A Kapton coated coaxial cable runs between opposite electrodes of the same quadrupole and from one of them to the pin of a MHV vacuum feedthrough.
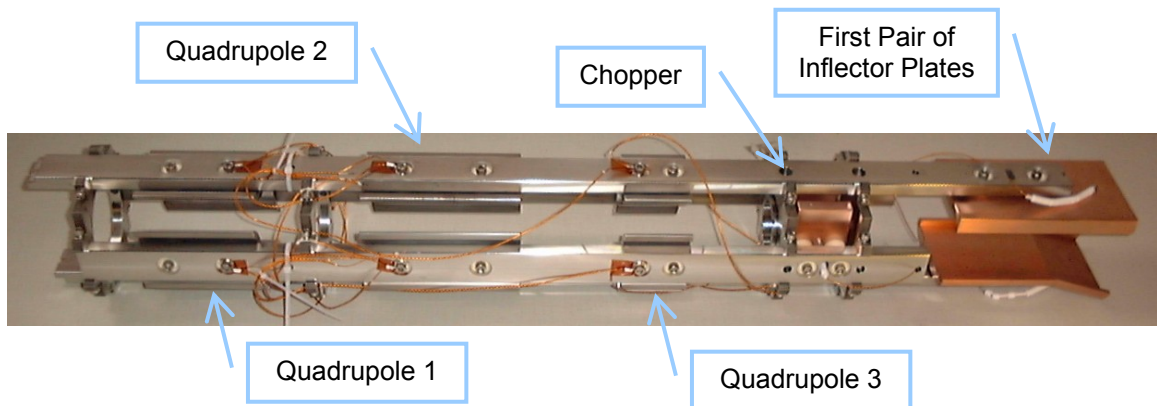
Figure 13: Picture of the quadrupole triplet, chopper and first pair of inflector plates held by a support frame before being assembled in the injection line of SIR.
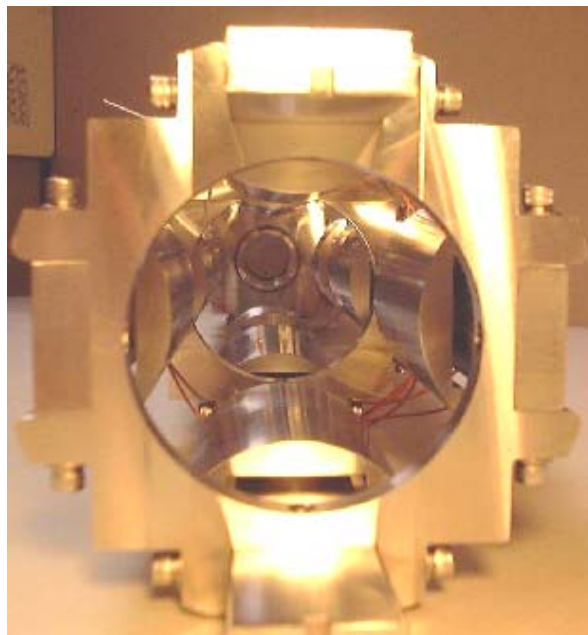
Figure 14: Picture of the triplet of electrostatic quadrupoles used in the injection line of SIR.

Each pair of opposite electrodes can be individually biased (i.e. the voltage of the three quadrupoles can be chosen independently from the others).

Ions were tracked in the calculated 3D fields using SIMION to calculate the focusing distance (in the focusing plane) for different voltages in the electrodes of each of the quadrupoles when the others were turned off. The results are shown in Figure 15. The different colors correspond to each of the quadrupoles.
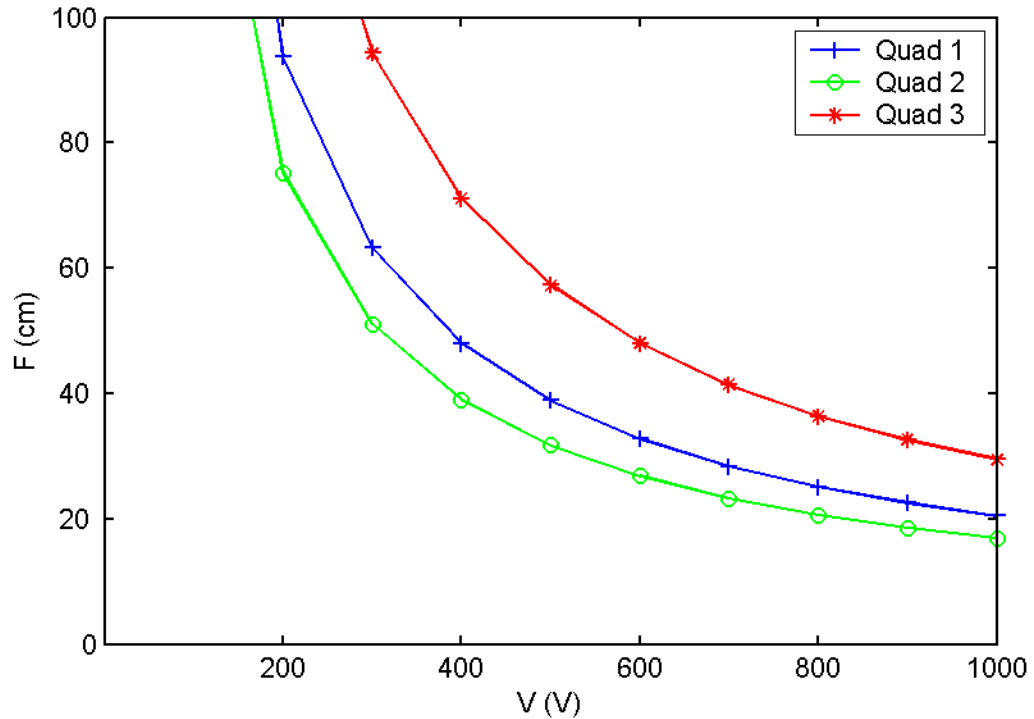
Figure 15: Focusing length for a 20 keV beam of the three quadrupoles used in the injection line of SIR.

2.10. Chopper

A pair of OFHC copper deflector plates that are pulsed by fast high voltage switches are used to chop the dc beam coming from the ion source into bunches of different lengths (Figure 16). The length of the plates is 5 cm and the gap between them is 4 cm. When the plates are biased to high voltage, the beam is deflected in the horizontal plane (parallel to the medium plane of the ring) hitting the vacuum chamber. When plates are grounded, the beam trajectory is not perturbed and the beam is injected in the ring.

The chopper is located immediately after the quadrupole triplet and before the first pair of inflector plates. It was placed as close to the injection point as possible to minimize the energy spread induced by longitudinal space charge forces in the drift space between chopper and injection point.
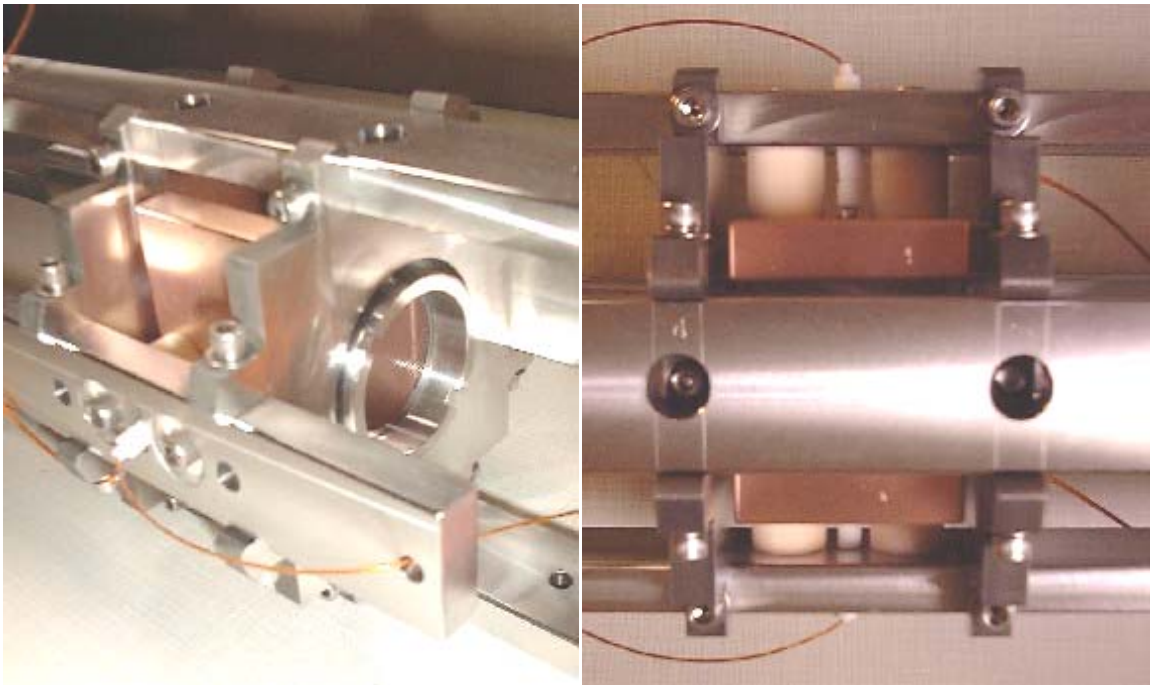
Figure 16: Pictures of the system used to chop the beam in the injection line of SIR.

Each of the deflecting plates is positioned with respect to the stainless steel frame that supports it by two alumina tubes and held by two screws inside the alumina tubes. The head of the screws are electrically isolated from the steel frame by alumina washers. The high voltage is carried from the pins of MHV vacuum feedthroughs to the chopper plates by Kapton coated cables surrounded by alumina beads to add electrical insulation (cable insulation is rated to ± 2 kV).

Originally just two deflecting plates were planned. But, the extension of the fringe field of the plates makes the length of the head and tail of the bunch fairly long. Ions are perturbed by the electric field of the chopper long before they reached the plates.

We define the head and tail of the bunch as the parts of the bunch whose ions have received a transverse kick that is not enough to completely deflect them and they are still injected in the ring. Part of this effect is due to the rise time of the high voltage pulse (< 25 ns). Although, even if the rise time were much smaller, some of the ions, that are already in the chopper when the high voltage is turned on, will not receive a full transverse kick. They need to enter the chopper when the full voltage has already been reached to receive a full kick.

To limit the extension of the fringe fields of the deflecting plates, two frames were added next to the plates. The gap between the plates and the frames is 0.5 cm. Molybdenum grids with 90 % transparency are attached to the frames and held by clamping rings pressed by two set screws.

To determine the length of the head and tail of the formed bunches, several transverse beam profile measurements were made using the horizontal

scanning wire located right after the first dipole of the ring. The objective of these measurements was to determine the value of the kick needed to make the beam hit the vacuum chamber and not be injected in the ring. In this experiment, the 20 keV H_2^+ beam was not chopped.
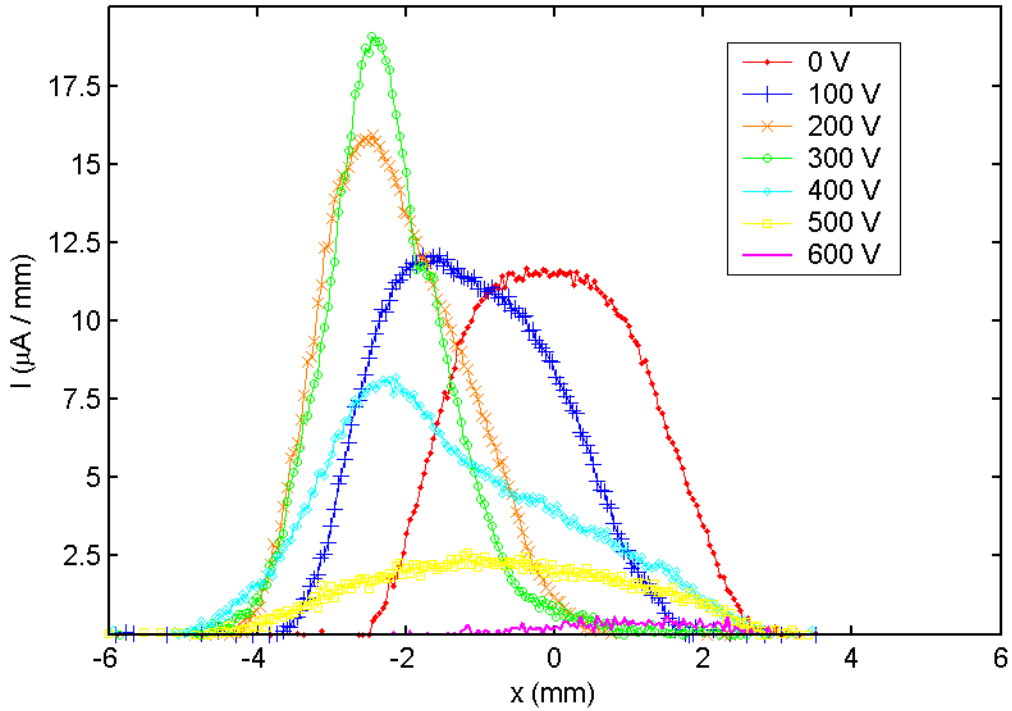
Figure 17: Transverse beam profiles measured with the first horizontal scanning wire for different voltages in the chopper. When the plates are biased to more than ±600V, the beam is deflected and is not injected.

The transverse profiles resulting from these measurements are shown in Figure 17. The different profiles correspond to different voltage values in the chopper. When the voltage is 0 V, the beam profile corresponds to the central part of a bunch. As the voltage is increased, different parts of the head and tail of the bunch can be observed. By the time the voltage of the plates reaches ± 600

40

V, the beam has almost completely disappeared. It hits the chamber before being injected.
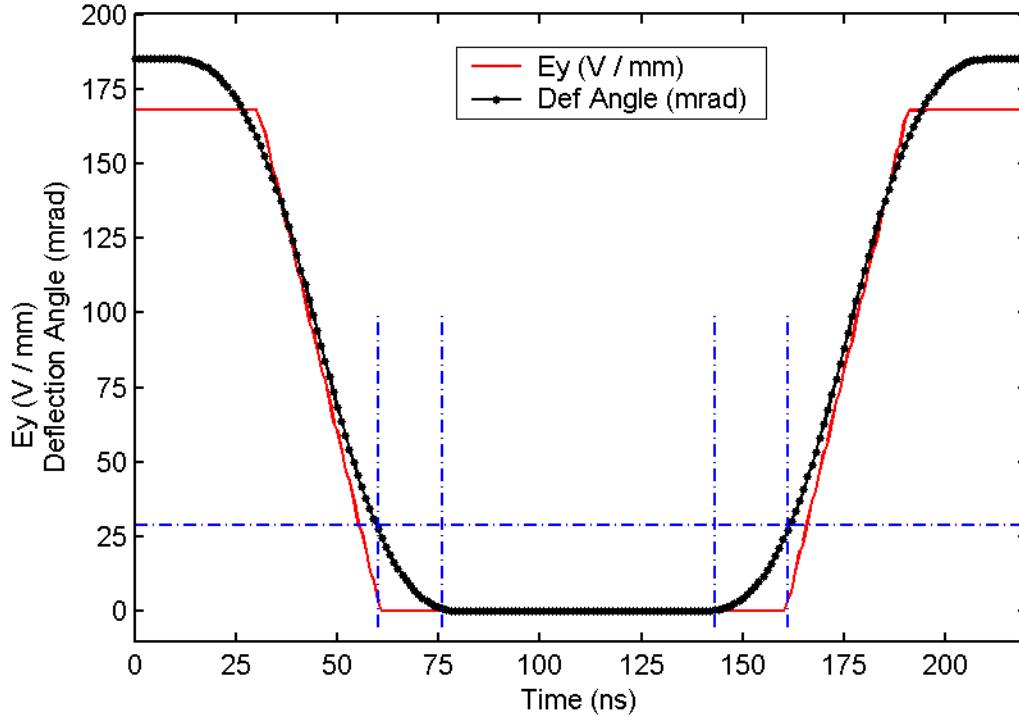
Figure 18: The deflection angle of a 20 keV H_2^+ beam as it goes through the chopper is plotted in black. The value of the electric field in the center of the chopper at the time the ions get there is plotted in red.

Simulations were performed using SIMION to calculate the electric field inside the chopper. It was determined that when the chopper plates were biased to ± 3500 V (maximum voltage the fast high voltage switches can generate), a beam with 20 keV energy was deflected by 185 mrad. So, since the tangent of the deflection angle is proportional to the deflecting voltage

$$\tan\left(\theta^{def}\right) = \frac{V}{V_{max}} \cdot \tan\left(\theta_{max}^{def}\right)$$

we can conclude that if ions are deflected by 29 mrad or more when they go through the chopper, they will not be injected in the ring. This value is also consistent with the geometry of the vacuum chamber.

For this particular beam (H_2^+, 20 keV) simulations were performed using SIMION to calculate the electric field and to track ions in this field. The chopper plates were biased to a voltage of ± 3500 V for 30 ns. Then, the voltage went down linearly to zero in another 30 ns. It was left equal to zero for another 100 ns and then the voltage was ramped up to ± 3500 V in another 30 ns. The deflection angle of ions arriving to the center of the chopper at different times was calculated. Figure 18 shows, in black, the deflection angle of those ions and, in red, the value of the transverse electric field when they reach the center of the chopper.

Those ions that reach the center of the chopper early enough ($t \leq 10 ns$) will exit the chopper before the voltage starts ramping down receiving a full 168 mrad transverse kick.

Those ions that reach the center of the chopper later in time ($10 ns \leq t \leq 30 ns$) will start feeling the ramping down of the voltage before they leave the chopper, even though the voltage in the plates was still the maximum voltage when they went through the center of the chopper.

In the same way, some ions will still receive a transverse kick, even if the voltage in the plates is off by the time they reach the center of the plates, if there was still some field left when they got in the chopper. These are the ions that will form the head of the bunch. A similar argument explains how the tail is formed.

As determined before, ions that receive a kick larger than 29 mrad will not be injected into the ring. The horizontal dashed lined in Figure 18 represents this level. With this information, the length of the head and tail for a 20 keV H_2^+ can be determined. We can expect it to be ~ 16 ns long.
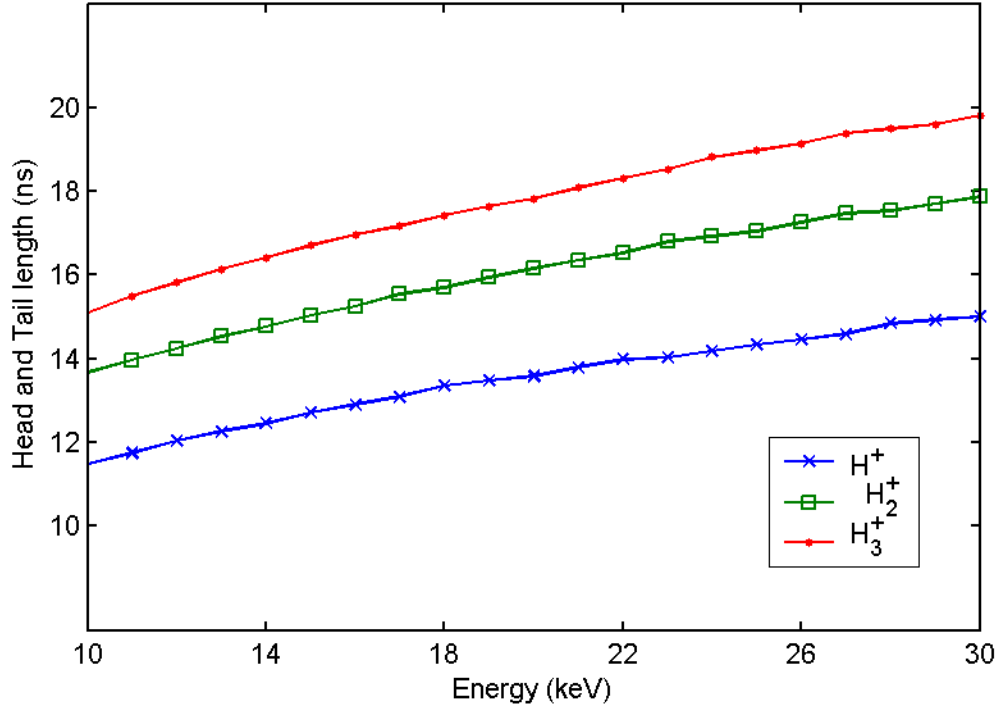
Figure 19: Length of the head and tail of the bunches produced by the chopper for different ion masses and energies.

In the hard edge approximation and for small deflecting angles, the deflection angle θ^{def} of an ion with mass m, charge q and energy E entering the chopper at a time t can be written as

Eq. 2

$$\tan\left(\theta^{def}\right) = \frac{q}{g \cdot \sqrt{2 \cdot m \cdot E}} \int\limits_{t}^{t+T} V(\tau) \cdot d\tau$$

where $T \equiv L_{eff} \cdot \sqrt{\dfrac{m}{2 \cdot E}}$ is the time it takes to go through the chopper, L_{eff} is the

effective length of the plates and g is the gap between chopper plates.

When the voltage is time independent, the traditional $\tan\left(\theta^{def}\right) = \dfrac{1}{2} \dfrac{q \cdot V}{E} \dfrac{L_{eff}}{g}$

is derived from Eq. 2. In our case, the deflecting angle will depend on both the

ion energy and mass. Using Eq. 2 with a maximum deflection angle equal to 29

mrad and effective length of the chopper equal to 4.5 cm (to reproduce the

deflecting angles previously calculated for a 20 keV H_2^+ beam), we can estimate

the dependence of the length of the head and tail of the bunch for different ion

mass and energy (Figure 19).

From this figure we can conclude that the chopper would be capable of

producing bunches as short as 40 or 50 ns. However, the shortest length is

limited to 100 ns by the width of the pulses generated by the digital delay line that

triggers the high voltage fast switches.

The high voltage fast switches are capable of injecting bunches with a

repetition frequency higher than 30 kHz but the maximum output current of the

high voltage power supplies that feed them (3 mA) limits the maximum frequency

to ~ 1.5 kHz.

2.11. Inflector Plates

Two pairs of OFHC copper plates deflect the beam toward the ring. The first pair is located right after the chopper (Figure 13). The second pair is located in between two of the dipoles in the ring (Figure 20).

The geometry of both pairs is identical and it is designed to deflect a 30 keV proton beam by 17.5° when they are biased to ± 3.5 kV. The lengthwise wings of the plates are meant to increase the region where the electric field is flat therefore minimizing nonlinear effects in the beam. Bending one of them increases the clearance between beam and plate. The most important dimensions of the plates are specified in Figure 21.
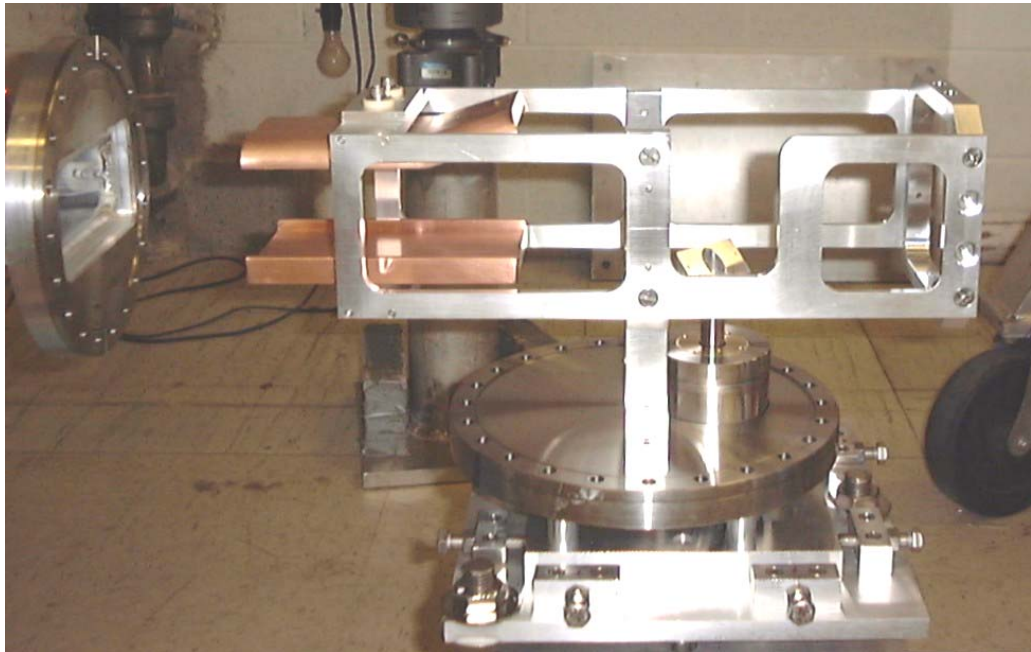
Figure 20: Picture of the second pair of inflector plates located in between two of the dipole magnets of the ring.
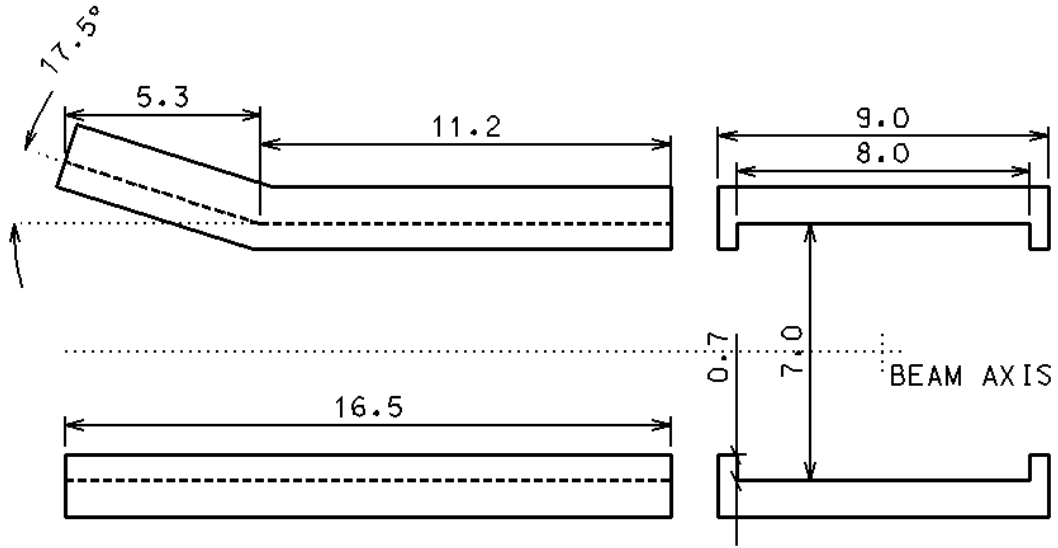
Figure 21: Front and side view of the Inflector Plates where main dimensions (in cm) are specified.

2.12.   Injection Line Faraday Cup

A shielded Faraday cup located at the end of the injection line is used to accurately measure the peak beam current injected in the ring. The chopper and the inflector that deflect the beam toward the ring are turned off and a picoammeter is used to determine the dc beam current. Since the beam is not bunched when it is injected (i.e. very small energy spread), the measured dc current is identical to the peak beam current of the chopped beam.

The Faraday cup consists of three metallic pieces supported by an 8" CF flange (Figure 22). The current collector of the Faraday cup is a disc made out of OFHC copper. A 5 mil thick Kapton foil is used to electrically insulate it from the flange. The aluminum ring next to it acts as an electron suppressor when biased negatively. It reflects the low energy (< 100 eV) secondary electrons emitted by

46

the collector when the ion beam hits it. The accuracy of the measurement can be guaranteed by verifying that no beam hits the second ring that acts as a shield.

The disc and the rings are aligned and electrically isolated from each other by alumina balls in between them. Four screws are used to clamp everything together. The screw heads are electrically insulated from the shield by alumina washers. Kapton coated cables are used to connect the different electrodes to the BNC vacuum feedthroughs.

The Faraday cup can also be used to verify that the beam is centered in the beam axis and that its size is reasonable (first step to match the injected beam to the closed orbit solution of the ring).
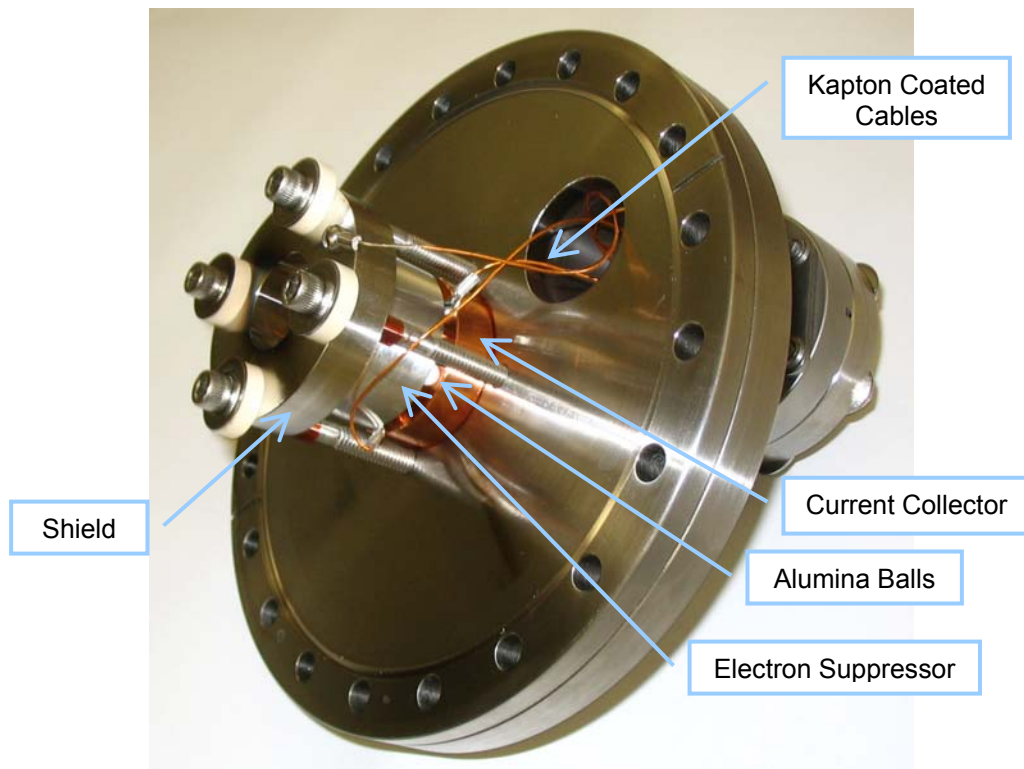
Figure 22: Picture of the Faraday cup at the end of the injection line of SIR.

2.13.   Beam Dynamics in the Injection Line

The first component of the injection line that was acquired was the ion source. The first step before designing the injection line was to determine some of its basic properties.

In particular, it was important to measure the extracted beam current to verify that it was able to cover the range of currents necessary to explore the expected space charge effects. Early measurements showed that the total extracted current (including H^+, H_2^+ and H_3^+) reached several hundred microamps. It was determined by simulations that several tens of microamps of a single mass state would be needed to be able to observe the clustering of the bunches. The source, therefore, fulfilled the extracted current requirements.

It was also important to measure the emittance of the extracted beam. The dynamic aperture of the ring and the injection line had to be large enough to accommodate this emittance.

To design the injection line, it was equally important to have an approximate idea of the transverse beam properties of the extracted beam (α and β parameters). One of the requirements of the injection line is to be able to inject beam that is transversely matched to the closed orbit solution of the ring. So, the injection line should be able to shape the beam coming out of the ion source into what is accepted by the ring.

In order to get this information, experiments were performed before the injection line design was finalized. To do this, a preliminary version of the emittance measurement system was assembled underneath the ion source and

the Einzel lens (the distance between the center of the lens and the first slit of the emittance measurement system was 17 cm).

Different phase-space measurements were made with representative ion source conditions, extraction voltages and Einzel lens voltages. Ions, representing different points of the phase-space region where current was measured, were tracked back through the Einzel lens to a point in between the puller and the plasma electrode of the source. A snap-shot of the phase-space at this point was determined and the beam transverse properties were taken as its initial conditions (independent of the Einzel lens voltage).
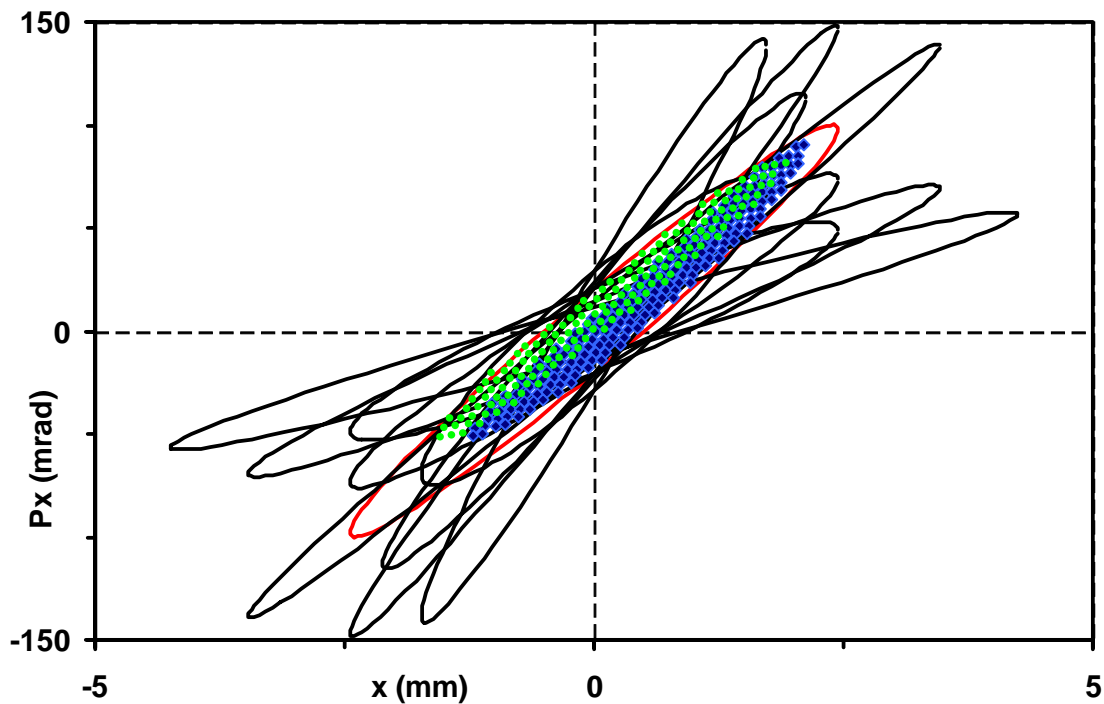
Figure 23: Ions representing different points of the phase space (measured with the emittance measurement system) were tracked back to the source and plotted in green and blue. An ellipse representing this ensemble in red and variations on this ellipse in black can be accommodated by the injection line and matched to the closed orbit solution of the ring when injected.

An example of the results of these experiments is given in Figure 23. Two different initial ensembles (corresponding to two different Einzel lens voltages but with the same 20 kV extraction voltage and the same source conditions) are plotted in green and blue. The agreement between both ensembles is reasonably good. The small discrepancy between them can be explained by possible small misalignments of the plasma electrode, puller and/or Einzel lens. The red ellipse ($\varepsilon = 50 \cdot \pi \cdot mm \cdot mrad, \; \alpha = -4.8, \; \beta = 0.12 m$) was chosen as a conservative representation of the extracted beam.

The injection line should not only be able to accommodate a beam with the previous parameters but also significantly different ones:

- The parameters determined before, correspond to a beam which is a combination of H^+, H_2^+ and H_3^+. The beam parameters of the individual mass states are expected to be different.

- The conditions in the source (gas pressure, filament current…) and the extraction voltage have a significant impact in the properties of the extracted beam.

For these reasons, we could comfortably assert that beams with significantly different transverse parameters (some of which are shown in black in Figure 23) could be shaped properly and matched to the closed orbit solution of the ring.

It was also verified that the size of the beam would never exceed the acceptance of the hardware installed inside the beam line. To do this, the injection line was first modeled using COSY Infinity [15]. Next, the voltages of the

Einzel lens and the quadrupole triplet necessary to match the chosen initial ensemble to the closed orbit solution of the ring at the injection point were calculated. Finally, the beam envelopes along the injection line were calculated for the chosen initial ensemble and voltage values.
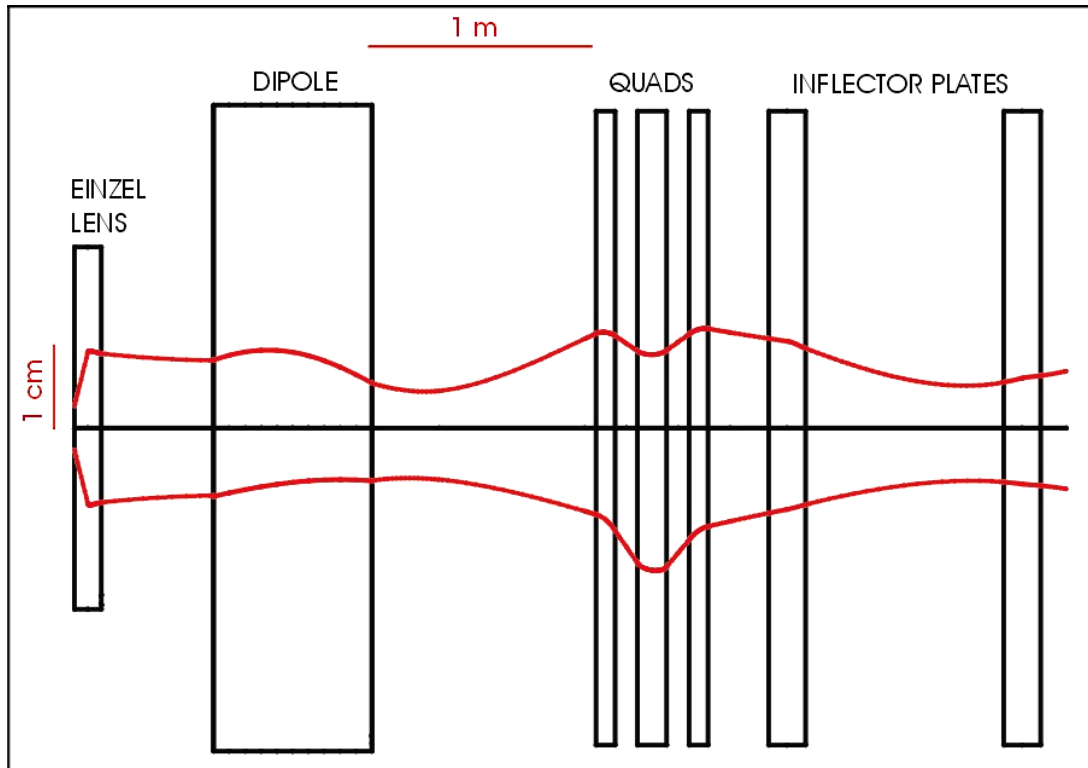
Figure 24: Envelope of the beam as it moves in the injection line of the SIR. The curve on top is the vertical beam envelope (perpendicular to the medium plane of the ring). The bottom curve corresponds to the beam envelope in the horizontal plane.

An example of the resulting horizontal and vertical beam envelope is plotted in Figure 24. The envelopes shown are for a 20 keV, H_2^+, $\varepsilon = 50 \cdot \pi \cdot mm \cdot mrad$ beam with initial $\alpha = -4.8$ and $\beta = 0.12 m$. The upper red curve in the figure corresponds to the vertical envelope (perpendicular to the medium plane of the ring), while the lower red curve shows the horizontal

envelope. The positions of the different elements of the injection line relevant in the beam dynamics are also specified.

COSY Infinity was used to model the first order beam dynamics in the injection line of SIR. Even though COSY includes many functions to represent different optical elements, it was determined that small corrections would have to be introduced to better represent some of the elements of the injection line. A description of the COSY model is discussed next.

The Einzel lens was modeled as a thin lens. To determine the relationship between the Einzel lens voltage and its focusing strength, first the electric field of the lens was calculated using SIMION. Then, an ion, which was radially displaced from the beam axis, was tracked in that field and its focusing distance was determined.

The dipole magnet was modeled as a dipole without edge focusing. A correction to take into account edge focusing was added after ions were tracked in the 3-D magnetic field produced by TOSCA [16] and a better matrix to represent the fringe fields was calculated.

The focusing strength of the quadrupoles for different voltages was calculated in a similar way as for the Einzel lens. Particles were tracked in the 3D electric fields produced by SIMION. Then, the voltages needed in the COSY model to have the same focusing strength as in the SIMION model were determined. (COSY uses a hard edge approximation to determine the focusing strength. So, it always underestimates it.)

The inflector plates have a focusing effect in the bending plane. The focusing is due to the different time particles above the medium plane (positive voltage) spend under the influence of the electric field compare to the time particles below the medium plane (negative voltage). The longer time in the electric field, the larger the deflection angle is. There is also a very weak focusing effect in the transverse plane due to the wings introduced in the geometry of the inflector plates. The focusing strength was calculated, as for the other optical elements, tracking particles in the 3D electric fields produced by SIMION.

These combined focusing effects were modeled in COSY as a thin lens located in the center of the inflector plates.

Snap shots of the beam ellipses (defining Y as the plane perpendicular to the medium plane of the ring and X as parallel) at different points of the injection line using the COSY model are shown in red in Figure 25. The two different ellipses correspond to beams with different emittances (10·π·mm·mrad and 50·π·mm·mrad).

Particles were also tracked in the 3D fields produced by SIMION and TOSCA along the whole injection line. They are shown in the same figure in black.

It can be observed that the non-linear effects are especially important for the 50·π·mm·mrad case. To determine the sources of these effects, each element was studied separately.

Ions, representing perfect ellipses in the phase space, were tracked through each individual optical element. The results showed a negligible contribution from all elements except the Einzel lens.

2.14. Other injection line schemes

Different injection line schemes were initially considered:

- Using a Wien filter instead of a dipole magnet to separate the different mass states. This option was discarded mainly because of lack of space. The overall length of the injection line would not be much longer than the one that was finally used, but the 90° bending magnet allows a more efficient use of the available space.

Using the same design for both the bending magnet and the ring magnets was also a reason not to choose the Wien filter since the latter would have required a larger investment in design.

- Using the chopper to deflect the beam toward the ring. The possibility of using the chopper to deflect the beam toward the ring at the same time was discarded because of the non-linearities that would have been introduced in the beam.

As discussed in section 2.10, grids in both sides of the deflecting plates of the chopper had to be added to limit the extension of the electric field. These same grids introduce significant non-linearities in the deflected beam but not in the one injected in the ring. It was, therefore, decided to separate the chopping of the beam and the deflecting toward the ring.
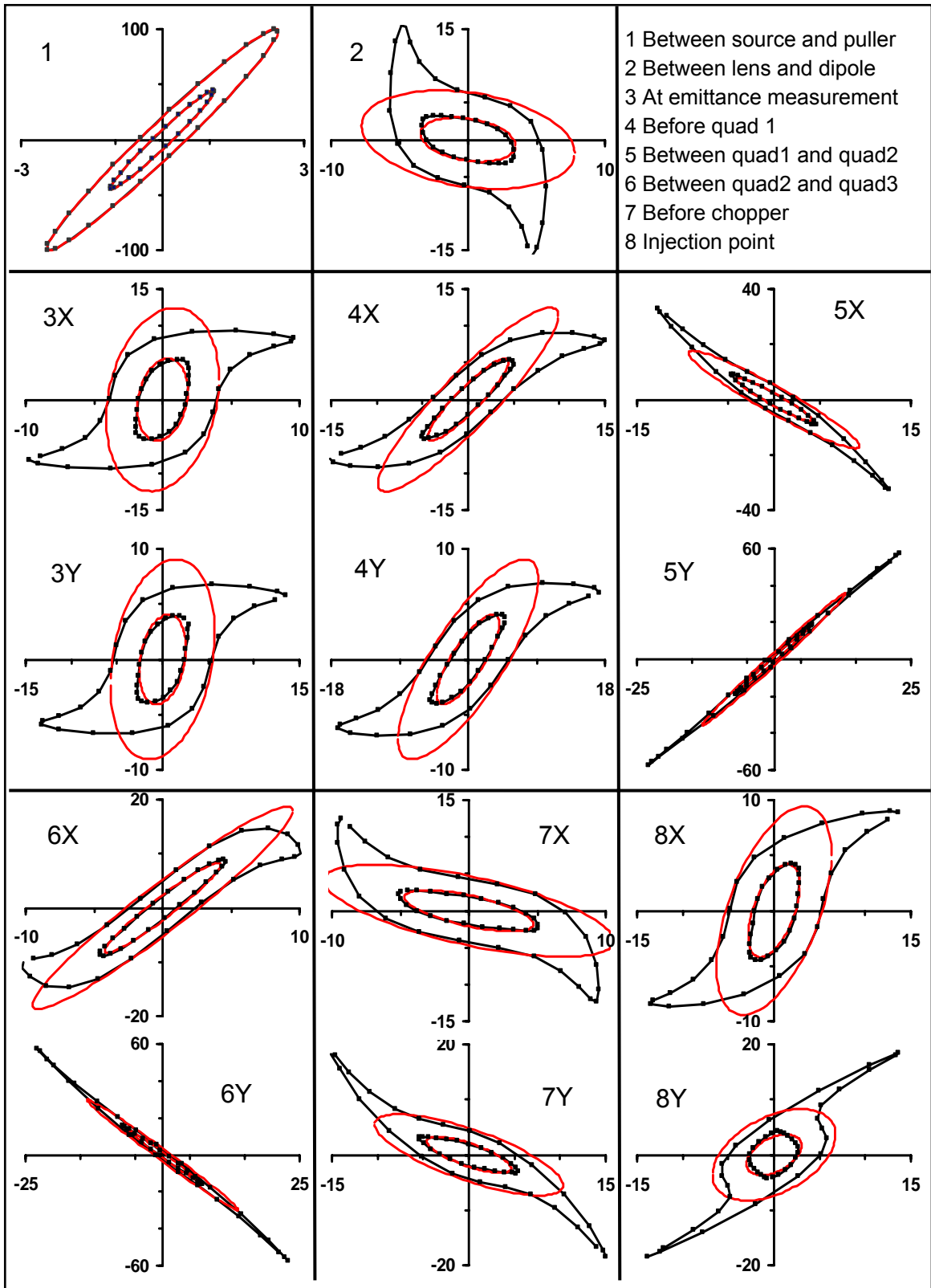
Figure 25: Snap-shots of the phase space of the beam in the injection line. Ellipses using COSY model in red. (Black in the 3D fields). Inner (outer) ellipses 10 (50) π mm mrad.

- Aligning the injection line to the 17.5^o injection angle instead of deflecting the beam by that same angle. Even though this option would have reduced the number of elements needed in the injection line eliminating the need for the first pair of inflector plates, the supports for the different elements of the injection line would have been much more complicated.

- Injecting the beam radially. The dipole magnets in the ring extend radially further away than vertically. In order to have enough clearance, a larger deflection angle would be needed making the design of inflector plates more challenging.

In addition, the drift between inflector plates would also need to be longer making it more difficult to find a good way to match the injected beam.

- Injecting beam from above or from below the ring. The decision to inject the beam from above was made because the residual magnetic field at floor level (probably due to magnetization of the reinforcing steel generated by the stray field of other large magnets in the building) is larger in the region where the injection line is placed than where the ring is. Raising the injection line reduces the impact of the residual fields in the beam trajectory. If the injection line had been lower, the medium plane of the ring would have had to be elevated. Accessing the center of the ring for assembly or maintenance would have been more complicated.

- Rotating the dipole magnet by 90° in such a way that the bending plane would be parallel to the medium plane of the ring. Even though the source would have been more accessible making the maintenance easier, the weight of the

source and gas feeding system would have needed an extra support. In addition, this option would effectively use more room.

- Using a second Einzel lens as opposed to a quadrupole triplet. The main advantage of this option is that the mechanical complexity of the quadrupole triplet is much larger than that of an Einzel lens which would have been easier and less expensive to build. The length of the injection line would also be reduced and the alignment of the different elements would have been simplified. On the other hand, adding a single extra Einzel lens would not give the same degree of flexibility as a quadrupole triplet to accommodate different initial beam ensembles. Four different parameters (α_x, α_y, β_x and β_y) need to be matched at the injection point and adjusting just the two knobs of the Einzel lenses do not guarantee a good match. So, several Einzel lenses would need to be used, reducing the advantages of this scheme. While ± 1 kV power supplies are needed to bias the quadrupoles effectively, voltages up to 30 kV (depending in the lens aperture and beam energy) are needed for the Einzel lenses with a consequent increase in the price of the power supplies. A safety cage (and the corresponding safety interlocks) would also need to be built around them since there are not commercially available enclosed vacuum feedthroughs rated for that voltage.

- Biasing the Einzel lens to a negative voltage. As was previously discussed, the Einzel lens after the source introduces more non-linear effects in the beam than any other element of the injection line. To minimize this effect the aperture of the lens was increased but the improvement was limited. The

possibility of biasing the Einzel lens negatively was also studied. In this case, the first ground to high voltage gap has a focusing effect and the second high voltage to ground gap a defocusing effect (the net effect is still focusing). Because of this focus-defocus as oppose to the defocus-focus of the lens when it is biased positively, the non-linear effects introduced are reduced dramatically. The only problem with this scheme is that in order to have the same focusing strength, the magnitude of the negative voltage would need to be much larger that the magnitude of the positive voltage (even a factor 2 larger). Delivering such a voltage (-50 to -60 kV) to the Einzel lens is technically fairly complicate. Therefore, this possibility was abandoned.

- Other Einzel lens schemes were also studied to try to reduce the non-linear effects of the solution finally used. Electric field calculations and particle tracking was performed with SIMION. Some of the options studied included breaking the single Einzel lens into several shorter lenses, changing the shape of the different electrodes, biasing the puller. None of them succeeded in reducing the problem significantly, so they were not adopted.

3.   EXTRACTION LINE OF SIR

3.1.   Introduction

This chapter describes different aspects of the extraction line of the Small Isochronous Ring (Figure 26). The extraction line is very short and it does not physically extend outside the extraction box of the ring. It is located 180° after the injection.
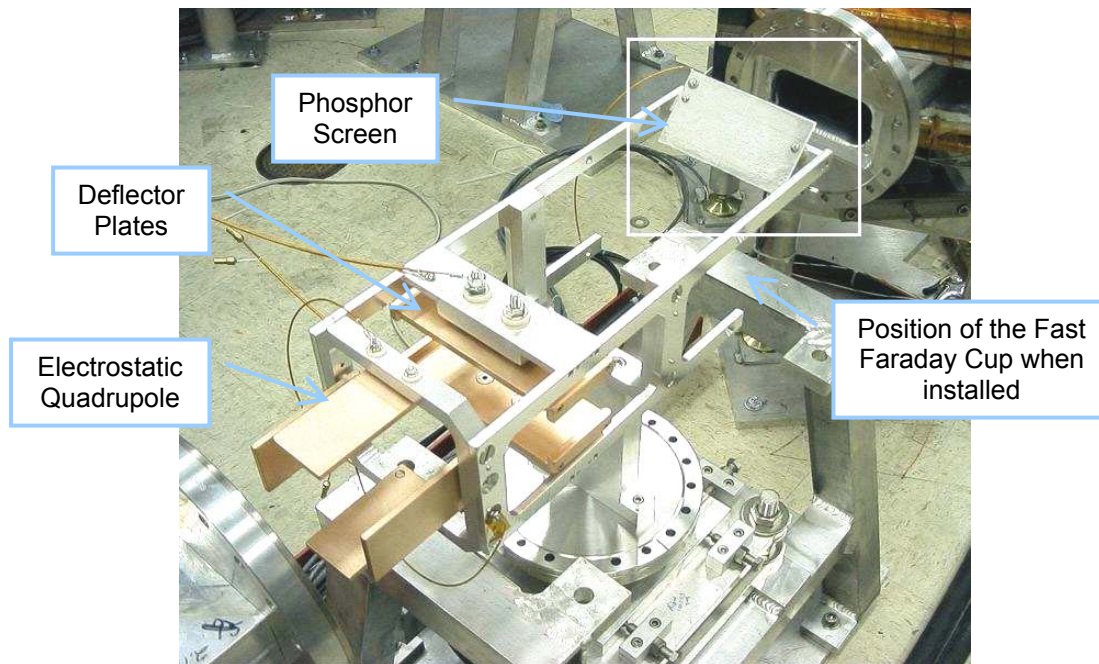
Figure 26: Picture of the extraction box of SIR during assembly.

It consists of a pair of deflector plates, a phosphor screen and a fast Faraday cup. The deflector plates are pulsed to high voltage to kick the bunch when extraction is desired. The bunch can be kicked above the medium plane toward a phosphor screen to study the transverse size of the beam (refer to section 4.6.1. of [3] for detais). By changing the polarity of the deflector plates,

59

the bunch can also be kicked below the medium plane of the ring toward a fast Faraday cup to study its longitudinal profile. Two different fast Faraday cups were developed for this purpose. One of them is a sector faraday cup capable of capturing the whole bunch at the same time. The second one is smaller and can be moved radially to capture parts of the beam allowing a better characterization of the energy spread of the incoming beam. It was designed to maximize its bandwidth.

The different elements are described in the following sections. The chapter ends with a brief description of other possible fast Faraday cups schemes that were also considered.

3.2.   Deflector Plates

A pair of OFHC copper plates is used to deflect the beam out of the medium plane of the ring (Figure 26). The length of the plates is 6.1 cm, the width is 14 cm and the gap between them is 5.1 cm. As it can be seen in the picture, the plates are not completely flat. Wings were added in the sides of each plate to increase the region where the electric field is flat. The dimensions of these wings are 6.3 mm by 6.3 mm.

Ions, which are above the medium plane of the ring when they are deflected down toward the fast Faraday cup, will take longer time to reach the Faraday cup than those that are below the medium plane of the ring. The main reason for this is that they have to follow a slightly longer path. There is also a

small contribution due to the loss of kinetic energy when going through the plates.

Simulations to quantify this effect were performed using SIMION. It was determined that the induced blurring of the longitudinal profile could be significantly reduced by aligning the surface of the fast Faraday cups to be perpendicular to the median plane of the ring instead of to the incoming beam. The residual effect in the longitudinal profiles was estimated to be around 1 ns which is much smaller than the size of the clusters we expected to observe.
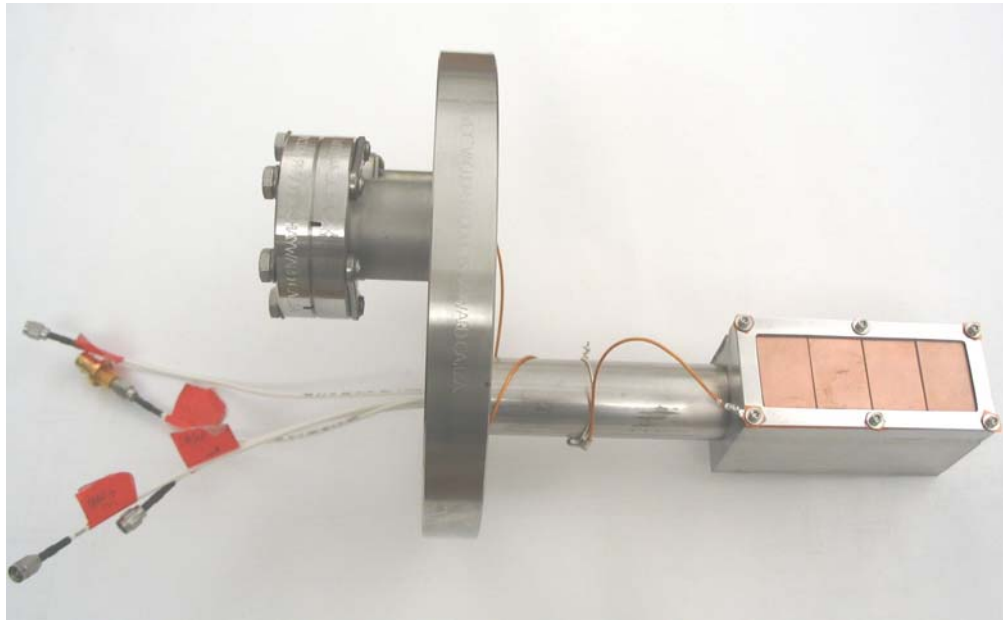
Figure 27: Picture of the sector fast Faraday cup used to measure beam longitudinal profiles when they are extracted from the ring.

3.3.   Sector Fast Faraday Cup

A sector fast Faraday cup (shown in Figure 27) is used to measure the longitudinal beam profile of the extracted bunches. Four OFHC copper

electrodes are used to collect the beam. Each of the electrodes is directly attached to the pin of an electrical SMA vacuum feedthrough using a set screw. 50 Ω RG-316 cables run inside a 1.5" diameter pipe from the SMA connectors to the exterior of the machine where they are individually connected to broadband amplifiers. The outputs of the amplifiers are connected to the four input channels of a digital oscilloscope. Refer to section 4.6 for a complete description of the electronics used.

The electrodes are positioned and electrically separated from each other and from the grounded parts of the Faraday cup by macor spacers.

A molybdenum grid is positioned 1.5 mm in front of the electrodes. The thickness and the line widths of the grid are 2 mils and spacing between lines is 20 mils (i.e. 81 % transparency). The grid is used to shield the electrodes from the incoming beam and from outside electromagnetic noise. It is clamped between two 1 mm thick stainless steel frames. The grid and the frames can be biased down to -100 V to suppress the secondary electrons emitted by the electrodes when they are hit by the incoming beam.

A Kapton coaxial cable attached to one of the six clamping screws is used to bias the system. This cable is connected to a BNC vacuum feedthrough attached to a 1 1/3" nipple welded to the 8" flange that supports the whole structure.

A Kapton foil electrically insulates the lower frame from the rest of the Faraday cup. Kapton washers insulate the upper frame from the six clamping screws.

A second 2 ¾" nipple was also added to the 8" flange to be used in the future if needed.

The radial size of each of the electrodes is approximately 2.5 cm and the vertical size is 3.5 cm. No gap is left between electrodes since a step-like structure ( ) is used.

Several factors limit the time resolution of the longitudinal profiles that can be measured with this Faraday cup:

- Electronics bandwidth. The 1.5 GHz bandwidth of the oscilloscope used to capture the profiles is limited by the high frequency limit of the bandwidth of the amplifiers (1 GHz) that are currently being used. This corresponds to a rise time (t_R) of 0.35 ns according to the formula below. Justification of this relationship can be found in [8].

$$t_R = \frac{0.35}{BW}$$

- The gap between current collector of the Faraday cup and shielding grid. This is especially important for low energy beams. Once the head of the bunch has gone through the shielding grid, it will start inducing a signal in the current collector. If the gap is 1.5 mm, a H_2^+ beam with energy equal to 20 keV will start inducing a signal ~ 1.1 ns before it actually hits the current collector. There are two main reasons why reducing the gap will not significantly improve this time. The distance between lines of the grid should be smaller than the gap to shield effectively. Since the thickness of the grid lines cannot be reduced below 1 or 2 mils for mechanical reasons,

reducing the distance between lines will simply lower the transparency of the grid. To compensate for this reduction of the transparency, the gain of the amplifier has to be larger. Typically, larger gain is correlated with smaller bandwidth for commercially available amplifiers. The other reason not to reduce the gap is that the capacitance of the Faraday cup would increase. The effect of this capacitance would perturb the matching of the impedance of the transmission line, thus perturbing the beam signal.

- Matching of the transmission line. Any mismatch of the transmission line will produce reflections of the high frequency components of the signal reducing the bandwidth of the system. The geometry of the electrodes of this Faraday cup was not optimized to match the 50 Ω of the rest of the transmission line because of the lack of space.

The best way to determine the time resolution of the Faraday cup is to use a time domain reflectometer (TDR) to generate a pulse with a very fast rise time (~ 100 picoseconds). This pulse can be sent toward the collector of the cup and the reflected pulse can be measured. The rise time of the reflected pulse would define the time resolution of the Faraday cup.

TDRs are expensive and are not available at the NSCL. So, the next best thing was done. A bunch was used to generate the pulse and its rise time was measured. Since the rise time of the bunch itself is not known, this method will only give an upper limit to the time resolution of the Faraday cup. Actually, based on how the beam is chopped to generate the bunches, it is very likely that the time resolution is significantly better than this estimate.

Figure 28 shows a typical bunch profile measured with one of the sectors of the Faraday cup. From the figure, it can be determined that the rise time (defined as the time to go from 10 % to 90 % of the maximum signal) is 3.2 ns. Using the relationship between rise time and bandwidth, we can determine that the bandwidth of the whole system (Faraday cup, amplifier, oscilloscope and cables) is larger than 110 MHz.
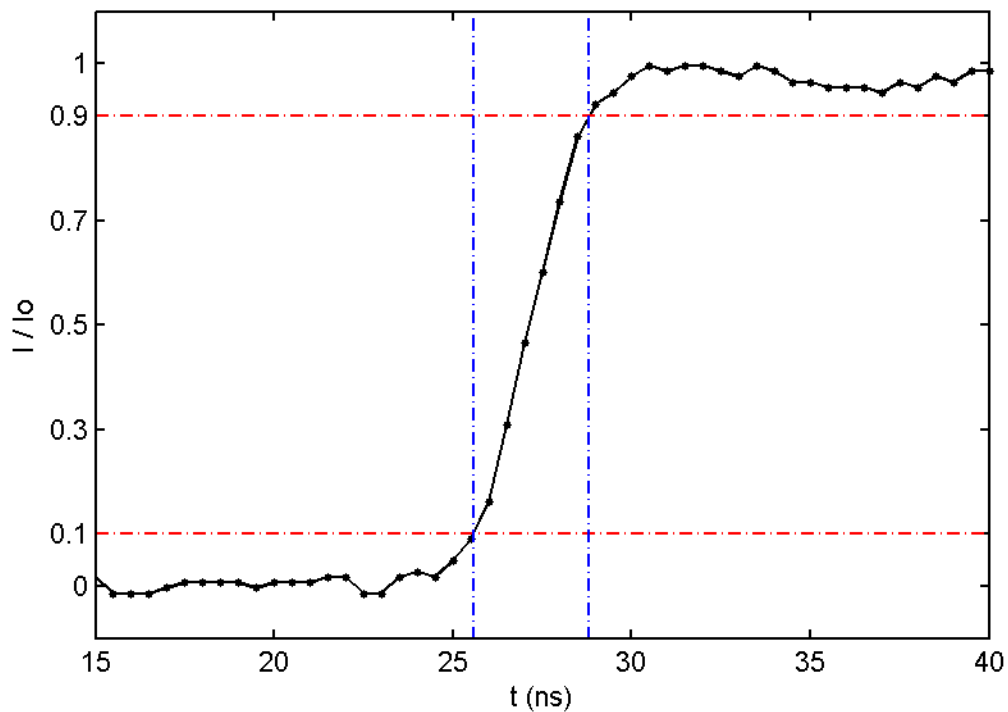
Figure 28: Measured rise time of the signal in one of the sectors of the fast faraday cup when a bunch hits it.

The proximity of the different sectors of the Faraday cup has the undesired effect of cross talk between channels since they are capacitively coupled.

To try to quantify this effect, the "rf out" channel of a network analyzer was connected to one of the central electrodes and the "rf in" channel was connected

to the other central electrode. A sinusoidal signal with a frequency that was swept between 300 kHz and 1.5 GHz was produced by the network analyzer (rf out) in one of the electrodes. The induced signal in the other electrode was measured (rf in). The relative value of these two signals is displayed in Figure 29. It can be observed that the maximum induced signal (-18.5 dB) is produced for a frequency of ~ 75 MHz. That is, a signal will be induced in one of the electrodes when the beam hits the other electrode. The amplitude of the 75 MHz component of the induced signal will be 12 % of the amplitude of the same frequency component of the incoming beam.
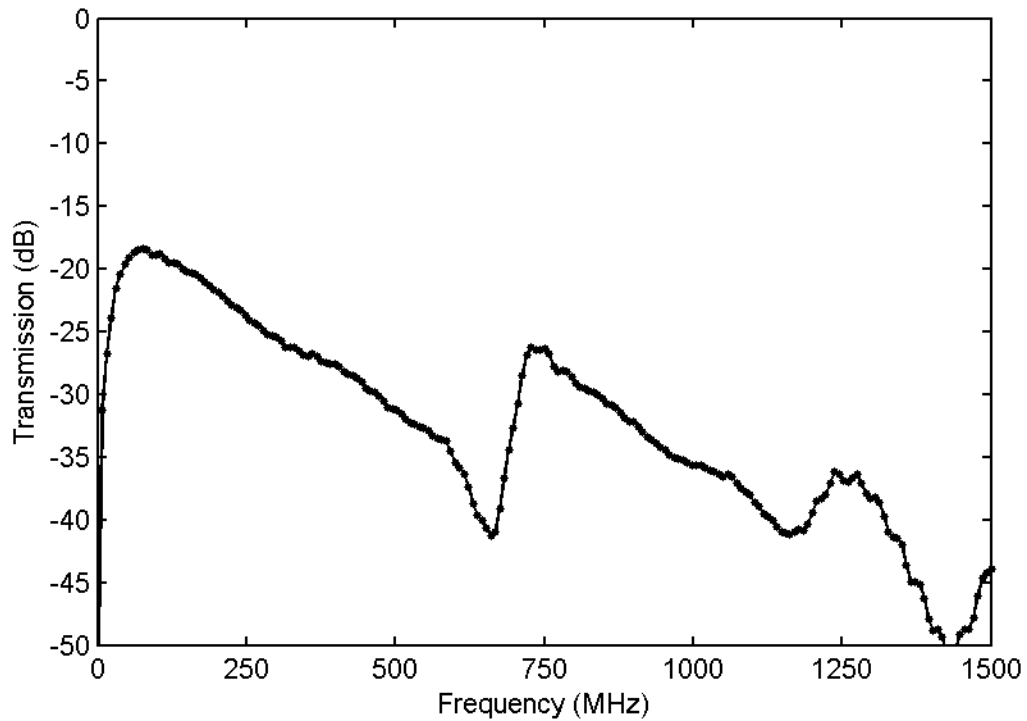
Figure 29: Measurement of the cross talk between central electrodes of the sector fast Faraday cup. The amplitude of the induced signal in one the central electrodes was measured when a signal was sent to the electrode next to it.

The signals induced in the Faraday cup due to electromagnetic noise were also studied in an effort to better understand the ratio between signal and noise levels. Figure 30 shows a measurement of the signal captured by one of the sectors of the Faraday cup when no beam is being injected in the ring. The noise induced when the chopper, second inflector and deflector plates are turned on, can be clearly identified.
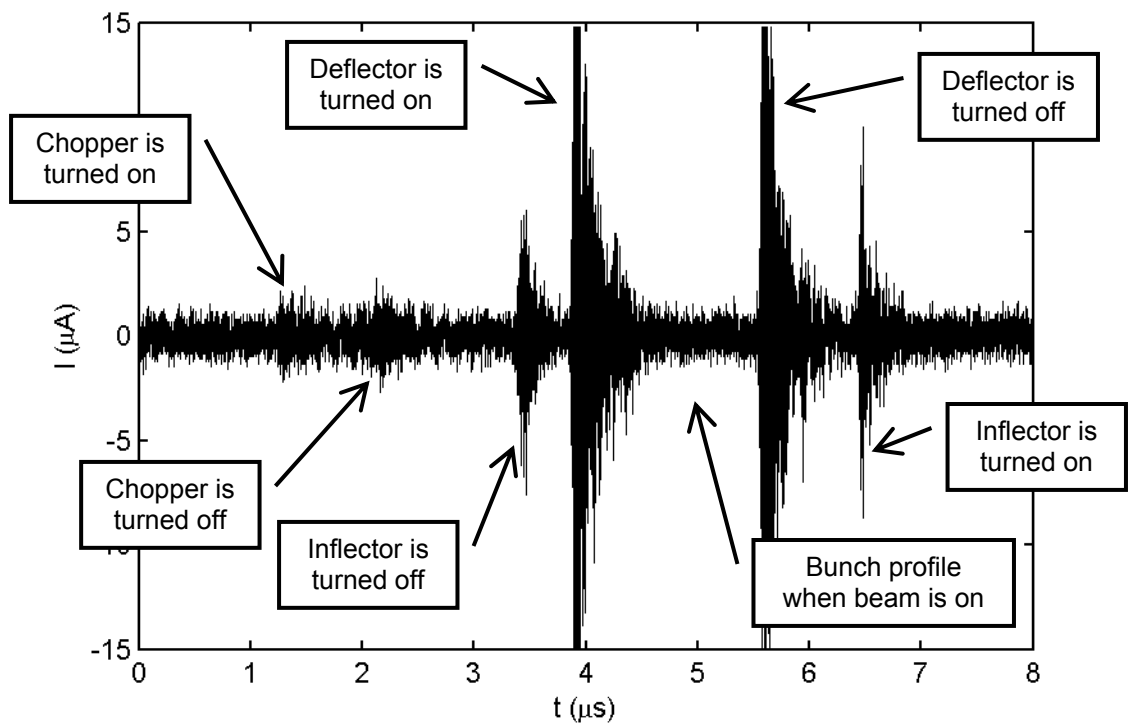
Figure 30: Noise induced in one of the electrodes of the sector Faraday cup when the chopper, inflector and deflector plates are turned on and off.

The amplitude of this noise is typically larger than the beam signal in the case of the deflector plates since they are closer to the Faraday cup than the other elements. This is not a problem because if the deflector is turned on 1 μs before the head of the bunch arrives and turned off 1 μs after the tail has hit the Faraday cup, the induced noise does not interfere with the beam signal.

Once the large noise sources were eliminated, a residual noise equivalent to a ± 0.5 µA (standard deviation) current remained. This is what defines the noise to signal ratio. For example, a 10 µA bunch will have a noise to signal ratio equal to 5 %.

3.4.   Movable Fast Faraday Cup

A movable fast Faraday cup can be used to measure the longitudinal bunch profiles as an alternative to the sector Faraday cup (Figure 31). It consists of an OFHC copper central electrode where the beam is collected. This electrode has a conical shape and it is attached to the pin of a 50 Ω type N vacuum feedthrough to which a type N to SMA right angle connector is attached. The bottom surface of this cone is used to collect the beam. It has a diameter equal to 16.25 mm. An RG-316 coaxial cable, which runs inside the tube, is used to transmit the beam signal to a broadband amplifier. The output of the amplifier is connected to a digital oscilloscope. Refer to section 4.5 for a complete description of the electronics used.

The electrical design of the Faraday cup is a modified version of those appearing in references [9] and [17]. The conical central electrode is surrounded by an empty conical stainless steel structure that acts as the shield of a coaxial transmission line. The impedance (Z_0) of a bi-conical transmission line like this one is equal to

$$Z_0 = \frac{1}{2\pi} \sqrt{\frac{\mu_0}{\varepsilon_0}} \ln\left(\frac{D}{d}\right)$$

where D is the inner diameter of the outer conductor and d is the outer diameter of the inner conductor. For the impedance to be equal to the 50 Ω of the rest of the transmission line, a ratio $\dfrac{D}{d} = 2.303$ was chosen.

Figure 31: Picture of the movable fast Faraday cup used to measure longitudinal beam profiles.

The previous discussion strictly applies only to infinitely long transmission lines. In our case, this length had to be limited to 2 cm due to the lack of space, leading to an 18.7° half angle for the inner cone. This angle is still significantly smaller than the 25° of reference [10] for which a bandwidth of 2 GHz is claimed.

A molybdenum grid is positioned 1 mm in front of the electrodes. The thickness and the line widths of the grid are 2 mils and the spacing between lines is 20 mils (i.e. 81 % transparency). The grid is used to shield the electrodes from the incoming beam and from outside electromagnetic noise. It is clamped between a 1.6 mm thick stainless steel ring and a 0.4 mm thick aluminum ring. The grid and the rings can be biased down to -100 V to suppress the secondary electrons emitted by the electrodes when they are hit by the incoming beam.

A Kapton coaxial cable, attached to one of the four clamping screws, is used to bias the system. This cable is connected to a BNC vacuum feedthrough attached to a 1 1/3" nipple welded to the 4½" flange that supports the whole structure.

A Kapton ring electrically insulates the lower ring from the rest of the Faraday cup. Kapton washers insulate the upper ring from the six clamping screws.

The whole system previously described is attached to a commercially available linear motion feedthrough that can be moved by a stepper motor.

The original intention was to use this Faraday cup to capture a portion of the beam at a certain radius (i.e. energy). Move it to a different radius to capture another portion of the longitudinal profile with different energy. These measurements would then be combined to reproduce the longitudinal profile of the bunch extracted after a given number of turns. The position of the Faraday cup when the measurements were made would be used to get information about the energy spread of the bunch.

The cluster formation process is highly sensitive to small perturbations of the beam extracted from the ion source what makes it impossible to overlap longitudinal profiles of different injected bunches. The Faraday cup is still useful to measure longitudinal profiles for a given radius.

Measurements similar to those performed for the sector Faraday cup to determine its time resolution were also performed in this fast Faraday cup yielding very similar results. We were able to determine that the bandwidth of the

fast Faraday cup is larger than 110 MHz. (In fact, we believed it is significantly larger since special care was put in the cup design to be able to maximize its bandwidth. But, the electronics necessary to performed more precise measurements are not currently available at the NSCL).

3.5.   Other types of fast Faraday cups that were also considered

A different kind of Faraday cup based on strip-lines was also considered. An example of such a kind can be found in reference [9]. The back of a prototype built to verify if it could be used is shown in Figure 32.
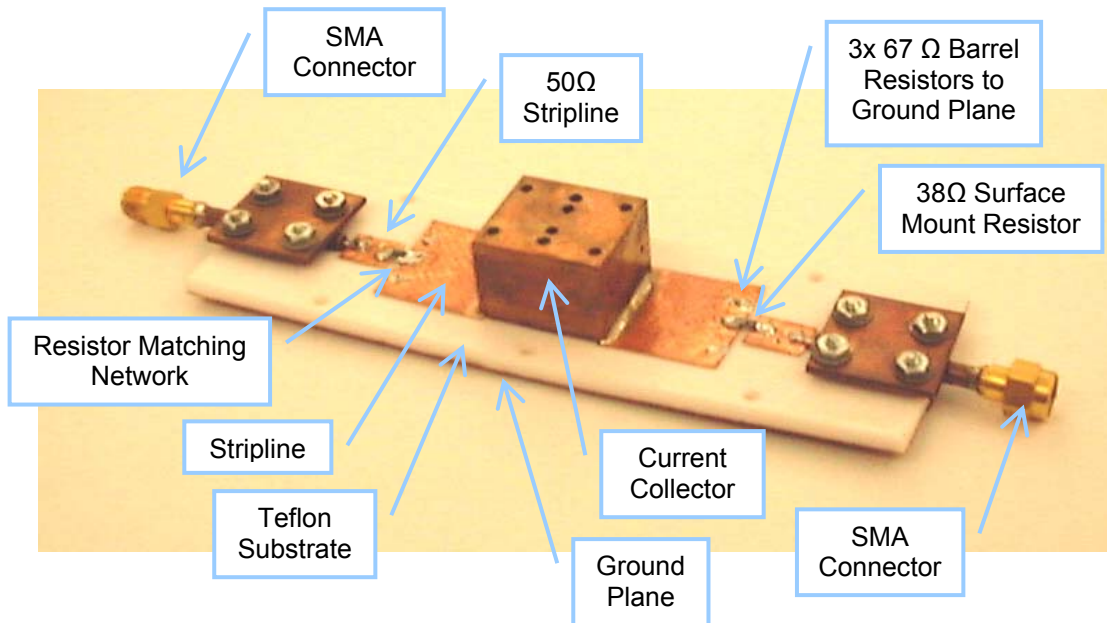
Figure 32: Picture of the back of the prototype stripline fast Faraday cup developed for SIR.

It consists of an OFHC copper current collector. It is soldered to a copper stripline with the same impedance. The whole line is matched using a network of matching resistors between this stripline, the 50 Ω stripline and the ground plane.

The main advantage of this kind of Faraday cup is its size. It can easily fit in the space available. But, a number of disadvantages make the designs described in previous sections more attractive:

- The matching resistor network acts as a splitter. Part of the signal is dissipated in the resistors reducing the output signal. To compensate for this loss an amplifier with larger gain would need to be used.

- The striplines are not shielded and are, therefore, very likely to pick up electromagnetic noise. Adding the necessary shielding would make the mechanical design more complicated.

- The most important problem is that it is not possible to make it high vacuum compatible. First, soldering of different elements is required. The residual flux in these points is not vacuum compatible. Second, coaxial cables with SMA connectors need to be used to bring the signal out of the vacuum chamber. There are no commercially available SMA connectors that are high vacuum compatible. Several tests were performed to quantify the effect of these non-high vacuum rated elements in the pumping time and the results showed that a system of this type was not acceptable.

4. ELECTRONICS AND CONTROL SYSTEM OF SIR

4.1. Introduction

This chapter describes the electronics and the control system used in SIR. Some possible future upgrades are also discussed. The chapter has been divided in sections that correspond to different subsystems of the machine. A brief description of some alternative solutions that were also considered is included at the end of the chapter. Some of the electronics used appear in Figure 96, Figure 97, Figure 101 and Figure 105.

Some of the requirements of the control system of SIR were:

- Low cost.

- Electronics available from previous projects had to be reused if possible to further lower the cost. (Although, in some cases, using old electronics increased the development time of the control software.)

- Independence from the control system of the rest of the NSCL.

- Easy upgradeability. New experiments based on the results of previous ones have been proposed. The flexibility of the control system allowed incorporation of new electronics for several tasks without major changes.

- Automation of the most time consuming tasks (like emittance measurements and longitudinal profile capture) improves the quality of the data (beam characteristics drift less over a short period of time), reduces human error and greatly simplifies the operation of the machine.

- Storage of experimental data for analysis. Even though some data analysis is performed by the data acquisition programs, all the raw information is saved for offline data processing.

With these constrains and requirements in mind, a PC-based option was chosen as the best compromise between low cost and high functionality. Most of the software was developed in LabVIEW [18] to reduce the development time since drivers to control most of the instrumentation in this language are typically provided by manufacturers. When extensive data processing was necessary, the LabVIEW programs were linked to MatLab [19] that is very well suited for data processing and visualization.

4.2. Scanning Wires

Two pairs of scanning wires can be used to measure transverse beam profiles in the ring. They are located in the vertical and horizontal plane of the ring after ¼ and ½ a revolution. Please, refer to [3 page 122] for a complete description of their design.

They are driven by stepper motors powered by a National Instruments MID-7604 power drive that is controlled by a National Instruments PCI-7334 motion controller.

The beam current, intercepted by the scanning wires, is read by a Keithley 6485 picoammeter after the right signal is selected with a Keithley 7001 equipped with a Keithley 7158 low current switch card. The analog output of the

74

picoammeter (output voltage is proportional to the measured current for a given scale) is redirected to one of the analog inputs of a National Instruments PCI-6036E DAQ for further analysis.

Both the picoammeter and the low current switch are controlled by a PC using GPIB (IEEE 488) communications. (Figure 33)
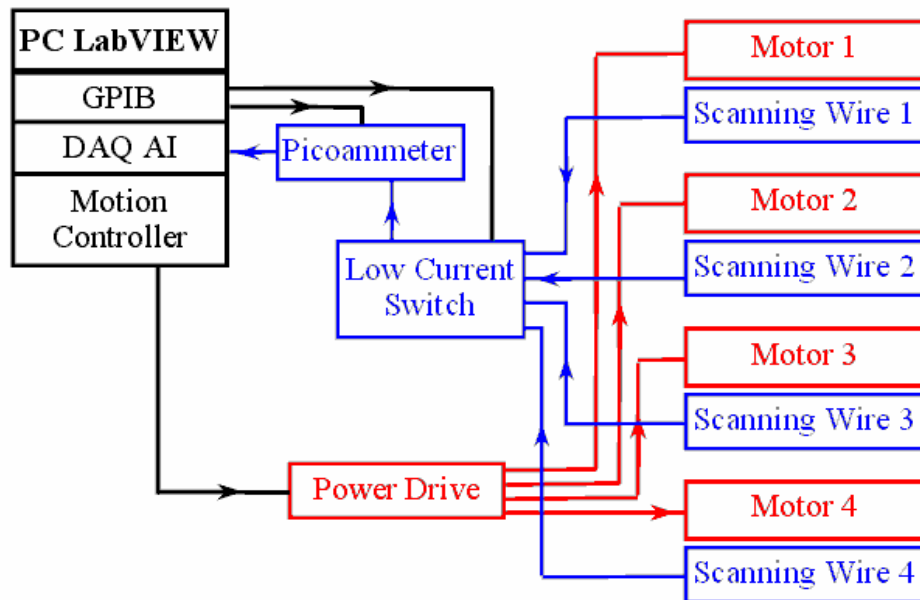
Figure 33: Layout of the scanning wires and their associated control electronics.

The control software has been developed using LabVIEW. A picture of the user interface is shown in Figure 34. The most important functionalities of the program are:

- It synchronizes the movement of the scanning wires with the data acquisition displaying it as current density as a function of the position of the scanning wire.

75

- The most important parameters of the last profile acquired are calculated and displayed. These parameters include the integrated beam current, the peak current density, the position and width of this peak.
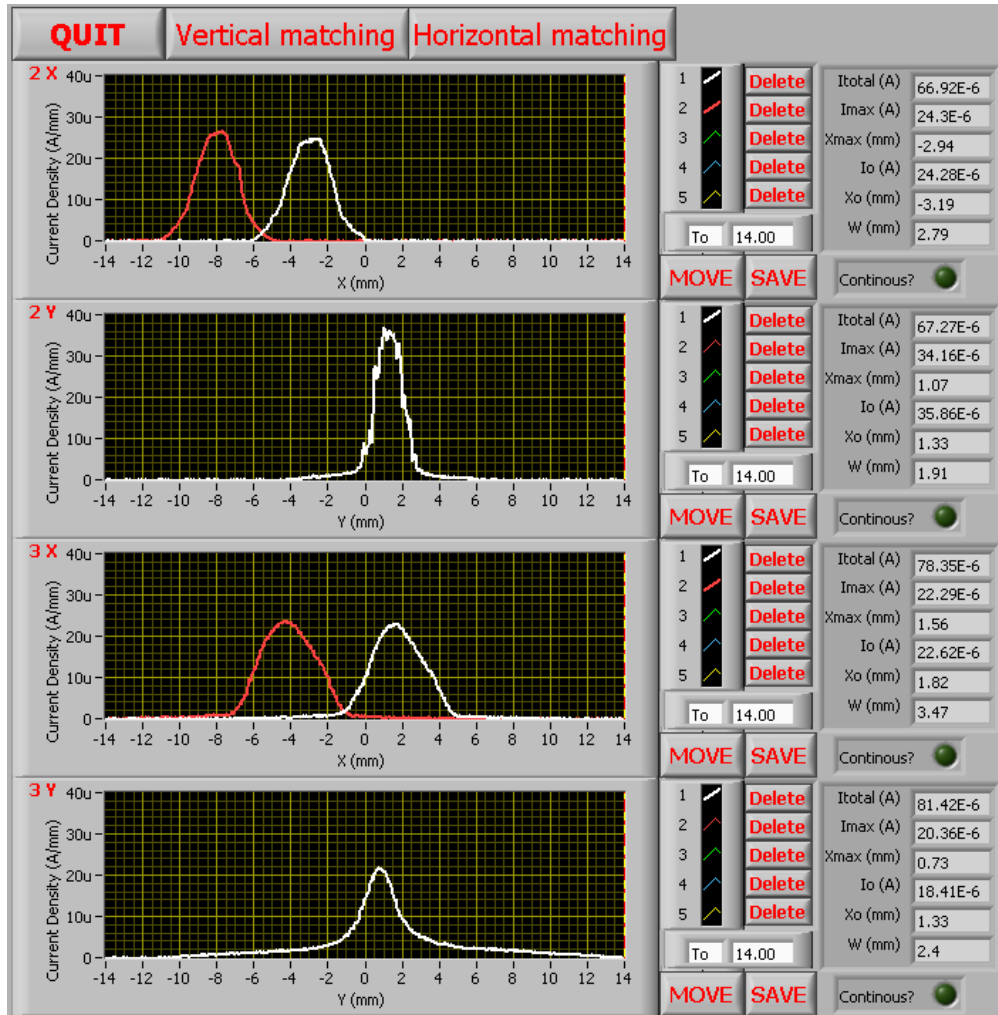
Figure 34: Front panel of the LabVIEW program used to control de scanning wires.

- The user can save the acquired data for further analysis.

- Voltages of the inflector plates needed to center the beam vertically are calculated based on information provided by the measured profiles (position of the peak current) for different voltages in the inflector plates.

- An analog functionality for horizontal beam centering using injection line horizontal steering correctors is included.

4.3. Emittance Measurement System

The Emittance Measurement System consists of a couple of movable slits. The portion of the beam that goes through both slits is collected by a shielded Faraday cup. The system is duplicated in the vertical and horizontal plane.

The layout of the control system is very similar to the one used for the scanning wires of the ring. (Figure 35)
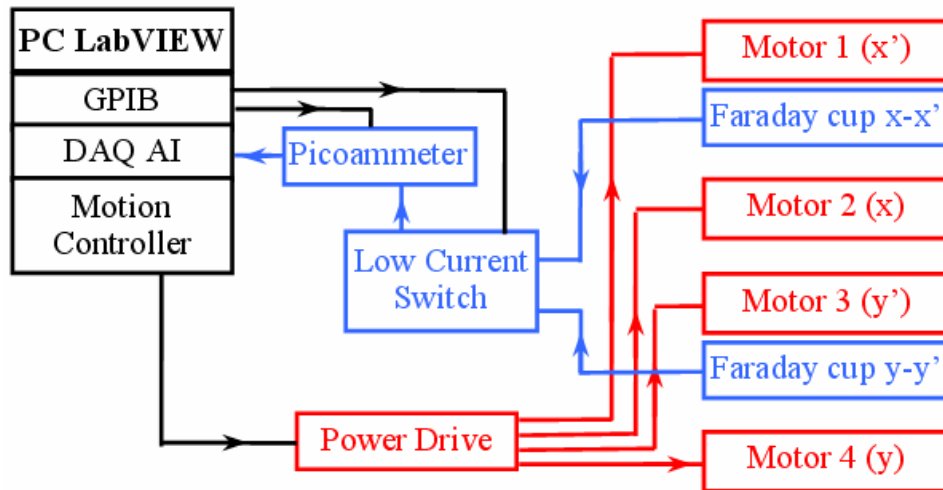
Figure 35: Layout of the emittance measurement system and its associated control electronics.

A LabVIEW program (Figure 36) was written to automatize the data acquisition. By taking data as the slits move, complete scans (typically 125 x 50 points) can be performed in less than ten minutes.

This same program also fits the measured data to an ellipse and displays its Courant-Snyder parameters (α, β and γ) as well as its rms-emittance (ε_{rms}).

The region of the phase space to be scanned is specified on the left of the front panel and the information about the beam is displayed on the right of the front panel once the scan has been completed. This information is later used to adjust the quadrupole triplet and the Einzel lens to match the injected beam to the closed orbit solution of the ring.

All the data taken is saved in a file for further analysis if necessary.
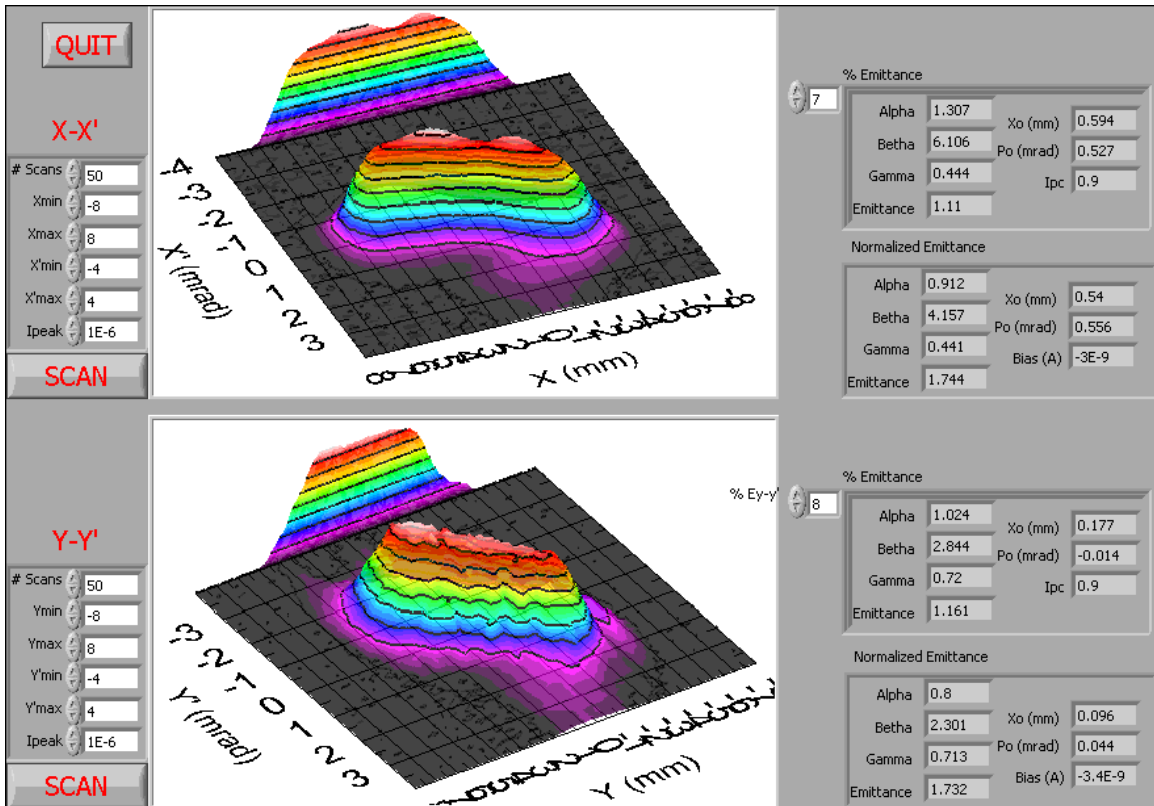
Figure 36: Front panel of the LabVIEW program used to control the emittance measurement system.

A full description of the Self Consistent, Unbiased Elliptical Exclusion (SCUBEEx) algorithm used to calculate the beam parameters can be found in references [20], [21] and [22].

4.4. Chopper, Inflector and Deflector Timing

A Thorlabs DG100N digital delay line is in charge of triggering the six DEI PVX-4140 high voltage fast switches at the right time. These switches produce up to ± 3.5 kV, down to 100 ns short pulses that are used to drive the different chopper, inflector and deflector plates.

Using a Tcl/Tk [23] program developed by Felix Marti, running in a PC, that communicates with the digital delay line though the network and a LanTronix UDS-10 TCP/IP to Serial Port converter, parameters such as the length of the bunches that we want to inject as well as for how many turns we want to keep them in the ring before extraction can be preset.
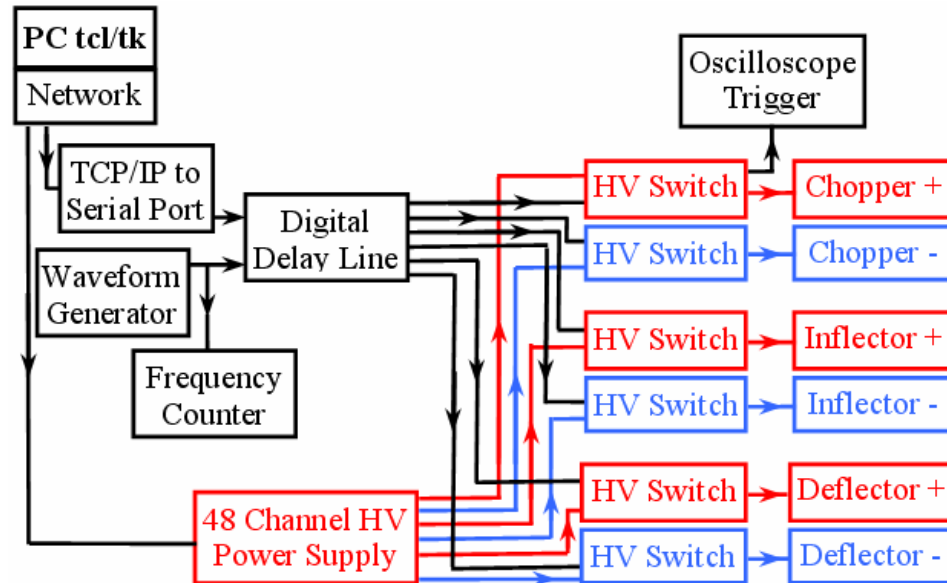
Figure 37: Layout of the chopper, inflector and deflector and their associated control electronics.

The voltage monitor of the high voltage switch of either one of the chopper plates or deflector plates is used to trigger the acquisition of the beam profiles in the oscilloscope.

The dc high voltage is provided by the CAEN SY2527 equipped with two A1733p and two A1733n power supply modules that is also controlled through the network with software provided by the manufacturer.

A square wave generated with a Leader LG1311 waveform generator is used to trigger the digital delay line. A HP-53131A frequency counter is used to precisely measure this frequency which determines how often bunches are injected in the ring (Typically ~ 1 kHz).

A National Instruments PCI-6602 counter/timer was also considered as a substitute for the digital delay line, the waveform generator and the frequency counter. Some of the advantages of this scheme include:

- The number of channels of the currently used digital delay line is 6. This is enough to trigger the 6 HV switches but not the oscilloscope which is triggered by the voltage output of the switch driving one of the chopper plates or one of the deflector plates. In contrast, the PCI-6602 card has 8 channels which would allow triggering the oscilloscope at the right time to simplify the data acquisition process.

- Lower cost.

- The frequency of the internal oscillator of the PCI-6602 is 80 MHz (i.e. delay time resolution is 12.5 ns) compared to 40 MHz for the DG100N (i.e. delay time resolution is 25 ns).

- Probably the most important difference is that the PCI-6602 is capable of generating trains of pulses as opposed to the single pulses of the DG100N. This would allow extracting consecutive bunches after a variable

number of turns which could be used to improve the matching procedure. Figure 38 shows how a typical beam looks like before matching is achieved. As the matching improves, the amplitude of the betatron oscillations is reduced. Eventually all the beam spots would collapse into a single spot when the beam is optimally matched.
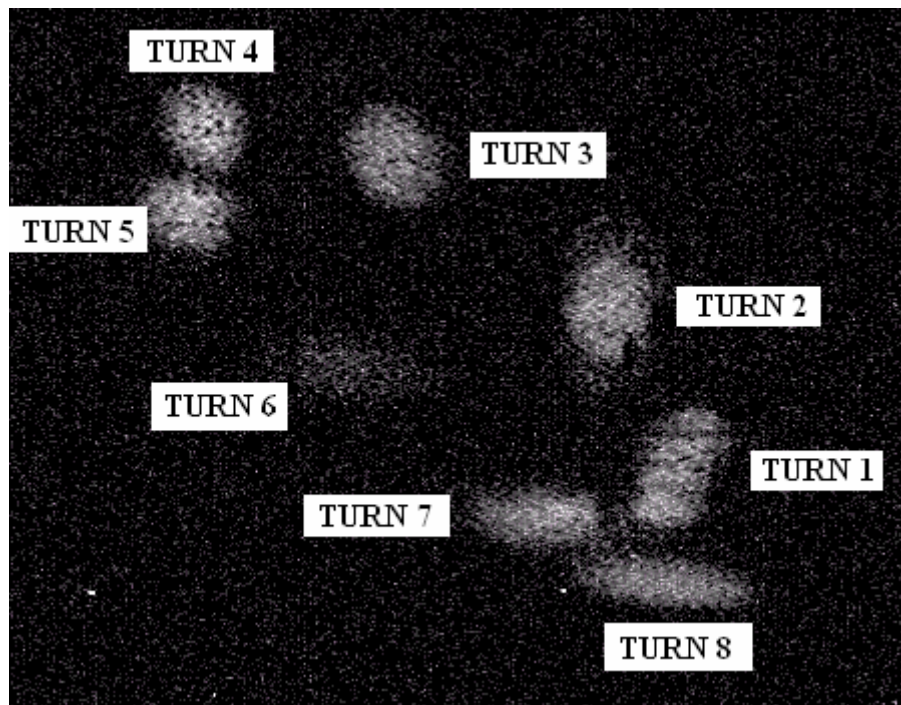
Figure 38: Superposition of pictures of extracted beam as seen in the phosphor screen before matching is performed.

Despite these advantages, the DG100N scheme was chosen because it is a stand alone instrument (i.e. independent of the PC operating system).

4.5.   Movable Fast Faraday Cup

A movable Fast Faraday Cup (FCC) is used to measure the longitudinal profile of the extracted bunches. The FFC is moved by a stepper motor powered

and controlled with the same type of power drives and motion controller as the scanning wires (Figure 39).

The beam current as a function of time is measured by a LeCroy LC-684DXL digital oscilloscope (1.5 GHz bandwidth, up to 8 GS/s, up to 16 MPoints memory) after the signal is amplified by a Miteq AM-1309 or a Miteq AM-1607-1000 broadband amplifiers (50 or 40 dB gain, 8 or 12 dBm maximum output power, 10 kHz - 1 GHz Bandwidth). Based on the specifications of the oscilloscope and amplifiers, beam current changes happening in time intervals as short as 1 ns can be accurately measured.

The voltage monitor of one of the high voltage switches is used to trigger the oscilloscope. The data can be downloaded from the oscilloscope using GPIB communications.

The electron suppressor system can be biased to measure real beam current or it can also be used to further amplify the signal adding to the incoming proton beam current the outgoing secondary e- current.
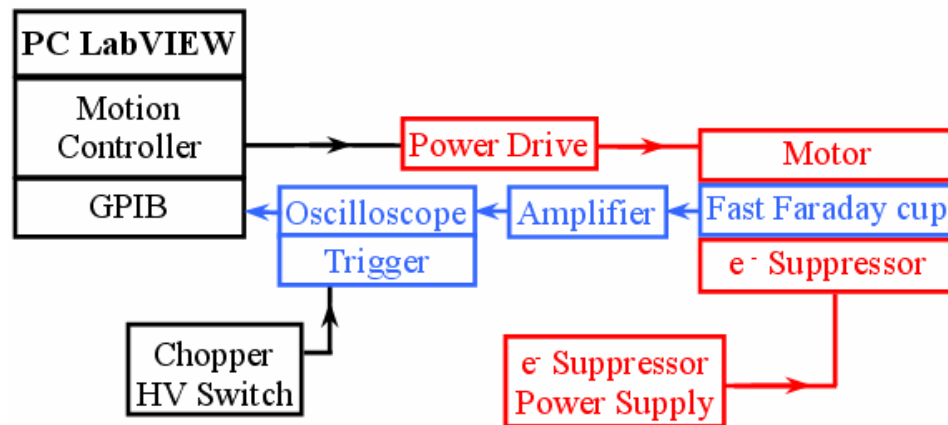
Figure 39: Layout of the fast faraday cup and its associated control electronics.

4.6. Sector Fast Faraday Cup

A sector fast Faraday cup can be used as an alternative to the movable fast Faraday cup. In this case, the four channels of the oscilloscope are used to measure the individually amplified signals of each sector. The rest of the system is analogous to the one described in the previous section for the movable fast Faraday cup. (Figure 40)
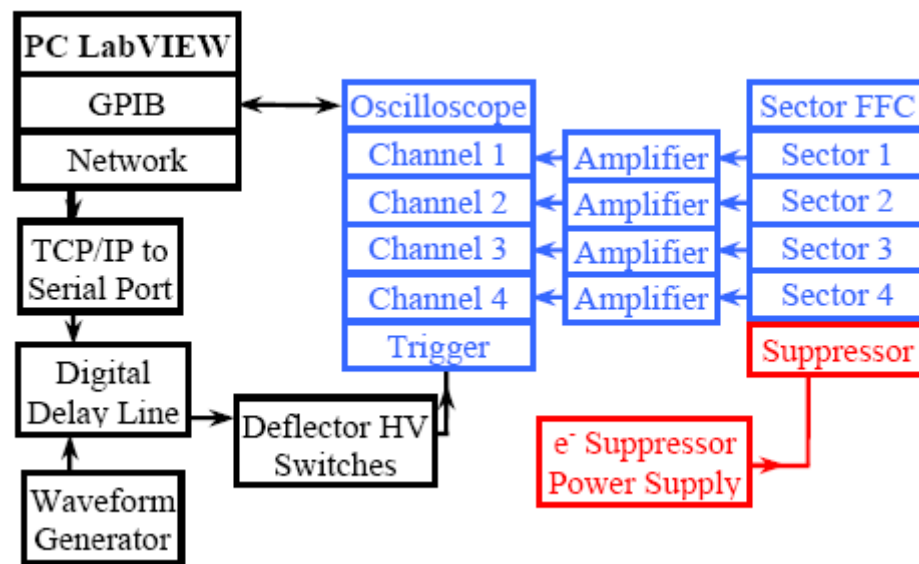
Figure 40: Layout of the sector fast faraday cup and its associated electronics.

A LabVIEW program (Figure 41) was developed to automate the data acquisition of the longitudinal profiles of the extracted bunches after a variable number of turns. The number of profiles to be acquired for a given turn number (typically ~ 100) and the range of turn number to be covered (typically 1 to 100) are specified on the left of the front panel. As the measurements are done the profiles are displayed and the data is saved for further analysis.
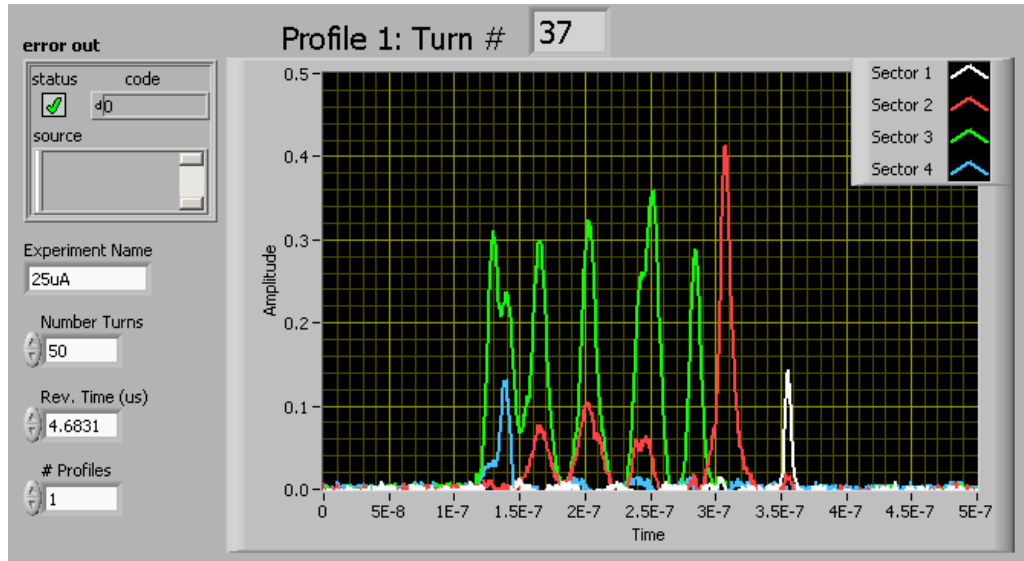
Figure 41: Front panel of the LabVIEW program used for the data acquisition of the sector faraday cup.

4.7. Dipoles, Quads, Steering, Einzel lens and Extraction Power Supplies

Since the energy of the beam is lower than 30 keV, we were able to effectively use a number of electrostatic elements (a quadrupole triplet in the injection line, four quadrupoles in between dipole magnets in the ring, six pairs of steering plates, chopper, inflectors and deflector).

A modular CAEN SY2527 crate with two A1733p (12 Channels positive 4 kV / 2 mA) and two A1733n (12 Channels negative 4 kV / 2 mA) cards was chosen because of the need to minimize the cost relatively high number of high voltage power supplies needed. (Figure 42)

Control software with basic functionality was provided by the manufacturer. A LabVIEW program to store and recover the status of all the channels was also developed.

Two 30 kV / 5 mA Spellman power supplies are used to bias the Ion Source and the Einzel lens. These units have analog outputs proportional to the voltage and current that were connected to the analog input channels of a National Instruments PCI-6036E data acquisition card installed in a PC. They also include an analog input that can be used to set the voltage of the supply that could be used in the future to automate changing the energy of the beam. New analog voltage output channels should be added since all the available ones are currently being used for other tasks.
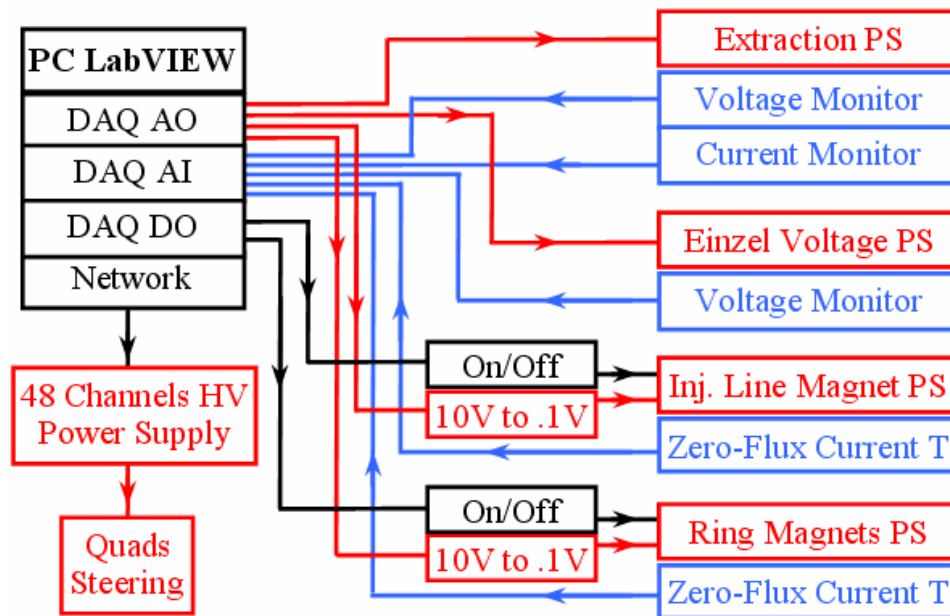
Figure 42: Layout of some of the power supplies used in SIR and their associated control electronics.

Two 135 A / 20 V TCR Electronic Measurement power supplies are used to drive the four ring dipole magnets connected in series and the injection line dipole magnet respectively. Two Holech Zero-flux current transformers are used to precisely measure the output current produced by the supplies. The output of

the controllers of the current transformers is connected to analog input channels of the DAQ card.

The ac power used by the these power supplies is automatically turned off if the temperature of the magnet coils reaches 80°C protecting the magnets if there is a failure of the cooling system.
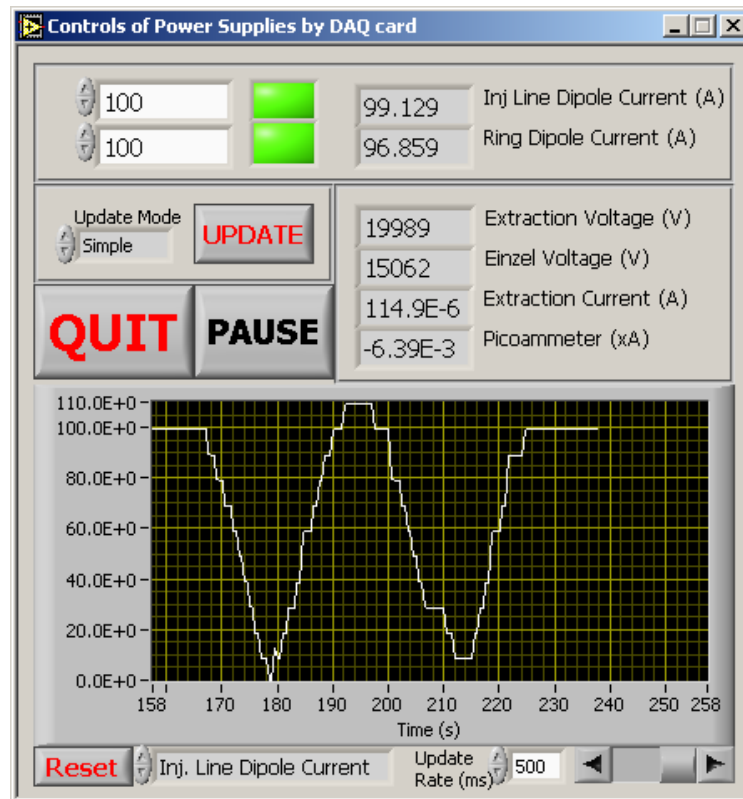
Figure 43: Front panel of the LabVIEW program to control the dipoles, extraction and Einzel lens power supplies.

A LabVIEW program was written to set and monitor the Einzel lens and extraction voltages as well as the dipole currents. Figure 43 shows its front panel. The main functionalities of the program are:

- Set and monitor the current in the coils of the dipoles as read by the Zero-Flux current transformers.

- Monitor the extraction voltage and the Einzel lens voltage.

- Plot any of these voltages or currents as a function of time to monitor long term variability of the power supplies.

4.8.   Phosphor Screens

Two phosphor screens provide visual information about the position and transverse profile of the beam. The first one is movable and is located in the injection section of the ring. It can be used to observe the beam either as it comes from the injection line or in the medium plane after a single turn.
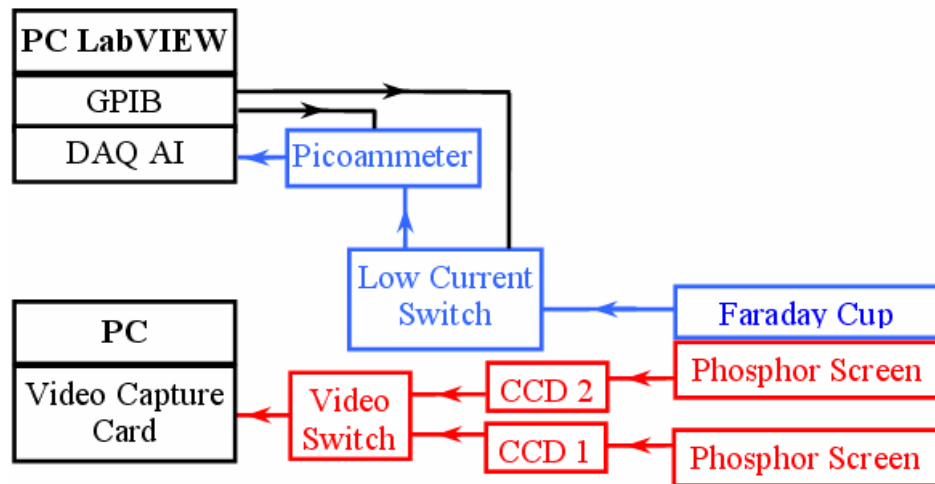
Figure 44: Layout of the phosphor screens and their associated control electronics.

The second one is permanently located above the medium plane of the ring, above the fast Faraday cup. The deflector plates can be used to kick the beam off the medium plane and direct it to the screen that can also be used as a non-shielded Faraday cup. Please, refer to [3 page 122] for a complete description.

Two CCD cameras, connected to a generic video capture card through a video switch, allow us to take digital pictures or movies using software developed at the NSCL by John Priller.

The fixed phosphor screen is connected to one of the channels of the same low current switch used for the scanning wires and the emittance measurement system to be used as a non-shielded Faraday cup.

Using a National Instruments PCI-1409 image acquisition board together with the LabVIEW and IMAQ [24] software packages was also considered. This option was discarded due to its higher cost. The main advantage of such a system is the specificity of the software that could be developed. It could allow, for example, calculating and displaying numeric values for the beam position and sizes in real time. It could also communicate these values to other control programs further automatizing the matching process. Upgrading to such a system is possible if these capabilities are needed in the future.

4.9.   Beam Lifetime Measurements

The sector Faraday cup can also be used to measure the average beam current when all the sectors are connected to a picoammeter (Figure 45).

The length of the injected bunch and the injection repetition frequency can be used to calculate the duty cycle. The reading of the picoammeter can then be corrected to calculate the average current of the injected bunch.

Measuring how the average bunch current decreases as the bunch is stored in the ring for a longer time, the beam losses can be quantified and the beam lifetime can be calculated.
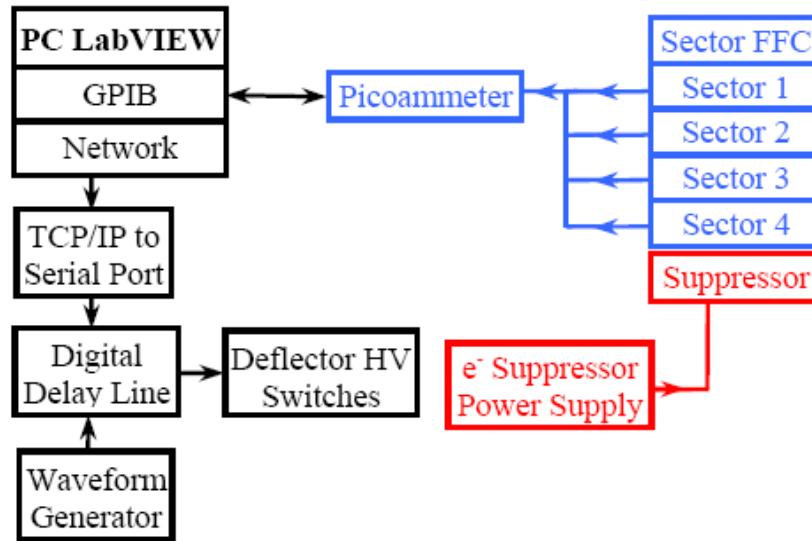
Figure 45: Layout of the beam lifetime measurement electronics and their control electronics.

A LabVIEW program was written to automatize this process. The program will automatically change the number of turns the bunch is stored in the ring and measure the beam current as read by the picoammeter. All the data is then saved in a file for further analysis.

4.10. Other Systems

There are other systems that are not currently computer controlled. Some of them are:

- Magnetic Quadrupole Correctors in the ring.
- Magnetic Dipole Correctors in the ring.

- Ion Source instrumentation.

- Pressure Gauges.

Two bipolar 12 A / 36 V Electronic Measurement power supplies are used to power the magnetic quadrupole corrector coils. They could be computer controlled in the future if necessary. Four 3 A / 15 V Agilent E3610A power supplies are used to power the magnetic dipole corrector coils. They do not have any kind of remote control capabilities.

The Ion Source instrumentation includes a filament power supply, an arc power supply and a Pirani gauge. They are all biased to the extraction voltage ($\leq$ 30 kV). They are currently operated manually using insulating rods attached to the different knobs. A fiber optic transition between high voltage and ground could be used to operate them remotely if necessary in the future since all of these devices have remote control capabilities.

Up to five ion gauges are used to monitor the pressure in different parts of the accelerator. The ion gauge controllers (Varian Ratiomatic 843) have analog outputs that could be used, for example, to record the pressure as a function of time.

4.11. A more integrated alternative control system

Alternative control systems based on VME, VXI and PXI technology were considered but these options were finally discarded due to their higher cost. Nevertheless, some considerations about the PXI (Pci eXtension for

Instrumentation) [25] option are enumerated here since future upgrades may require new capabilities.

A PXI system is, simplifying, a regular PC with a higher number of PCI slots and added synchronization capabilities. The number of PCI cards (GPIB communications, DAQ, Motor Controllers, Video Capture…) that a regular PC can host is limited to 3 or 4. On the other hand, a PXI system can host 18 or more of these cards.

Several PCs had to be used to perform all needed functions relying on the network connection to communicate among them. In some applications where the timing is critical (ex. beam profiles taken with scanning wires: beam current is read as stepper motors move), synchronization using the network is not possible since timing is not guaranteed.

A PXI system can host many more modules increasing the possible functionalities and providing a more integrated solution, simplifying communication and synchronization among the modules at the same time.

4.12. Conclusion

An inexpensive PC-based control system for SIR has been completed. A good number of electronic components previously available in the lab have been reused further lowering the overall cost of the project.

The performance is considered satisfactory and able to cover all present needs. Future upgrades are possible if considered necessary. Some of them have been discussed.

Please, refer to page 200 for a detailed description in how to use some of the most important control programs to perform different experiments.

5.   BEAM VARIABILITY

5.1.   Introduction

Different sources of variability have been identified and their impact on the beam has been studied. Three different time scales were defined. The expression "short term variability" is used when changes in the beam characteristics can take place within a single bunch (hundreds of nanoseconds to a few microseconds). We refer to "long term variability" when changes in the beam can arise over a period of time longer than seconds. Finally, we refer to "bunch-to-bunch variability" when changes between consecutive bunches may be induced by the variability (part of a millisecond to several milliseconds).

The main source of beam variability is the ripple of power supplies. Particularly important are the power supplies that drive the dipole magnets and the one that defines the extraction energy (i.e. ion source bias voltage). Their impact on the beam is discussed in the next two sections of the chapter. The variability of the ion source is described section 5.4. A brief description of other sources of beam variability and a series of long term measurement of the y-y' beam phase space characteristics are also included in this chapter.

5.2.   Variability of the magnetic field of the dipoles

The long term variability of the magnetic field produced by the dipoles in the ring and in the injection line mass separator was measured by monitoring the

current needed to drive them over a period of 10 hours (using zero-flux current transformers). The nominal current (Io) was set to 109 A that corresponds to a magnetic field of ~ 610 Gauss [3 page 173] and a beam energy of ~ 21 keV for H_2^+ ions. The results of this test are shown in Figure 46.
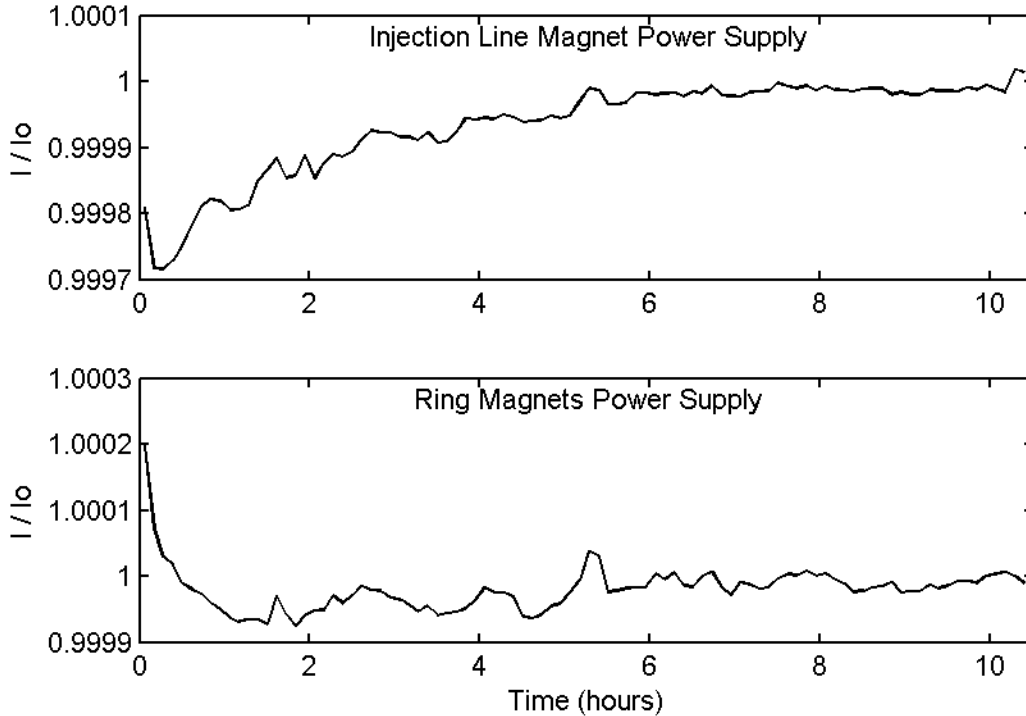
Figure 46: Long term variability of the injection line and ring dipoles power supply. Io is 109 A that corresponds to a 21 keV H_2^+ beam. Deviations around this value were monitored over a 10 hour period of time.

It can be observed that the current is stable within ± 10^{-4} of the nominal value after an initial transition period of 1 hour in the ring magnets power supply and 2 to 3 hours in the injection line magnet power supply.

There will be no fast changes in the magnetic field that could have an impact on the short term variability of the beam. Since the dipoles behave as a

RL low band filter, signals with a frequency higher than its cut-off frequency (f_c) are damped.

$$f_C = \frac{R}{2 \cdot \pi \cdot L}$$

The inductance (L) and resistance (R) of the coils of the dipoles were measured (L = 120 µH, R = 40 mΩ) yielding a frequency cut-off equal to 53 Hz.

There may still be differences in the magnetic field felt by consecutive bunches since oscillations in the ± 10^{-4} level were measured in the millisecond time range.

The impact of these variabilities on the beam at the injection point was calculated using the COSY Infinity model described in section 2.13. It was determined that a ± 10^{-4} relative change in the nominal value of the current of the injection dipole yields less than ± 1 mm error in the vertical position of the beam at the injection point. This error is considered acceptable since it is just a small fraction of the beam size at that point (~ 1 cm).

5.3. Variability of extraction and Einzel lens voltages

In a similar way as described in the previous section, the variability of the extraction power supply and the Einzel lens power supply was monitored. The results of these tests are shown in Figure 47.

The extraction voltage is stable within ± 10^{-4} of the nominal value (20 kV) after an initial transition period of 1 hour. On the other hand, the Einzel lens

power supply requires 2 hours to be stable within $\pm 10^{-3}$ of its nominal value (16.5 kV). Both power supplies are supposed to be identical (same manufacturer and model number) and this difference between them can not be explained by the load they drive since they were interchanged with similar results.

The Einzel lens voltage has been readjusted before experiments to maintain its focusing strength constant over time. The effect in the vertical position of the beam at the injection point due to a fluctuation in the beam energy is approximately half of that of a similar fluctuation in the magnetic field of the dipole. Therefore the drift in voltage is also considered acceptable after a couple of hours of warm-up time.
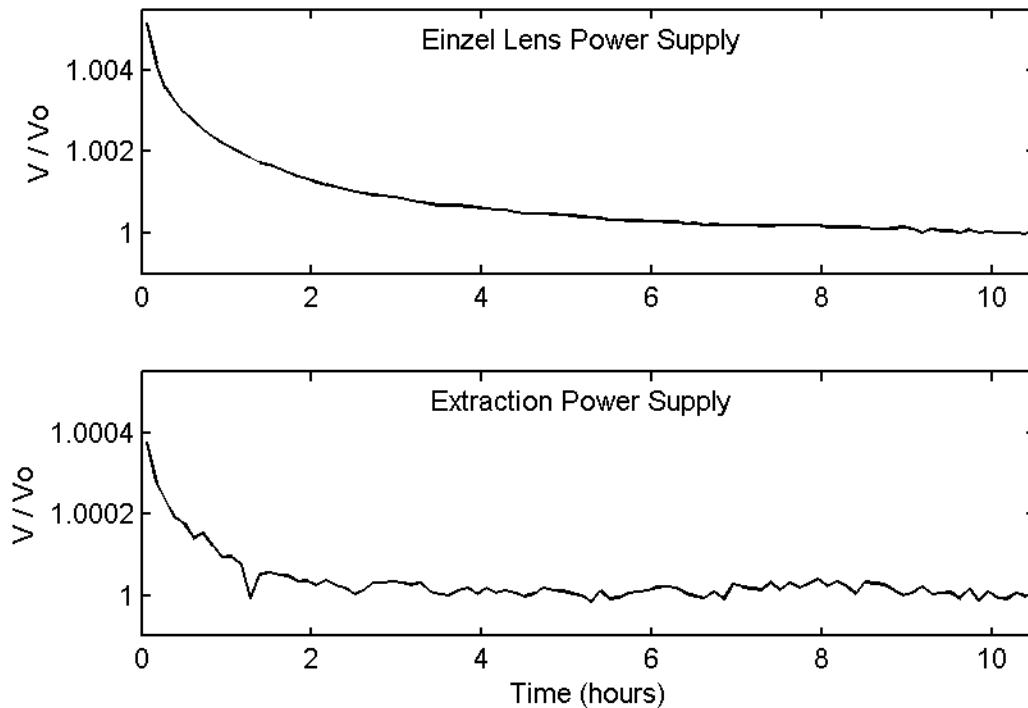
Figure 47: Long term variability of the extraction and Einzel lens power supplies. Vo for the Einzel lens power supply is 16.5 kV and for the extraction power supply is 20 kV. The variability of these voltages was monitored over a period of 10 hours.

5.4. Ion source variability

The extracted beam current was monitored for different source conditions (gas pressure and filament current) over periods of ten minutes. It was determined that the extracted current fluctuated around its nominal value with a standard deviation approximately equal to ± 0.4 %.
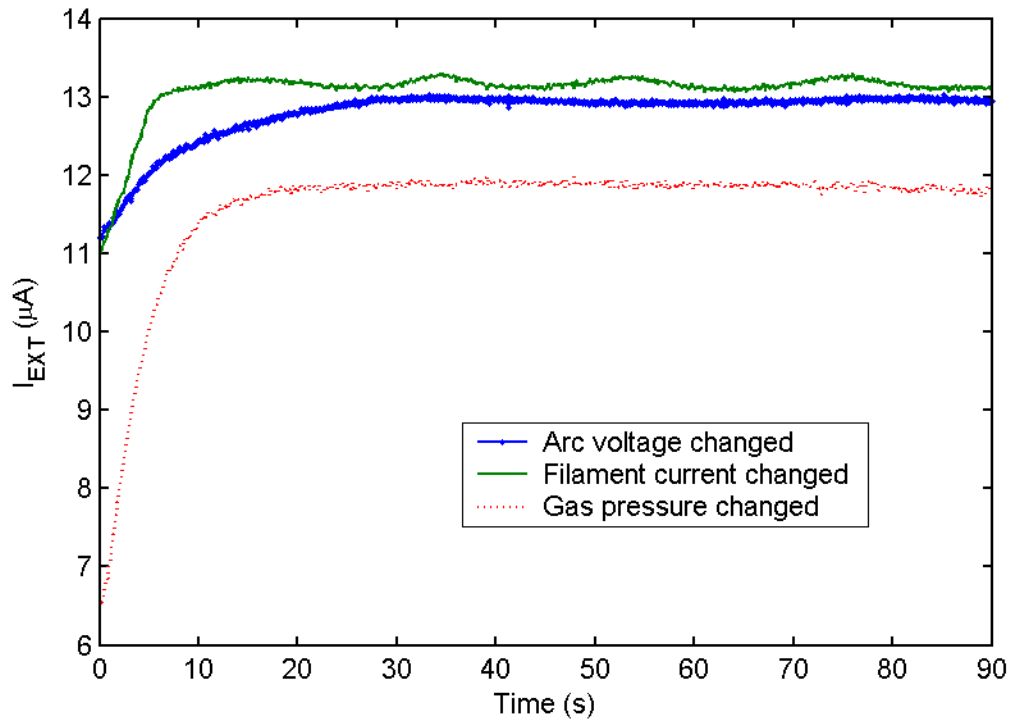
Figure 48: Variability of the extracted beam current when the conditions in the ion source are changed.

With respect to the short term variability, the fast Faraday cup was used to measure fast changes in the beam current after half a revolution. This method is limited by the noise picked up by the cup. This noise level is equivalent to a ± 0.5 µA beam current as discussed in section 3.3. Therefore, extracted beam current fluctuations below this level could not be measured properly. Larger fluctuations

than that where observed when the gas pressure in the source was too low (corresponding to < $3 \cdot 10^{-8}$ Torr pressure in the ring).

The extracted current was measured while different source conditions were changed in order to determine the time necessary for the source to stabilize. Some of the results are shown in Figure 48. It can be observed that it takes less than a minute for the extracted beam current to stabilize when the arc voltage or the gas pressure is changed. Some oscillations in the extracted beam current can be observed when the filament current is changed. They typically last for two to three minutes and are believed to be related to ripple of the filament power supply.

5.5.   Other sources of variability

The isolation transformer, used to power the ion source instrumentation, was found to produce a time dependent magnetic field that perturbed the beam. The transformer was moved further away and its magnetic field was shielded with sheets of mu-metal (nickel-iron alloy with very high magnetic permeability).

The perturbation in the beam introduced by the rest of the power supplies used to bias the quadrupole triplet, steering plates and inflector and deflector plates is negligible compared to the ones previously discussed.

5.6. Beam drift over time

To evaluate the combined effect that the previously described voltage and current drifts have on the beam, the emittance measurement system was used to characterize the beam over time.

The injection line was set up to inject a 20 keV H_2^+ beam in the ring. An hour after it was turned on, the first y-y' (perpendicular to the medium plane of the ring) phase space scan was performed. Measurements were repeated over the next 6 ½ hours. An ellipse was fitted to each data set. The RMS-emittance (ε_{RMS}), the Courant-Snyder parameters (α, β and γ) and the center of the ellipses (X_0, P_0) are shown in Figure 49.
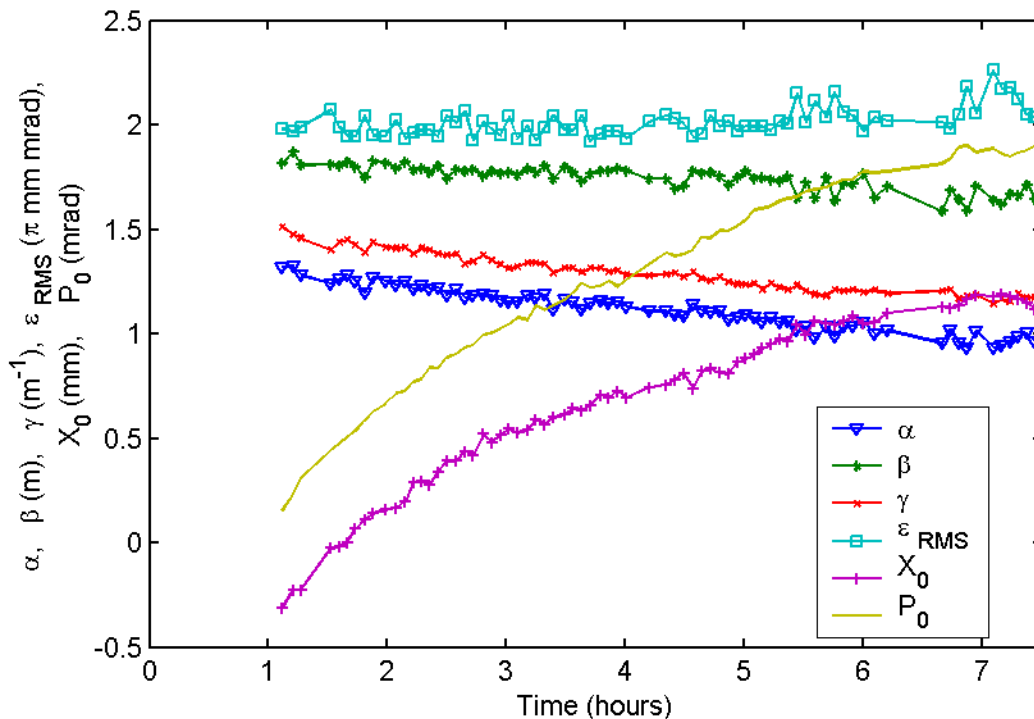
Figure 49: Y-Y' phase space characteristics over a 6 ½ hours period of time 1 hour after turning on the machine. The injection line was set up to be able to inject a 20 keV H_2^+ beam in the ring.

6. ION SOURCE CHARACTERIZATION

6.1. Introduction

As discussed in section 2.4, a filament driven multi-cusp ion source is used to produce the beam. The source was borrowed from Lawrence Berkeley National Laboratory. Some of its characteristics can be found in [12].

A complete characterization of the source requires measuring the beam current and emittance of the three different mass states (H^+, H_2^+ and H_3^+) for different source conditions. These conditions are defined by the gas pressure in the source, the extraction voltage, the filament current (and filament resistance) and the arc current (and voltage). It is easy to realize that the large number of possible combinations makes a complete characterization unfeasible. The picture gets more complicated since, on some occasions, the previous history of the source has an impact on the properties of the extracted beam. For these reasons, we will limit this discussion to some general trends that have been consistently observed when a single source parameter was changed.

In the next section, an example of the relationship between extracted current and extraction voltage for the three mass states is discussed. The impact that changes in the extracted beam current have on the phase space of the beam is analyzed in section 6.3. The chapter is closed with a brief review of other relationships between conditions in the source and properties of the extracted beam that have been observed.

6.2. Extracted current for different extraction voltages

The extracted beam current for different extraction voltages was measured for the three mass states. The source conditions are enumerated in Table 4 and the results of the measurements are shown in Figure 50.

$I_{FILAMENT}$ (A)	$V_{FILAMENT}$ (V)	I_{ARC} (A)	V_{ARC} (A)	P_{RING} (Torr)
38.6	5.4	0.63	100	$9 \cdot 10^{-8}$

Table 4: Source conditions used in the measurements shown in Figure 50.

The extracted current I_{EXT} (i.e. charge per unit time) can be expressed as a function of the energy (E), ion mass (m) and charge per unit length $\dfrac{dQ}{dl}$ as

$$I_{EXT} = \frac{dQ}{dl} \cdot \sqrt{\frac{2E}{m}}$$

Fitting the experimental values to this equation, it can be estimated with 95 % confidence level that the charges per unit length for the different masses are (with these source conditions):

$$H^+ : \quad \frac{dQ}{dl} = 2.31 \cdot 10^{-12} \frac{C}{m} \quad (\pm 3\,\%)$$

$$H_2^+ : \quad \frac{dQ}{dl} = 2.07 \cdot 10^{-11} \frac{C}{m} \quad (\pm 0.5\,\%)$$

$$H_3^+ : \quad \frac{dQ}{dl} = 3.97 \cdot 10^{-12} \frac{C}{m} \quad (\pm 2\,\%)$$

We can also conclude that, for these conditions in the source, around ¾ of the extracted current corresponds to H_2^+ and the rest is equally divided between

the other two mass states. It is worth noting here that the relative abundance of the differences masses depends strongly on the gas pressure in the source. It has been observed that the most abundant mass state is H_3^+ for higher pressures.
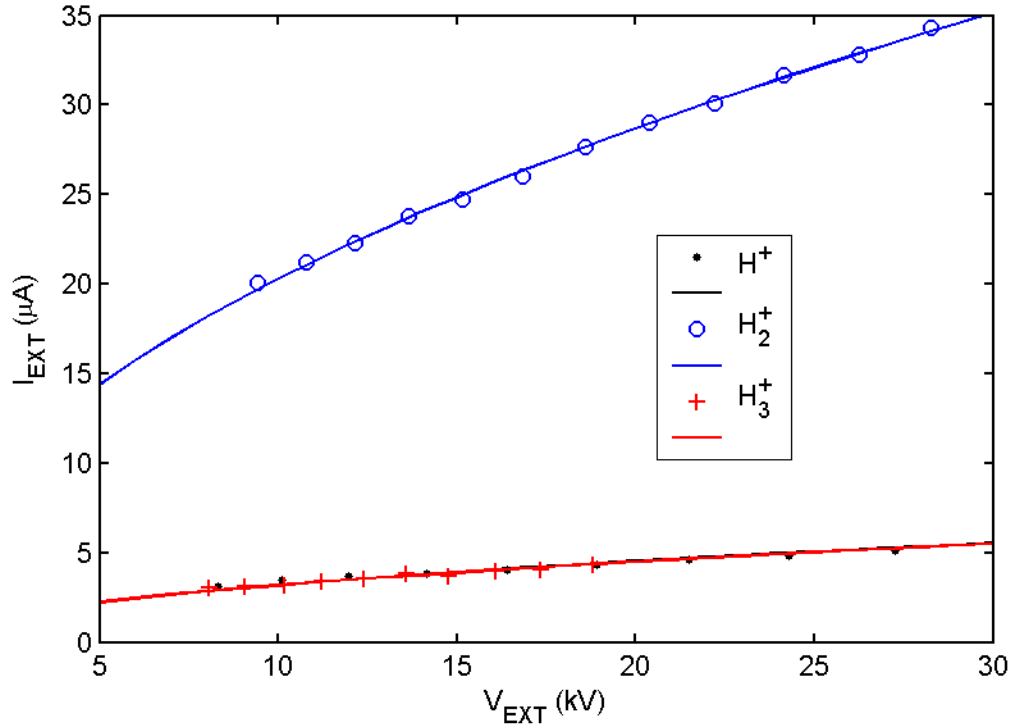
Figure 50: Extraction current versus extraction voltage for different ion masses. The conditions in the source are enumerated in Table 4.

6.3.   Beam transverse phase space for different extracted currents

The emittance measurement system was used to characterize the x-x' (parallel to the medium plane of the ring) phase space of the extracted beam for different extraction currents.

A 20 keV H_2^+ beam was selected with the mass separator after being focused with the Einzel lens (16.5 kV). The pressure in the ring was $6.5 \cdot 10^{-8}$ Torr (due to gas flow from the source) and the arc voltage was 100 V throughout the experiment. The filament power was first set to 243 W yielding 2.12 A of arc current. The H_2^+ extracted current amounted to 29.2 µA for these conditions. At this time, the first phase space scan was performed.

V_{EXT} (kV)	V_{EINZEL} (kV)	Ion	I_{EXT} (µA)	I_{ARC} (A)	V_{ARC} (V)	P_{RING} (Torr)
20	16.5	H_2^+	3.5 - 21.2	0.1 - 2.1	100	$6.5 \cdot 10^{-8}$

Table 5: Value of main parameters used in the experiment described in this section.
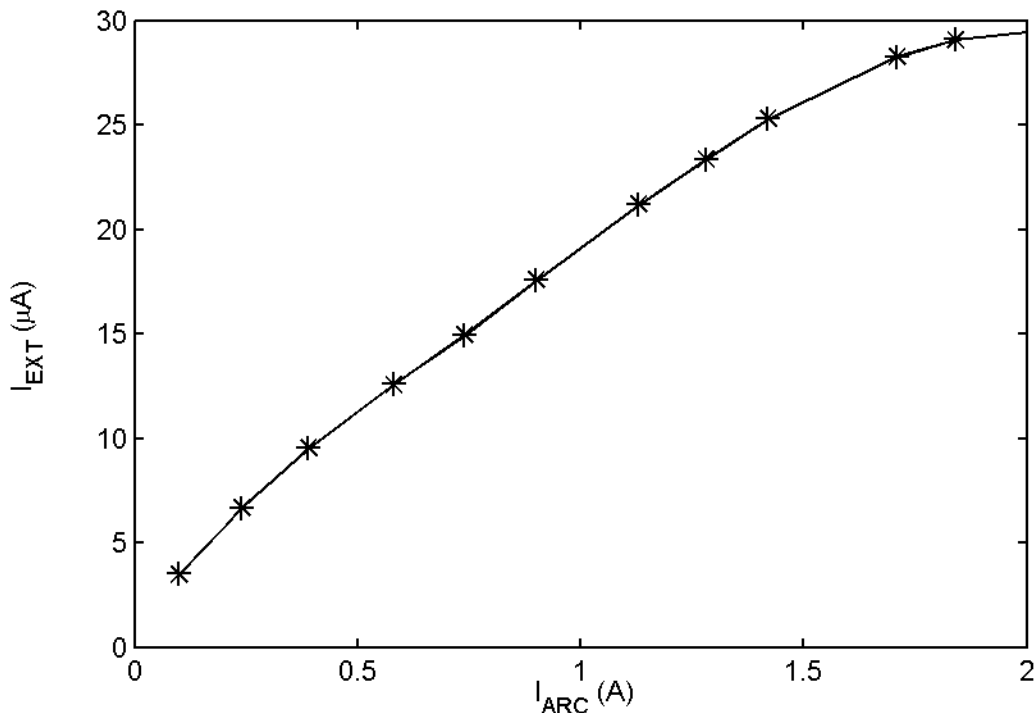
Figure 51: Relationship between arc current and the extraction current of H_2^+ ions when the filament power is changed as shown in Figure 52. The value of the arc voltage, extraction voltage and pressure are kept constant. (Values are listed in Table 5.)

The filament power was lowered yielding lower arc currents and extracted beam currents. The beam phase space was scanned at different points during this process. The relationship between the arc current and the filament power is shown in Figure 52. The relationship between arc current and extracted current is plotted in Figure 51. Some of the phase space maps measured, are shown in Figure 53.
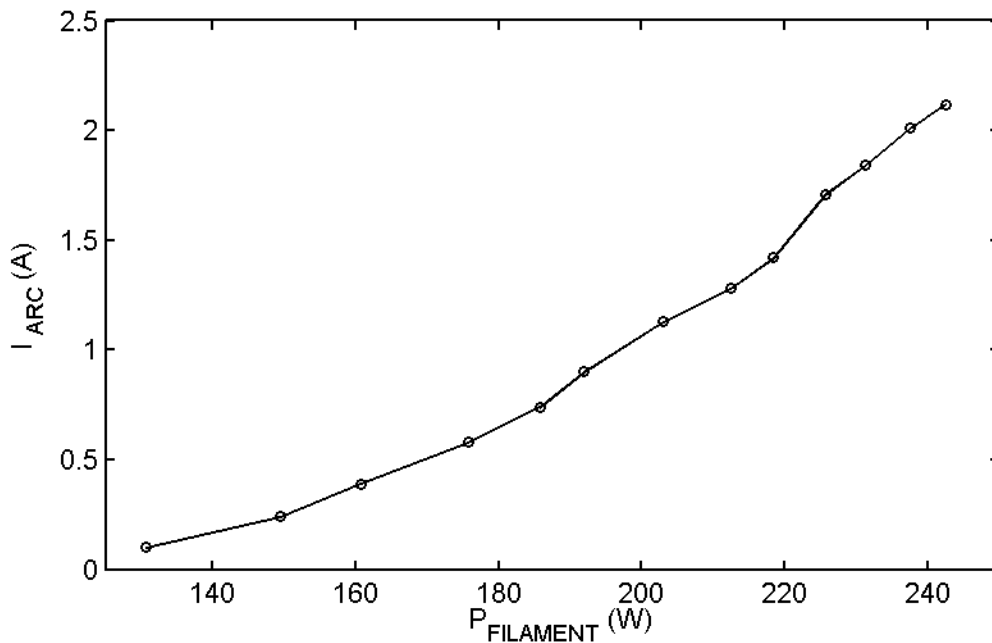
Figure 52: Relationship between arc current and filament power measured for constant value of the arc voltage, extraction voltage and gas pressure. (Values are listed in Table 5.)

It can be observed that, as expected, the emittance of the beam grows as the extracted current increases due to the larger transverse space charge effects in the extraction region. It can also be seen that the beam tilts more when the extracted current is higher. Said in a different way, the waist of the envelope of the beam is reached further down the injection line when the extracted current is higher. Since the strength of the Einzel lens was not changed throughout the

experiment, we can conclude that the angle divergence of the beam in the puller is larger when the extracted current increases. This larger divergence is also due to the higher transverse space charge forces in the extraction region.

To quantify these effects, an ellipse was fitted to the measured data using the Self Consistent Unbiased Elliptical Exclusion (SCUBEEx) algorithm described in references [20], [21] and [22]. The rms-emittance and the values of the Courant-Snyder parameters of these ellipses are shown in Figure 54.
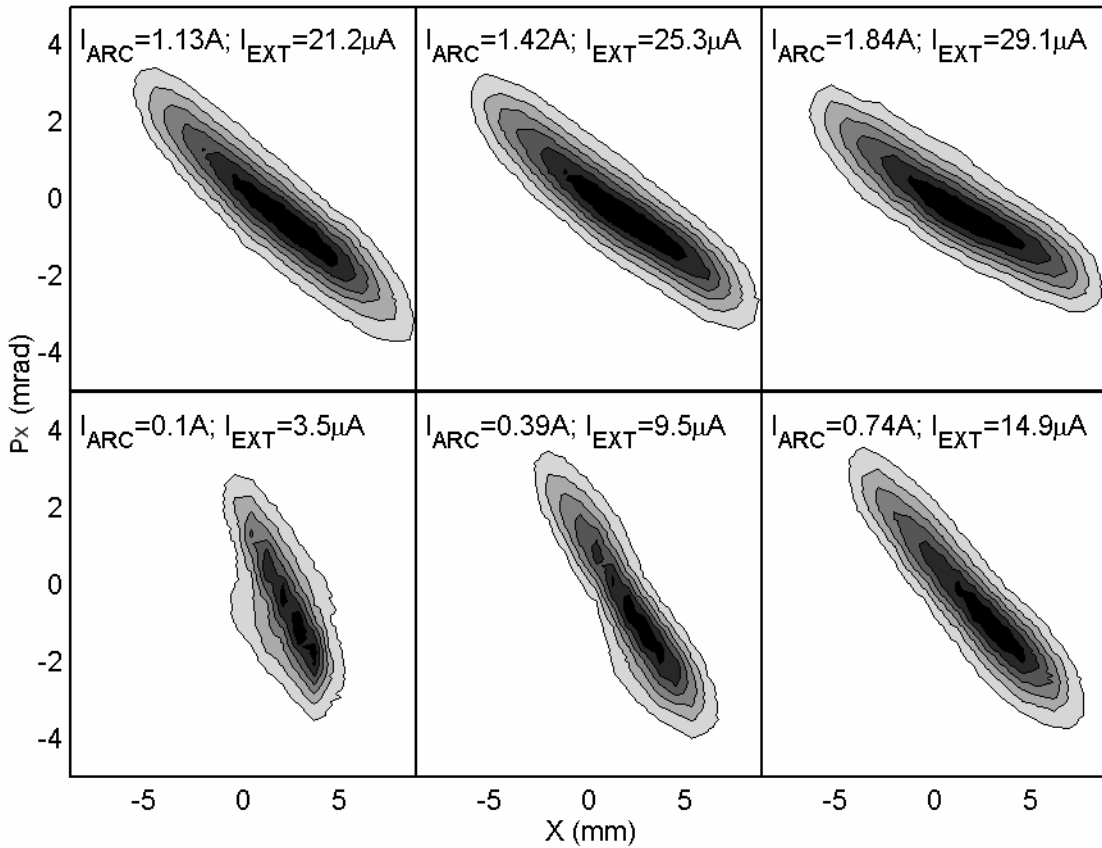
Figure 53: X-Px phase space measurements for different extraction currents. (We define the x plane as that parallel to the medium plane of the ring.) The corresponding arc current and extracted beam current are shown in the figure. The rest of the source parameters are listed in Table 5. Growth in the emittance and in the tilt of the beam when the extracted current is increased (due to stronger transverse space charge effects in the extraction region) can be observed.
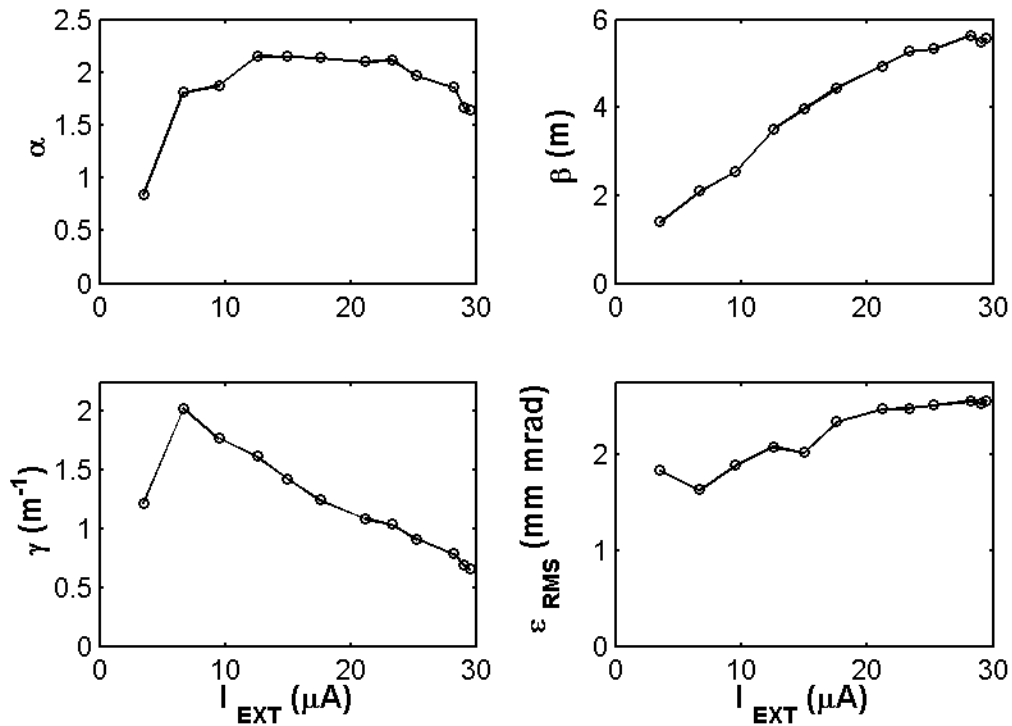
Figure 54: Value of the RMS-emittance and the Courant-Snyder parameters as a function of the extracted beam current for the source conditions listed in Table 5.

6.4. Other relationships between conditions in the source and properties of the extracted beam

Two sets of experiments were conducted to measure the extracted beam current as a function of the gas pressure. In the first set, the extraction voltage (20 kV), the arc voltage (100 V) and the filament power (290 W) were fixed. As the gas pressure was increased, so did the arc current and the extracted beam current. In the second set of experiments, the extraction voltage, the filament power and the arc current were fixed. As the gas pressure was increased, the arc voltage was free to self adjust keeping the arc current constant. The extracted

106

beam current did not significantly change for a given arc power when the pressure was changed.

The results of these experiments seem to confirm that the arc power is the most important parameter to determine the extracted beam current once the filament power and gas pressure reach a threshold value. Reasonable conclusion since the electrons emitted from the filament (i.e. arc current) ionize the gas in the source forming the plasma.

The mission of the filament power is to facilitate the electron emission from the filament. (I.e. a lower arc voltage is necessary to produce a given arc current). Just a fraction of the gas in the source is ionized. Increasing the pressure by itself does not significantly increase the extracted current.

7. BEAM LIFETIME EXPERIMENTS

7.1. Introduction

The injected beam peak current plays a critical role in most of the experiments performed using SIR since it is the most important single parameter to characterize space charge effects. Special attention was paid to make sure it could be measured accurately using a Faraday cup at the end of the injection line. The same attention has to be paid to minimize and quantify the beam losses in the ring:

- The acceptance of the ring is large enough to accommodate the large energy spread induced by the space charge effects. Refer to chapter 3 of [3] for a complete discussion of the beam dynamics in the ring.

- Collisions with residual gas in the ring produce beam losses (mostly by electron capture and scattering in the 10^{-7} to 10^{-8} Torr range of pressures and in the 10 to 30 keV range of energies). The strict cleaning procedure described in page 199 was used for the elements inside the vacuum chamber to limit the component of the residual pressure due to outgassing to less than 10^{-8} Torr. Differential pumping in the injection line reduces the component of the residual pressure due to gas flowing from the ion source to 10^{-7}-10^{-8} Torr depending on the source working pressure. Refer to page 126 and page 174 of [3] for a complete discussion on this issue.

The lifetime measurements of H_2^+ and its dependence on turn number, residual gas pressure and beam energy will be discussed in this chapter.

7.2. Beam lifetime dependence on extraction turn number and pressure in the ring

The normalized bunch average current (I/Io) as the number of turns the bunch is stored in the ring (N) behaves as:

$$\frac{I}{Io} = \exp\left(-\frac{N}{No}\right)$$

The constant No depends on the gas pressure and the energy of the beam. Figure 55 shows the decay of the normalized average beam current as N increases for a 21 keV H_2^+ beam. Different curves correspond to different gas pressures in the ring.
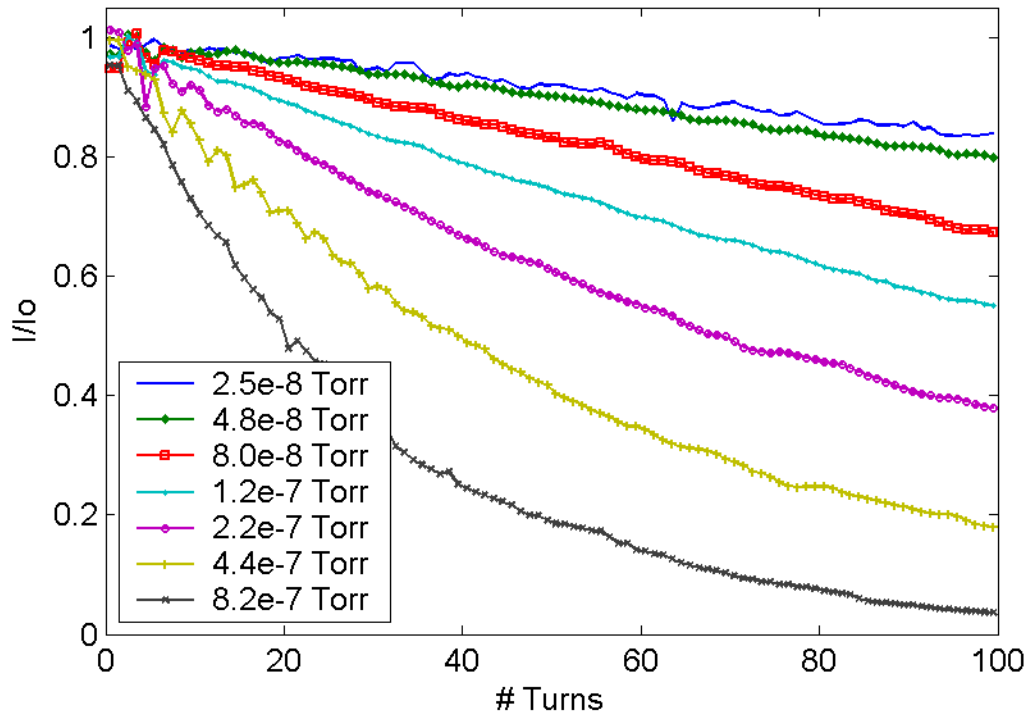
Figure 55: Normalized beam current versus turn number for different gas pressures. (21 keV H_2^+)

The values of No were calculated for the different pressures by fitting the experimental data to Eq. 3. The results are shown in Figure 56.
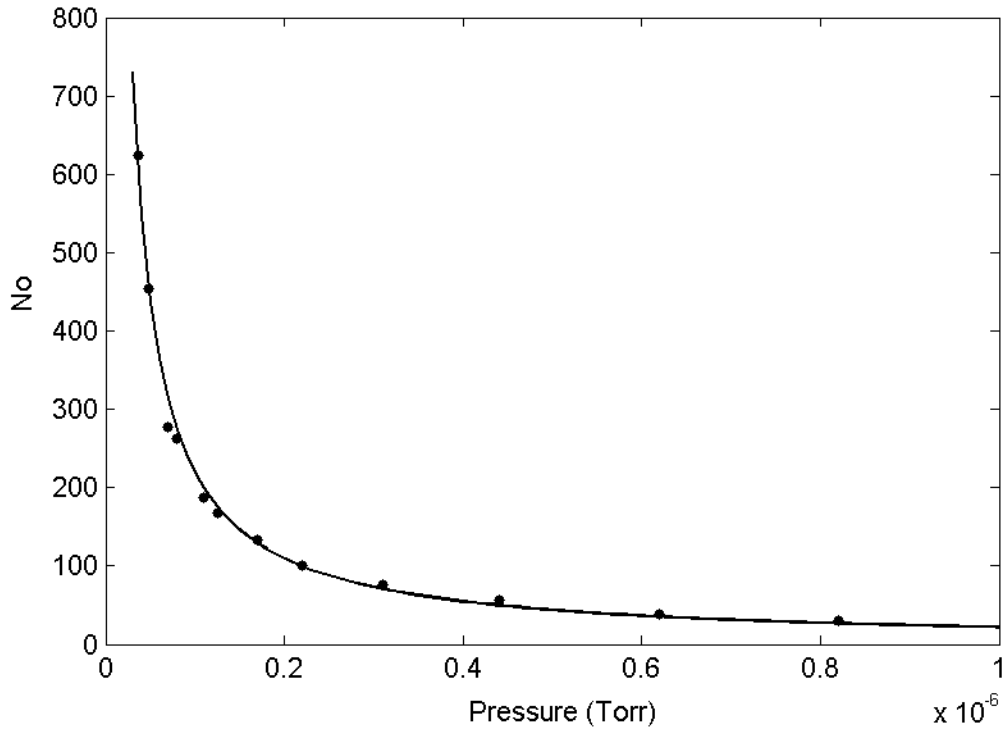
Figure 56: No as a function of the pressure in the ring for a 21 keV H_2^+ beam.

The dependence of No with the pressure can be described as:

$$No = 100 \cdot \frac{P_{100}}{P}$$

where the constant P_{100} only depends on the beam energy. This result was expected since the probability of collision with the residual gas is proportional to the distance traveled, measured in mean free path units (i.e. increasing the pressure by a factor two is equivalent to decreasing the traveled distance by the same factor).

7.3. Beam lifetime dependence on the beam energy

Similar experiments were conducted to determine the influence that the energy of the beam has in determining its lifetime. The results are summarized in Figure 57.
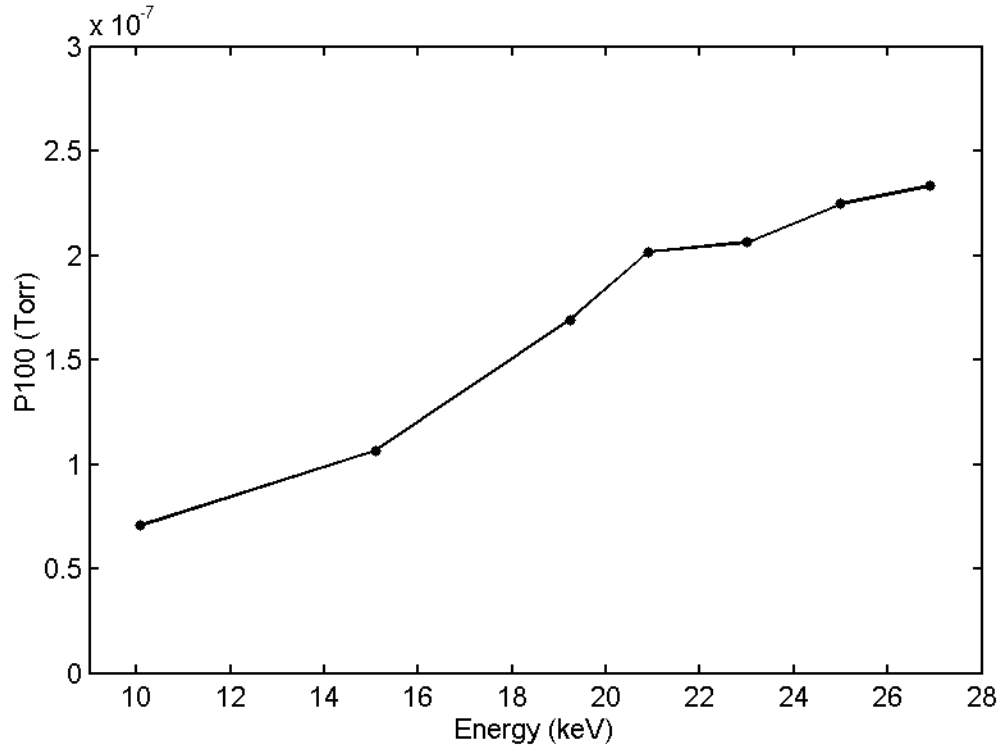
Figure 57: P_{100} as a function of the beam energy.

In the range of energies of our interest (20 to 30 keV), these relationship can be approximated linearly as $P_{100} = k \cdot E$ where $k \cong 8.8 \cdot 10^{-9} \dfrac{Torr}{keV}$ (± 8 % with 95 % confidence level). Combining these last results with Eq. 3 and Eq. 4, the following semi-phenomenological relationship for H_2^+ ions can be derived:

Eq. 5

$$\frac{I}{Io} = \exp\left(-1.13 \cdot 10^6 \frac{keV}{Torr} \cdot \frac{N \cdot P}{E}\right)$$

Eq. 5 will later be used to estimate the beam losses in different experimental conditions. As a representative example, some of these values appear in Table 6.

$\left|\frac{I - Io}{Io}\right|$	P (Torr)	E (keV)	N_{TURNS}
0.1	$3 \cdot 10^{-8}$	20	62
0.1	$3 \cdot 10^{-8}$	25	78
0.05	$3 \cdot 10^{-8}$	20	30
0.05	$3 \cdot 10^{-8}$	25	38

Table 6: Estimated beam losses for different working conditions

7.4. Conclusion

The lifetime of H_2^+ bunches for different residual gas pressures, different extraction turn number and different beam energies has been measured and a semi-phenomenological relationship among them has been determined.

The results of these experiments indicate that in order to minimize the beam losses, the hydrogen pressure in the ion source should be kept as low as possible (the pressure in the ring is proportional to the pressure in the source).

In these conditions, the beam losses will be limited to less than 5 % in the tens of turns necessary to observe the space charge effects.

8. BEAM DYNAMICS SIMULATIONS WITH CYCO: PRELIMINARY CONSIDERATIONS

8.1. Introduction

CYCO was developed by Eduard Pozdeyev to simulate the beam dynamics of intense beams in isochronous cyclotrons. Refer to chapter 2 of reference [3] for a complete description of the code. CYCO has also been used to study different aspects of the beam dynamics in SIR.

A large number of simulations have been performed to characterize the impact that parameters such as the peak current, energy or emittance have on the longitudinal beam dynamics of SIR. The results of these simulations are presented in chapter 9. This chapter is meant to be an introduction to those results.

Different methods used to represent the information product of these simulations are described in the next section of the chapter. This section is followed by a discussion of the methodology used to analyze the data. The stability of the results produced by CYCO when different computational parameters are changed (such as the number of times the space charge electric field is calculated per revolution), is studied in section 8.4. This section is followed by a discussion of the impact that the choice of the microscopic representation of the bunch to be studied has in its dynamics. The chapter closes with a conclusion where the results are summarized.

8.2. Data representation

CYCO outputs the value of the six coordinates of every macroparticle (typically ~ 300000) with a frequency that can be defined by the user (typically once per revolution in the ring). Since bunches are tracked for ~ 75 turns, it is easy to realize that the amount of data generated for every simulation performed is large.

Representing all this information in a way in which the relevant features are enhanced and become apparent was the first problem that we faced when analyzing the data. Some of the ways data will be presented include:

- Particles are projected on a plane where each of them is represented as a dot. Information in the other four coordinates is not used. In these projections, we have defined the z axis as that perpendicular to the medium plane of the ring, the y axis is parallel to the injection line and the x axis is perpendicular. Clustering of the injected bunches due to the space charge forces can clearly be observed when represented this way.

The main problem with this representation is that in some regions, where the concentration of macroparticles is large, the picture saturates. In some cases, a randomly selected subset of macroparticles is plotted to avoid this problem.

- Another way to prevent saturation is to use contour lines to represent particle densities in a plane.

- Both of the above methods clearly show details in the structure of bunches for a given turn number. In order to better understand how this structure

evolves in time, movies were created where consecutive frames showed the bunch after a variable number of turns.

- As discussed in chapter 10, the measurements performed with the fast Faraday cups are restricted to beam current as a function of time. This information has to be compared with the simulations. In some cases, the results of the simulations are shown that way, to facilitate direct comparison (red curve in Figure 59).
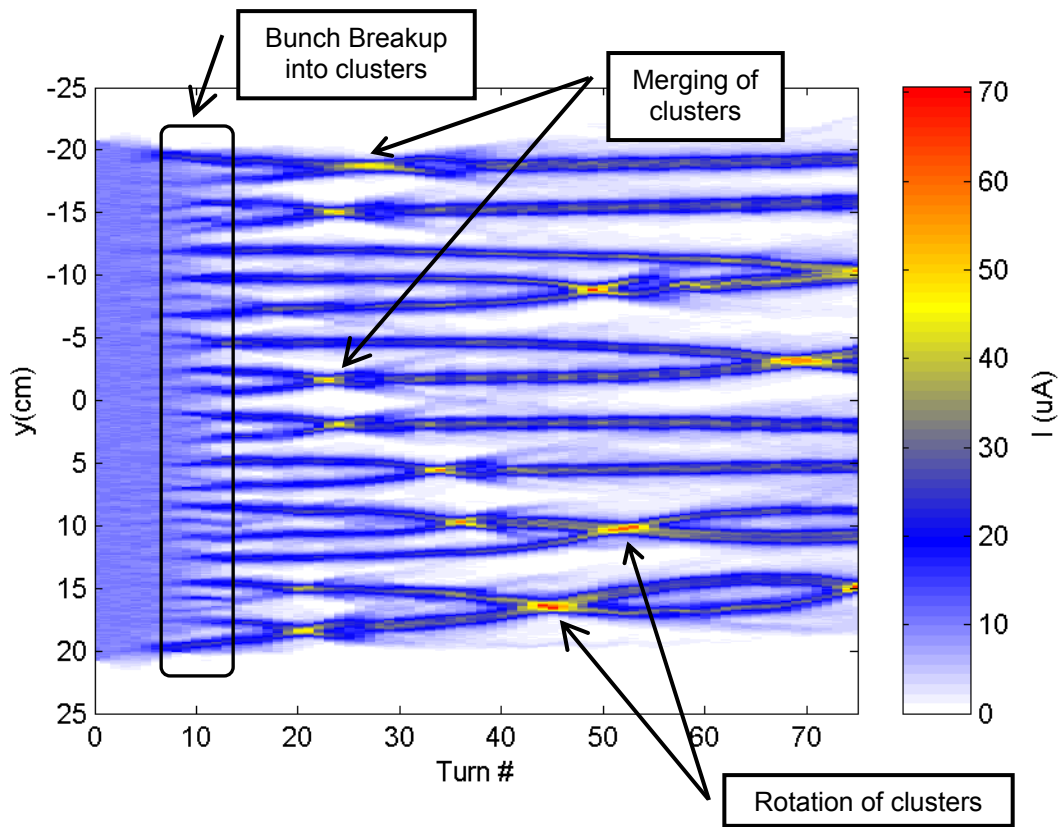
Figure 58: Example of waterfall diagram for a 300 ns long H_2^+ bunch with energy 20 keV, peak current 10 µA and emittance 30 π mm mrad. The longitudinal bunch profile is plotted after a variable of turns.

- Waterfall diagrams have proven to be a very convenient way to visualize relevant information as an alternative to the movies previously discussed (Figure 58). Longitudinal profiles for consecutive turn numbers are shown next to each

other in a color map where the color represents the local beam current. Several important questions can be answered by comparing these diagrams:

Turn number at which bunch breaks up into clusters.

How the size and density of clusters evolve with turn number.

How fast clusters merge together. In some cases, the clusters rotate around each other. These two events are difficult to distinguish when individual longitudinal profiles are studied. It becomes apparent when a top view of the beam is observed. As an alternative, the behavior of the longitudinal profiles for later turn numbers can be used to distinguish between both possibilities.

8.3.   Description of the methodology used in the analysis of data

Counting clusters in longitudinal profiles

As discussed in the following chapters, the beam current, emittance and energy have a big impact in the evolution of the number of clusters formed when the breakup occurs. Counting the number of clusters of the longitudinal bunch profiles requires establishing criteria to define what we consider a cluster.

These criteria are described with the help of the following example. Figure 59 shows the top view (in black) and the longitudinal profile (in red) of a H_2^+ bunch, sixty turns after being injected according to simulations. The energy, when it was injected, was 20 keV, the peak current 10 μA, the length 300 ns and the emittance 30 π mm mrad.

First, the peak current of the injected bunch is calculated (I_{PEAK}). In the simulations, this is a known parameter (10µA plotted as a solid blue line).

In the experiments, the peak current is calculated for every longitudinal profile measured after half a turn (typically ~ 100 profiles). The average of these values is used as the reference peak current. (Frequently, there is dispersion in these values due to small fast fluctuations in the extracted current from the source).
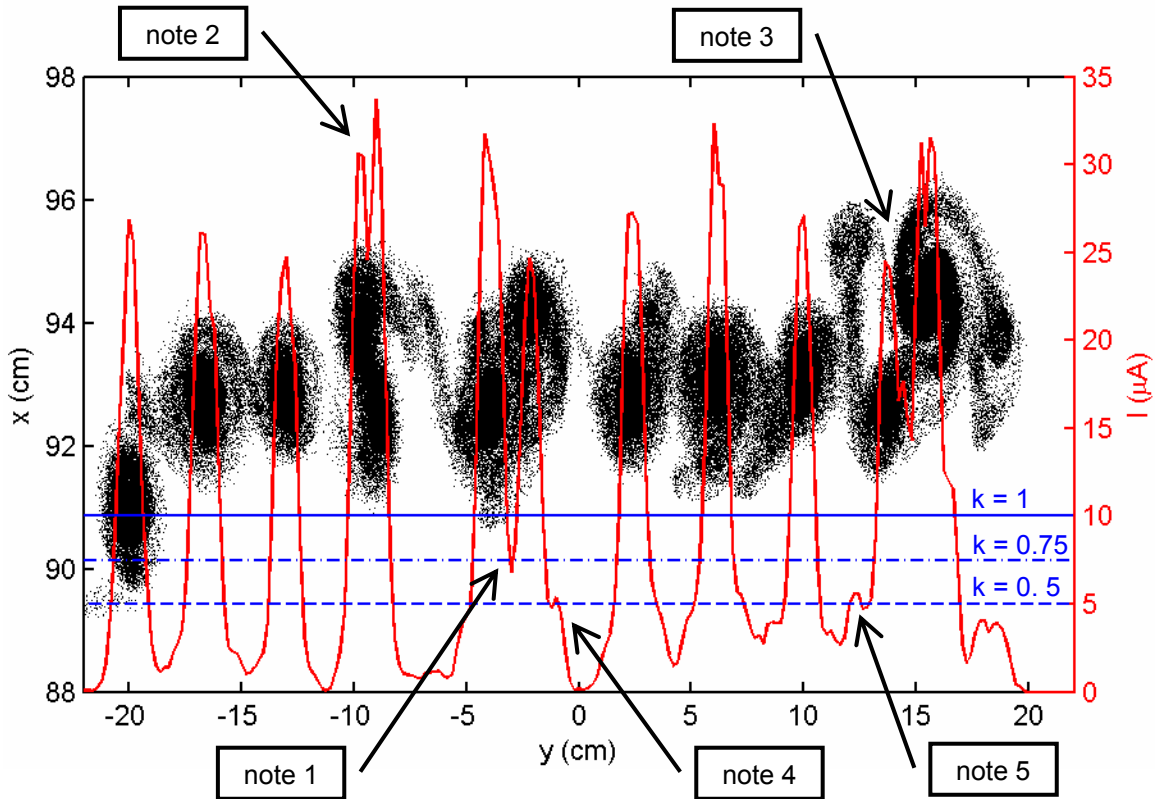
Figure 59: Top view (in black) and longitudinal profile (in red) of a H_2^+ bunch 60 turns after being injected. The energy when it was injected was 20 keV, the peak current 10 µA, the length 300 ns and the emittance 30 π mm mrad.

A threshold current is defined by the user. This value is typically a fraction of the average current calculated before ($I_k = k\ I_{PEAK}$). Two values where chosen

in this example: $k_1 = 0.5$ and $k_2 = 0.75$ yielding to $I_{k1} = 5$ μA and $I_{k2} = 7.5$ μA (plotted as dashed blue lines).

The intersection points between these lines and the longitudinal profile are calculated and grouped in pairs. Each pair represents a candidate to cluster.

Out of all these candidates, just some of them will qualify depending on their width (W_{min}) that is also defined by the user (typically 2 mm to 5 mm or the equivalent time in the case of experimental profiles). This process is necessary to prevent counting peaks produced by electromagnetic noise picked up by the fast Faraday cup. It also prevents wings of clusters from being counted (like the ones shown in note 3 and 4 in Figure 59).

Those clusters that qualify are counted.

In this example, the number of clusters counted is ten (when $k = 0.75$ and $W_{min} = 5$ mm). Two peaks that are barely distinguished are labeled note 1. Two more possible clusters (see note 2 and 3) are not counted here. In some cases, clusters rotate around each other. When this happens, sometimes it is not possible to distinguish them in the longitudinal profiles since they appear combined as one.

When $k = 0.5$ and $W_{min} = 5$ mm, the number of clusters counted is 9 since clusters partially hidden behind each other (see note 1, 2 and 3) are not counted and the width of the other two candidates (note 4 and 5) is not enough to qualify them as clusters.

Figure 60 shows the number of clusters, counted with the method just described, for other values of k and W_{min}. There is not unique way to count

clusters. In most of the cases, k was chosen equal to 0.5 and W_{min} equal to 5 mm or the equivalent time for measured longitudinal profiles.

In any case, the values of k and W_{min} were identical every time the "number of clusters counted" were compared (between simulations, between experiments or between simulations and experiments).

Even though this does not guarantee that all the clusters were counted, it does guarantee that results can be compared among them and dependencies can be established.

For example, the values of k and W_{min} used to count clusters in Figure 66 were the same for all the curves and equal to 0.5 and 5 mm respectively.
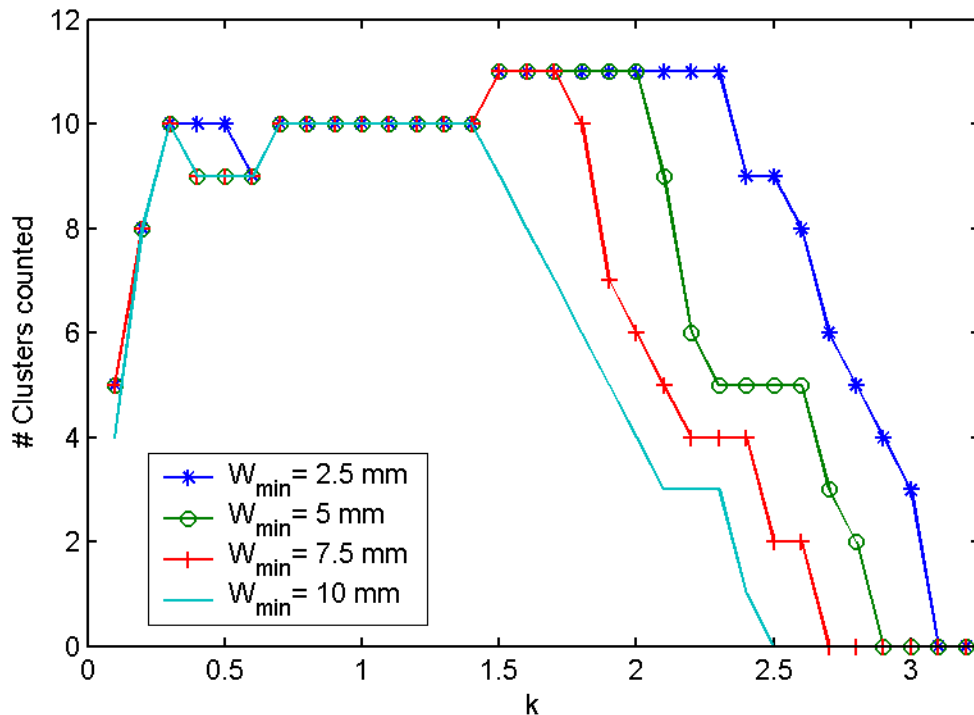
Figure 60: Number of clusters counted in longitudinal profile in Figure 59 for different values of the user defined parameters k and W_{min}.

8.4. Numerical stability: Computational parameters

In order to determine the reliability of the code CYCO, a number of simulations were performed where different computational parameters (such as how often the space charge electric field is calculated or grid size of the FFT algorithm) were changed. For the code to be trusted, it is expected that changes in these parameters will not have a significant impact on the beam dynamics compared to changes in physical parameters of the beam such as the peak current, energy or emittance.

The calculations will also allow us to determine reasonable values for these parameters. After certain level, the improvement of the accuracy of the results due to, for example, further decreasing the grid size of the FFT algorithm does not compensate for the increase in computation time.

Physical Parameters	Value	Computational Parameters	Value
Ion	H_2^+	Ne	180
Energy	20 keV	Nz	2^6
Emittance	10 π mm mrad	Nxy	2^{15}
Length	70 ns	dxy	1 mm
Inj. Peak Current	20 μA		
Number Turns	30		
Vac. Chamber Size	5 cm		

Table 7: Default parameters used in the simulations performed in this section to determine the impact that changes in computational parameters have on the dynamics of the bunch.

All the calculations on this section where performed on a bunch with the characteristics and computational parameters listed in Table 7 unless specified otherwise.

Parameter changed: "Ne"

"Ne" is the number of times the space charge electric field is calculated per revolution. The electric field is assumed to change slowly and does not need to be recalculated every integration step.
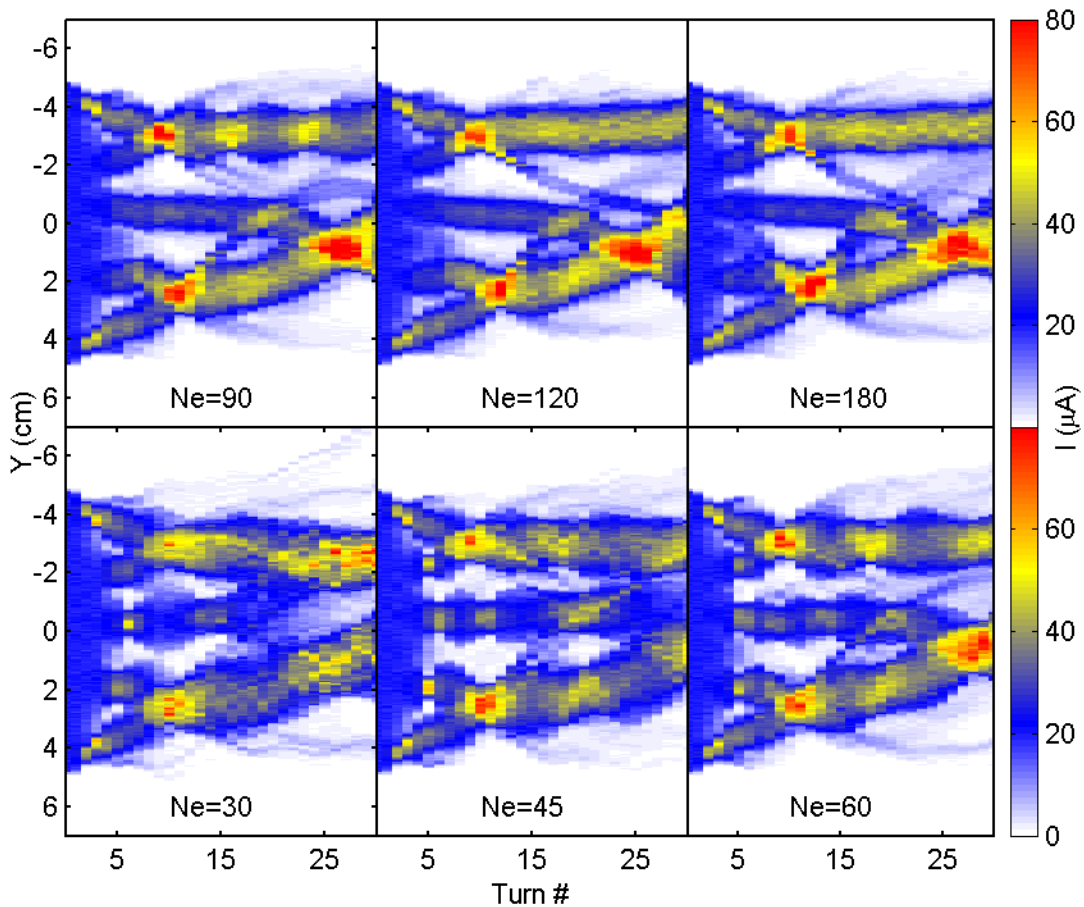
Figure 61: Evolution of the longitudinal profile of a bunch with characteristics listed in Table 7 for different values of Ne (Number of times the space charge electric field is calculated per revolution).

Figure 61 shows the evolution of the longitudinal bunch profile as turn number is increased for different values of "Ne".

It can be observed that increasing its value above 90 or 120 does not introduce significant qualitative changes in the bunch evolution. It will become more apparent that these changes are very small compared to the ones produced by increasing or decreasing beam current or emittance later on in the chapter.
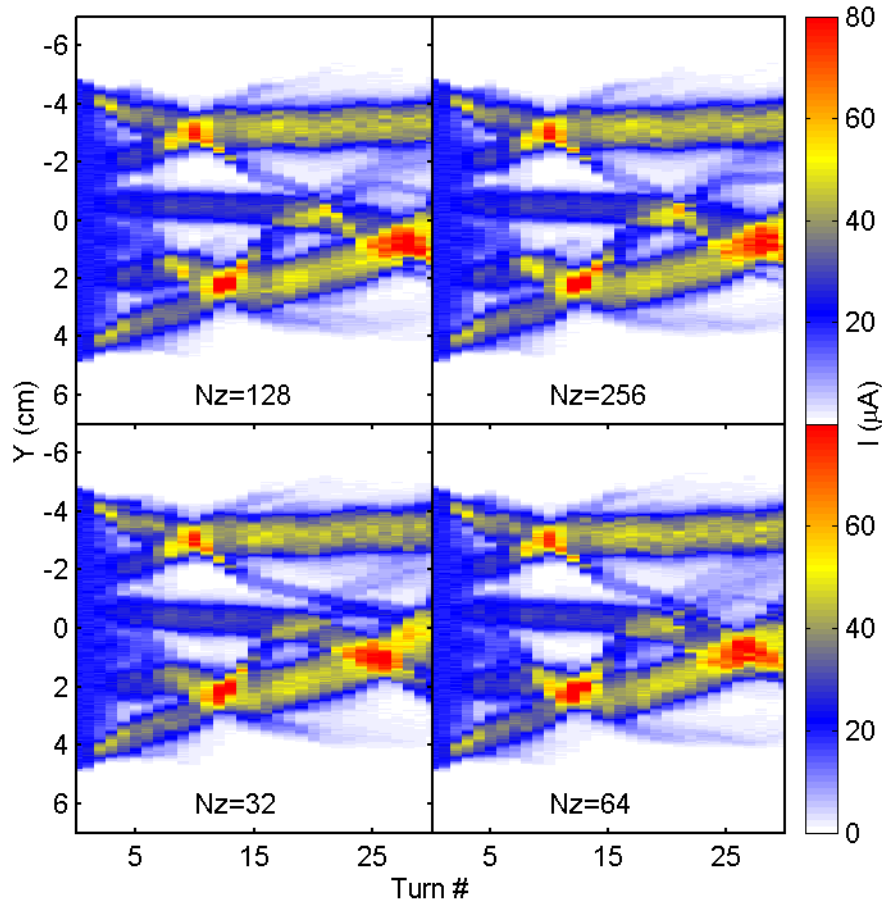
Figure 62: Evolution of the longitudinal profile of a bunch with characteristics listed in Table 7 for different values of Nz (Number of grid points in the FFT algorithm used to calculate the space charge electric field in the z direction (perpendicular to the medium plane of the ring)).

Parameter changed: "Nz"

Nz is the number of vertical (perpendicular to the medium plane of the ring) grid points of the mesh used in the FFT algorithm used to calculate the space charge electric field. The dimensions of the mesh size in this direction can be calculated dividing the full height of the vacuum chamber (5 cm) by Nz.

Figure 62 shows the evolution of the longitudinal bunch profile as turn number is increased for different values of "Nz". The impact in the bunch evolution of increasing the value of this parameter seems to be very small. Almost no difference can be observed between Nz = 32 and Nz = 256.

Parameter changed: "Nxy" and "dxy"

"Nxy" is maximum value for the product of the number of grid points of the mesh in the x axis and the number in the y axis used in the FFT algorithm used to calculate the space charge electric field. The x and y axis form a plane parallel to the medium plane of the ring. "dxy" is the default transverse mesh size in this plane.

As mentioned before, the vertical size of the box, in which the space charge electric field is calculated, is fixed throughout the problem and is equal to the vertical size of the vacuum chamber. On the other hand, the transverse sizes of the box increase as the transverse size of the beam grows due to the energy spread induced by the space charge forces. CYCO uses "dxy" as the mesh size in this plane until the number of points needed to continue with that size reaches "Nxy". At which point, the mesh size will be equal to the product of the transverse sizes of the box divided by "Nxy".

123

Figure 63 shows the evolution of the longitudinal bunch profile as turn number is increased for different values of "Nxy". The value of "dxy" is equal to 1 mm. Although, this value is not used throughout the calculations because the total number of points needed would be larger than "Nxy".
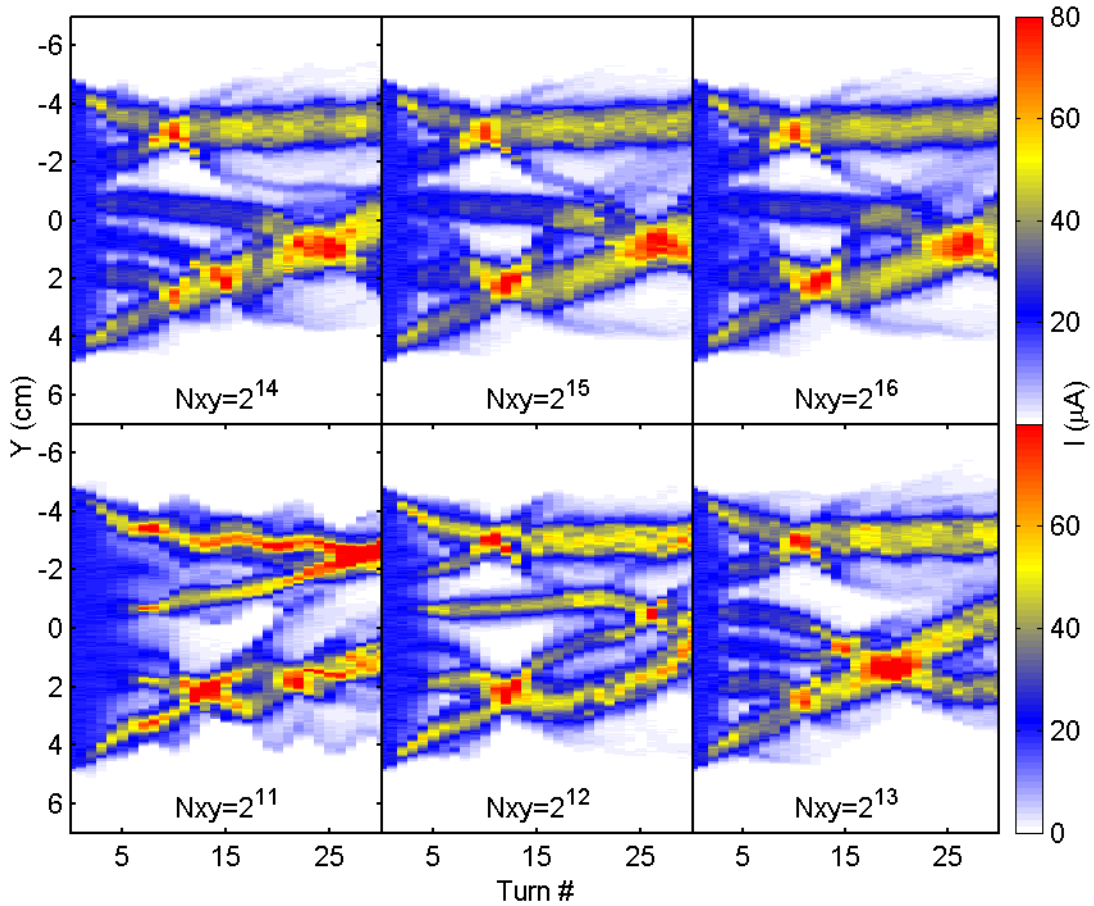
Figure 63: Evolution of the longitudinal profile of a bunch with characteristics listed in Table 7 for different values of Nxy (Maximum number of grid points in the FFT algorithm used to calculate the space charge electric field in the x-y plane (parallel to the medium plane of the ring)). The value of dxy is 1 mm in all cases.

Significantly different evolution can be observed when Nxy is not large enough. On the other hand, the cases where Nxy=2^{15} and Nxy=2^{16} are qualitatively very similar.

Figure 64 shows the evolution of the longitudinal bunch profile as turn number is increased for different values of "dxy" when the $Nxy=2^{16}$ is high enough not to have an impact in the dynamics.

Small qualitative changes are observed especially among the cases where dxy = 1 mm, dxy = 0.5 mm and dxy = 0.2 mm implying that the simulations are stable as long the size of the grid is a fraction of the beam diameter.
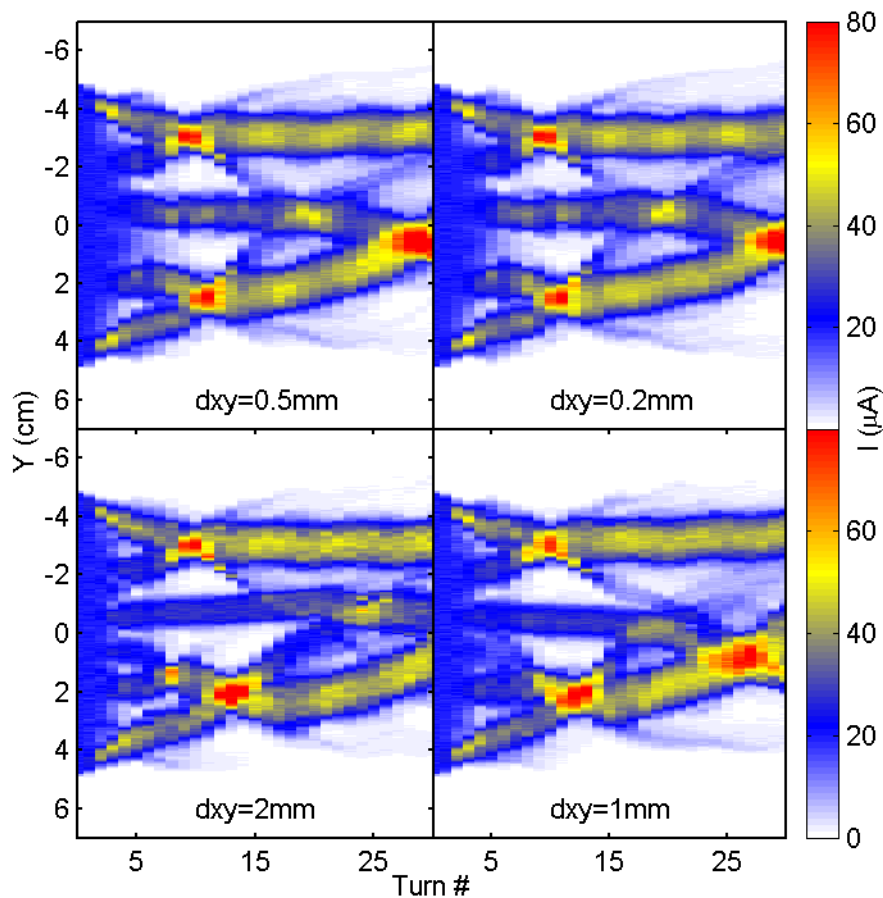
Figure 64: Evolution of the longitudinal profile of a bunch with characteristics listed in Table 7 for different values of dxy (grid size in the FFT algorithm used to calculate the space charge electric field in the x-y plane (parallel to the medium plane of the ring)). The value of Nxy is 2^{16} in all cases.

8.5. Numerical stability: Different initial ensemble

Besides the intrinsically computational parameters described in the previous section, the choice of the microscopic representation of the bunch should also have a limited impact on the bunch evolution compared to its macroscopic characteristics.

In addition to CYCO, Eduard Pozdeyev also developed a support program to generate a microscopic representation of the bunch to be studied. Macroscopic characteristics of the bunch such as length, emittance, energy, radial position and beta functions at the injection point are specified in an input file. The charge and mass of the ions, the number of macroparticles representing the bunch and a seed number used to randomly generate the position of these particles, are also included in the input file.

When the program is executed, it generates a file with a microscopic realization of the desired bunch that is later used as an input to CYCO. Different realizations of the bunch will be produced when the seed number is changed. Several simulations were performed to determine the impact that changing the microscopic representation of a bunch has on its dynamics. Three different ensembles with the characteristics listed in Table 8 were generated by changing the seed number used to create them.

The evolution of the three different ensembles is shown in Figure 65 for two different values of the charge that each macroparticle represents. On the left column, the bunch peak current (Io) is equal to 10µA (i.e. $Q_{macroparticle}$ = 62.4 e). On the right column, Io is equal to 5µA (i.e. $Q_{macroparticle}$ = 31.2 e).
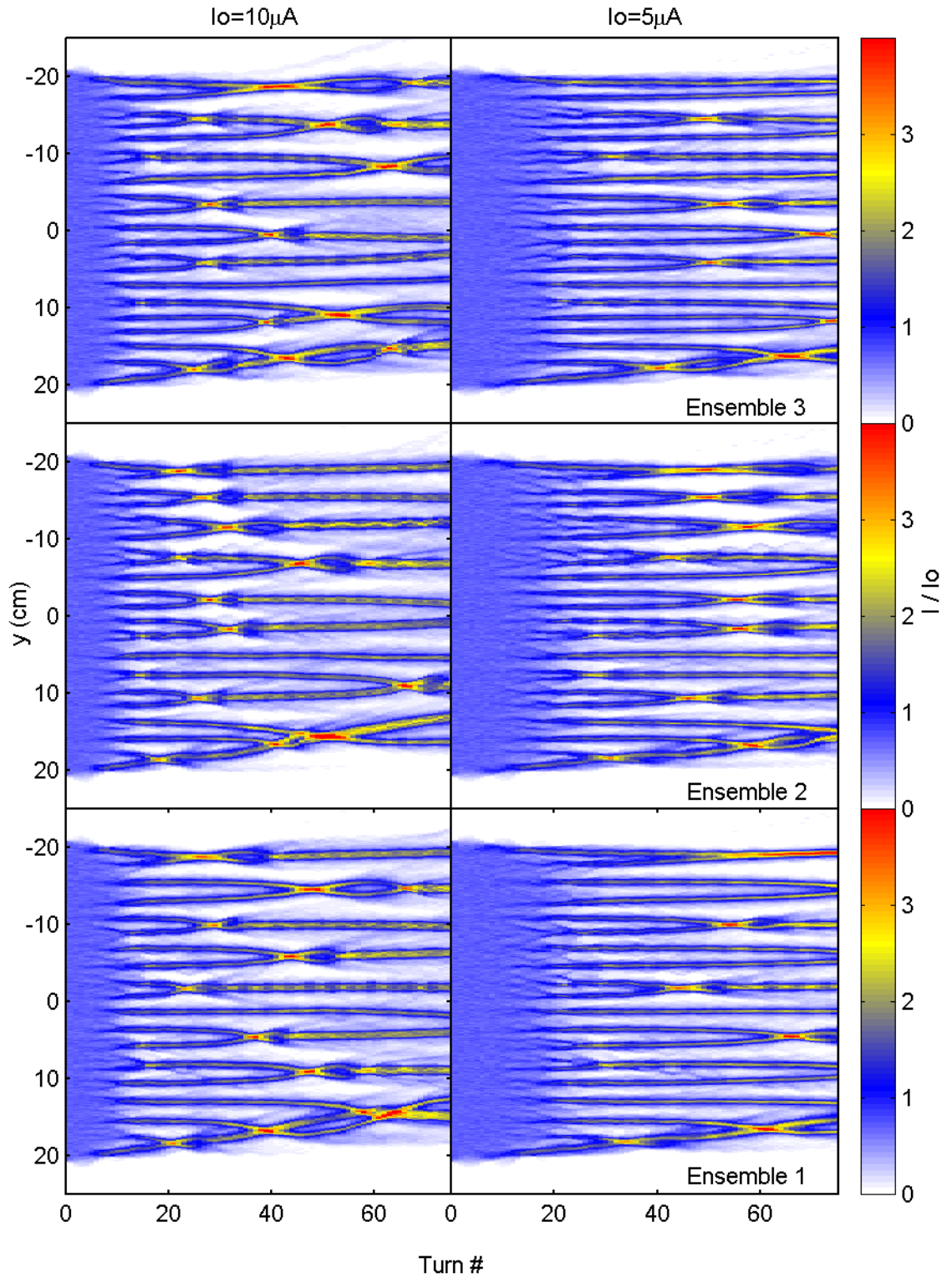
Figure 65: Evolution of the longitudinal profile of three different microscopic representations of a bunch with the characteristics listed in Table 8. Two different peak currents were used to compare characteristics of the evolution.

Physical Parameters	Value	Computational Parameters	Value
Ion	H_2^+	Ne	180
Energy	20 keV	Nz	2^6
Emittance	30 π mm mrad	Nxy	2^{15}
Length	300 ns	dxy	1 mm
Inj. Peak Current	5 or 10 μA		
Number Turns	75		
Vac. Chamber Size	5 cm		

Table 8: Parameters used in the simulations to determine the effect of the microscopic representation of a bunch in its dynamics compared to changes in its peak current.

There are significant qualitative differences in the evolution of the longitudinal profiles depending in the microscopic realization of the bunch. The position of the formed clusters and the neighbors they merge with, change depending on the initial ensemble chosen.

This behavior denotes a strong dependence of the clustering process on the initial conditions. Small changes in the initial distribution have a noticeable effect on the macroscopic evolution.

On the other hand, some other macroscopic characteristics such as when the break up of the bunch occurs or how fast clusters merge, follow a trend that is relatively insensitive to the initial ensemble chosen. It is clear that the bunch break up occurs sooner when the current is 10 μA than when the current is 5 μA.

To quantify these similarities, the number of clusters was counted as a function of the turn number for the six different problems studied in Figure 65. The results are shown in Figure 66.
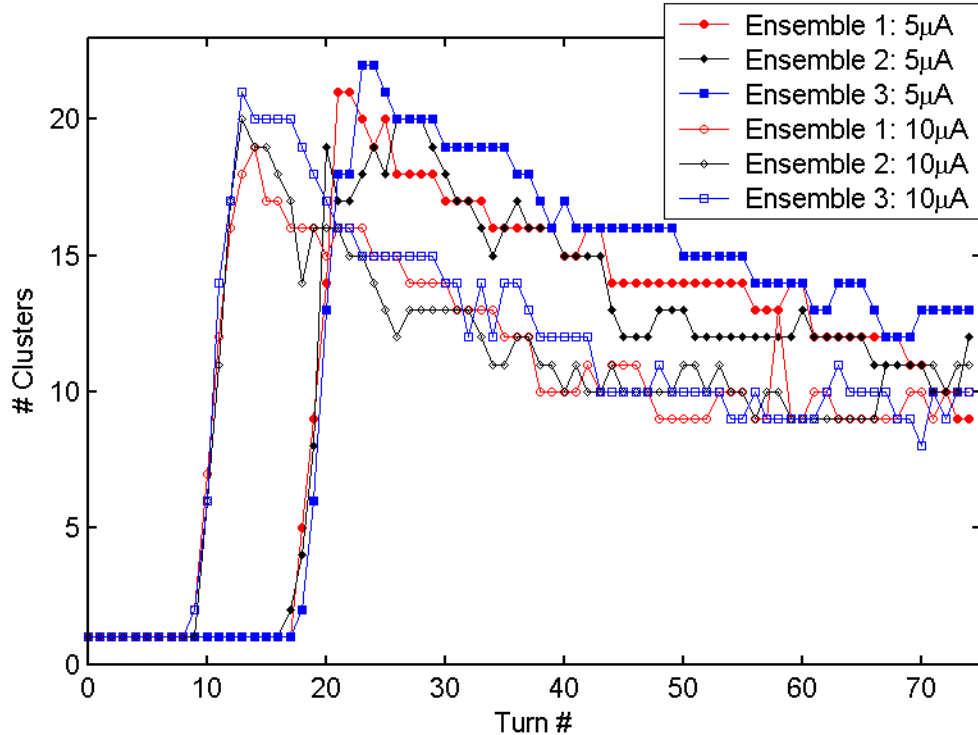
Figure 66: Number of clusters versus turn number for three different initial ensembles representing bunches with two different peak currents. The rest of the bunch characteristics are listed in Table 8.

A significant dispersion in the number of clusters at a fixed turn number exists among different initial ensembles. However, these differences are still significantly smaller than those due to changes in the bunch peak current.

Other simulations were performed in which different macroscopic characteristics of the bunch were changed for different microscopic realizations. The results were similar to the ones just discussed.

These strong dependences of the macroscopic evolution of the bunch on the initial conditions have also been observed experimentally as is discussed in chapter 10.

8.6. Conclusion

The procedure used to count the clusters in longitudinal profiles from simulations and experiments was described in detail. Even though two parameters are defined by the user, comparisons of the number of clusters for different longitudinal profiles can be carried out as long as these values are held constant.

It was established that the results of the simulations of CYCO did not significantly depend on computational parameters when reasonable values were chosen. The code was, therefore, stable in the respect to changes in those parameters.

It was established that the choice of the microscopic representation of the injected bunch had a significant impact in the evolution of the bunch. However, it was also shown that these changes are small compared to the ones introduced by changes in the beam properties (such as beam current, emittance or energy).

9. BEAM DYNAMICS SIMULATIONS WITH CYCO: RESULTS OF SIMULATIONS

9.1. Introduction

As mentioned in the previous chapter, the program CYCO, developed by Eduard Pozdeyev, has been used to perform the simulations of the beam dynamics in SIR. The main results of these simulations are described in this chapter.

The chapter starts with a discussion of the differences in the results that can be expected from the choice of the microscopic representation of a bunch. It is an effort to show that the differences found when the characteristics of the bunch are changed, later in the chapter, can not be explained just by the choice of the representation of the bunch.

The impact of the length of the bunches on their dynamics is analyzed in section 9.3. It will be shown that the number of clusters formed scales with bunch length. In a similar way, the differences in evolution due to changes in peak current and beam energy are studied in sections 9.4 and 9.5. Increasing the peak current accelerates the cluster formation while increasing the energy, decelerates the process.

In section 9.6, it will be shown under what conditions the vertical size of the vacuum chamber does not have a significant effect on the dynamics. The impact of the emittance of the beam will be studied in section 9.7 and in sections 9.8 and 9.9 we will analyze how different perturbations of the initial bunch affect

its evolution. The energy spread induced by space charge forces will be covered in section 9.10 and growth of the radial size of the beam in 9.11.

The chapter will be closed stating some questions that will have to be addressed by future research.

9.2. Dispersion in the number of clusters

As discussed in section 8.5, the choice of the microscopic representation of a bunch has a significant impact on the formation of the clusters. It is important to quantify the impact of this choice relative to more fundamental parameters like the beam peak current or energy.

Fourteen different microscopic realizations of bunches with characteristics listed in Table 9 and peak currents equal to 5, 10 and 20 µA were generated (ten realizations for the 20 µA case). Their evolutions were calculated for 75 turns and the number of clusters at a given turn number was counted in each case. Then, their average value and standard deviation were calculated.

The results are shown in Figure 67. The solid lines represent the average value and the shaded areas around them are limited by ± one standard deviation around the average. The value of the standard deviation after the initial break-up is around 1.1 clusters and does not depend on the value of the average number of clusters. Therefore, if the difference between the number of clusters counted in two different situations is several times the standard deviation, we will be able to affirm that is not due to the choice of the microscopic representation.

Physical Parameters	Value	Computational Parameters	Value
Ion	H_2^+	Ne	180
Energy	20 keV	Nz	2^6
Emittance	30 π mm mrad	Nxy	2^{15}
Length	300 ns	dxy	1 mm
Inj. Peak Current	5, 10 & 20 µA	k	0.5
Number Turns	75	W_{min}	5 mm
Vac. Chamber Size	5 cm		

Table 9: Bunch characteristics and computational parameters used in the simulations performed to determine the effect that the choice of the microscopic realization of the bunch has on the number of clusters formed.
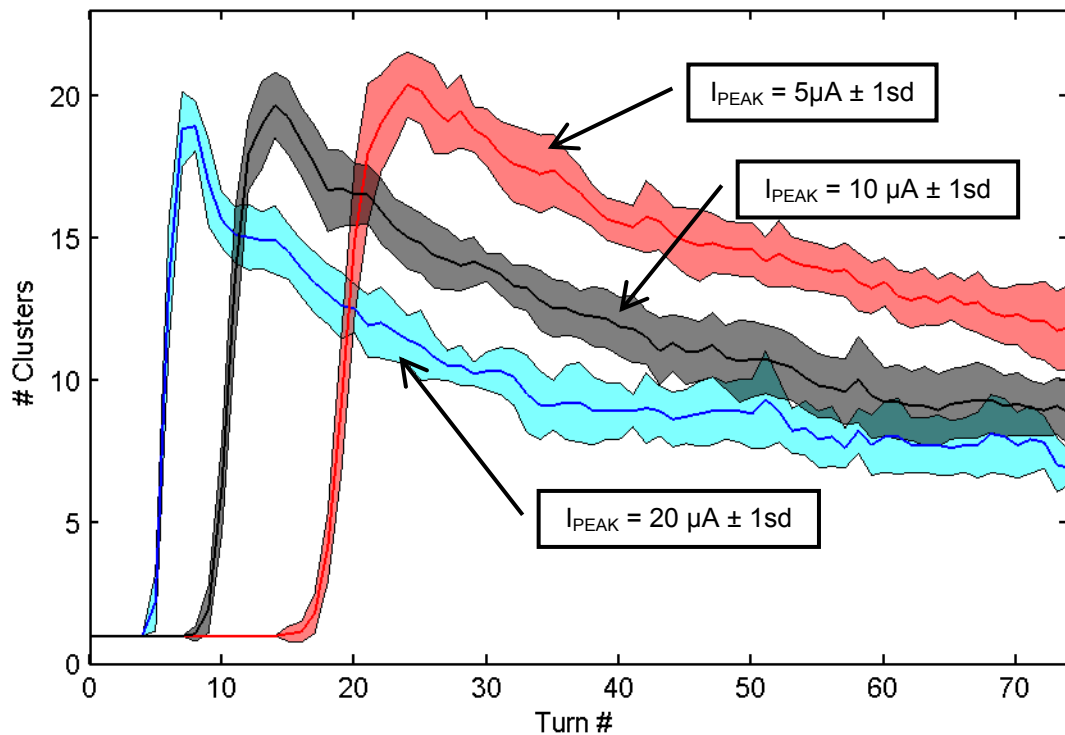
Figure 67: Average value and standard deviation of the number of clusters formed for three different peak currents. The dispersion in values is due to the choice of the microscopic representation of the bunch.

9.3. Scaling with bunch length

In order to determine the impact of the length of the injected bunch on its evolution, simulations using bunches with lengths ranging from 40 ns to 200 ns were performed. The other characteristics of the bunches and the computational parameters used in the simulations are listed in Table 10.

The number of clusters formed were counted after 10, 20 and 30 revolutions. The results are shown in Figure 68. The number of clusters any time after the initial break-up is proportional to the length of the original bunch. Therefore, a cluster density can be properly defined and the results obtained for a given bunch length can be scaled to describe bunches with different lengths.
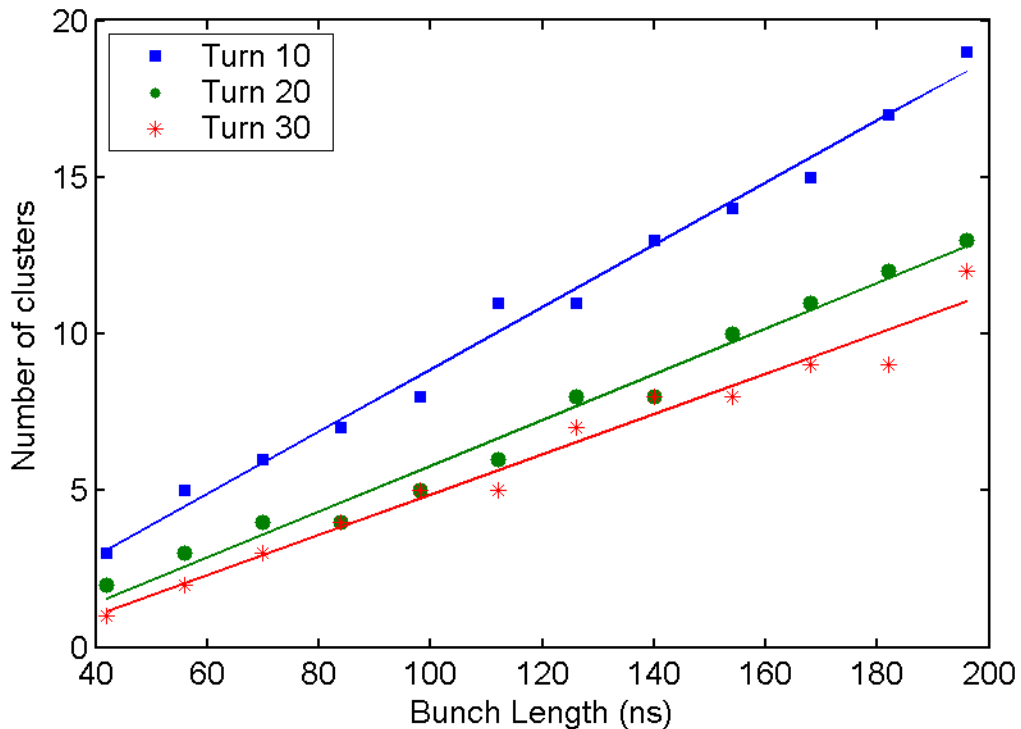
Figure 68: Number of clusters formed after 10, 20 and 30 revolutions for different initial bunch lengths. The computational and physical parameters used in the simulations are listed in Table 10.

Physical Parameters	Value	Computational Parameters	Value
Ion	H_2^+	Ne	180
Energy	20 keV	Nz	2^6
Emittance	10 π mm mrad	Nxy	2^{15}
Length	40 - 200 ns	dxy	1 mm
Inj. Peak Current	7.14 μA	k	0.5
Number Turns	30	W_{min}	5 mm
Vac. Chamber Size	5 cm		

Table 10: Physical and computational parameters used in the simulations performed to determine how the number of clusters formed scales with the length of the bunch after it breaks up.

9.4. Scaling with bunch current

To determine the effect that the bunch peak current has on its dynamic, a number of simulations were performed where the current was increased from I_0 (= 1.43 μA) to $16 \cdot I_0$ in I_0 current steps. The rest of the bunch characteristics including its microscopic representation (i.e. number, position and momentum of all the macroparticles) and computational parameters used (Table 11), were identical in the sixteen cases. The number of ions that each macroparticle represents is the only difference between them.

The evolution of the longitudinal beam profiles of the bunches in the first eight cases (lower current) are shown in Figure 69 and the rest in Figure 70. Several events (merging of clusters or rotations around each other) were labeled with letters A thru F.
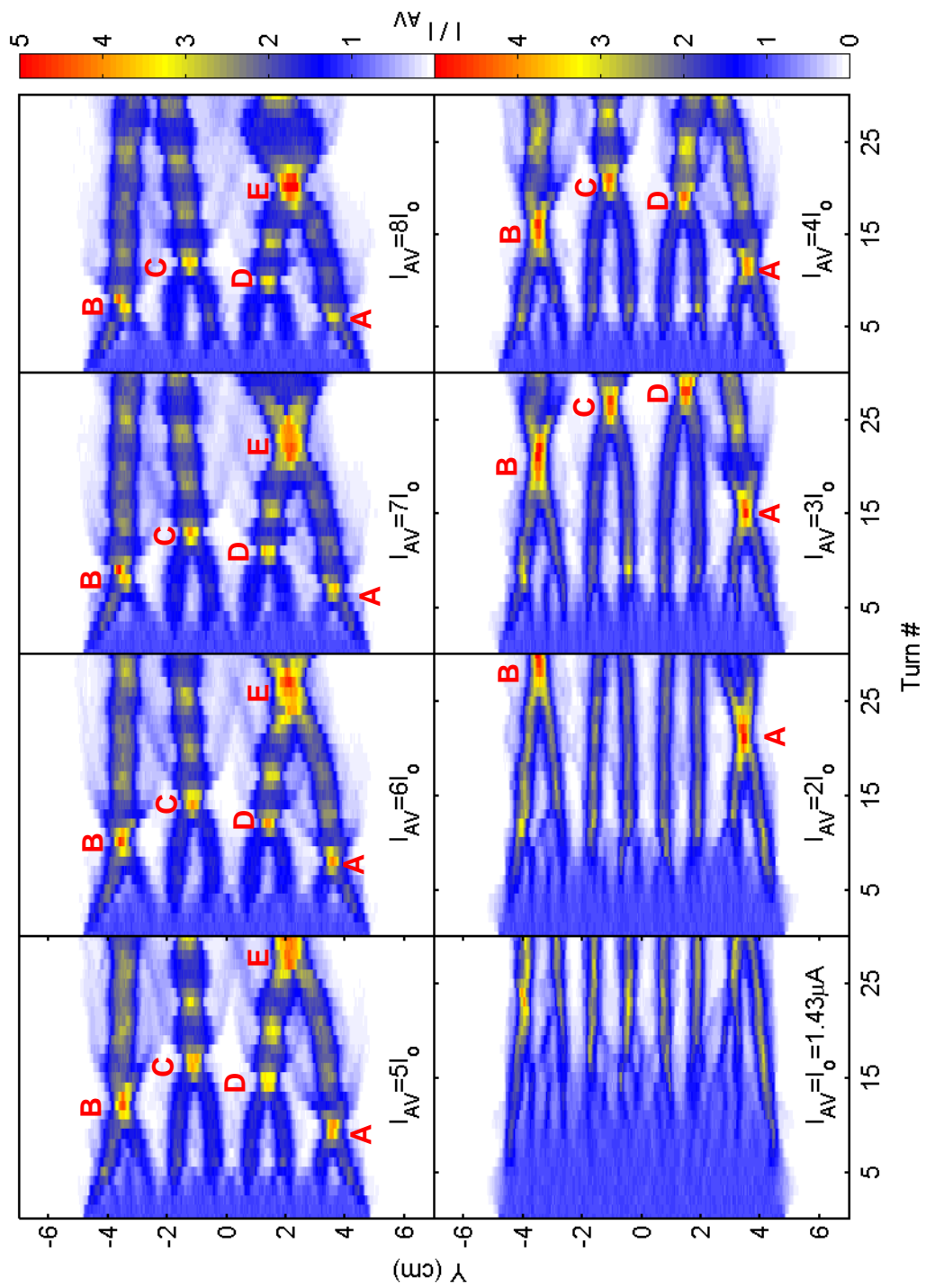
Figure 69: Waterfall diagrams representing the evolution of the longitudinal bunch profile for peak currents ranging from 1.43 μA to 11.44 μA. The other parameters that characterize the bunch are listed in Table 11. Some events have been labeled with letters A-F.

136
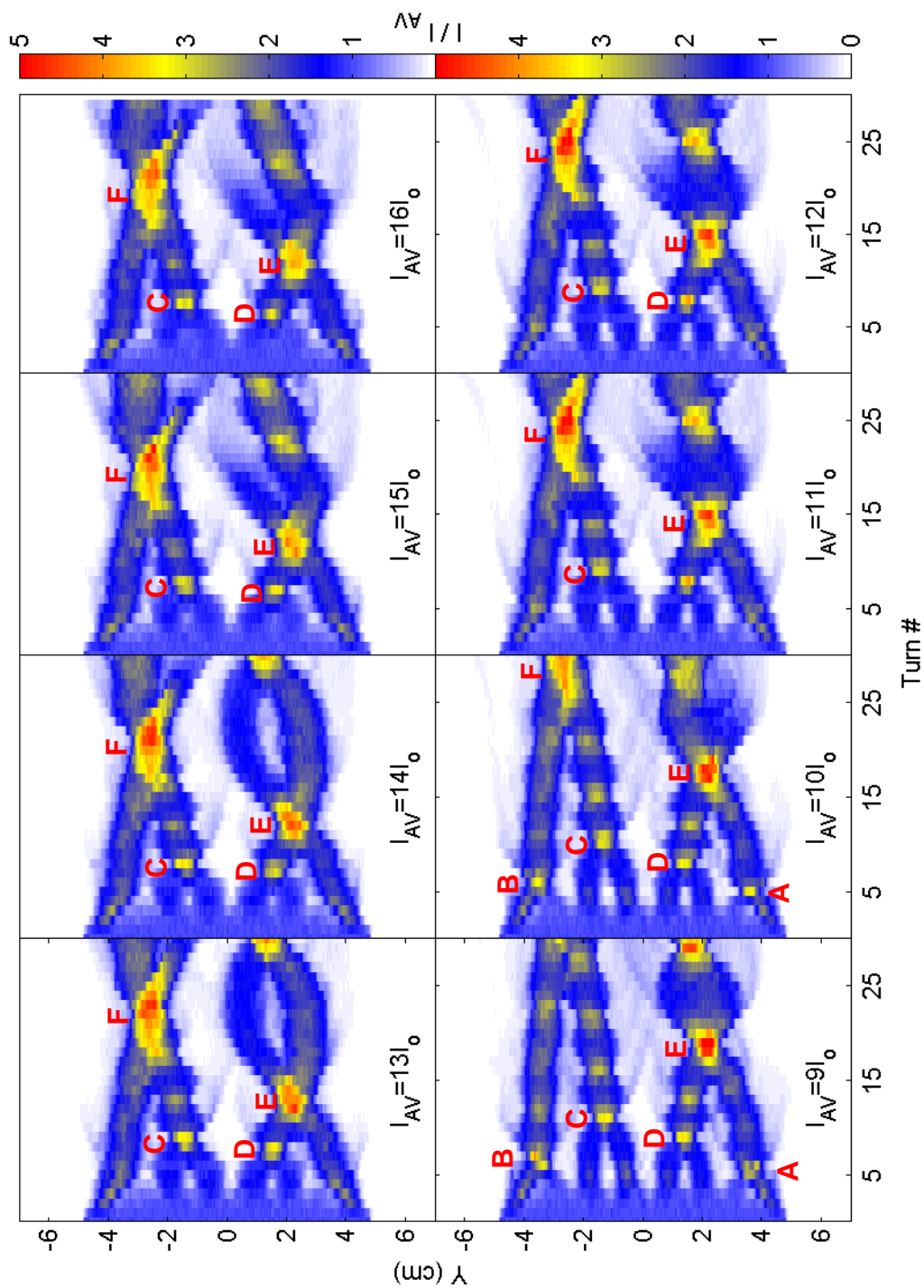
Figure 70: Waterfall diagrams representing the evolution of the longitudinal bunch profile for peak currents ranging from 12.87 μA to 22.88 μA. The other parameters that characterize the bunch are listed in Table 11.

Physical Parameters	Value	Computational Parameters	Value
Ion	H_2^+	Ne	180
Energy	20 keV	Nz	2^6
Emittance	10 π mm mrad	Nxy	2^{15}
Length	70 ns	dxy	1 mm
Inj. Peak Current	1.43 – 23 µA		
Number Turns	30		
Vac. Chamber Size	5 cm		

Table 11: Bunch characteristics and computational parameters used in the simulations performed to determine the effect of the peak current on the dynamics of the bunch.
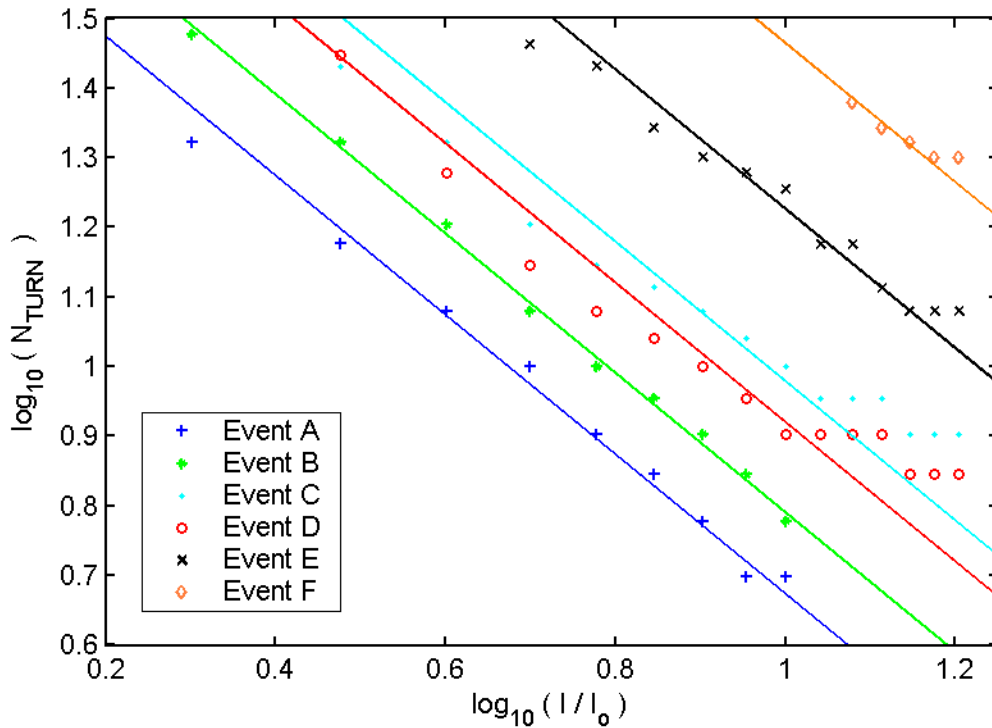
Figure 71: Turn number when the events labeled A thru F in Figure 69 and Figure 70 occur for different peak currents.

Since the microscopic realization of the bunch is the same and the differences in the dynamics due to changes in the peak current are not large, the same event can be identified in the different cases studied.

Figure 71 shows, on a logarithmic scale, how the turn number changes with the peak current when these events occur. The data is reasonably well represented by straight lines with slope equal to -1. Therefore, we can conclude that the time (i.e turn number) it takes for a specific event to happen is approximately inversely proportional to the peak current of the bunch.

Similar simulations were conducted in bunches with the characteristics listed in Table 10. Two different microscopic realizations of 1 and 2 µA peak current bunches, fourteen of 5 and 10 µA and ten of 20 µA were used. The results of the calculations for one of these realizations are shown in Figure 72. In addition to the evolution of the longitudinal profiles, the number of clusters counted for the five different currents are shown in the lower right corner.

The different values obtained for the different microscopic realizations were averaged and their standard deviation was calculated. The results are shown in section 9.2 (Figure 68).

If the time it takes for a specific event to happen is inversely proportional to the peak current, the turn number at which the total number of clusters is N_C should also be inversely proportional to the current (I).

We can define an equivalent turn number as $T_{EQ} \equiv T \cdot I(\mu A)$. The number of clusters as a function of this "equivalent turn number" should be, consequently, independent of the beam current.
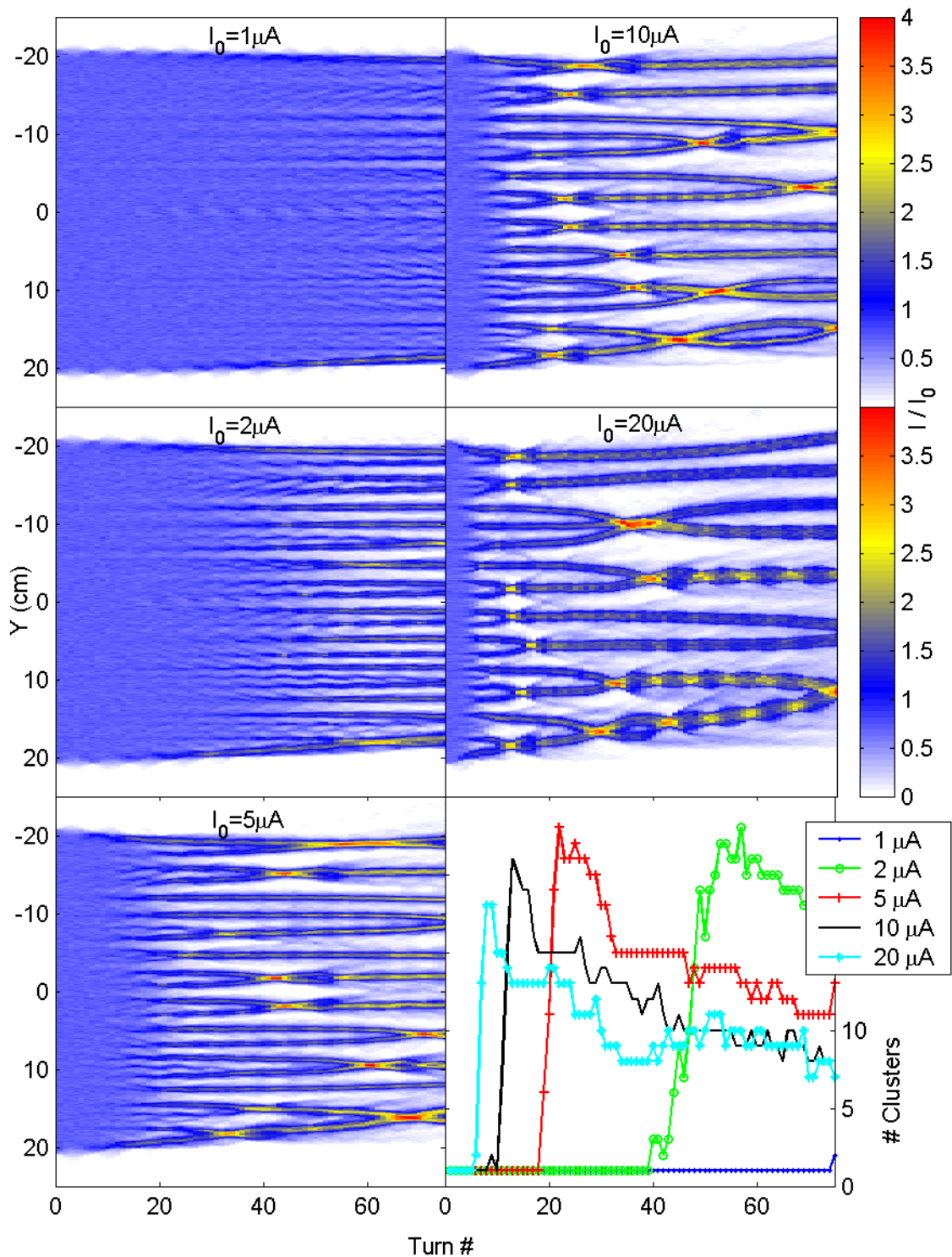
Figure 72: Waterfall diagrams representing the evolution of the longitudinal bunch profile for 1, 2, 5, 10 and 20 μA peak currents. The other parameters that characterize the bunch are listed in Table 9. The number of clusters counted is shown in the lower right corner of the figure.

Figure 73 shows the same information as Figure 67 represented as a function of the equivalent turn number. It can be clearly seen that the scaling described before works very well.
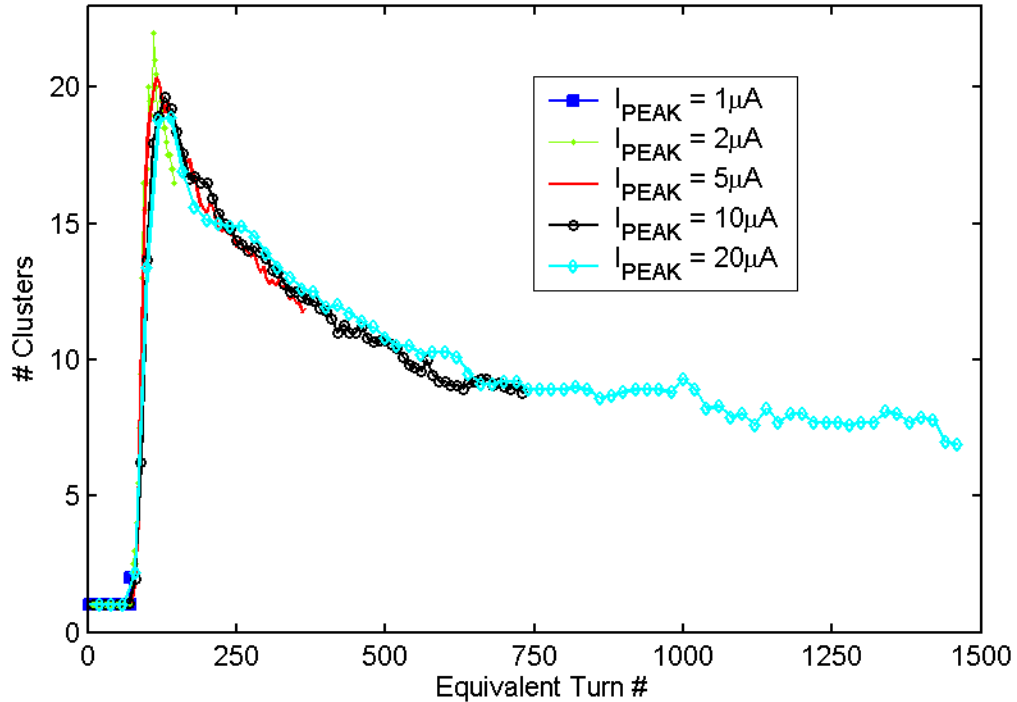
Figure 73: Number of clusters as a function of the equivalent turn number (N_{EQ}) for different peak currents.

9.5. Scaling with energy of the bunch

In order to determine the effect that the energy of the bunch has on its dynamics, a number of simulations were performed where the energy was increased from 12 keV to 28 keV in 2 keV energy steps. The rest of the bunch characteristics including its microscopic representation and computational parameters used are listed in Table 12.

It is worth noting here that the linear charge density was not changed. Therefore, since the energy changes, the peak current will also change.

Physical Parameters	Value	Computational Parameters	Value
Ion	H_2^+	Ne	180
Energy	12 - 28 keV	Nz	2^6
Emittance	30 π mm mrad	Nxy	2^{15}
Length	41.52 cm	dxy	1 mm
Total Charge	$1.5 \cdot 10^{-12}$ C	k	0.5
Number Turns	75	W_{min}	5 mm
Vac. Chamber Size	5 cm		

Table 12: Bunch characteristics and computational parameters used in the simulations performed to determine the effect of the energy on the dynamics of the bunch.
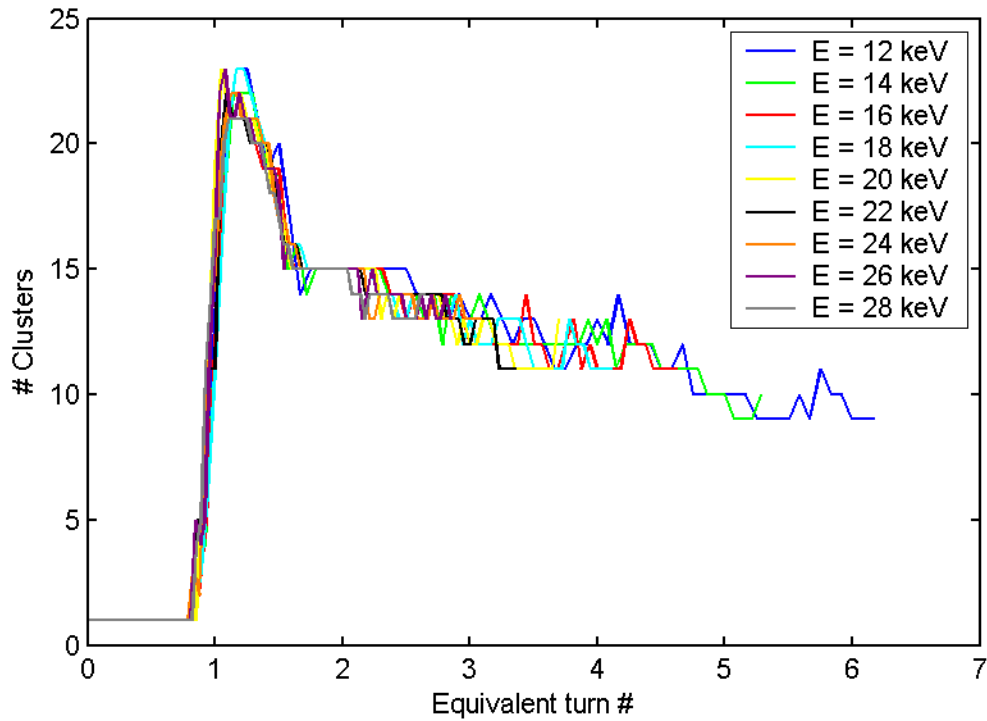
Figure 74: Number of clusters as a function of the equivalent turn number for different energies.
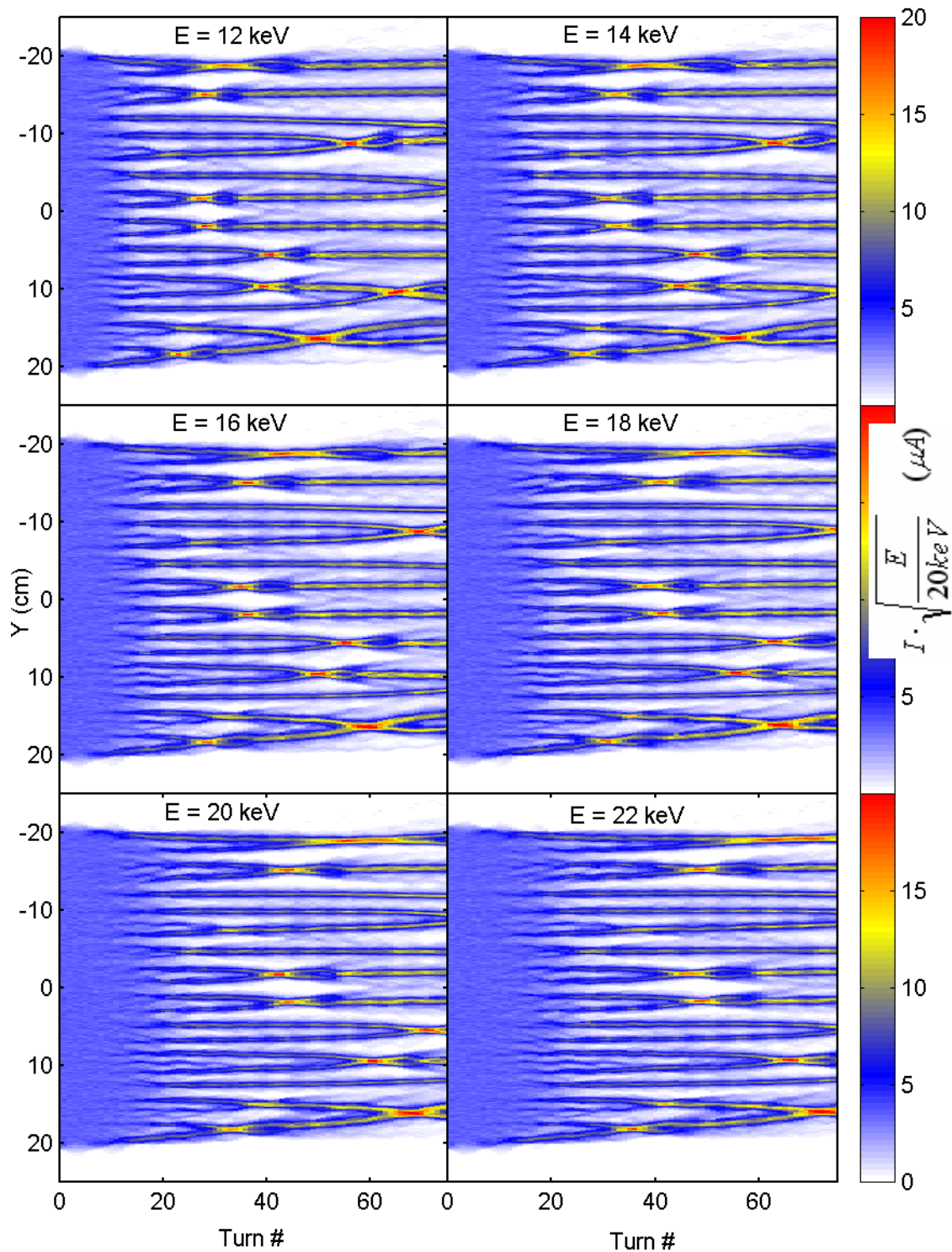
Figure 75: Waterfall diagrams representing the evolution of the longitudinal bunch profile for energies ranging from 12 keV to 22 keV. The other parameters that characterize the bunch are listed in Table 12.
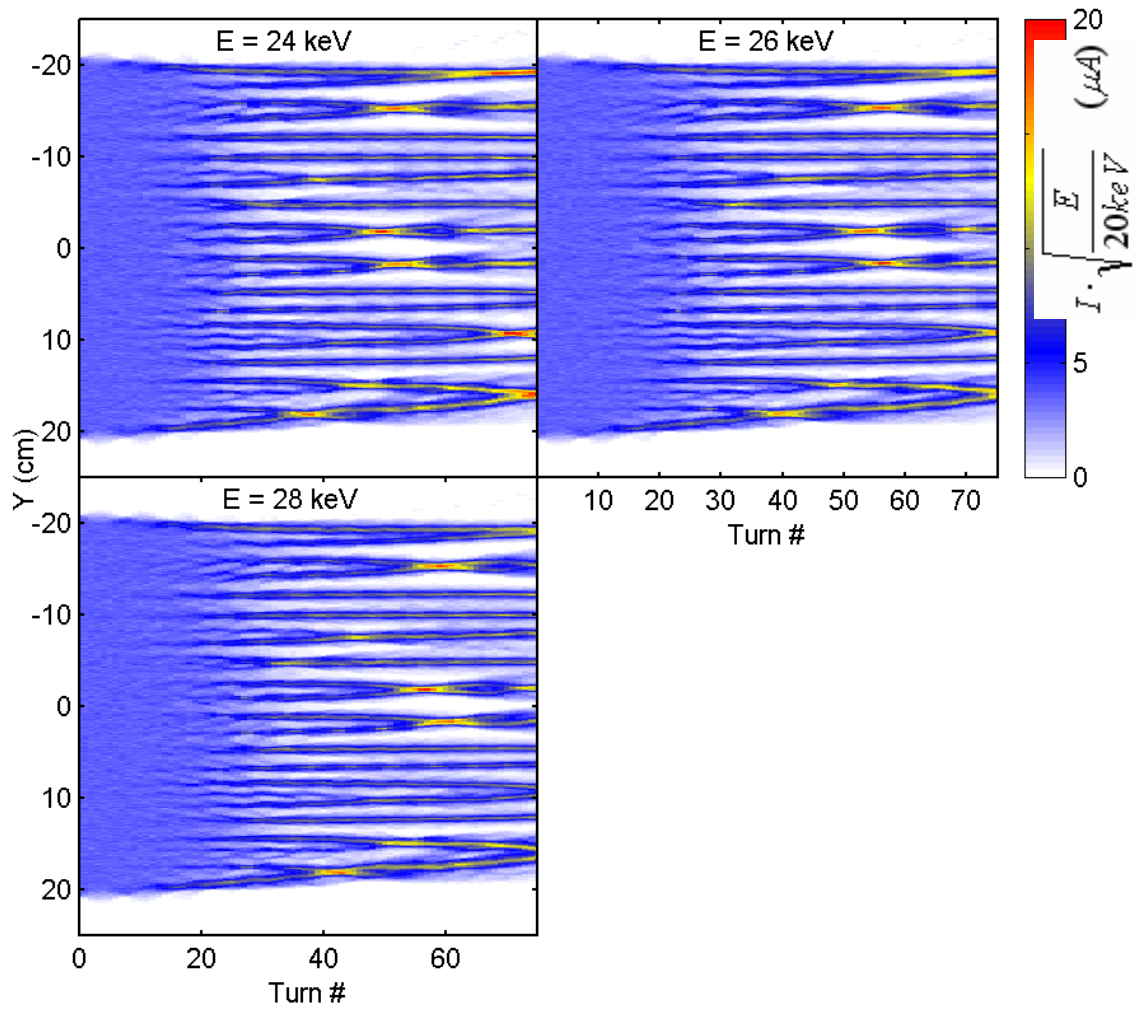
Figure 76: Waterfall diagrams representing the evolution of the longitudinal bunch profile for energies ranging from 24 keV to 28 keV. The other parameters that characterize the bunch are listed in Table 12.

The results of these simulations are shown in Figure 75 and Figure 76. In a similar way as done for different peak currents, an equivalent turn number

$$T_{EQ} \equiv \frac{T}{E(keV)}$$

can be defined. If the evolution of the bunch scales with the energy in such way, the number of clusters counted as a function of the equivalent turn number should be independent of the energy. The results shown in Figure 74 confirm the validity of this scaling.

9.6.   Vacuum chamber size

To determine the effect that the size of the vacuum chamber has on the bunch dynamic, a number of simulations were performed where its vertical size (g) was increased from 2 cm to 15 cm. The rest of the bunch characteristics including its microscopic representation and computational parameters used (Table 13), were not changed.

The results of the simulations are shown in Figure 77. Several events were identified and labeled with letters A thru G. The turn number when they occur as a function of size of the vacuum chamber is shown in Figure 78. We can conclude that while the size of the chamber has a significant impact on the dynamics of the beam when the size is close to 2 cm, it quickly decreases when the size is increased.

Physical Parameters	Value	Computational Parameters	Value
Ion	H_2^+	Ne	180
Energy	20 keV	Nz	2^6
Emittance	30 π mm mrad	Nxy	2^{15}
Length	300 ns	dxy	1 mm
Inj. Peak Current	10 μA		
Number Turns	75		
Vac. Chamber Size	2 - 15 cm		

Table 13: Bunch characteristics and computational parameters used in the simulations performed to determine the effect of the size of the vacuum chamber on the dynamics of the bunch.
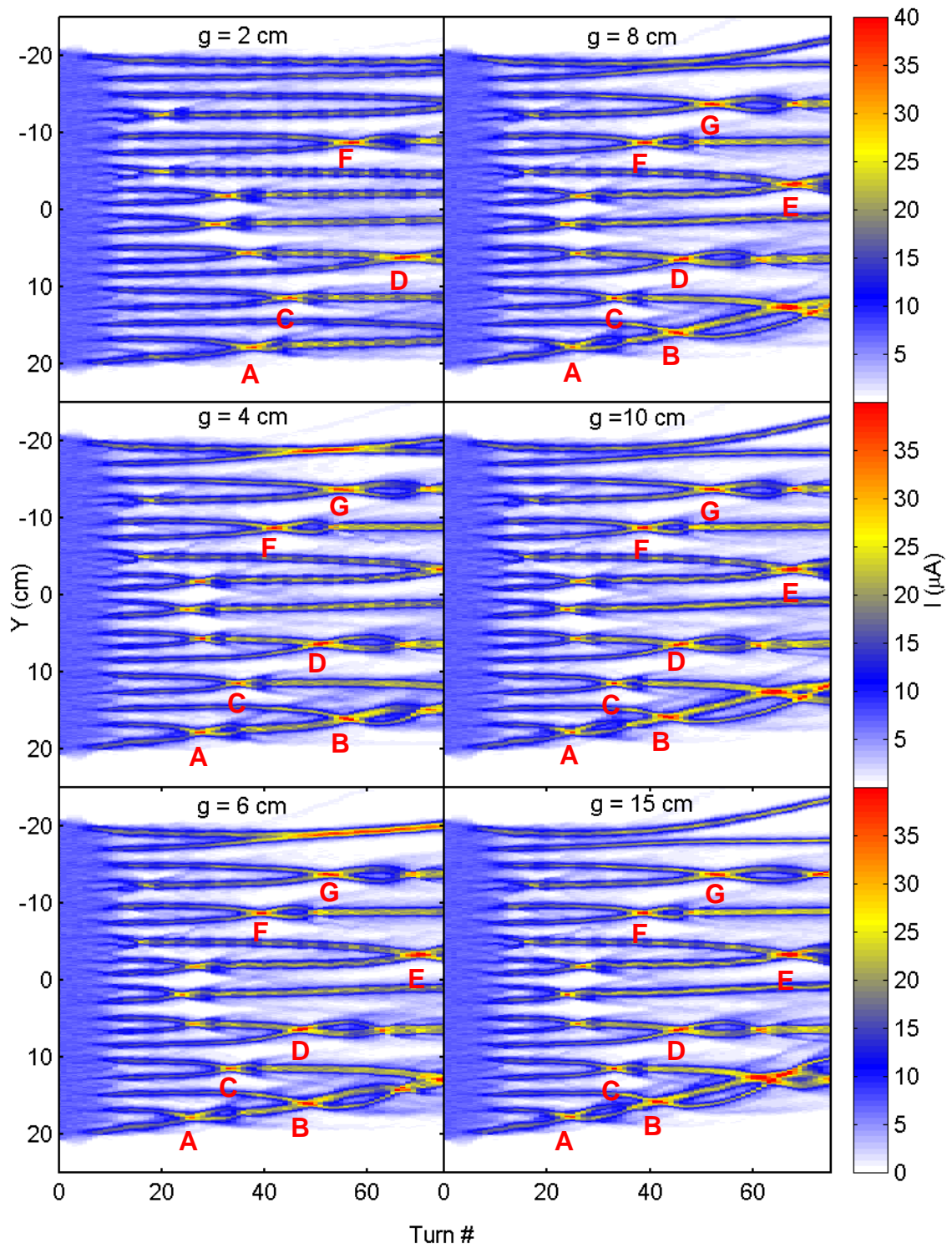
Figure 77: Waterfall diagrams representing the evolution of the longitudinal bunch profile for sizes of the vacuum chamber ranging from 2 cm to 15 cm. The parameters that characterize the bunch are listed in Table 13.
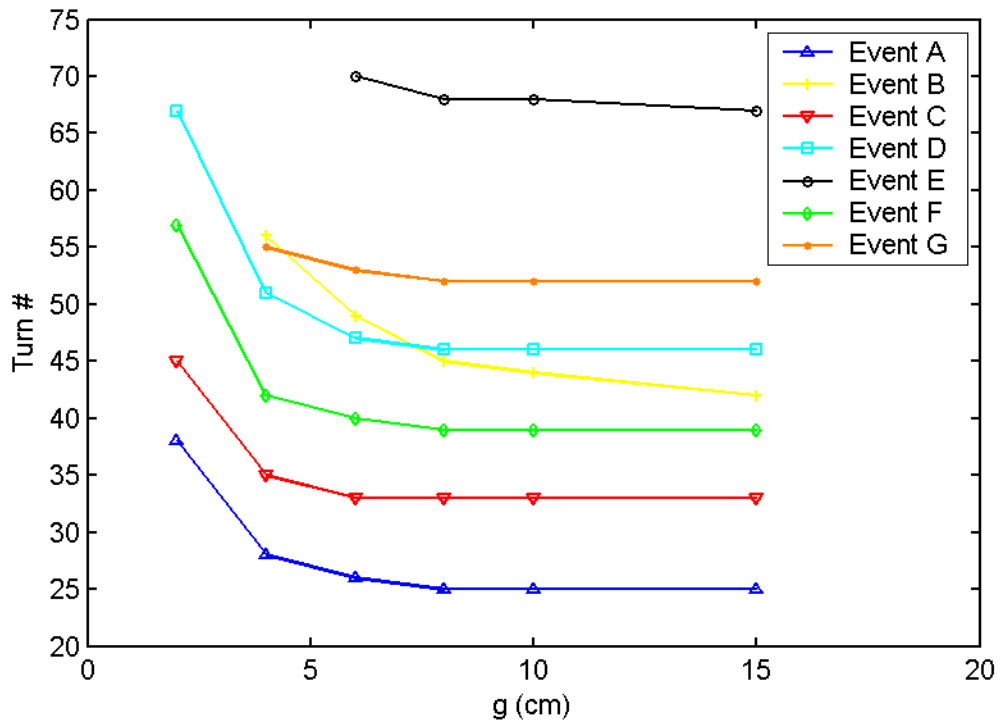
Figure 78: Turn number when the events labeled A thru G in Figure 77 occur when the size of the vacuum chamber is changed.

9.7. Transverse emittance

To determine the effect that the emittance of the beam has on the bunch dynamic, a number of simulations were performed where the emittance was increased from 5 to 40·π·mm·mrad. The remaining bunch characteristics and computational parameters (Table 14) used were not changed.

The results of the simulations are shown in Figure 79. The evolution of the number of clusters was determined and it is shown in Figure 80.
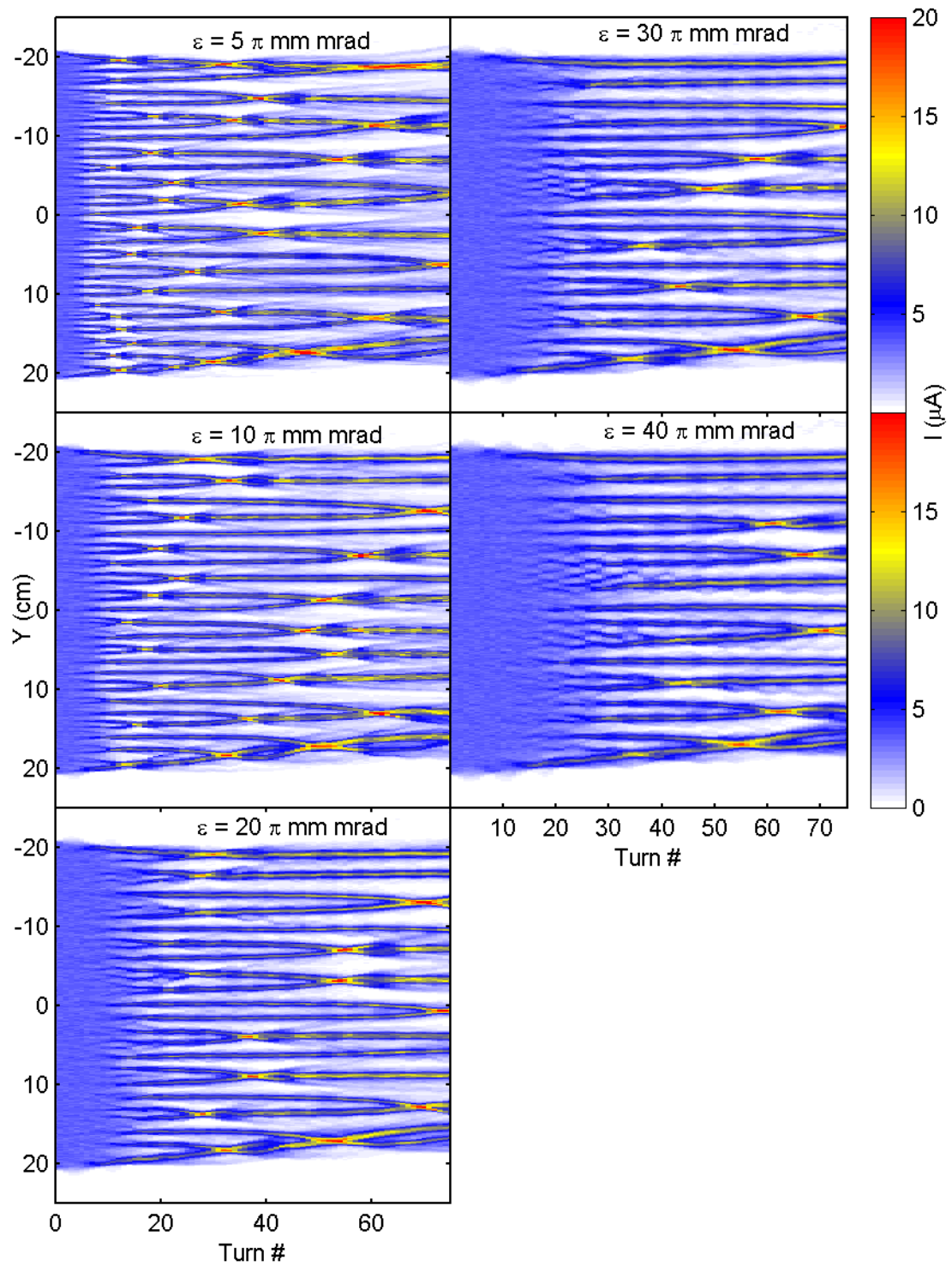
Figure 79: Waterfall diagrams representing the evolution of the longitudinal bunch profile for beams with emittances ranging from 5 to 40·π·mm·mrad. The parameters that characterize the bunch are listed in Table 14.

Physical Parameters	Value	Computational Parameters	Value
Ion	H_2^+	Ne	180
Energy	20 keV	Nz	2^6
Emittance	5 - 40 π mm mrad	Nxy	2^{15}
Length	300 ns	dxy	1 mm
Inj. Peak Current	5 µA	k	0.5
Number Turns	75	W_{min}	5 mm
Vac. Chamber Size	5 cm		

Table 14: Bunch characteristics and computational parameters used in the simulations performed to determine the effect of the emittance of the beam on its dynamics.
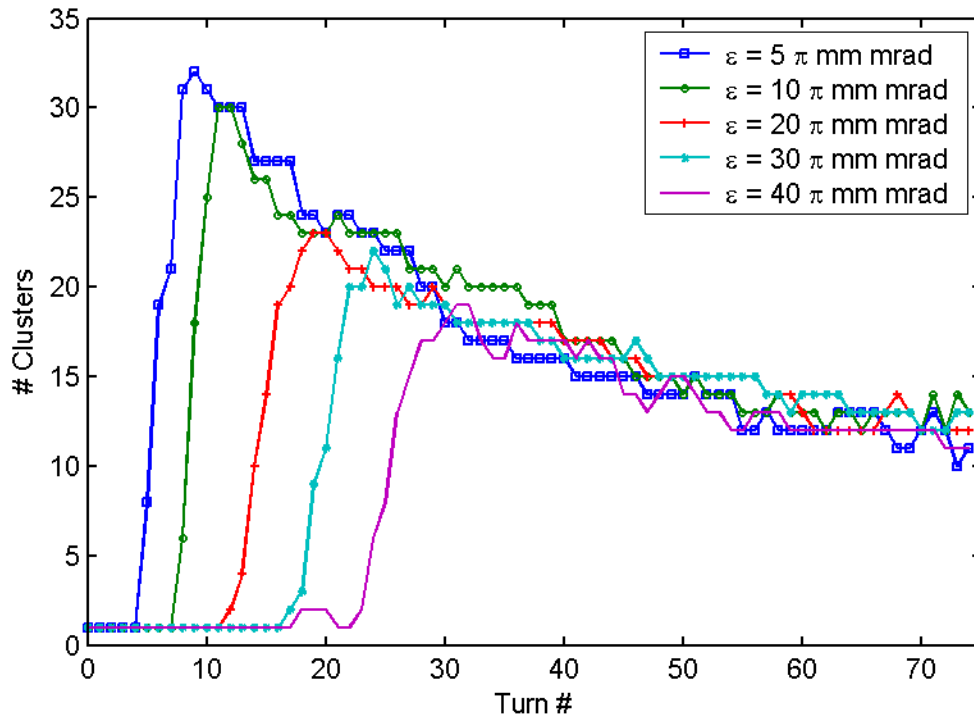

Figure 80: Number of clusters as a function of the turn number for different beam emittances.

We can conclude that while the emittance of the beam plays an important role in initiating the bunch break up (turn number at which it occurs), its influence in the dynamics afterwards (rate at which clusters merge and final cluster density) is not important. The information about the transverse properties of the beam is lost after the break up.

9.8. Macroscopic perturbation

To understand the effect that perturbations of the local current density have on the beam dynamics of the bunch, the evolution of two different bunches with the characteristics listed in Table 15 was calculated. Although the average current density in both cases was the same (5 µA), in one case the local charge density was perturbed.

Physical Parameters	Value	Computational Parameters	Value
Ion	H_2^+	Ne	180
Energy	20 keV	Nz	2^6
Emittance	30 π mm mrad	Nxy	2^{15}
Length	300 ns	dxy	1 mm
Inj. Current	5 µA (Average)		
Number Turns	75		
Vac. Chamber Size	5 cm		

Table 15: Bunch characteristics and computational parameters used in the simulations performed to determine the effect that local density fluctuation have on the bunch dynamics.

150

The longitudinal beam profiles of the bunches, when they are injected as well as their evolution in the ring, can be seen in Figure 81.

It can be observed that the break up of the bunch occurs earlier in the region of the bunch where the local density is higher. Moreover, the break up starts at the same time it would have started if the average current of the bunch was equal to the local density at that point. Said in a different way, it is the local current density the one that determines when the break up occurs.
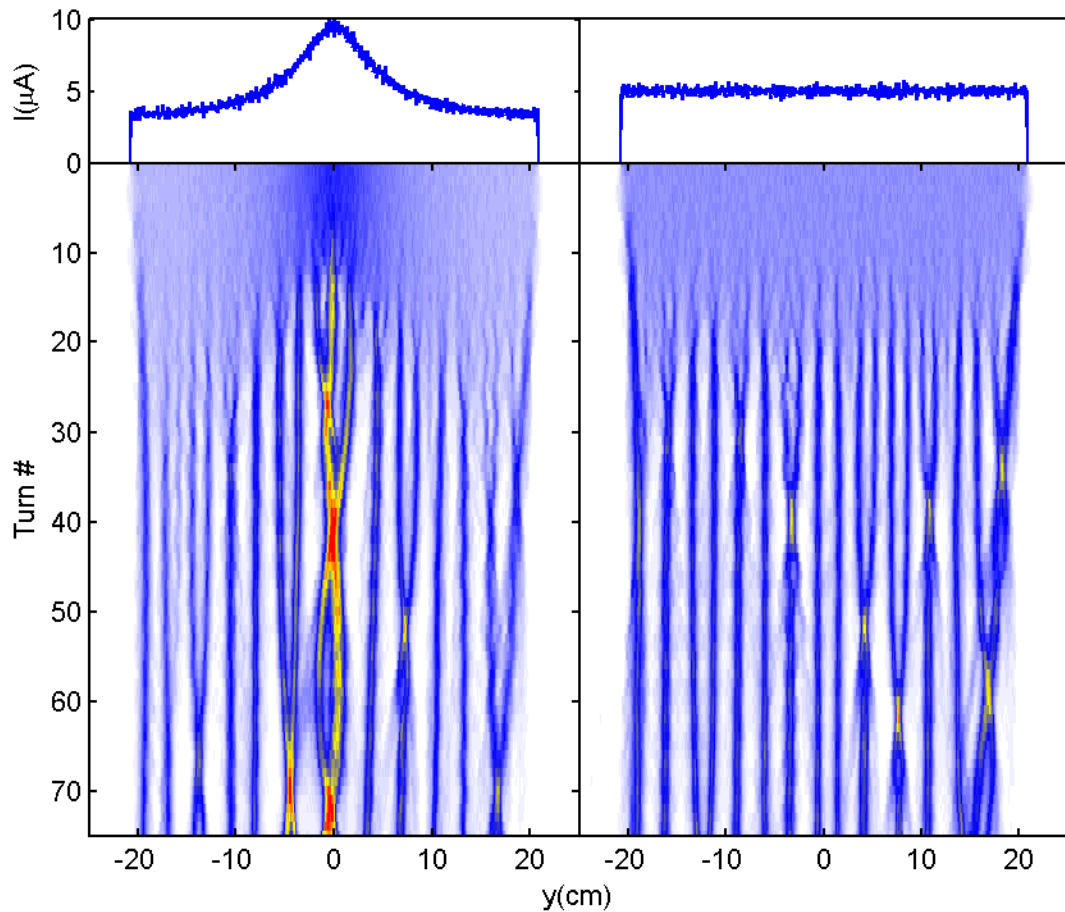
Figure 81: Waterfall diagrams representing the evolution of the longitudinal bunch profile for two bunches with different initial longitudinal profile (top left and right). The initial microscopic representation of the bunch in the left was generated by displacing macroparticles toward the center of the bunch. The parameters that characterize the bunch are listed in Table 15.

9.9.   Microscopic perturbation

As discussed in sections 8.5 and 9.2, the choice of the microscopic representation of a bunch has a significant impact on its macroscopic dynamics. To better understand this process, the dynamics of two different microscopic realizations of a bunch with characteristics listed in Table 16 was studied. The only difference between the two realizations is that one macroparticle out of the $0.3 \cdot 10^6$ was removed in one of them. Therefore, the charge per macroparticle also changed slightly.

Physical Parameters	Value	Computational Parameters	Value
Ion	H_2^+	Ne	180
Energy	20 keV	Nz	2^6
Emittance	30 π mm mrad	Nxy	2^{15}
Length	300 ns	dxy	1 mm
Inj. Peak Current	20 µA	# macroparticles (N_T)	$0.3 \cdot 10^6$ (-1)
Number Turns	75		
Vac. Chamber Size	5 cm		

Table 16: Bunch characteristics and computational parameters used in the simulations performed to determine the effect that very small changes in the choice of the microscopic representation of a bunch have on its dynamics.

The distance between the positions of a given macroparticle in both realizations was calculated for every particle and turn number. The results are shown in Figure 82 where the vertical axis is the turn number (T_N) and the horizontal axis is the distance between positions (Δd). The color scale represents

the percentage of particles that have been displaced Δd by turn T_N from the position they would have if that single macroparticle had not been removed. The contour lines represent the percentage of particles that have been displaced more than Δd by turn T_N.

It can be observed that more than 10 % of the macroparticles have been displaced more than 2.5 cm by turn number 75 due to the very small perturbation in the initial representation of the bunch.
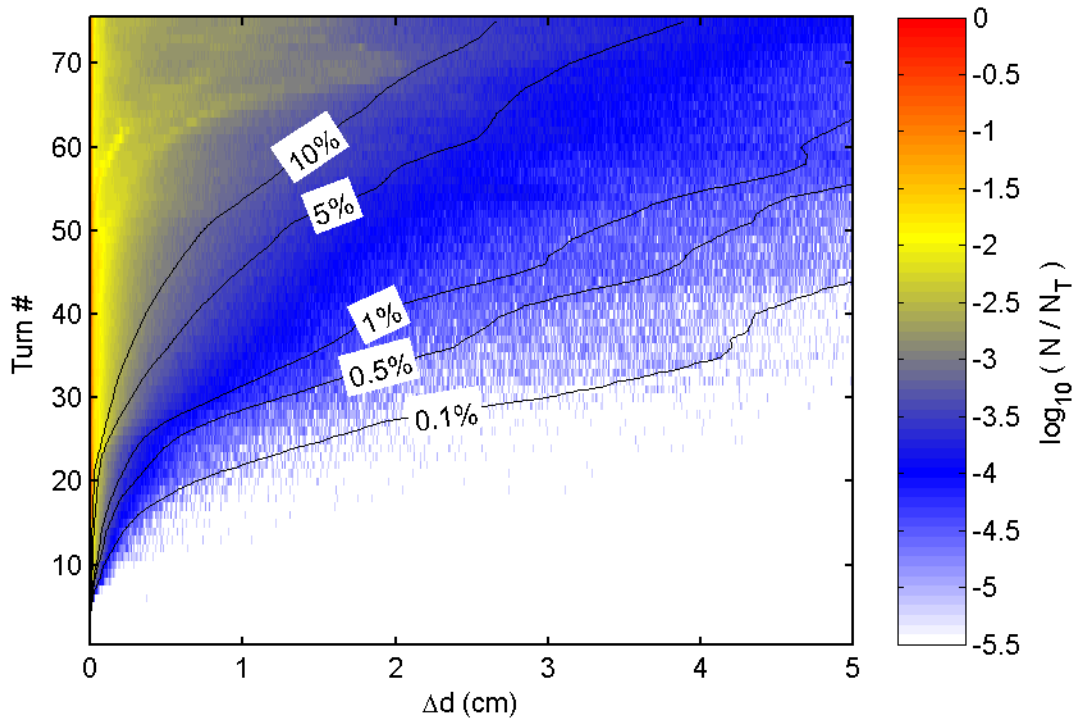
Figure 82: Effect in the evolution of the position of the macroparticles when one of them is removed from the initial ensemble. The percentage of particles that have been displaced Δd at a given turn number is represented with different colors. The percentage of particles that have been displaced more than Δd at a given turn number is represented by contour lines.

9.10. Energy spread within a bunch

The energy spread induced by space charge forces has been studied for different beam currents and energies. The dynamics of different bunches with the characteristics listed in Table 17 has been studied.

As expected, the energy spread grows faster when the peak current is larger or the energy is lower as is shown on the left of Figure 83. At first, the energy spread grows linearly but after some time the growth slows down probably reaching an asymptotic value at the end although this has not been verified.

It can be observed that the scaling laws, used in previous sections, also work very well to describe the energy spread differences. See plots on the right of the figure where the energy spread is shown as a function of the equivalent turn number.

Physical Parameters	Value	Computational Parameters	Value
Ion	H_2^+	Ne	180
Energy	22 - 28 keV	Nz	2^6
Emittance	30 π mm mrad	Nxy	2^{15}
Length	41.52 cm	dxy	1 mm
Total Charge	$(0.6 – 6) \cdot 10^{-12}$ C		
Number Turns	75		
Vac. Chamber Size	5 cm		

Table 17: Bunch characteristics and computational parameters used in the simulations performed to determine the energy spread induced by space charge forces.
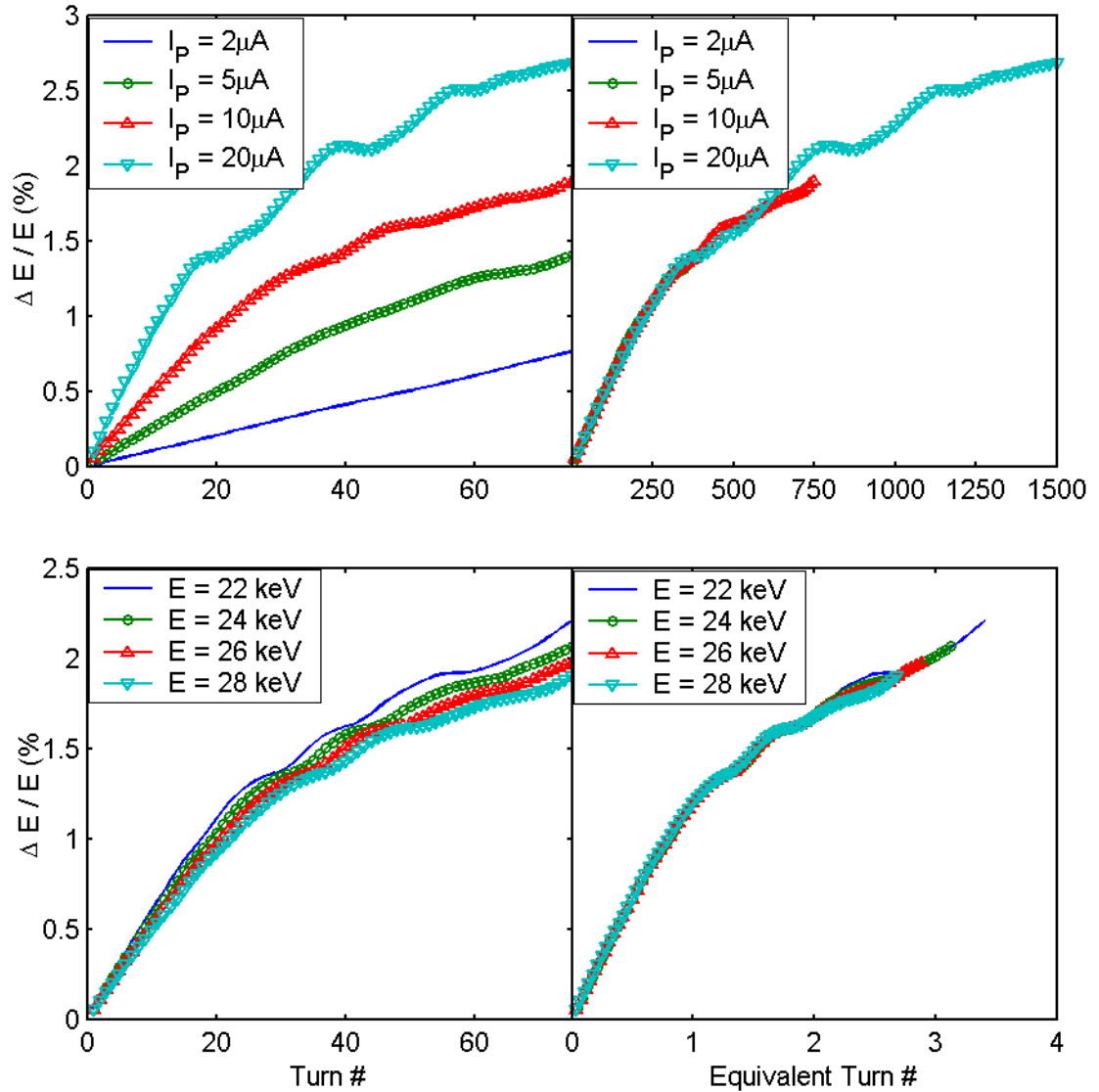
Figure 83: Energy spread induced by space charge forces as a function of the turn number for different beam energies (bottom of figure) and different beam currents (top of figure). The same data is displayed on the right as a function of the equivalent turn number. The rest of the parameters of the bunches are specified in Table 17.

9.11.   Beam radial size

As described in section 1.1, the longitudinal space charge electric field induces energy spread within the bunch. Ions in the head of the bunch gain energy as they are pushed by the rest, while those in the tail lose it.

155
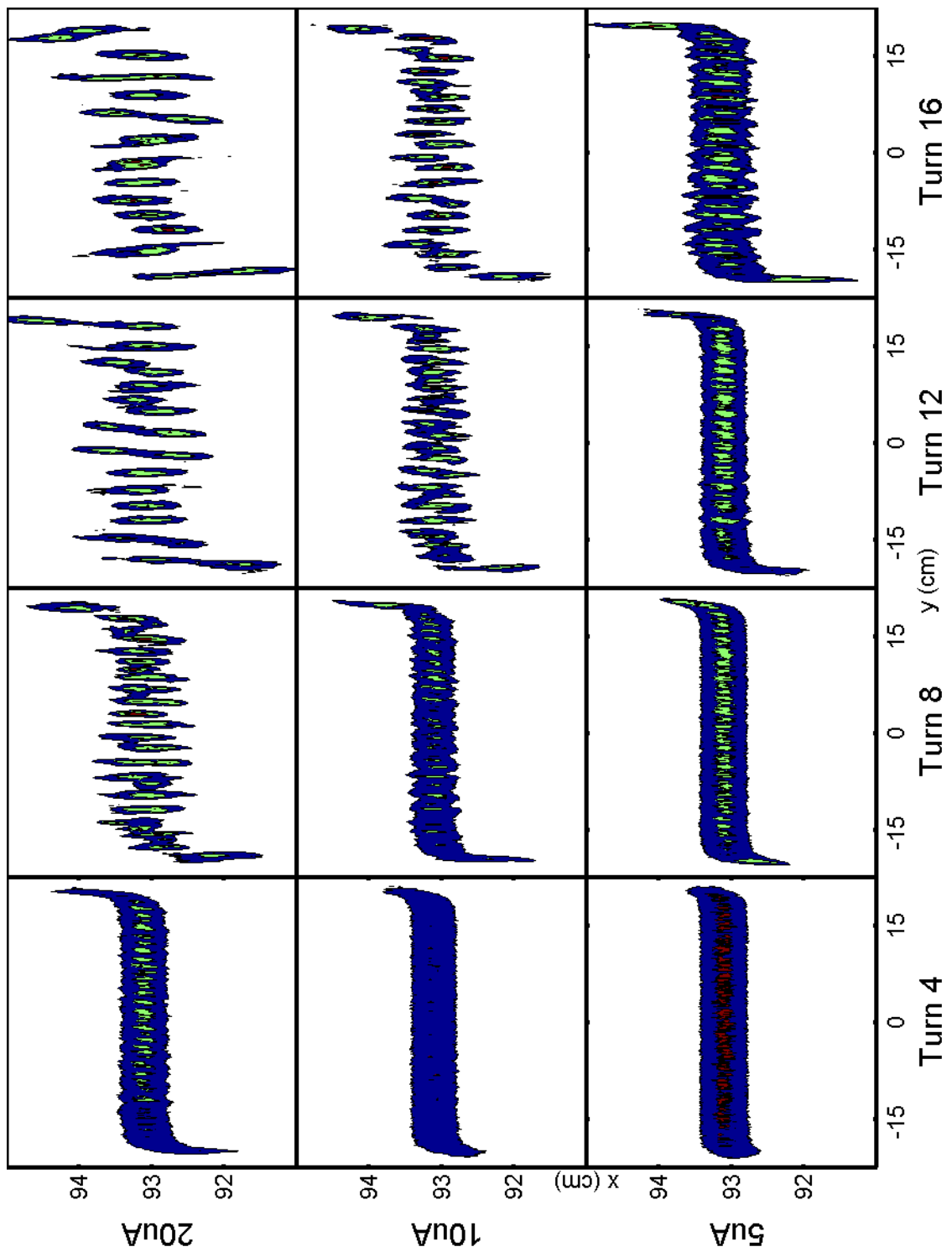
Figure 84: Top view of three bunches with characteristics listed in Table 9 after a variable number of turns. The energy spread induced by space charge forces can be observed in the tilting of the beam.

Since the ring is isochronous, the length of the bunch does not increase but the radial size of the bunch does. Ions in the head describe a trajectory with a larger radius maintaining the revolution frequency constant despite of their higher energy. In a similar way, the radial position of those in the tail is reduced.

This behavior is reproduced by the simulations. Figure 84 shows the top view of bunches with characteristics listed in Table 9 several turns after being injected. It can be observed that after four turns the head of the bunch has shifted toward a larger radius while the tail shifted toward a smaller radius. This effect is more accentuated when the beam current is higher.

9.12.   Asymptotic cluster density and merging rate

As discussed in previous sections, the number of clusters formed after the initial break up for ten different microscopic representations of bunches with the characteristics listed in Table 9. The average number of clusters is shown as circles in Figure 85. These data can be fitted to a curve (solid line) like:

$$N = N_\infty + \left(N_0 - N_\infty\right)\cdot\exp(-\frac{T}{\tau})$$

From which, the following values for N_∞, N_0 and τ can be calculated with a 95 % confidence level:

$$N_\infty = 7.52 \pm 3\% \qquad N_0 = 23.79 \pm 5\% \qquad \tau = 16.61 \pm 9\%$$

As discussed in previous sections, N_∞ does not depend either on the size of the vacuum chamber nor on the beam energy, current or emittance. It

was determined that it is proportional to the length of the bunch which allows

defining a final cluster density $n_\infty = \dfrac{N_\infty}{L_{BUNCH}}$ that will be independent of the

length of the bunch. Questions on the nature of n_∞ are opened. What defines its

value is not clear and needs to be studied.

In a similar way, the rate at which clusters merge (τ) is independent of the

beam energy, current or emittance when the number of turns is expressed as

equivalent turn numbers.
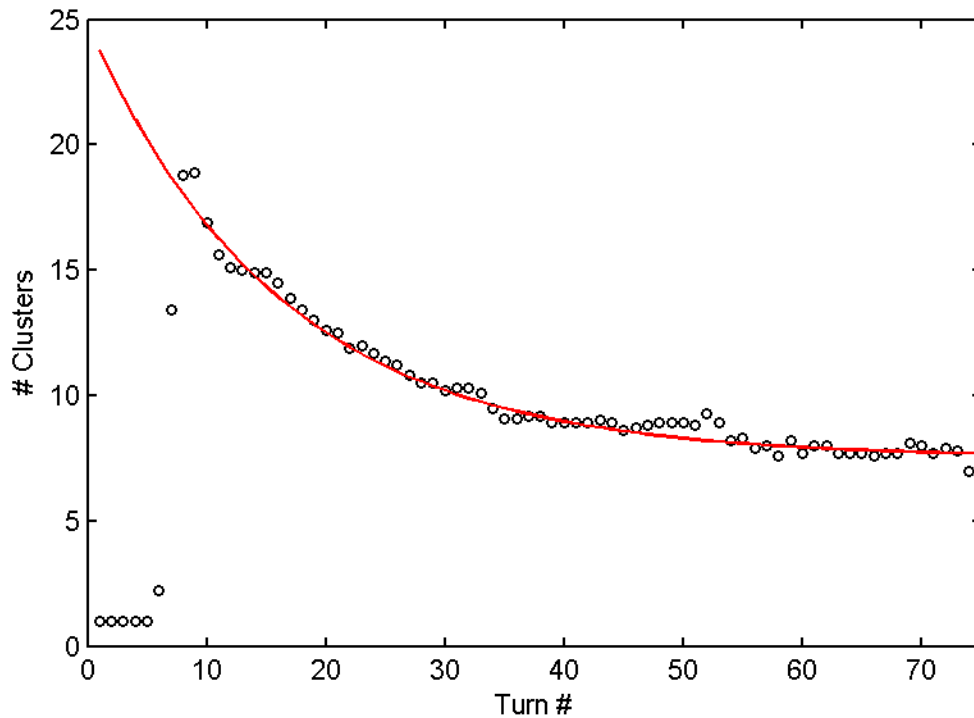
Figure 85: In black circles: number of clusters (averaged over ten initial representations) formed for a 20 µA peak current (rest of bunch characteristics are listed in Table 9). The data was fitted to an offset decaying exponential (solid red line).

9.13. Conclusion

Extensive simulations have been performed to evaluate the impact that different changes in beam parameters have on the bunch dynamics. The main results are summarized next:

- Some dispersion in the number of clusters counted (± 1.1) should be expected because of the slightly different dynamics due to the choice of microscopic representation of the bunch.

- The number of clusters after the break up occurs is proportional to the length of the bunch.

- Increasing the beam current accelerates the break up process of the bunch. Events that occur at turn number N when the beam current is I, will occur at turn $\dfrac{N}{k}$ when the current is $k \cdot I$.

- Increasing the beam energy decelerates the break up process of the bunch. Events that occur at turn number N when the beam energy is E and linear charge density is $\dfrac{Q}{L_{BUNCH}}$, will occur at turn $k \cdot N$ when the energy is $k \cdot E$ with the same linear charge density.

If what is kept constant is the beam current I, from the relationship

$$I = \frac{Q}{L_{BUNCH}} \cdot v = \frac{Q}{L_{BUNCH}} \cdot \sqrt{\frac{2 \cdot E}{m}}$$

where v is the velocity of the ions, events that take place at turn number N when the beam energy is E, will happen at turn $k \cdot N$ when the energy is $k \cdot E^{3/2}$.

Therefore, the results of the simulations confirm the validity of the scaling law discussed in 1.3 in the range of beam energies and currents studied.

- The effect of the vertical size of the vacuum chamber is very small if the size is larger than 4 cm.

- The emittance of the beam plays an important role in determining when the bunch break up occurs. It is not very important in defining the dynamics afterwards.

- The evolution of the bunch is highly sensitive to the initial conditions of the bunch. Very small perturbations in the initial conditions have a significant effect in dynamics of the bunch.

10. BEAM DYNAMICS EXPERIMENTS WITH SIR

10.1. Introduction

Bunches with different characteristics have been injected into the ring and their longitudinal profiles have been measured after a variable number of turns using the Faraday cup described in section 3.3.

In section 10.2, the repeatability of these measurements will be discussed. It will be shown that the details of the longitudinal profiles of bunches with similar characteristics (energy, peak current and emittance) are not identical when they are extracted after the same number of turns. It is believed that these differences are due to the impact that small perturbations of the initial conditions have on the bunch evolution. It will also be shown that more general characteristics (such as when the bunch break up occurs, the number of clusters formed at that point or the rate at which they merge afterwards) have less variation. We will use those general characteristics to study differences in dynamics due to changes of the bunch length (section 10.4) and current (10.5). The number of longitudinal profiles needed to determine the value of those general characteristics with a high confidence level will be discussed in section 10.3.

The correlation between energy of the ions and their radial position will be briefly mentioned in section 10.6. The chapter will close with a direct comparison between simulations and experiments of the evolution of the number of clusters with turn number for four different bunch currents.

10.2. Repeatability of the experimental measurements

As shown in sections 8.5 and 9.2, the choice of the microscopic representation of a bunch has a significant impact on its computed dynamics. It was also shown that the effect of changes in more fundamental beam parameters, such as its peak current or energy, is larger than that due to the choice of microscopic representation.

The same sensitivity to initial conditions is also observed experimentally. Three longitudinal beam profiles, measured after the bunch was stored for 29 ½ turns, are shown on the left of Figure 86. The profiles on the right were measured after 98 ½ turns. The characteristics of the bunch are listed in Table 18. It can be observed that, although the details of the profiles differ from measurement to measurement for bunches with the same extraction turn number, these differences are small compared to those when extraction turn number changes. In particular, the number of clusters is significantly different.

The method used to count the number of peaks is identical to that described in section 8.3 for the results of the simulations. In this example and in the rest of the experimental results discussed in this chapter, the value chosen for the parameter k is 0.5 and 5 mm for W_{min}.

The dashed blue line shown in Figure 86 represents the value of the current at which the number of clusters is evaluated. In this case, $I_K = k \cdot I_{PEAK} = 0.5 \cdot 14\ \mu A = 7\ \mu A$. The red solid line represents the clusters that are counted.

Note that one of the clusters in the lowest right profile does not qualify since it is not wide (i.e. long) enough.
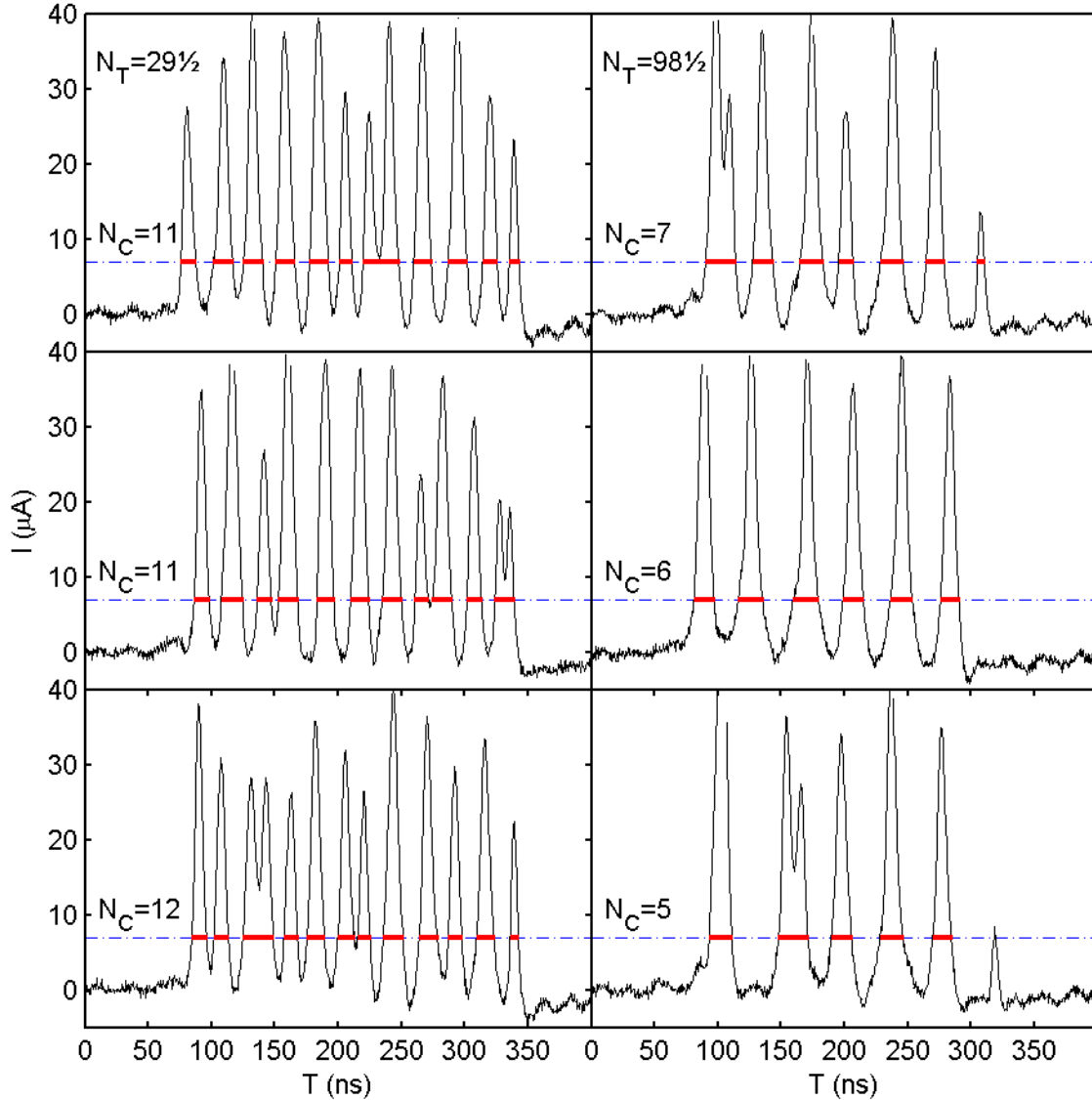
Figure 86: Longitudinal bunch profiles measured with the sector Faraday cup after the bunch was stored for 29 ½ turns (on the left) and 98 ½ (on the right). The characteristics of the bunches, when they were injected, are listed in Table 18. The number of clusters counted (N_C) is shown next to the corresponding profile.

The number of clusters counted (N_C) is not the same for all the profiles measured at a given extraction turn number. There is some dispersion in their

values. Note that a similar dispersion was also observed in the results of the simulations when the microscopic representation of the bunch was changed (Figure 66). In any case, it is clear that the average number of clusters in turn number 29 ½ and 98 ½ are different.

In a similar way, it will be shown, in the rest of the chapter, that the average number of clusters formed at a given turn number is different when the bunch length or peak current are changed.

Beam Parameters	Value	Beam Parameters	Value
Ion	H_2^+	Length	300 ns
Energy	20.8 keV	Emittance	~ 30 π mm mrad
Current	14 µA		

Table 18: Main parameters of the bunches used in the discussion on repeatability of measurements.

10.3. Justification of the number of profiles measured

In order to determine the number of profiles needed to calculate the average number of clusters with a high confidence level, the profiles of 250 bunches were measured 55 ½ turns after injection. (The main characteristics of the injected bunches are listed in Table 19.) The number of clusters in each profile were counted (N_C). The results are shown on the left of Figure 87. It can be observed that the number of clusters ranged between five and twelve.

The average number of clusters (N_C^{AV}) and its standard deviation (N_C^{STD}) as a function of the number of profiles included to calculate them are shown on the figure on the right.

Beam Parameters	Value	Beam Parameters	Value
Ion	H_2^+	Length	300 ns
Energy	20 keV	Emittance	~ 30 π mm mrad
Current	10 μA	Number Turns	55

Table 19: Main parameters of the bunches used in the discussion on the justification of the number of longitudinal profiles measured.
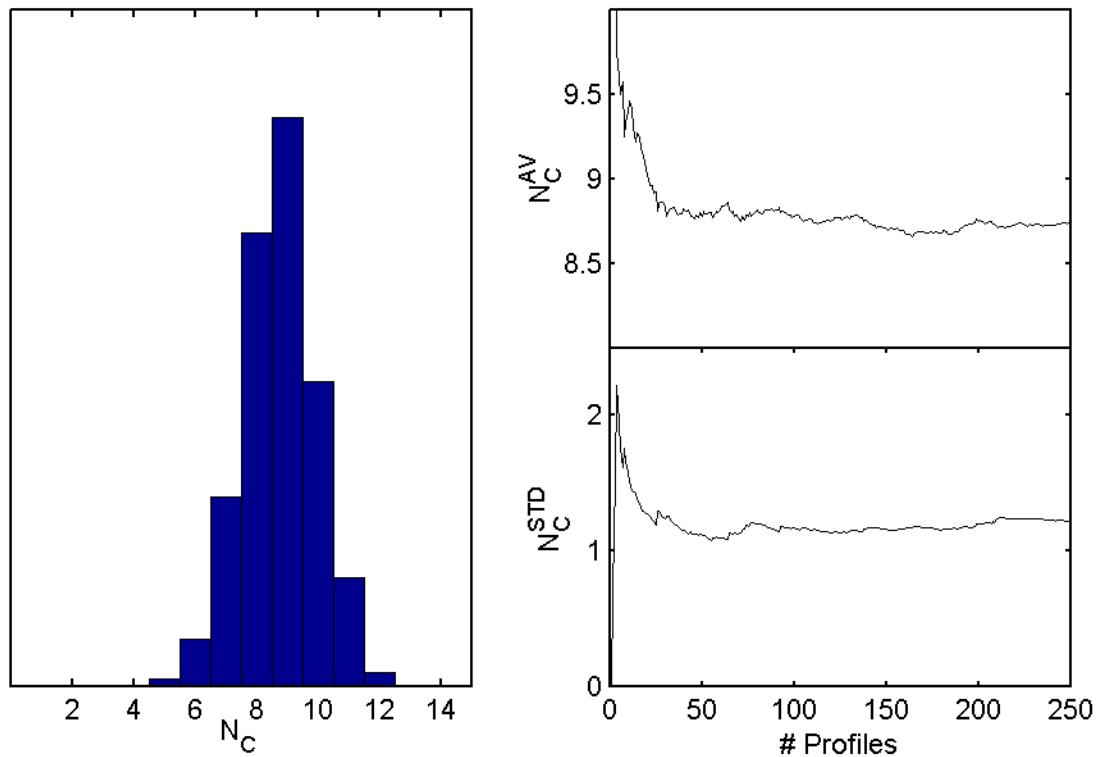
Figure 87: Dispersion in the number of clusters counted (N_C) when a bunch with the characteristics listed in Table 19 was extracted after 55 turns (on the left). Convergence in the average (N_C^{AV}) and standard deviation (N_C^{STD}) of the number of clusters counted as the number of profiles included is increased (on the right).

Based on this information, it was decided to use 100 profiles to determine the average number of clusters and its standard deviation. The experiment showed that no significant changes are seen measuring beyond that number of profiles.

In the rest of this chapter, we will refer to the average number of clusters obtained from the 100 measured profiles simply as "number of clusters". In some occasions, the number of clusters will be represented as a colored region limited by the average number of clusters ± one standard deviation. See, for example Figure 88.

10.4. Scaling with bunch length

Several scaling laws were discussed in chapter 9. In particular, it was determined that, according to the simulations, the number of clusters formed when the bunch first breaks up and during its evolution afterwards is proportional to its length.

In order to verify this scaling law experimentally, bunches with lengths ranging from 150 ns to 600 ns and characteristics listed in Table 20 were injected in the ring and their longitudinal profiles were measured. The number of clusters counted for every extraction turn number and bunch length are shown in the top of Figure 88. The corresponding densities of clusters are shown in the bottom of the figure.

It can be observed that the scaling law works very well especially for the longer bunches. The turn number at which the break up occurs and the rate at which the clusters merge afterwards do not depend on their original length.
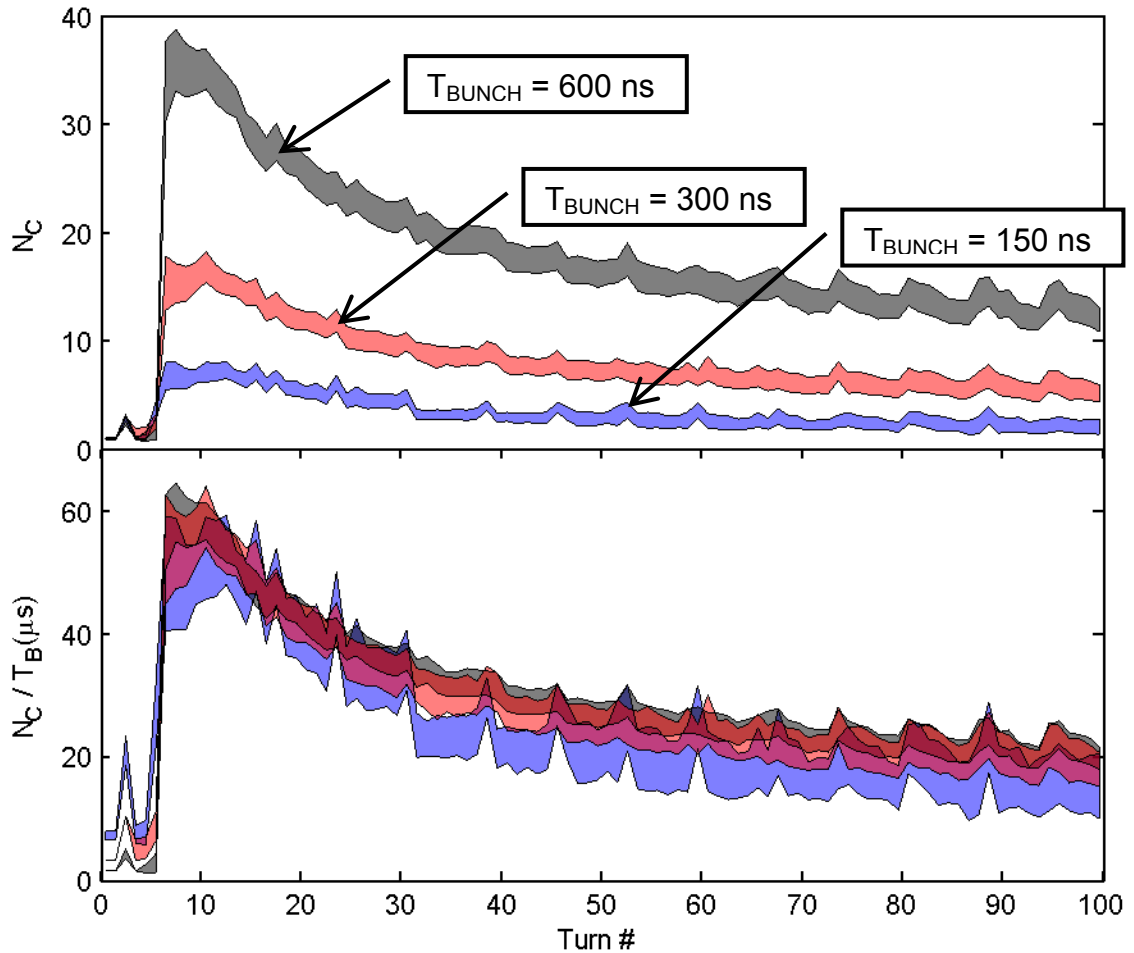
Figure 88: Experimental verification of the scaling law with the bunch length. The number of clusters counted for bunches with characteristics listed in Table 20 scales with the length of the bunches as it can be seen in the bottom of the figure where the density of clusters is plotted.

Note that the beam was not perfectly matched to the close orbit solution of the ring when it was injected as it can be inferred from the small oscillations in the average number of clusters. The frequency of these oscillations is the same as the betatron frequency.

Beam Parameters	Value	Beam Parameters	Value
Ion	H_2^+	Length	150, 300 & 600 ns
Energy	20.8 keV	Emittance	~ 30 π mm mrad
Current	19.9 µA	Number Turns	100

Table 20: Main parameters of the bunches used in the discussion of scalability with length of the number of clusters formed after the initial bunch break up and during its evolution afterwards.

10.5. Scaling with bunch current

In order to verify the scaling law described in section 9.4 experimentally, bunches with different peak currents (5.0, 9.9 and 19.9 µA) were injected into the ring and the evolution of their longitudinal profiles was measured. The rest of the characteristics of the bunches are listed in Table 21.

The evolutions of the number of clusters with turn number for the three different peak currents are shown in the top of Figure 89. The evolutions as a function of the equivalent turn number (defined in section 9.4: $T_{EQ} \equiv T \cdot I(\mu A)$) are shown in the bottom figure.

The experimental results clearly corroborate the validity of the scaling of space charge effects with peak current that was discussed in section 1.3 and that had already been verified by the simulations in the previous chapter.

These experiments were repeated for bunches of different energies (24.92 and 16.75 keV) obtaining similar results.
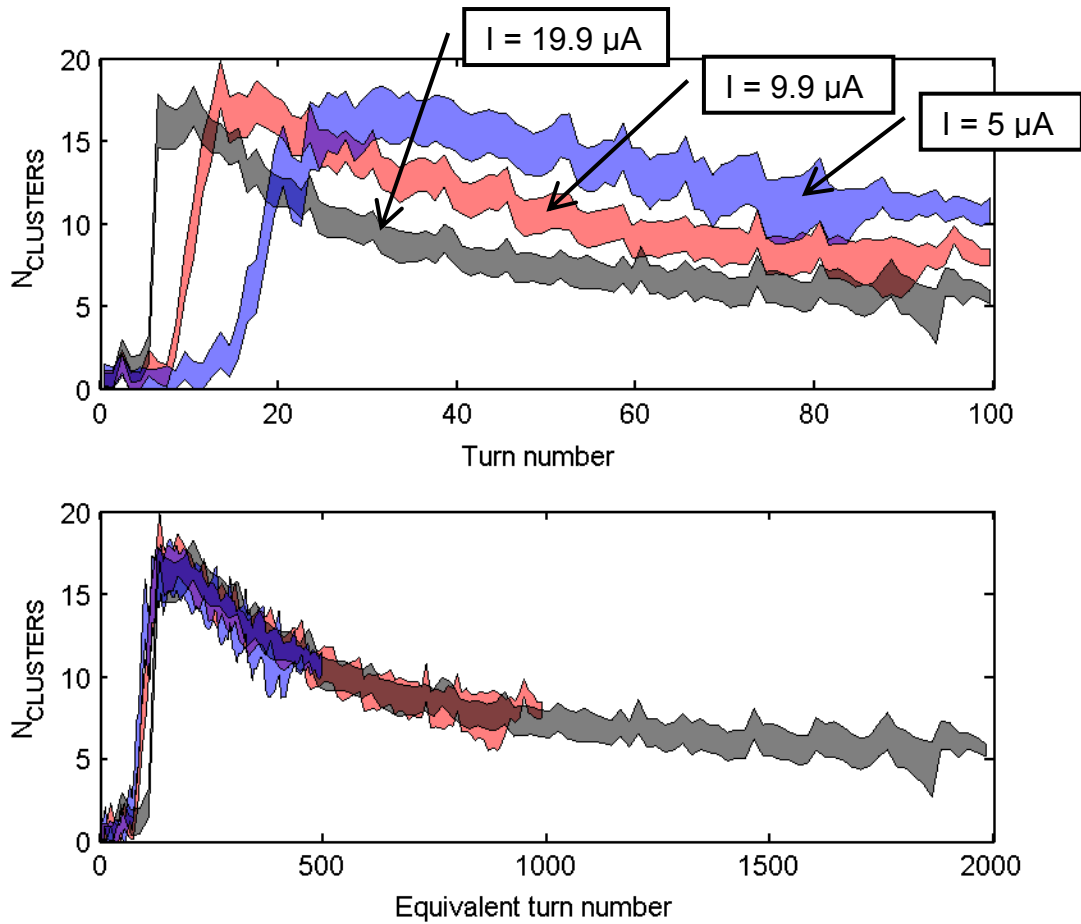
Figure 89: Experimental verification of the scaling law with the bunch current. The number of clusters counted for bunches with characteristics listed in Table 21 scales with the peak current of the bunches as it can be seen in the bottom of the figure where the number of clusters is plotted as a function of the equivalent turn number.

Beam Parameters	Value	Beam Parameters	Value
Ion	H_2^+	Length	300 ns
Energy	20.8 keV	Emittance	~ 30 π mm mrad
Current	5.0, 9.9 & 19.9 µA		

Table 21: Main parameters of the bunches used in the discussion of scalability of space charge effects with peak current.

10.6. Correlation between energy and radial position of the clusters

When the sector Faraday cup is used to measure the longitudinal profiles, the beam is typically divided among sectors. As it can be seen in Figure 90, the beam hits the two central current collectors when it is extracted after half a turn. About two thirds of it hit the outer radius one versus one third hitting the inner radius one.
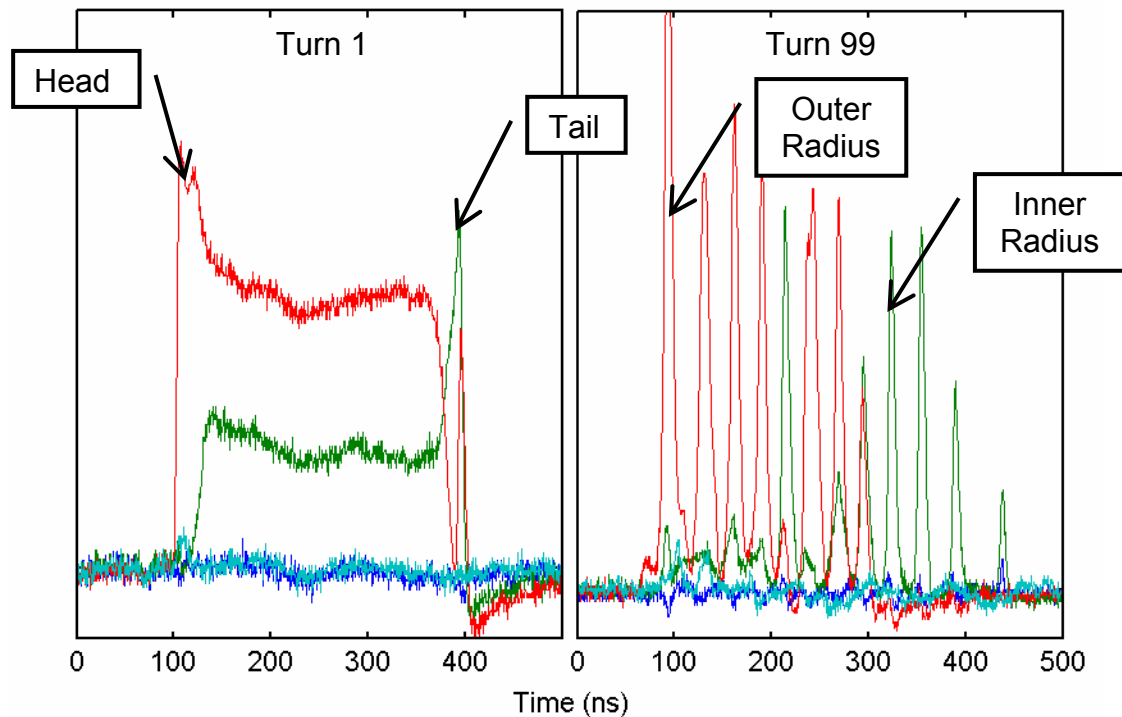
Figure 90: Correlation between energy of the ions and radial position. When the bunch is extracted after ½ a revolution, it hits part of the two central electrodes of sector Faraday cup (green and red). After 99 ½ revolutions, those clusters in the head of the bunch hit the outer radius central electrode while those in the tail hit the inner radius electrode.

As previously described, the head of the bunch gains energy while the tail loses it due to longitudinal space charge forces. Since the ring is isochronous,

ions in the head will describe a circumference with a larger radius than those in the tail. This effect can be observed in the longitudinal profile after 99 ½ turns. Clusters in the head of the bunch hit the outer radius collector while those in the tail hit the inner radius one.

10.7. Direct comparison of the results of the experiments and the simulations.

Up to this point, we have discussed the experimental verification of some scaling laws that had already been studied in the simulations performed in chapter 9. At the beginning of this chapter, it was shown that due to the high sensitivity of the break up process to the initial conditions direct comparison of the longitudinal profiles was not possible. Although, it was still possible to study the evolution of the average number of clusters.

At this point, we would like to compare directly the results of these measurements with some of the simulations in the previous chapter. In particular, we will compare the simulations performed with bunches with characteristics listed in Table 9 with the measurements of bunches with the characteristics listed in Table 21.

Simulations are shown in grey in Figure 91 while experiments are shown in red. It can be observed that the agreement is remarkably good. The simulations describe when the break up of the bunch occurs as well as the merging rate of the clusters for the three higher peak currents.
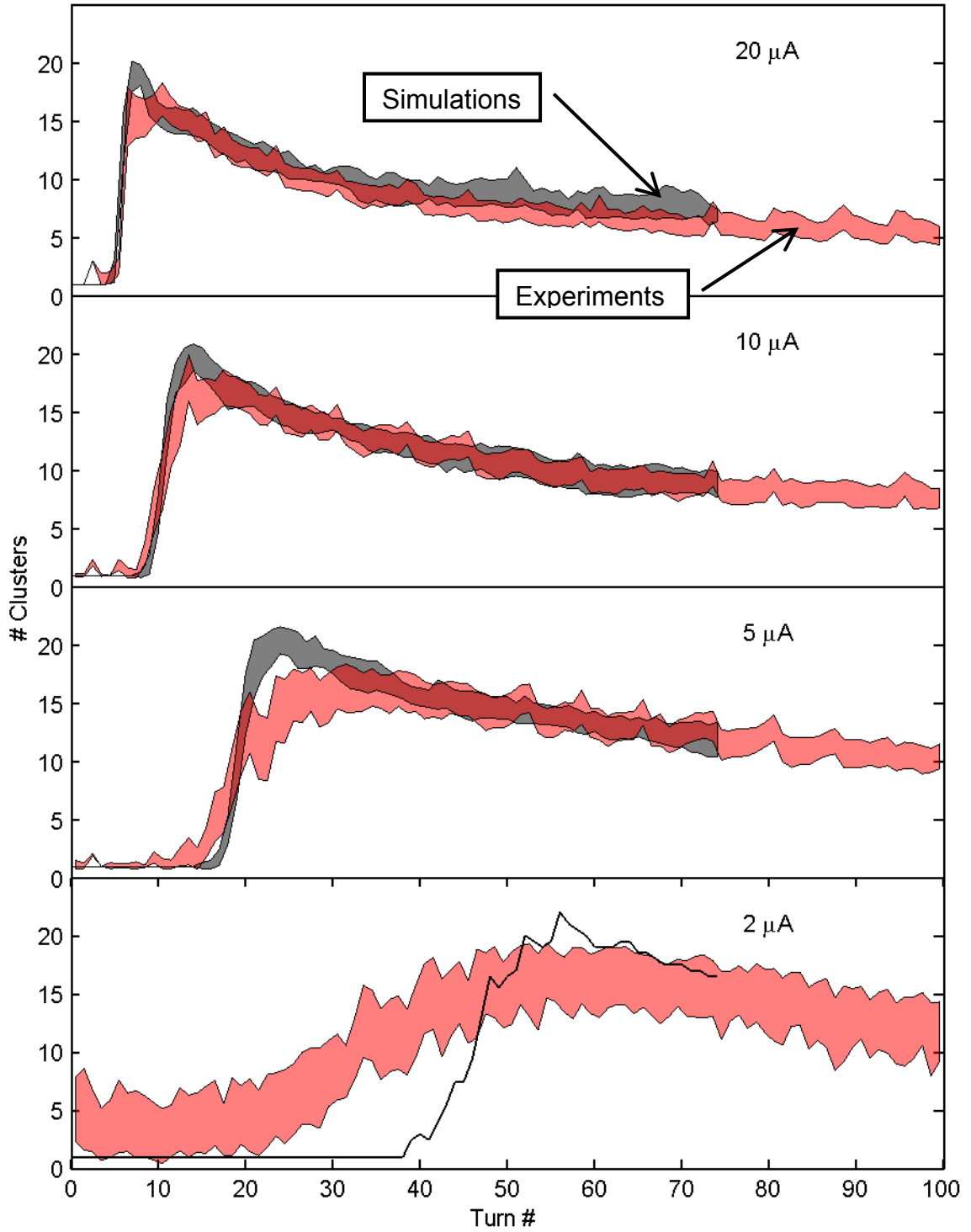
Figure 91: Comparison in the evolution of the average number of clusters between simulations (characteristics of the bunches listed in Table 9) and experiments (characteristics listed in Table 21).

172

The 2 μA case is not very interesting. The noise to signal ratio in the measurements for such low currents is very high. In some cases, this noise is misread as clusters. This explains why the standard deviation is much larger than in other cases as well as why the average number of clusters counted is larger than one before the break up occurs.

Just two different microscopic representations of the bunch were used in the simulations in this case. For this reason, only the evolution of average number of clusters is shown. The standard deviation is not significant.

11. CONCLUSION

Partial conclusions were included at the end of several chapters of this dissertation. We will summarize here the most important ones:

The Small Isochronous Ring (SIR) has been completed and it is working well. In particular, all the requirements of the injection and extraction lines described in this dissertation have been achieved.

The control and data acquisition systems of SIR have been finalized.

Extensive simulations have been performed using CYCO to study the longitudinal beam dynamics in the ring. The impact of beam emittance, peak current and energy have been studied and the scaling law described in section 1.3 has been numerically validated.

The evolution of the longitudinal profiles of bunches with different characteristics have been measured. Although the details of these profiles are not repeatable and therefore not exactly described by the simulations, general features such as when the break up occurs, into how many clusters it breaks and how fast the clusters merge afterwards are accurately described by the simulations.

The simulations have also shown that the beam variability observed experimentally is compatible with the small perturbations of the initial conditions likely to happen when the beam is extracted from the ion source.

The good agreement between simulations and experiments give us confidence that CYCO can be used to describe the longitudinal beam dynamics in other isochronous machines where space charge forces are strong.

Some questions remain open and more research will be necessary to answer them in the future. Especially intriguing is the nature of the final cluster density (n_∞) or the rate at which clusters merge (τ) that were briefly mentioned in section 9.12. It would also be very interesting to find a simple explanation to justify why the bunch as a whole is not as stable as the cluster distribution into which it evolves.

APPENDIX A: OPERATING PROCEDURES FOR SIR

The Small Isochronous Ring (SIR) has a variety of subsystems that must be operated in a safe manner both for machine protection and personal safety. Different procedures have been developed to perform some of the most common tasks on the machine and included in this appendix to be used as a reference by future users. There is not a unique way to operate the machine. Some of the steps may be performed in different order and some of them can be skipped in certain conditions. Although, it is not recommended until full familiarity with the machine has been achieved.

It is worth mentioning here that:

The sections that have been biased to high voltage must be grounded with the grounding rod immediately after the ion source cage is unlocked.

There is not exception to this rule.

A.1. – Procedure to turn on SIR

COOLING OF THE MACHINE (See Figure 92)

- Open the main low conductivity water (LCW) return valve. The pressure reading should be around 30 psi.

- Open the main LCW supply valve. The pressure reading should be around 135 psi. A differential of pressure between the supply and the return line of around 100 psi is necessary to guarantee that the flow of water in the

system is sufficient to dissipate the heat fast enough to avoid a temperature rise that could damage different components of the machine.

- Open the secondary LCW supply valves for the ion source, injection line magnet, emittance measurement system and magnets in the ring.

- Open the secondary LCW return valves for the ion source, injection line magnet, emittance measurement system and magnets in the ring.

Note: Opening the return valves before opening the supply valves guarantees that the pressure in the water circuits is not too high thus preventing leaks.
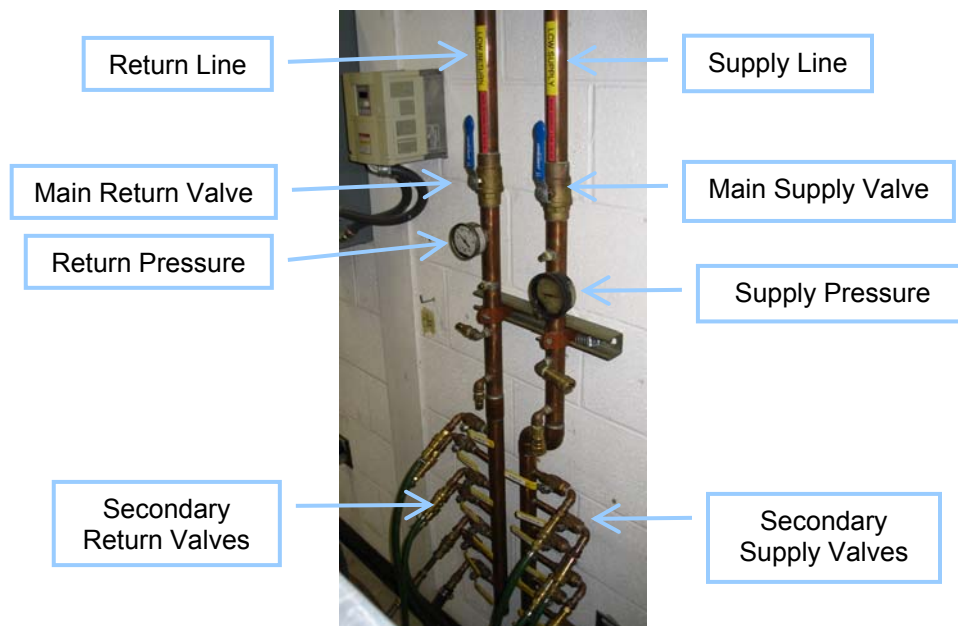
Figure 92: Picture of the low conductivity water manifold used to cool down the ion source, the emittance measurement system and the dipole coils.

HIGH VOLTAGE PROTECTION

- Verify Einzel lens power supply is off. (Figure 96)

- Verify extraction power supply is off.

- Verify high voltage monitor reads zero kV and high voltage light is off.

- Unlock and open the door of the high voltage cage. (Figure 93)

- **Ground high voltage parts with grounding rod.**

Note: Even though all the high voltage parts of the system are grounded automatically when the door is unlocked, they must be manually grounded to guarantee personal safety if automatic system fails.

Note: The ion source hardware and its power supplies must be grounded with the grounding rod independently. A short in the cable connecting them could leave one of them floating at high voltage.
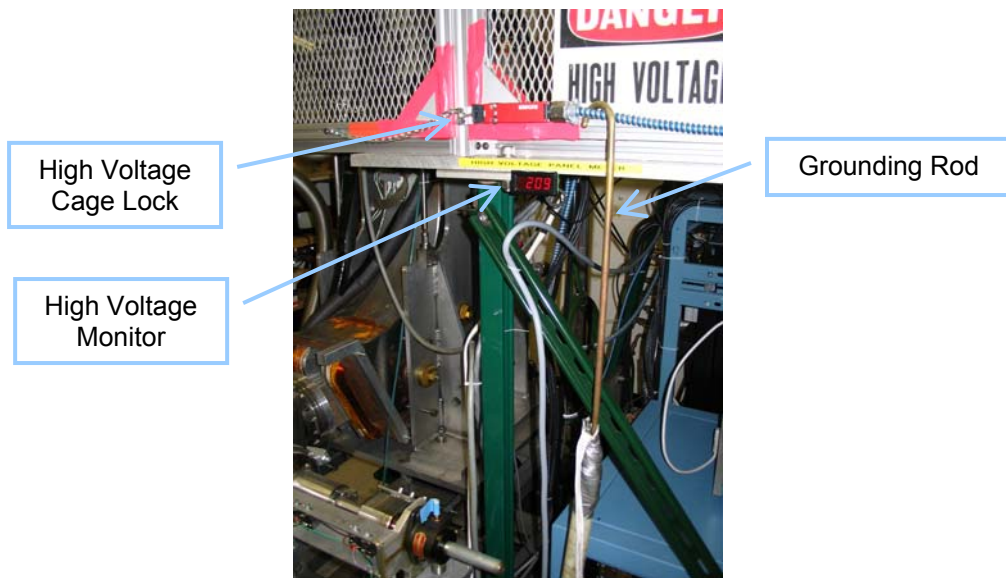
Figure 93: Picture of the high voltage monitor, grounding rod and lock of the ion source high voltage cage.

FEEDING GAS TO THE ION SOURCE

- If the source has not been used in several weeks or if the injection line has been vented since last time the source was used, refer to the procedure to clean the hydrogen line.

- Close the needle valve in the cage using isolation rod. A needle valve is used to control the flow of hydrogen into the ion source. This flow and the conductances of the different portions of the vacuum chamber determine the pressure distribution in the whole machine. (Figure 94)

- Open the right angle valve in the cage. A right angle valve is used to guarantee that there is not continuous flow of hydrogen into the source when the machine is not being operated. The needle valve by itself does not work as an open/close valve.
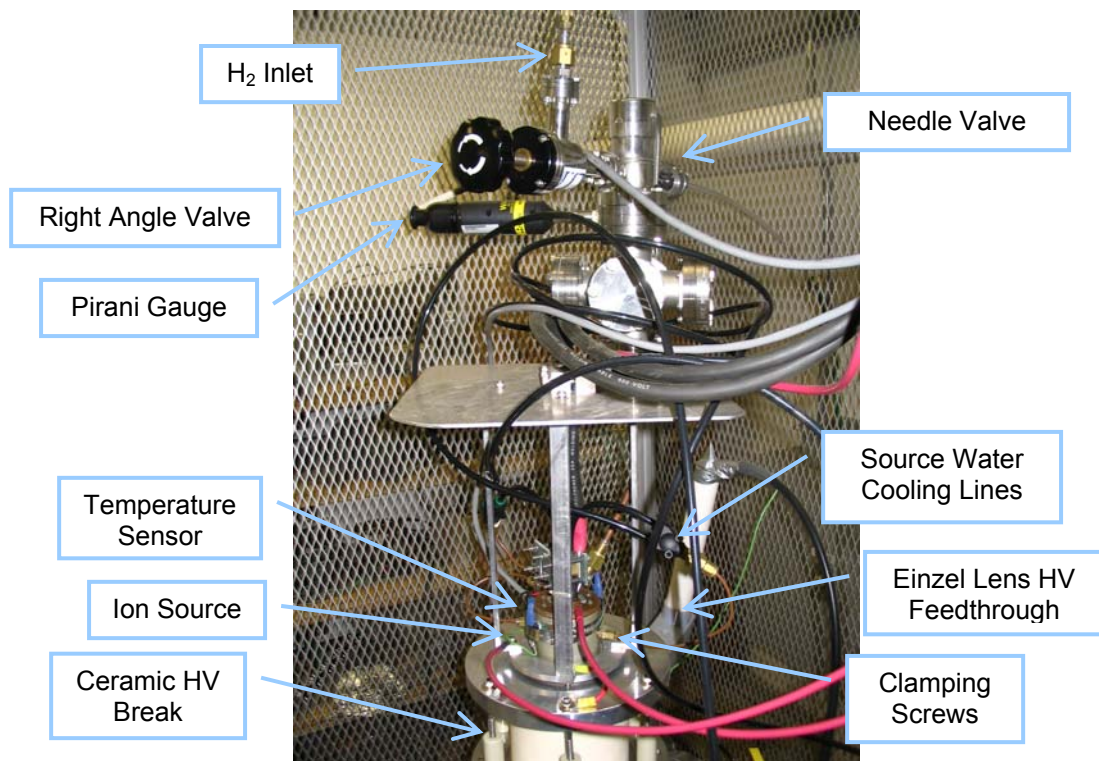
Figure 94: Picture of the ion Source and its associated gas handling system.

- Open the valve in the hydrogen tank. (Figure 95)

- Verify gas pressure after regulator is around 20 psi. A regulator is used to reduce the pressure from the gas tank to a pressure a little bit higher than

atmospheric. No air will penetrate in the line if a leak develops thus preventing contamination of the hydrogen.
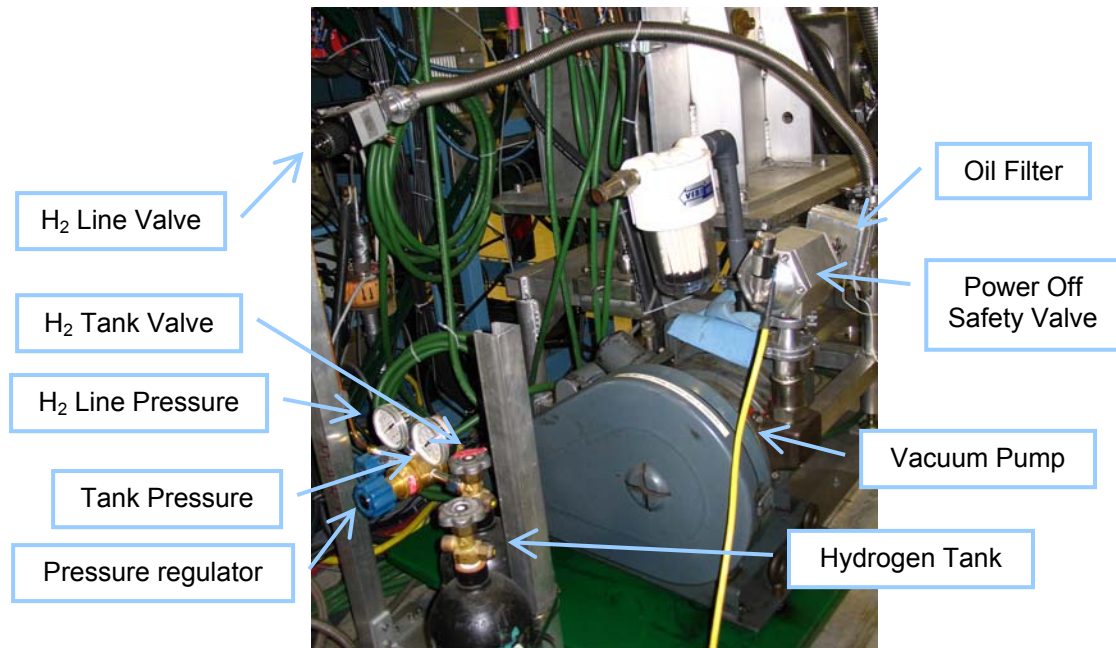
Figure 95: Picture of the hydrogen tank and regulator.

TURNING ON THE ELECTRONICS

- Turn on digital multimeter in the cage. A digital multimeter is used to measure the arc current. The analog dial of the power supply is not accurate enough. (Figure 96)

- Verify that the distance between high voltage elements and ground elements in the high voltage cage is at least 8 to 10 cm to prevent sparks.

- Close and lock the door of the high voltage cage. (Figure 93)

- Set the current of the filament power supply to zero. If the machine is turned on with a non-zero filament current, the thermal shock in the filament may break it. The filament current has to be ramped up slowly.

- Set voltage in the Einzel lens and extraction power supply to zero. If the machine is turned on with the high voltage on, sparks may be produced and the polished surfaces of the puller or Einzel lens may be damaged. The extraction voltage and the voltage of the Einzel lens have to be ramped up slowly.
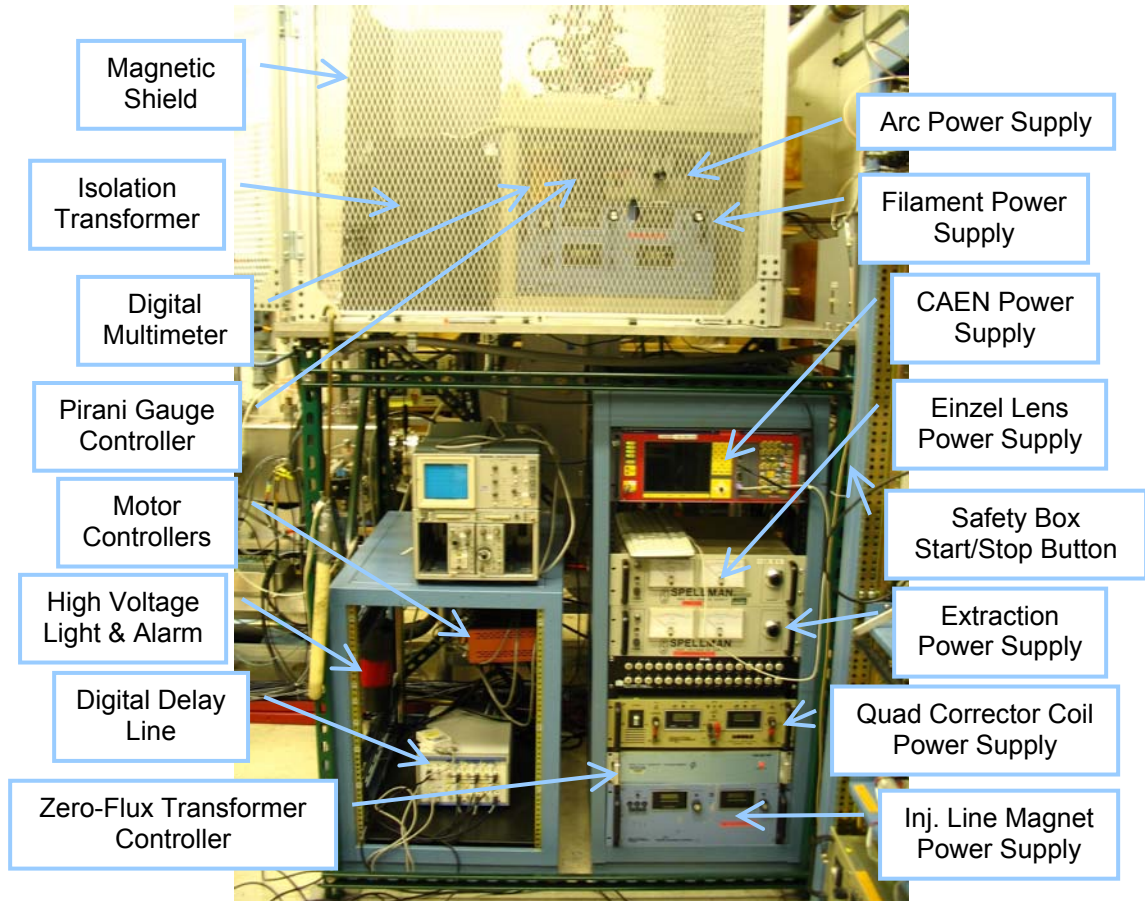
Figure 96: Picture of the ion source and injection line associated electronics.

- Turn on injection line magnet and ring magnets power supplies.

- Start program to control the magnet power supplies. Execute 'Computer 1' > 'Drive C' > 'Folder SIR' > 'Folder Applications' > 'PowerSupplies Controls'. (Figure 43).

Power Supplies Control
Scanning Slits
Scanning Wires
Emittance Measurement
Oscilloscope Data Acq.
Beam Lifetime Meas.

CAEN PS Control
Video Capture
Delay Line Control

CPU 3

Video Switch

CPU 1:
Data Acquisition Card
Motor Controller Card
GPIB Card

CPU 2:
Video Capture Card
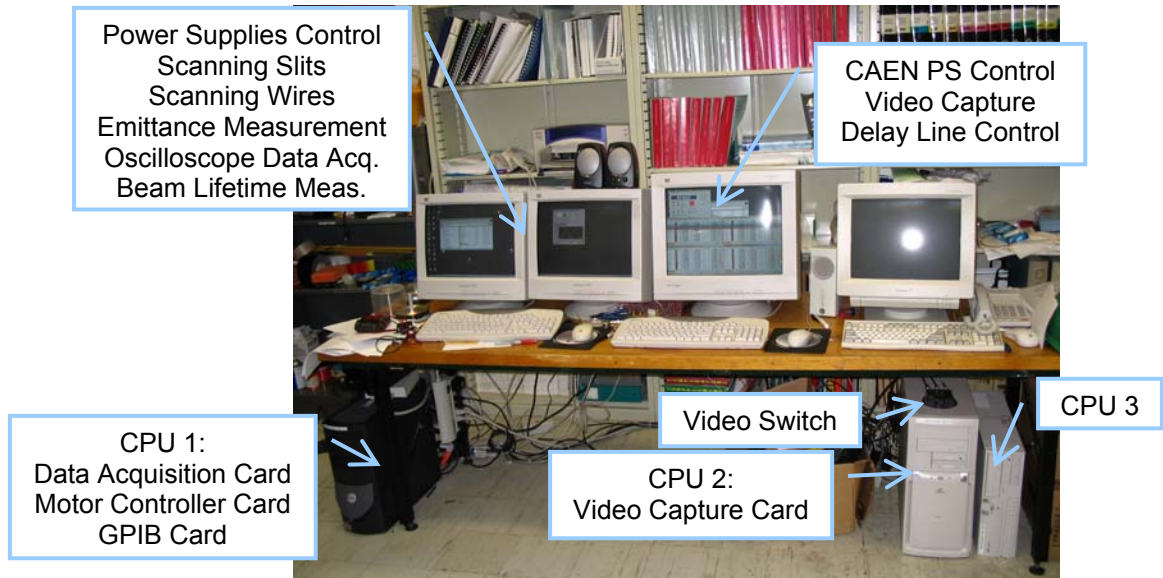
Figure 97: Picture of the PCs used for data acquisition and control of SIR.

- Retract emittance measurement system slits. Execute 'Computer 1' > 'Drive C' > 'Folder SIR' > 'Folder Applications' > 'ScanningSlits' after verifying that the motor drive (Figure 98) is connected to control them. This program will automatically retract the slits every time it is restarted.

- Turn on the CAEN power supply.

- Start program to control the CAEN power supplies (quads, inflector, deflector, chopper, steering…). Execute 'Computer 2' > 'Drive C' > 'Folder SIR' > 'Folder Applications' > 'HVPS Controller'. (Figure 99)

- Verify that all the elements inside the vacuum chamber are grounded or connected to the corresponding instrumentation. If any of these elements are left floating and the beam hits it, it will charge up and spark.

- Start program to monitor phosphor screens. Execute 'Computer 2' > 'Drive C' > 'Folder SIR' > 'Folder Applications' > 'VMonitor'. (Figure 99).

182
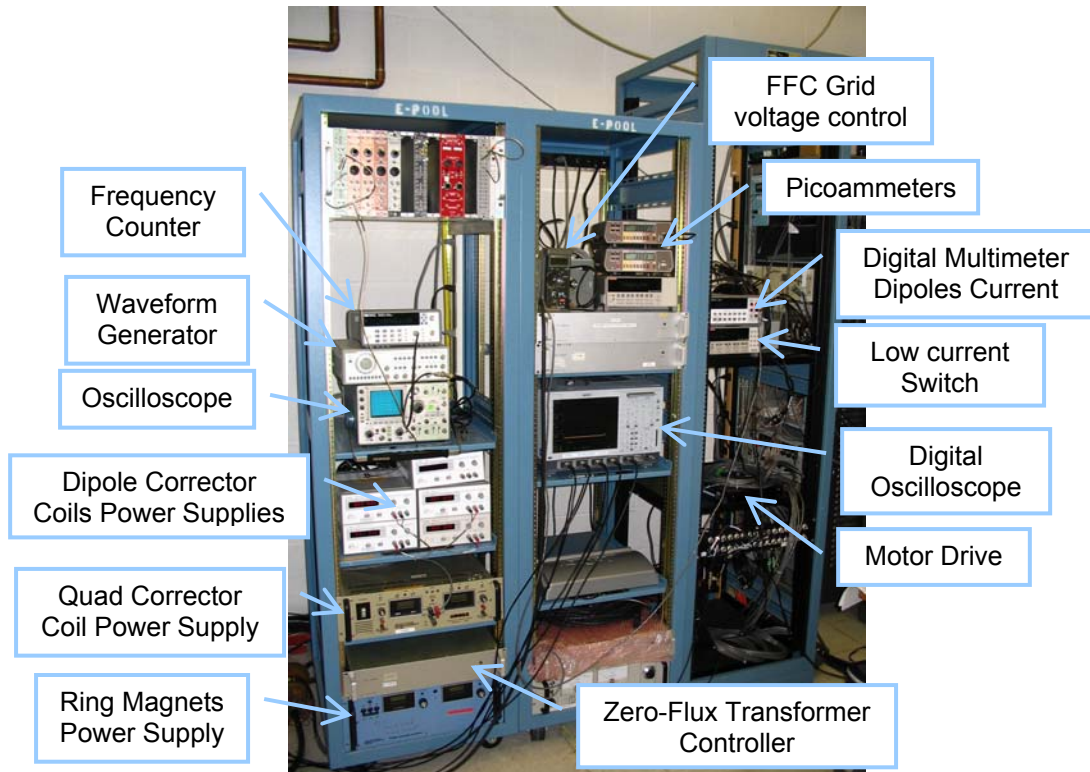
Figure 98: Picture of the ring and extraction line associated electronics.

Figure 99: User interface of the video capture and high voltage power supply control programs.

- Select video channel corresponding to the injection point CCD camera. (Figure 97)

- Retract the phosphor screen at the injection point (Figure 100). The beam power dissipated in the phosphor screen should be as low as possible in order to maximize the lifetime of the phosphor. This can be achieved by lowering the duty cycle of the chopper if it is important not to change the transverse beam properties.
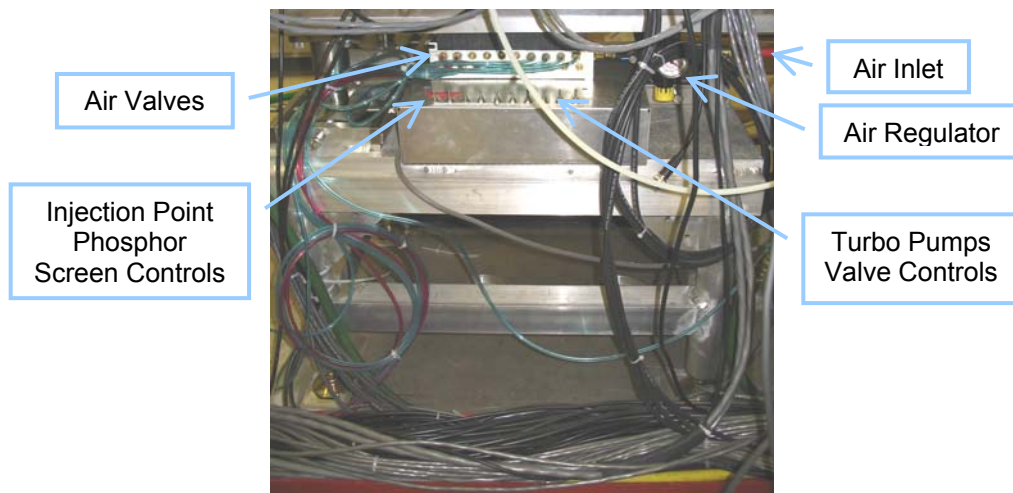
Figure 100: Picture of the compressed air control system. The two furthest left switches are used to position the injection point phosphor screen. The four furthest right switches open or close the valves in between turbo pumps and mechanical pumps.

- Retract scanning wires in the ring (Figure 34). Execute 'Computer 1' > 'Drive C' > 'Folder SIR' > 'Folder Applications' > 'ScanningWires' after verifying that the motor drive (Figure 98) is connected to control them. This program will automatically retract the wires every time it is restarted.

- Turn on and enable the six fast high voltage switches (Figure 101). They were placed next to their load to minimize the raising time since most of the capacitance of the load is due to the length of the coaxial cables. (The

184

rise time of the generated pulses is longer when the capacitance of the load is larger.)

High Voltage Switches:
Positive Chopper
Negative Chopper

Injection Point
CCD Camera

Compressed
Air Controller

High Voltage Switches:
Positive Inflector
Negative Inflector
Positive Deflector
Negative Deflector
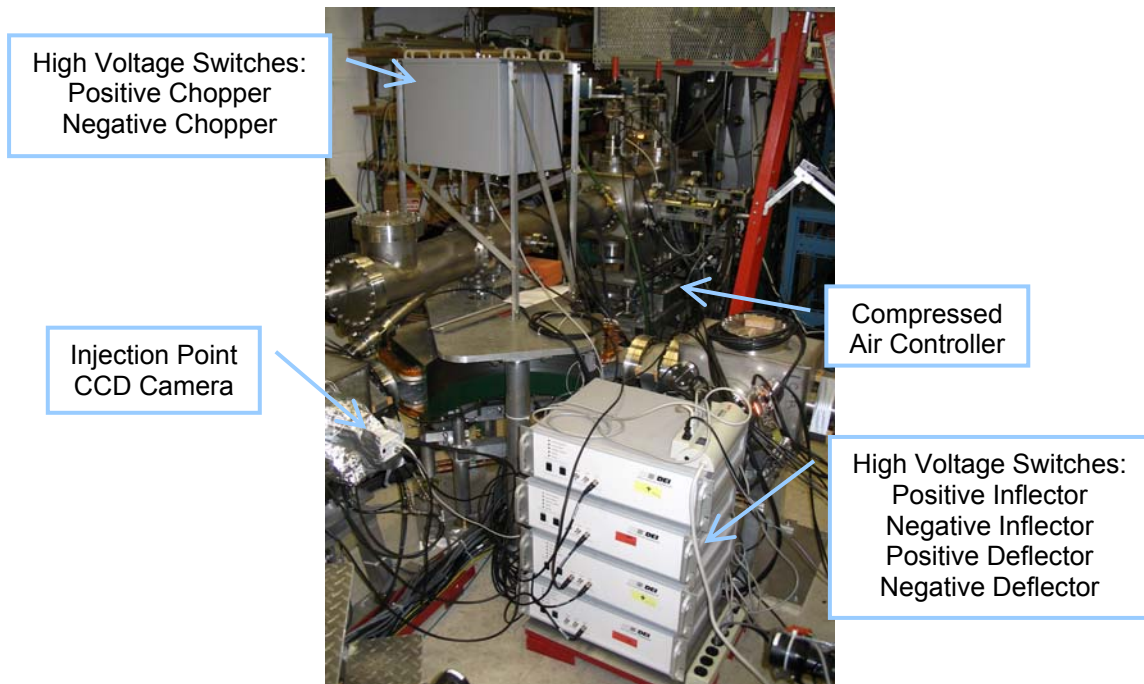
Figure 101: Picture of the fast high voltage switches used to pulse the chopper, second pair of inflector plates and deflector plates.

- Push the START button located underneath the safety electric box in between Ion source cage and LCW manifold wall. (Figure 96)

- Verify the sound alarm is on. The purpose of the alarm is to warn the user if the high voltage is still on when the cage is opened. This event should only happen if the high voltage relay, used to ground the whole system automatically, fails. The alarm will also sound every time the system is turned on and the high voltage is set below a hundred volts. The purpose of the alarm in this mode is to let the user know that the alarm is working. If the alarm does not sound, the machine should be turned off and the electronics department should be contacted.

- Turn on the extraction power supply. (Figure 96)

- Turn the extraction voltage up to ~ 1 kV.

- Verify the sound alarm went off. If this is not the case, the safety system is not working properly. The machine should be turned off and the electronics department should be contacted.

- Turn on the Einzel lens power supply.

- Use program 'PowerSuppliesControls' in PC 1 to cycle the magnets in injection line and ring. Three cycles (0 to 130 A and back to 0 in 10 A steps) are typically performed before the current is again ramped in 10 A steps to the working current for the desired ion mass and beam energy. (Figure 43). Even with the maximum current (130 A), the steel in the magnets is far from saturation. Refer to page 172 in reference [3] for the measured hysteresis curve of one of the magnets.

- Start program to control the digital delay line that triggers the high voltage switches that drive the chopper, inflector and deflector. Execute 'Computer 2' > 'Drive C' > 'Folder SIR' > 'Folder Applications' > 'Delay'.

Ion	H_2^+
Energy	20.9 keV
Beam Current	20 μA
Bunch length	300 ns
Repetition Rate	1 kHz

Table 22: Beam parameters when the machine is adjusted to the values listed in Table 23.

- Adjust different devices to the desired working values. An example of those working values that can be used as a starting point are specified in Table 23. They correspond to a beam with approximately the characteristics listed in Table 22.

  Note: Special care must be taken when adjusting the filament current. The knob is very sensitive and too much current will burn the filament.

  Note: The extraction voltage, Einzel lens voltage and filament current should be ramped up slowly over a period of 5 to 10 minutes.

Table 23: Example of the values of different parameters of SIR to produce bunches with the characteristics listed in Table 22.

Parameter	Value	Comment
Extraction Voltage	20 kV	As read by 'PowerSuppliesControls' program.
Einzel Lens Voltage	16.5 kV	
Gas Pressure in the Source	~ 1-10 mTorr	There is not direct way to measure the gas pressure in the source. The pressure in the injection line, ring and in the source inlet are monitored instead.
Gas Pressure in the ring	~ $6 \cdot 10^{-8}$ Torr	As read from ion gauge controllers (Figure 105). This pressure in the ring corresponds to the right source working pressure.
Gas Pressure in the Source inlet	~ 0.01-0.1 Torr	As read from Pirani gauge controller.

Injection Line Dipole Current	109.1 A	As read by digital multimeter connected to the controller of the Zero-flux transformer. (Figure 98)
Ring Dipoles Current	108.6 A	
Ring Dipole correctors: Magnets 1& 2 Magnets 3 & 4	+ 0.3 A - 0.3 A	As read by the dipole correctors power supplies.
Repetition Frequency	1 kHz	As read by frequency counter.
Arc Voltage	100 V	As read by analog indicator of arc P.S.
Arc Current	0.4 A	As read by digital multimeter next to power supply. The arc current is adjusted by slowly increasing the filament current keeping the arc voltage to 100 V.
Filament Voltage	~ 5 V	The filament voltage is not really adjusted. The knob should be set in such a way that the filament current is not limited by the maximum voltage drop.
Filament Current	~ 35 A	The filament current should be increased until the arc current reaches 0.4 A. The resistance of the source filament will increase over time as it deteriorates thus decreasing the needed filament current.

Inj. Line Steering	IL_ST_1X± IL_ST_1Y± IL_ST_2X± IL_ST_2Y±	0 V	As read by the control program of the CAEN power supply for Slots 0 and 1. (Figure 99)
Inj. Line Triplet	IL_QUAD_1±	0 V	
	IL_QUAD_2±	± 400 V	
	IL_QUAD_3±	± 800 V	
Chopper Plates		± 3500 V	
Inflector Plates 1		±2400 V	
Inflector Plates 2		±2280 V	
Deflector Plates		±2000 V	
Ring Steering	RG_ST_1Y± RG_ST_2Y± RG_ST_3Y± RG_ST_4Y±	0 V	As read by the control program of the CAEN power supply for slots 2 and 3.
Electron Shields		- 150 V	
Ring Quad		0 V	
Beam Energy		20.9 keV	As read by digital delay line control program.
Bunch Length		475 mm	
Tail Length		1 µs	
Ion		H_2^+	

A.2. – Procedure to turn off SIR

- Slowly turn down to zero the filament current. (Figure 96)

- Turn down to zero the arc voltage.

- Turn down to zero (in 10 A steps) the current in the ring and injection line magnets using the program 'PowerSuppliesControls'. (Figure 43)

- Turn off all the CAEN high voltage power supply channels using program 'HVPS Controller' (Figure 99). Close the program.

- Turn off the CAEN power supply.

- Retract the phosphor screen at the injection point (Figure 100).

- Retract emittance measurement system slits using program 'ScanningSlits' if necessary.

- Retract scanning wires using program 'ScanningWires' if necessary.

- Close needle valve using extension rod. (Figure 94)

- Close hydrogen tank valve. (Figure 95)

- Turn down to zero the Einzel lens voltage. Then, turn off the power supply. (Figure 96)

- Turn down to zero the extraction voltage. Then, turn off the power supply.

- Verify sound alarm is on. The purpose of the alarm is to warn the user if the high voltage is still on when the cage is opened. This event should only happen if the high voltage relay, used to ground the whole system automatically, fails. The alarm will also sound every time the system is turned off or the high voltage is set below a hundred volts. The purpose of

the alarm in this mode is to let the user know that the alarm is working. If the alarm does not sound, the electronics department should be contacted.

- Turn off the extraction power supply. The sound alarm should still be on.

- Push the STOP button located underneath the safety electric box in between Ion source cage and LCW manifold wall. (Figure 96)

- Verify the sound alarm went off.

- Verify high voltage monitor reads zero kV and high voltage light is off.

- Unlock and open the door of the high voltage cage. (Figure 93)

- **Ground high voltage parts with grounding rod.**

Note: Even though all the high voltage parts of the system are grounded automatically when the door is unlocked or the STOP button is pressed, they must be manually grounded to guarantee personal safety if automatic system fails.

Note: The ion source hardware and its power supplies must be grounded with the grounding rod independently. A short in the cable connecting them would leave one of them floating at high voltage.

- Close the right angle valve in the cage. (Figure 94)

- Turn off digital multimeter in the cage. (Figure 96)

- Close door of the high voltage cage.

- Close the main low conductivity water (LCW) supply valve.

- Close the main LCW return valve.

Note: Closing the supply valve before closing the return valve guarantees that the pressure in the water circuits is not too high thus preventing leaks.

A.3. – Procedure to replace ion source filament

- Close valve separating injection line from ring.

- Follow procedure to vent the injection line.

- Follow the procedure to clean the hydrogen line. Skip the last step. Do not let hydrogen back into the line.

- Disconnect all the cables from the source including the filament and arc cables, Pirani gauge, temperature sensors…

- Disconnect gas line. (Figure 94)

- Disconnect water cooling lines.

- Disconnect isolation rod from needle valve.

- Unscrew the four clamping screws. (Figure 102)
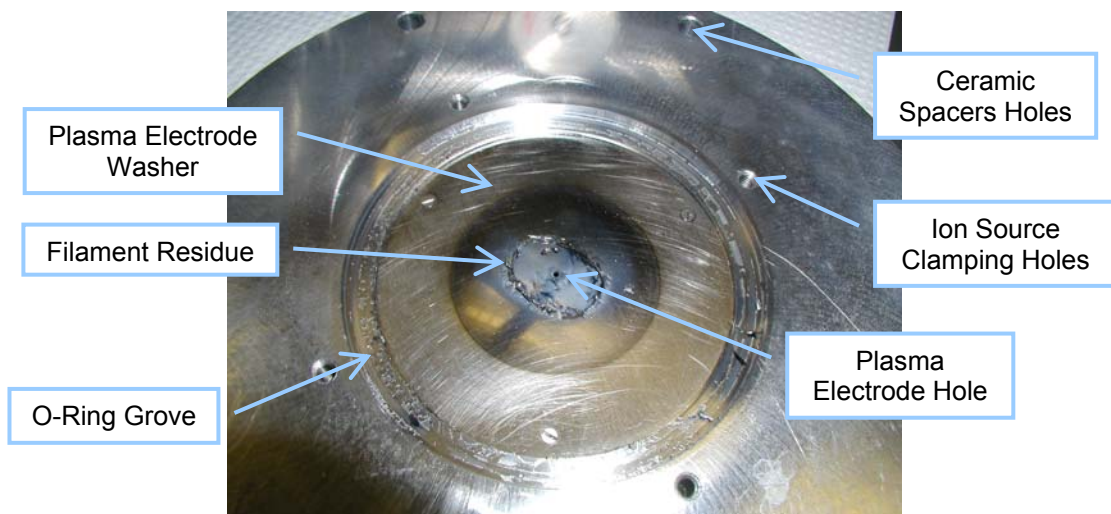
Figure 102: Picture of the flange that holds the ion source and the plasma electrode washer.

- Carefully remove ion source and gas handling system.

- Cover plasma electrode hole while plasma electrode washer and the o-ring grove are cleaned. Any residue falling through this hole may deposit in top of the puller producing a spark when high voltage is turned back on. This could damage the polished surface of the puller.

- Remove broken filament. (Figure 103)

- Remove the o-ring and carefully clean it. Inspect it for scratches and if it is in good condition, cover it with vacuum compatible grease. If it is damaged, replace it with a new Viton o-ring. (Viton is rated to resist higher temperatures.)
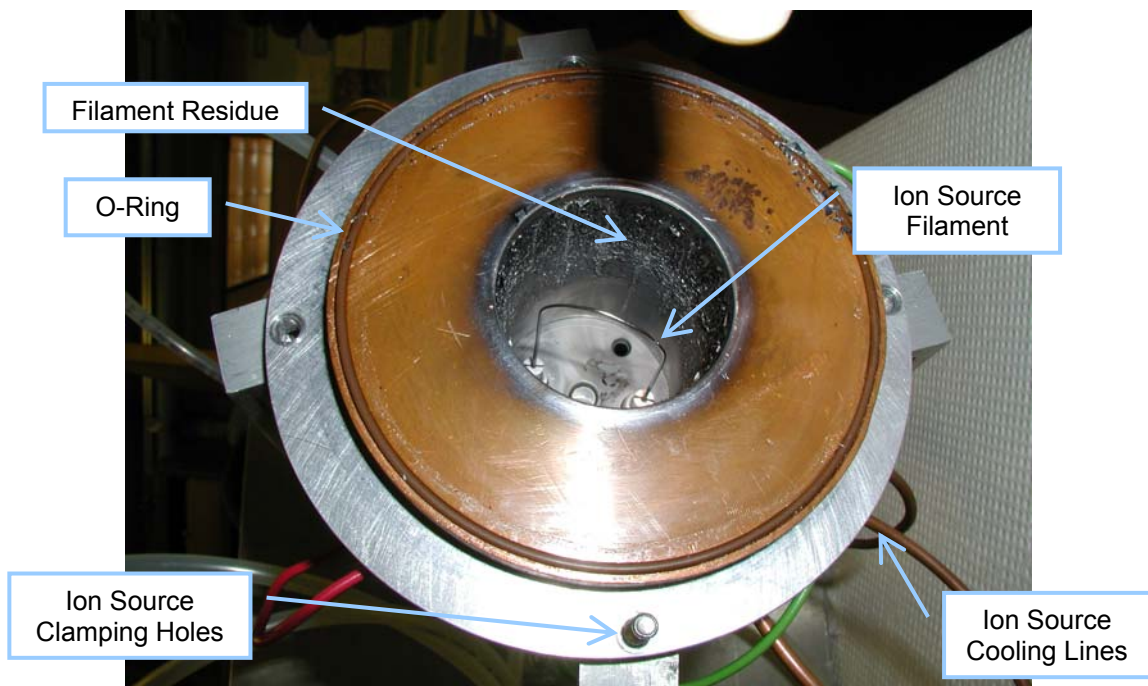
Figure 103: Picture of the broken filament in the ion source

- Clean the filament residue deposited in the ion source internal walls and elsewhere.

- Install new filament. The filaments are made out of a modified thoriated molybdenum welding rod.

- Install the Viton o-ring.

- Install the ion source. Attach the four clamping screws.

- Connect all the cables, water cooling lines and gas line as they were before. The ion source wiring is described in Figure 5.

- Follow procedure to pump the injection line.

- Follow procedure to clean hydrogen line.

A.4. – Procedure to clean the hydrogen line

- Close right angle valve inside the cage. (Figure 94)

- Slowly open needle valve to release the hydrogen trapped between it and right angle valve. The pressure in between the two valves is ~ 20 psi. If the valve is not opened slowly, the hydrogen would be released too quickly and the ion gauges and turbo pumps would automatically turn off.

- Close valve of hydrogen tank. (Figure 95)

- Close compressed air driven valves of the two injection line turbo pumps (Figure 100). The pressure in the injection line will go up since turbo pumps are not working in this mode. The pressure will quickly go down again when the valves are opened again.

- Open hydrogen line valve. (Figure 95)

- Wait until pressure in hydrogen line is below 500 mTorr as measured by thermocouple gauge in the line. (Figure 105)

- Close hydrogen line valve.

- Wait until pressure in hydrogen line is below 200 mTorr as measured by thermocouple gauge in the line.

- Open compressed air driven valves of the two injection line turbo pumps.

- If the injection line is not going to be vented, open the hydrogen tank valve and verify that the pressure after the regulator is ~ 20 psi.

A.5. – Procedure to vent the ring

- Close the right angle valve in the ion source cage. (Figure 94)

- Slowly open the needle valve to release the hydrogen trapped in between right angle valve and needle valve. The pressure in between the two valves is ~ 20 psi. If the valve is not opened slowly, the hydrogen would be released too quickly and the ion gauges and turbo pumps would automatically turn off.

- Close the gate valve that separates the injection line and the ring if just the injection line or the ring needs to be vented. (Figure 104)

- Turn off the ion gauges. (Figure 105)

- Close the compressed air controlled valves in between the turbo pumps and the mechanical pumps. (See Figure 100 and Figure 104)

- Turn off the turbo pumps (Figure 105).
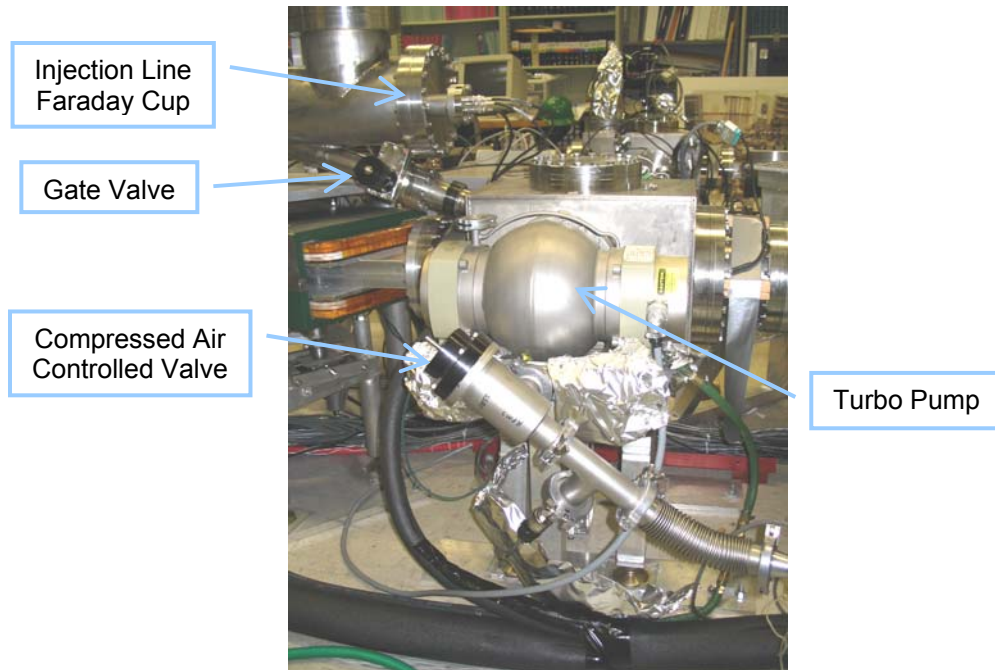
Figure 104: Picture of the box in between two of the ring magnets where the beam injected.

- Wait until turbo pumps have stopped rotating (Typically ~ 30 minutes). To verify that they have stopped, they can be briefly turned on and the speed indicator can be checked.

  NOTE: The rotating blades of the turbo pumps will be damaged if air flows into the chamber through them before they have fully stopped.

- Shut down the cooling water for the turbo pumps.

- Unplug the power of the power-off safety valve in between turbo pumps and mechanical pumps. (Figure 95)

- Turn off the mechanical pumps.

- If the gate valve in between injection line and ring is closed, the machine can be left in this mode for weeks or months if necessary. Not much water will be trapped in the walls since the pressure inside will stay in the

hundreds of millitorr range for a long time thus reducing the pumping time to go back to the high vacuum conditions afterwards.

- Slowly open venting valve (Figure 106). The system can be vented either with air or with dry nitrogen to minimize the amount of water trapped in the walls (i.e. the pumping time will be reduced).
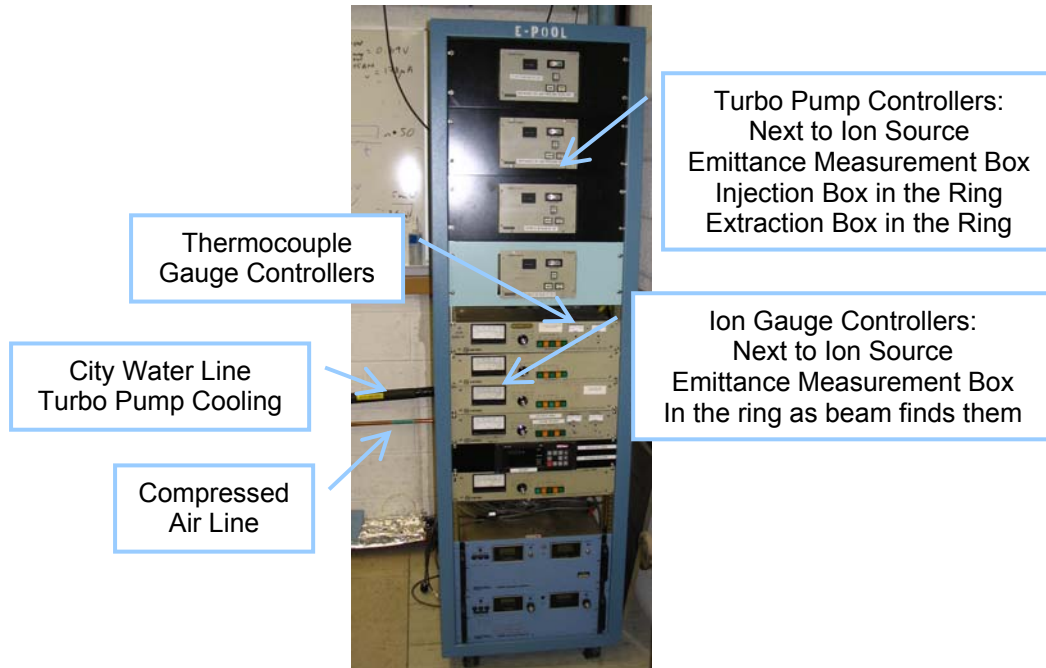
Figure 105: Picture of the vacuum system control area.

A.6. – Procedure to pump in the ring

- Close venting valve. (Figure 106)

- Turn on the mechanical pumps.

- Plug the power of the power-off safety valve in between turbo pumps and mechanical pumps. (Figure 95)

- Open the compressed air controlled valves in between the turbo pumps and the mechanical pumps. (Figure 100 and Figure 104)

197
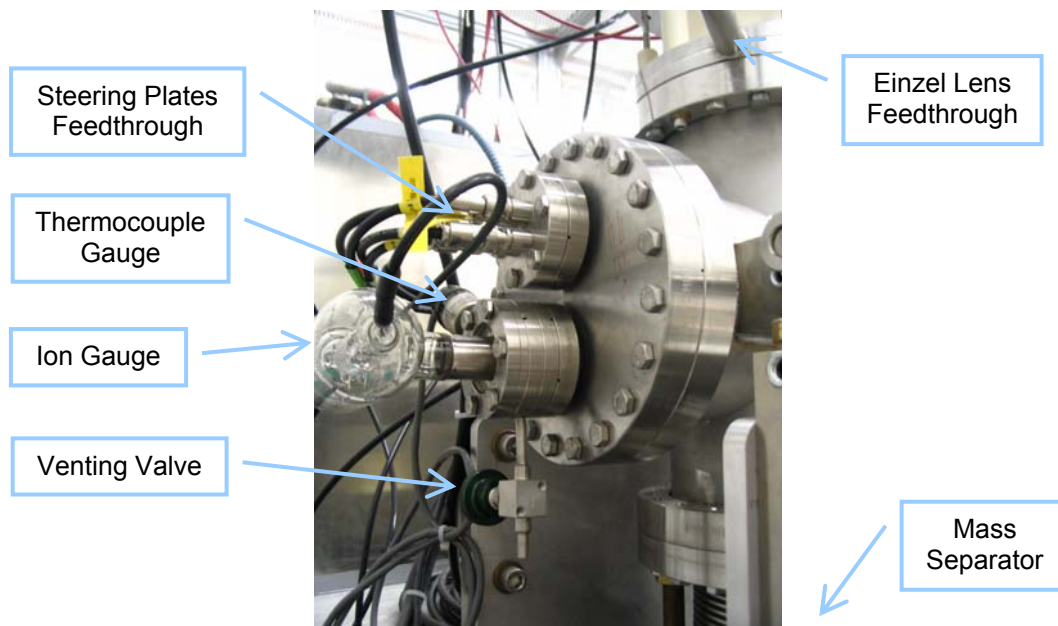
Figure 106: Picture of the venting valve and one of the thermocouple gauges used in the injection line of SIR.

- Wait until the pressure inside the vacuum chamber is around 100 mTorr as read by the thermocouple controllers (Figure 106). It should take ~ 30 minutes to reach this pressure.

- Open the cooling water for the turbo pumps.

- Turn on the turbo pumps (Figure 105). Wait until they reach full speed.

- Turn on the ion gauges.

- Wait until the pressure in the ring goes below 10^{-7} Torr before restarting experiments.

A.7. – Procedure to clean components to be installed inside vacuum chamber

- Wear powder free latex gloves during the whole cleaning and installation procedure. Use q-tips to reach inside the tapped holes or difficult areas in every step that follows.

- If the material of the piece is copper, scrub thoroughly with a Scotch Brite sponge damped in lemon juice. Lemon juice is very effective to remove the oxide layer formed in copper when in contact with air.

- Rinse with abundant water.

- If the material of the piece is aluminum, stainless steel, copper, alumina or macor, scrub thoroughly with a Scoth Brite sponge damped in a solution of Alconox detergent. Most of the oil used when the pieces are machined will be removed in this step.

- Rinse with abundant water.

- Use acetone to clean the detergent and water residue.

- Use ethanol to clean the acetone residue.

- Dry the ethanol spraying with compressed air.

- Install the piece in the vacuum chamber as soon as possible after it has been cleaned.

APPENDIX B: CONTROL PROGRAMS DESCRIPTIONS

B.1. – Scanning Wires

Every time the program is started, the user will be asked to choose an initialization file. This file contains the information listed in Table 24 about each of the drives.

Parameter	Comment
Name = "Box2 X"	Name of the Scanning Wire.
Use = TRUE	Is this drive going to be used?
Reset = TRUE	Does this drive need to be reset when the program is restarted?
Steps/mm = 1575	Relationship between stepper motor steps and linear distance moved.
SwToAxis = -58.62	Distance between limit switch and beam axis (mm).
RestPosition = -49	Distance between beam axis and rest position (mm).
NegativeLimit = -56	Maximum distance from beam axis where movement is allowed (mm) in negative direction.
PositiveLimit = 38	Maximum distance from beam axis where movement is allowed (mm) in positive direction.
Speed = 4000	Maximum movement speed (steps/second).
Acc = 10000	Maximum movement acceleration (steps/second^2).
Channel # = 7	Low current multiplexer channel where wire is connected.

Table 24: Scanning wires initialization parameters

The program will reset the drives and move them to the rest position if specified in the init file before the user can operate the program. (Figure 34)

The yellow vertical cursor specifies the current position of the wire. The red vertical cursor specifies the position where the wire is going to move when the "Move" button is pressed. Change the number in the control "To" or move directly the cursor to change this value. Press the "Continuous" button instead of the "Move" button to continuously move the wire between its starting and final position until the button "Continuous" is pressed again.

Change the vertical scale (Current density) to change the scale in which the picoammeter acquires the data.

All the profiles, that are taken, will be displayed in the graph until the corresponding "Delete" button is pressed. The last profile taken will be displayed as number 1, displacing the previous ones down in the list.

Press the button "Save" to save the data currently displayed in the corresponding graph. A new window with the information to be saved will be opened at which point, the user will be able to modify it if needed. Press the "Save" button in this window to save the modified data.

Acquire three different profiles with different voltages in the inflector plates before pressing the "Vertical matching" button to center the beam vertically. A new window will open where the used voltage values can be specified. The correct values to center the beam will appear afterwards. Proceed in a similar way to center the beam radially.

A very similar program was developed to use the scanning slits of the emittance measurement system. Please, use these instructions as a reference to use that program.

BIBLIOGRAPHY

List of papers published about the SIR project:

J. Rodriguez, E. Pozdeyev, F. Marti. "Control System of the Small Isochronous Ring". EPAC 2004. Page 830.

J. Rodriguez, E. Pozdeyev, F. Marti, R. York. "Experimental Results of the Small Isochronous Ring". EPAC 2004. Page 2191.

J. Rodriguez, E. Pozdeyev, F. Marti. "Beam Diagnostics of the Small Isochronous Ring". EPAC 2004. Page 2795.

F. Marti, E. Pozdeyev, J. Rodriguez. "Study of Space Charge Effects using a Small Storage Ring that works in the Isochronous Regime". Cyclotrons 2004.

J. Rodriguez, E. Pozdeyev, F. Marti, R. York. "Initial experimental Results of the Small Isochronous Ring". PAC 2003. Page 2649.

E. Pozdeyev et al. "Progress Report on the Small Isochronous Ring Project at NSCL". PAC 2003. Page 138.

E. Pozdeyev, J. Rodriguez. "Computer Simulations of the Beam Dynamics in the Small Isochronous Ring Project at NSCL". EPAC 2002. Page 1398.

E. Pozdeyev, F. Marti, J. Rodriguez. "Small Isochronous Ring Project at NSCL". EPAC 2002. Page 1395.

J. Rodriguez, E. Pozdeyev, F. Marti. "Injection Line of the Small Isochronous Ring". EPAC 2002. Page 1401.

E. Pozdeyev. "A Small Isochronous Ring for experimental study of the Longitudinal Space Charge Effect in Isochronous Cyclotrons". PAC 2001. Page 3549.

E. Pozdeyev. "A fast Code for simulation of the Longitudinal Space Charge Effect in Isochronous Cyclotrons". Cyclotrons 2001. Page 411.

General bibliography:

A. Chao. "Handbook of Accelerator Physics and Engineering". World Scientific.

D. Carey. "The optics of charged particle beams". Harwood academic publishers.

J. Livingood. "Principles of cyclic particle accelerators". D. Van Nostrand Company.

[1] M. M. Gordon. "The longitudinal space charge effect and energy resolution". Cyclotrons 1969. Page 305.

[2] P. A. Schmelzbach, et al. "The PSI high intensity cyclotron and its extrapolation to a 10 MW driver". High Intensity and High Brightness Hadrons Beams. 2002. Page 197.

[3] E. Pozdeyev. "CYCO and SIR: New Tools for Numerical and Experimental Studies of Space Charge Effects in the Isochronous Regime". Dissertation. Michigan State University, 2003.

[4] V. P. Dmitrievsky, et al. "The high current cyclotron complex for an electronuclear way of production of energy". Cyclotrons 2001. Page 434.

[5] L. Calabretta, et al. "A superconducting ring cyclotron to deliver high intensity proton beams". EPAC 2000. Page 918.

[6] T. Kuo, et al. "A possible high current H- injector for cyclotron-based energy amplifier accelerator".

[7] G. Kim, et al. "A superconducting isochronous cyclotron stack as a driver for a thorium-cycle power reactor". Cyclotrons 2001. Page 437.

[8] Application Notes Tektronix. "Understanding Oscilloscope Bandwidth, Rise Time and Signal Fidelity".

[9] M. Bellato, A. Dainelli, M. Poggi. "Design and test for the fast Faraday Cup of the ALPI post-accelerator". Nuclear Instruments and Methods in Physics Research A 382. 1996. Page 118.

[10] Princeton Scientific Corporation. "Coaxial Faraday Cup Type DF040". www.princesci.com

[11] A. Chao. "Handbook of Accelerator Physics and Engineering". World Scientific.

[12] Y. Lee et al. "A Compact filament-driven Multicusp Ion Source". Nuclear Instruments and Methods in Physics Research B 119. 1996. Page 543.

[13]   Huashun Zhang. "Ion Sources". Springer. 1999

[14]   David A. Dahl. "SIMION 3D v.7.0. User's manual". 2000.

[15]   M. Berz. "COSY Infinity". www.bt.pa.msu.edu/index_files/cosy.htm.

[16]   "TOSCA". Vector Fields. www.vectorfields.com

[17]   M. S. Zucker, J. W. Bittner. "A Faraday Cup with High Frequency Response for a 200 MeV LINAC Proton Beam". 0-7803-0135-8/91 IEEE. Page 1270.

[18]   "LabVIEW 7.0", National Instruments, www.ni.com.

[19]   "MatLab 6.5". The MathWorks. www.mathworks.com.

[20]   M. P. Stockli et al. "Self-Consistent, Unbiased Exclusion Methods of Emittance Analysis". PAC 2003. Page 527.

[21]   M. P. Stockli et al. "Variable Exclusion Method for Self-consistent, Unbiased Emittance Analysis". EPAC 2004.

[22]   M. P. Stockli, R. Welton, M. Leitner. "Emittance Measurements and Analysis". ECRIS 2004.

[23]   "Tcl/Tk". www.tcl.tk.

[24]   "IMAQ". National Instrument. www.ni.com.

[25]   "PXI Techonology Review". www.pxionline.com.